Science and Technology of Nuclear Installations

Passive Safety Systems in Advanced PWRs

Guest Editors: Xu Cheng, Yanhua Yang, Walter Ambrosini, and Dino A. Araneo

Passive Safety Systems in Advanced PWRs

Science and Technology of Nuclear Installations

Passive Safety Systems in Advanced PWRs

Guest Editors: Xu Cheng, Yanhua Yang, Walter Ambrosini, and Dino A. Araneo

Contents

Hindawi Publishing Corporation
Science and Technology of Nuclear Installations
Volume 2009, Article ID 643950, 2 pages
doi:10.1155/2009/643950

Editorial
Passive Safety Systems in Advanced PWRs

Xu Cheng,[1] Yanhua Yang,[1] Walter Ambrosini,[2] and Dino A. Araneo[3]

[1] *Shanghai Jiao Tong University, Shanghai, China*
[2] *Department of Mechanics, Nuclear and Production Engineering (DIMNP), University of Pisa, Italy*
[3] *San Piero a Grado Research Group (GRNSPG), Department of Mechanics, Nuclear and Production Engineering (DIMNP), University of Pisa, Pisa, Italy*

Correspondence should be addressed to Xu Cheng, chengxu@sjtu.edu.cn

Received 31 December 2009; Accepted 31 December 2009

Passive safety systems have been widely applied to advanced water-cooled reactors (WCRs), to enhance the safety of nuclear power plants. For the near term and medium term, the Chinese government decided for advanced pressurized water reactors with an extensive usage of passive safety systems. The International Workshop on Passive Safety Systems of Advanced PWR (IPASS'08) was held in Shanghai on April 28–30, 2008, coorganized by the Shanghai Jiao Tong University and the Pisa University. The main purposes of the Workshop IPASS'08 are (a) to provide a platform to the international nuclear community for exchanging research results and design experience on passive safety systems applied to advanced WCR and (b) to enhance the contact and collaboration between the Chinese research institutions and international partners.

More than 100 scientists and nuclear engineers from eight countries, that is, Canada, China, France, Germany, Italy, Korea, Pakistan, and USA, were participating in this workshop. More than 60 technical papers were presented covering the following topics:

(a) safety injection and decay heat removal systems,

(b) passive containment cooling systems and hydrogen safety research,

(c) passive systems for severe accident mitigation,

(d) assessment and application of numerical tools,

(e) single effect and integral verification experiments,

Eight papers were selected for this special issue. The first paper of Cheng et al. [1] gives a summary about the Chinese research activities on passive safety systems of advanced PWR. Experimental studies and validation of numerical codes are presented in the following two papers [2, 3]. The paper of Gou et al. [4] deals with numerical analysis of the performance of passive safety systems; whereas the methodology for the reliability assessment of passive safety systems is investigated in the paper of Pierro et al. [5]. The last three papers are devoted to hydrogen safety issue, which is a main topic of the workshop [6–8].

The editors of this special issue express thanks to all authors for their contribution.

Xu Cheng
Yanhua Yang
Walter Ambrosini
Dino A. Araneo

References

[1] X. Cheng, Y. H. Yang, Y. Ouyang, and H. X. Miao, "Role of passive safety systems in Chinese nuclear power development," *Science and Technology of Nuclear Installations*, vol. 2009, Article ID 573026, 7 pages, 2009.

[2] M. Carelli, L. Conway, M. Dzodzo, et al., "The SPES3 experimental facility design for the IRIS reactor simulation," *Science and Technology of Nuclear Installations*, vol. 2009, Article ID 579430, 12 pages, 2009.

[3] W. Reactors, W. Ambrosini, M. Bucci, N. Forgione, A. Manfredini, and F. Oriolo, "Experiments and modelling techniques for heat and mass transfer in light," *Science and Technology of Nuclear Installations*, vol. 2009, Article ID 738480, 11 pages, 2009.

[4] J. Gou, S. Qiu, G. Su, and D. Jia, "Thermal hydraulic analysis of a passive residual heat removal system for an integral pressurized water reactor," *Science and Technology of Nuclear Installations*, vol. 2009, Article ID 473795, 12 pages, 2009.

[5] F. Pierro, D. Araneo, G. Galassi, and F. D'Auria, "Application of REPAS methodology to assess the reliability of passive safety systems," *Science and Technology of Nuclear Installations*, vol. 2009, Article ID 768947, 18 pages, 2009.

[6] J. Xiong, Y. Yang, and X. Cheng, "CFD application to hydrogen risk analysis and PAR qualification," *Science and Technology of Nuclear Installations*, vol. 2009, Article ID 213981, 10 pages, 2009.

[7] P. Royl, J. R. Travis, W. Breitung, J. Kim, and S. B. Kim, "GASFLOW validation with panda tests from the OECD SETH benchmark covering steam/air and steam/helium/air mixtures," *Science and Technology of Nuclear Installations*, vol. 2009, Article ID 759878, 13 pages, 2009.

[8] J. Xiao, J. R. Travis, and W. Breitung, "Non-Boussinesq integral model for horizontal turbulent buoyant round jets," *Science and Technology of Nuclear Installations*, vol. 2009, Article ID 862934, 7 pages, 2009.

Hindawi Publishing Corporation
Science and Technology of Nuclear Installations
Volume 2009, Article ID 573026, 7 pages
doi:10.1155/2009/573026

Review Article

Role of Passive Safety Systems in Chinese Nuclear Power Development

X. Cheng,[1] Y. H. Yang,[1] Y. Ouyang,[2] and H. X. Miao[2]

[1] *School of Nuclear Science and Engineering, Shanghai Jiao Tong University, Dongchuan Road 800, Shanghai 200240, China*
[2] *Experts Committee, State Nuclear Power Technology Cooperation, 17 Financial Street, Xicheng District, Beijing 100032, China*

Correspondence should be addressed to X. Cheng, chengxu@sjtu.edu.cn

Received 14 November 2008; Accepted 9 April 2009

Recommended by Dino A. Araneo

Passive safety systems have been widely applied to advanced water-cooled reactors, to enhance the safety of nuclear power plants. The ambitious program of the nuclear power development in China requires reactor concepts with high safety level. For the near-term and medium-term, the Chinese government decided for advanced pressurized water reactors with an extensive usage of passive safety systems. This paper describes some important criteria and the development program of the Chinese large-scale pressurized water reactors. An overview on representative research activities and results achieved so far on passive safety systems in various institutions is presented.

1. Introduction

The operating experience of more than five decades civil utilization of nuclear energy shows significant advantages of nuclear power with respect to environment protection, economic competitiveness, and power supply stability. Nowadays nuclear power produces about 16% of the total electricity worldwide. The complicated and unstable situation of the international relationship and the rapidly growing energy demand force the international community to reassess the role of nuclear power.

Since the start of the economic reform in the 1970s, the Chinese economics has been undergoing rapid development. One of the bottlenecking issues in the Chinese economics development is a sustainable and environment friendly energy supply. By the middle of this century the primary energy demand in China will be four times as that of today. For the time being, more than 70% of the primary energy comes from fossil fuel. A higher portion (about 80%) is found in the electricity production. Development of environment friendly energy supplies becomes thus a crucial issue in the future Chinese economy. Due to the well-known limitation in renewable energy and hydro-power, nuclear power is considered as a safe, clean, sustainable and economic energy source.

In November 2007, China issued an ambitious program of mid-term nuclear power development [1]. The total nuclear power installation will reach 40 GW or higher by 2020. According to the estimation of the Chinese nuclear experts, the nuclear power installation will be around 250 GW by the middle of this century. That is about 15% of the total electricity production at that time. Figure 1 shows schematically the expected nuclear power development in China.

From the technology point of view, the development of nuclear power technology worldwide has undergone four generations. To the first generation belong mainly the demonstration plants of small power capacity. Based on the experience gathered from the first generation, many standardized concepts of nuclear power plants (NPPs) were proposed and the second generation of NPP was born. The most nuclear power plants operating nowadays belong to the second generation. After the accidents of TMI and Chernobyl intensive efforts were made to improve the safety features of the second generation NPP, and the third generation of nuclear power technology was developed. Compared to the second generation, the third generation owns a much higher safety level. The core damage frequency (CDF) is lower than 10^{-5} per reactor-year. It is expected that in the next 2-3

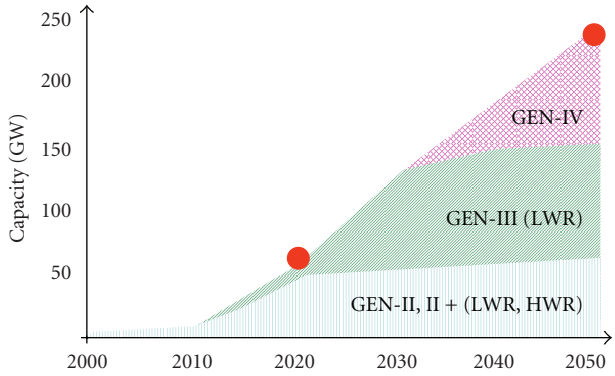

Figure 1: Expected nuclear power development in China.

decades, the new constructed NPP use mainly reactors of generation III (GEN-III).

Various types of GEN-III pressurized water reactors (PWR) are now available. Two of the most representative ones are AP1000 of Westinghouse [2] and EPR of AVERA [3]. One of the common features of the GEN-III reactors is their enhanced safety performance. This is achieved using different approaches, from the improvement of human reliability to the introduction of completely new subsystems. Passive safety systems are widely applied, especially in the AP1000 concept of Westinghouse. Passive safety systems are recommended to be applied wherever it is feasible.

As shown in Figure 1, water-cooled reactors of GEN-II or GEN-II extension will make the major contribution to the nuclear power generation until 2020. After then light water reactors (LWRs) of GEN-III will start to be built in large scale. This paper discusses the state of the art and the future development of the technology lines of Chinese NPP. Emphasis will be put on the application of passive safety systems. A brief overview of research activities on passive safety systems is given.

2. Chinese Nuclear Power Technology

Based on the experiences gathered worldwide in the nuclear power development of the past five decades, attention has to be paid to the following issues, to ensure a safe, economic, and fast development of nuclear power:

(i) selection of technology lines;

(ii) realization of self-reliance technology;

(iii) nationwide coordination.

2.1. Selection of Technology Lines. It is well agreed that realization of the ambitious nuclear power program requires urgently the decision of the technology lines for the future nuclear power plants. At present 11 units are under operation with a total installed capacity of 9 GW, and 12 units are now under construction with an installed capacity of 12 GW. There are additional 18 units; which construction will start in the next three years. All of these NPP units consist of water-cooled reactors. Therefore, water-cooled reactors have clearly been selected as the main reactor type for the next decades.

The operating NPP units are from four different technology lines, that is, the Chinese PWR of 300 MW/600 MW class, the Canadian CANDU of 700 MW, the French PWR of 900 MW, and the Russian WWER of 1000 MW. The existing experience emphasizes the necessity to reduce the number of technology lines for the future NPP. It is highly desired to define a single major technology line for the future Chinese nuclear power generation. Considering the Chinese specific situation and the experience gathered in the national and international nuclear community, it is well agreed and decided that water-cooled reactors of GEN-III will be the main reactor type for the future Chinese nuclear power generation, at least for the mid-term. Passive safety systems should be key features of the Chinese GEN-III PWR. In addition it should fulfill the following requirements:

(i) system simplicity;

(ii) economical competitiveness;

(iii) operating reliability and easy maintainability;

(iv) advanced passive engineering safety features;

(v) compliment with the latest safety codes for severe accident prevention and mitigation measures issued by China National Nuclear Safety Administration (NNSA) and IAEA;

(vi) digital instrumentation and control system;

(vii) advanced human factor engineering technique and advanced main control room.

The above technology requirements justify the choice of AP1000 technology of Westinghouse as the reference technology for the Chinese GEN-III PWR.

2.2. Self-Reliance Technology. As soon as the future technology lines are defined, extensive efforts should be made to develop self-reliance technology, so as to reduce the strong technology dependence on other countries, as it is at the present stage. To achieve the mid-term target, China issues twofold strategy. In one side construction of NPPs based on existing GEN-II PWR technology will be continued. Minor modification of the GEN-II PWR power plants will be undertaken with respect to reactor fuel management and safety performance. The improved GEN-II PWR power plants make the main contribution to the newly installed nuclear power plants in the next 10 years. Most of the NPPs nowadays under construction or receiving the construction license do belong to this category, for example, Qinshan Phase-II extension which bases on Chinese PWR technology of 600 MW class and CPR (improved reactor type based on French M310).

In the other side large efforts are made to accelerate the self-reliance process of the GEN-III PWR technology. The Chinese government has issued a large national program to develop technology of advanced large-scale pressurized water reactors [4] and to accelerate the self-reliance of the

Chinese nuclear technology. The Nuclear Power Self-reliance Program has been launched with Sanmen project in Zhejiang Province and Haiyang project in Shandong Province as supporting projects [5]. Three steps will be taken for the development of the "Chinese large-scale advanced PWR nuclear power plant."

(i) *Transfer of AP1000 technology*. In this stage, design and construction of 4 units AP1000 will take place under the guidance of Westinghouse. Chinese engineers and scientists will actively participate in this procedure.

(ii) *Design of modified AP1000 NPP*. Based on the experience gathered in the first stage, the existing AP1000 will be modified. This work will be carried out by Chinese engineers and scientists in collaboration with Westinghouse.

(iii) *Design and construction of self-reliance large-scale PWR*. The Chinese AP1000 will be extended with respect to enlarging reactor power (larger than 1400 MW) and improving economics. At the end of this stage (2020) a prototype reactor of the Chinese self-reliance GEN-III PWR will be constructed and put into operation.

2.3. Nationwide Coordination. Realization of the self-reliance of nuclear technology requires a high-quality coordination, including various institutions for design, research, manufacture, and education. For this purpose a new organization, the State Nuclear Power Technology Corp. LTD (SNPTC), was founded in 2007. SNPTC is responsible for the self-reliance of the Chinese GEN-III PWR technology and has established subcompanies for research, design, and manufacture, respectively. In addition, SNPTC is also the direct partner for Westinghouse related to the AP1000 technology transfer. The Contracts between SNPTC and Westinghouse signed on July 2007 came into force in September 2007. Four AP1000 units will be put into commercial operation from 2013 to 2015, respectively.

3. Research Activities on Passive Safety Systems

Passive safety systems for advanced PWR have achieved significant interests of Chinese nuclear community since 1980s [6]. Since that time China National Nuclear Corporation (CNNC) was developing an advanced Chinese PWR of 600 MW (AC600). The basic philosophy of AC600 is similar to that of AP600 of Westinghouse and equipped with sophisticated passive safety systems. Extensive R&D activities were carried out, especially at the Nuclear Power Institute of China (NPIC).

Studies on passive safety systems were also carried out with respect to small power water-cooled reactors. A low-temperature, integral type PWR is proposed by NPIC, as indicated in Figure 2, which utilizes passive systems for safety injection decay heat removal and containment pressure suppression [7]. The reactor thermal power is 250 MW. The primary loop has an operating pressure of 2.2 MPa and temperature of 158°C/199°C.

Table 1

Total height:	23 m
Volume scale:	1/395
Design pressure:	8.6 MPa
Design temperature:	316 C
Heating power:	500 kW

At the Institute of Nuclear and New Energy Technology (INET) of the Qinghua University, another type of small power integral water-cooled reactor design is proposed [8]. The reactor system is similar to that of the International Reactor Innovative and Secure (IRIS, [9]). No pumps are required for both normal and abnormal operating conditions. Two passive safety systems are applied, that is, passive decay heat removal and passive boron injection.

Recently, with the decision on the technology line for the Chinese GEN-III PWR passive safety systems attract again the major attention and interests of the Chinese nuclear community. R&D activities were initiated at various research institutions. The International Workshop on Passive Safety Systems in Advanced PWRs took place in Shanghai in April 2008, to provide a platform for the international nuclear community to exchange research results and design experience on the passive safety systems applied to advanced PWRs, to enhance the contact and collaboration between the Chinese research institutions and international partners, and to give the Chinese nuclear community and Chinese government authorities an insight into the actual research and design status and future research needs in the passive safety system of advanced PWRs.

In the frame of the AP1000 technology transfer, analysis of the performance of AP1000 passive safety systems has been carried out at various institutions such as Shanghai Nuclear Engineering Research and Design Institute (SNERDI) [10] and the Shanghai Jiao Tong University [11]. In addition, both experimental and numerical investigations were carried out at NPIC on the performance of passive safety systems proposed for large-scale PWR. Figure 3 shows schematically the experimental facility constructed at NPIC for passive decay heat removal systems of advanced Chinese PWR. Some technical specifications are shown in Table 1.

3.1. Passive Containment Safety Systems. As the last safety barrier containment integrity has achieved strong attention of the Chinese nuclear community. Passive containment safety systems were widely applied to advanced water-cooled reactors [13]. As a long-term passive decay heat removal AP1000 uses the natural convection of air combined with thermal radiation in the annuli between both containment shells. For the short-term (the first 72 hours) additional water-film evaporation heat transfer will be provided [2].

To investigate the cooling capability of this passive system and the involved microscopic mechanisms, both experimental and numerical studies are carried out at Shanghai Jiao

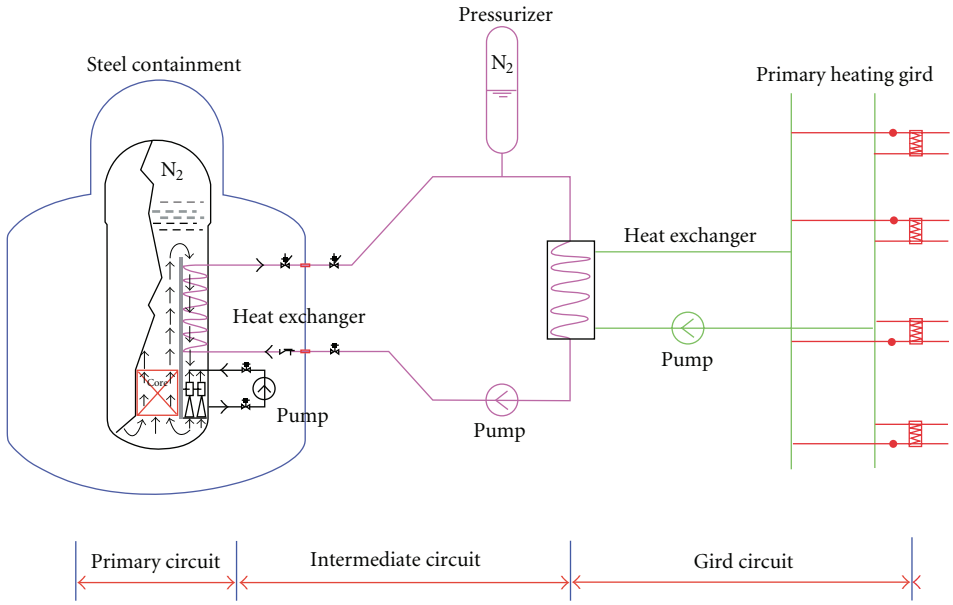

Figure 2: Low temperature, integral PWR proposed by NPIC [7].

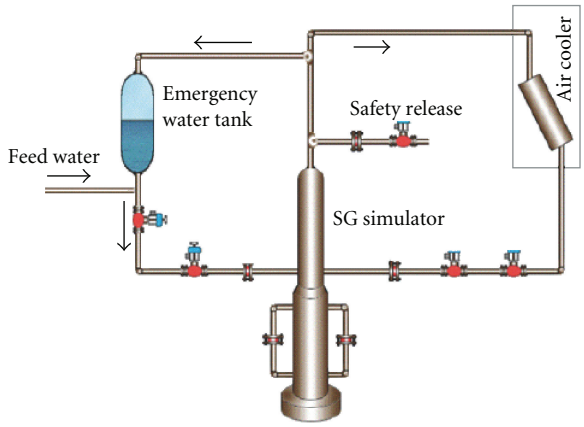

Figure 3: Decay heat removal test facility at NPIC [12].

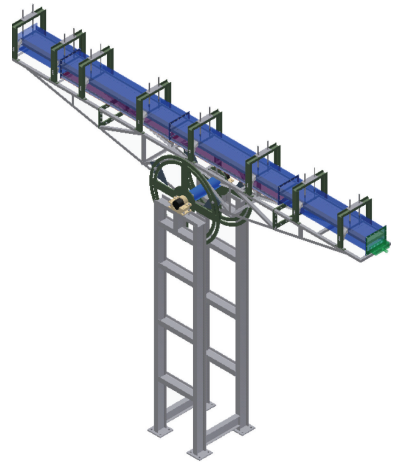

Figure 4: Test facility MICARE.

Tong University. Figure 4 shows the test section MICARE, which is a square flow channel with the maximum cross-section of 400 mm × 250 mm. One side of the channel is electrically heated. The heated wall consists of 16 heating plates, which are separately heated to achieve a well uniform distribution of the heated wall temperature. The orientation of the flow channel can be changed arbitrarily. The test section has a total height of 8 m, of which 6 m (in the middle) can be heated. The test section can be connected to an auxiliary equipment to realize a forced flow of air into the test channel using a compressor.

The heating power of each heated plate is separately controlled, to achieve a uniform wall temperature distribution. The wall temperature can be varied up to 200°C. The test facility is equipped among others with a large number of thermocouples to measure the distribution of wall temperatures. Hot-wire anemometer and thermocouples are applied to measure the air velocity and air temperature distribution in the flow channel. Calibrations were performed to determine the heat loss from the heated wall to the ambient surroundings at different values of the heated wall temperature.

In addition to the experimental work, numerical simulation is carried out, to understand the microscopic phenomena involved in the mixed convection in a square channel with various orientation. Figure 5 shows an example of numerical results, presenting the heated wall surface temperature along the middle line in the flow direction. The numerical results are obtained with CFD code using various low Reynolds number k-epsilon models. As seen, the selection of turbulence models affects strongly the numerical simulation.

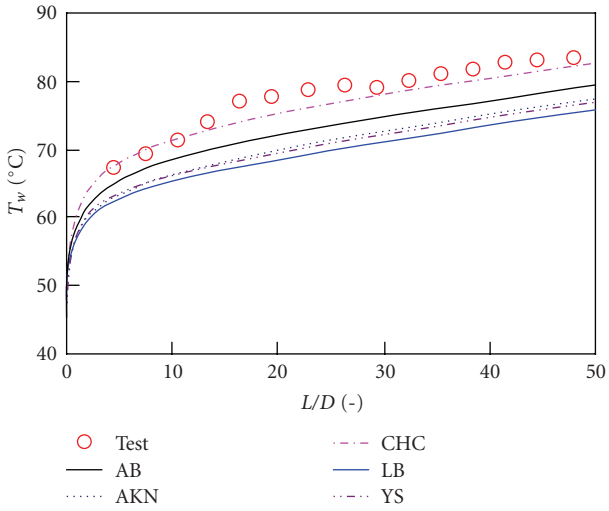

Figure 5: Comparison of numerical results with experimental data. AB: model of Abid; AKN: model of Abe/Kondoh/Nagano; CHC: model of Chang/Hsieh/Chen; LB: model of Lam/Bremhost; YS: model of Yang/Shih.

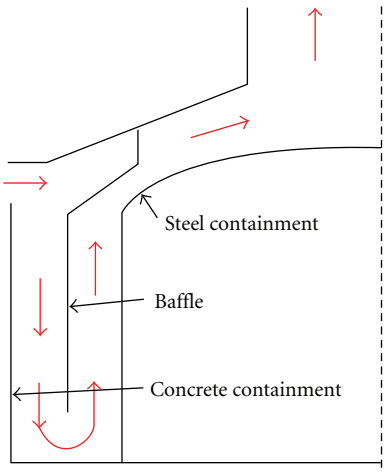

Figure 6: Containment model for lumped parameter analysis [x].

To assess the heat removal capability of AP1000 passive containment cooling system, simplified analysis using lumped parameter approach is carried out at SJTU [14]. The lumped parameter model is illustrated in Figure 6. Effects of various parameters on the heat removal capability are investigated. Figure 7 gives an example indicating the effect of the thermal conductivity of the buffer plate on heat removal. Results are obtained with a containment temperature of 150°C and the wall emissivity 1. It is seen that a higher thermal conductivity leads to an increase in heat removal of about 15%. A strong effect is observed in the region of low thermal conductivity (<0.5 W/m K). The maximum removable heat from the containment is about 7.5 MW.

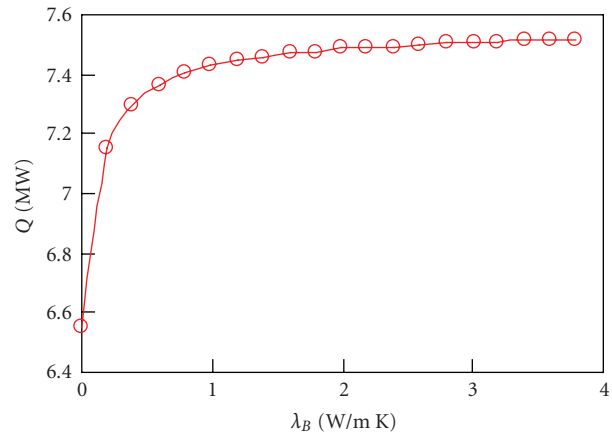

Figure 7: Effect of thermal conductivity of the buffer plate λ_B on heat transfer capability Q.

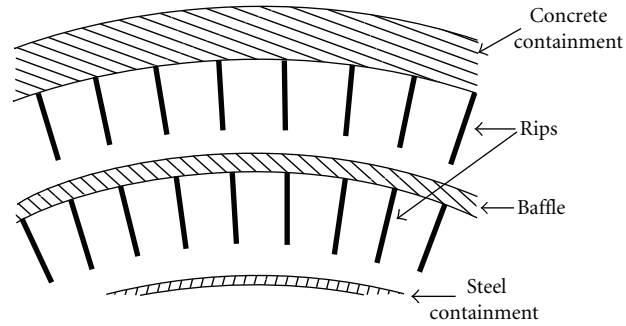

Figure 8: Improvement for heat removal using ribs [14].

According to the thermal power of AP1000 (3400 MWth) and the simplified decay heat curve

$$Q(t) = 0.062 \cdot Q_0 \cdot t^{-0.2}. \quad (1)$$

Here $Q(t)$ is the time dependent decay heat power, Q_0 the reactor thermal power before shutdown, and t time in seconds. The decay heat in an AP1000 goes down to the level 7.5 MW 40 days after the shutdown of the reactor. Obviously, this passive system is insufficient to remove decay heat and needs improvement, especially for the Chinese GEN-III PWR with a much larger thermal power. Therefore, various improvement suggestions are proposed. One of the possibilities to enhance the heat removal is to introduce ribs, as shown in Figure 8. Detailed analysis shows that with this new structure, an increase of 15% in heat removal capability can be achieved [14].

3.2. Ex-Vessel Cooling of In-Vessel Retention. During the transient phase of severe accident (SA) progression, integrity of the reactor pressure vessel (RPV) lower head is threatened by a wide spectrum of phenomena, for example, various melt relocation scenarios, potential steam explosion, jet impingement, and so forth. A limiting case and strategy in late phase of SA is maintenance of lower head integrity through external cooling of the lower head of reactor

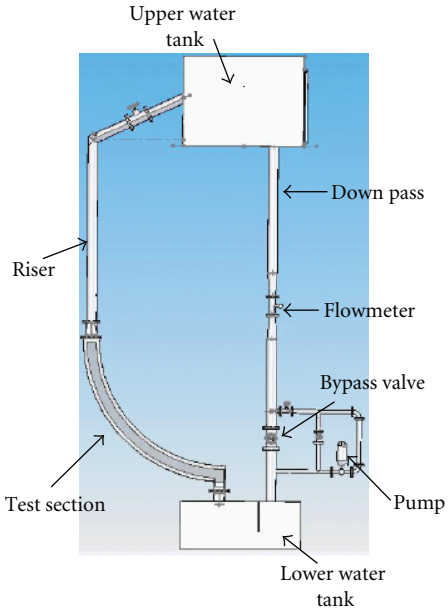

(a) Scheme of the REPEC facility

(b) Photograph of the REPEC

Figure 9: Test facility REPEC for ERVC-IVR.

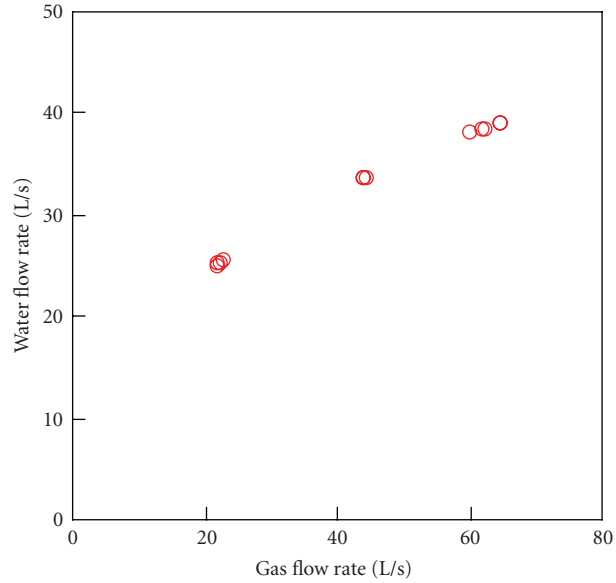

Figure 10: Dependence of induced waters flow rate versus injected air flow rate.

pressure vessel to reach the in-vessel retention of molten pool (IVR-ERVC).

The IVR-ERVC concept was first investigated and explored for the Loviisa pressurized water reactor (PWR) in Finland. It was accepted as the major accident management measure by the Finnish regulatory agency. In the USA, the design of the advanced passive reactor AP600 and AP1000 employs reactor ex-vessel flooding as an accident management scheme [2]. The safety strategy of AP1000 is to keep RPV intact at any conditions, including severe accident core melt conditions. There is no core catch outside RPV. Late on, IVR-ERVC was also proposed for other PWRs and BWRs such as Korean APR-1400 [15] and German SWR1000 [16].

For the past years, the thermal loading imposed by the core melt on the reactor pressure vessel (RPV) lower head has been the major focus of the above studies. The objectives were to determine, (a) whether the imposed heat flux exceeds the heat removal capability (CHF) on the external surface, (b) the potential for melting of the vessel wall under the thermal loading from the molten pool, and (c) the pressure bearing capability of the vessel wall held at high temperature inside and low temperature outside.

In China, SNERDI has adopted IVR-ERVC concept in the design of Chashima-2 300 MW NPP. Engineering investigation has been conducted during the design period. Furthermore, China Guangdong Nuclear Power Corporation (CGNPC) is also considering to apply IVR-ERVC strategy in the CPR1000 design.

For extending the reactor power of AP1000 to higher level, for example, 1400 MW, the feasibility of the passive IVR-ERVC concept becomes one of the bottlenecking factors and attracts extremely strong attention of the Chinese nuclear community. Both experimental and theoretical studies were initiated at SJTU two years ago, in collaboration with SNERDI and CGNPC. Figure 9 shows schematically the test facility REPEC built at SJTU. The experimental study consists of three phases, as summarized as follows.

(i) *Phase I*. Cold tests: in this phase air is used to simulate steam. The main purpose is to study two-phase flow characteristics in the test section and the natural circulation capability of the passive system.

(ii) *Phase II*. Hot tests: the test section is electrically heated to produce steam. The main purpose of this test phase is to study two-phase flow and heat transfer behavior, including critical heat flux, in the gap and on the surface of the reactor pressure vessel. Stability

of the natural circulation is also one of the main phenomena under consideration.

(iii) *Phase III*. Small-scale three-dimensional ERVC assessment test and scaling law.

The cold tests have been started in October 2008. Figure 10 shows one preliminary result indicating the total water flow rate in dependence on the injected air flow rate under natural circulation conditions. The higher the air mass flow rate, the larger the induced water flow rate. These test data can be used for the validation of system analysis codes.

4. Summary

Development of environment friendly energy supplies becomes a crucial issue in the future Chinese economy. Due to the well-known limitation in renewable energy and hydro-power, nuclear power is considered as a safe, clean, sustainable, and economic energy source. Recently, the Chinese government issued an ambitious program of mid-term and long-term nuclear power development. Nuclear safety was well recognized having the top priority in the nuclear power development. For the near-term and medium-term, the Chinese nuclear community decided for advanced pressurized water reactors with an extensive usage of passive safety systems.

As the reference concept of the advanced PWR of GEN-III, China introduces the AP1000 NPP of Westinghouse and is organizing the corresponding technology transfer. In the other side large efforts are made to accelerate the self-reliance process of the GEN-III PWR technology. The Chinese government has issued a large national program to develop self-reliance technology of "Chinese large-scale advanced PWR nuclear power plant". A central organization, the State Nuclear Power Technology Cooperation, was established, to coordinate the nationwide activities.

Nowadays, research activities on passive safety systems have been initiated at various institutions, such as Shanghai Jiao Tong University (SJTU), Shanghai Nuclear Engineering Research and Design Institute (SNERDI) and, Nuclear Power Institute of China (NPIC). A rapid expansion of R&D activities in this field is expected. Considering the global importance of nuclear safety and the existing experience worldwide in nuclear safety research, especially related to passive safety systems, an enhanced exchange and collaboration with international nuclear community is highly desired. The International Workshop on Passive Safety Systems in Advanced PWRs (IPASS'80), which was held on April 28–30, 2008 at SJTU, is an important step toward this direction. Continuation of this kind of efforts by national and international nuclear communities will significantly contribute to the progress of nuclear safety research in China and to a sustainable nuclear power development worldwide.

References

[1] Nuclear Power Medium and Long-Term Program (2005–2020), "National Development and Reform Commission (PRC)," 2007.

[2] W. E. Cummins, M. M. Corletti, and T. L. Schulz, "Westinghouse AP1000 advanced passive plant," in *Proceedings of International Congress on Advances in Nuclear Power Plants (ICAPP '03)*, Cordoba, Spain, May 2003.

[3] J. Czech, F. Bouteille, and G. Hudson, "EPR: an advanced evolutionary design," in *Proceedings of the International Congress on Advances in Nuclear Power Plants (ICAPP '04)*, pp. 133–141, Pittsburgh, Pa, USA, June 2004, paper 4198.

[4] National Medium and Long-Term Science and Technology Plan (2006–2020), "The State Council of the People's Republic of China," 2006.

[5] Y. Ouyang, "Development strategy and process of world nuclear power states and nuclear power development in China," *China Nuclear Power*, vol. 1, no. 2, pp. 118–125, 2008.

[6] P. Bo and Z. Tan, "Passive safety system design for AC-600," *Nuclear Power Engineering*, vol. 10, no. 5, 1989 (Chinese).

[7] C. Lu, Z. Qin, W. H. Niu, and S. X. Luo, "Passive safety systems research and design of LIPR," in *Proceedings of International Workshop on Passive Safety Systems in Advanced Chinese PWRs*, Shanghai, China, April 2008, paper D02.

[8] J. R. Wang, "Boron injection system in a nuclear heating reactor," in *Proceedings of International Workshop on Passive Safety Systems in Advanced Chinese PWRs*, Shanghai, China, April 2008, paper D06.

[9] M. D. Carelli, et al., "IRIS reactor design overview and status update," in *Proceedings of the International Congress on Advances in Nuclear Power Plants (ICAPP '05)*, Seoul, Korea, May 2005, paper 5095.

[10] K. M. Cao, "Analysis of two-phase natural flow through the flow path between RPV and insulation of AP1000 passive plant with RELAP5 Code," in *Proceedings of International Workshop on Passive Safety Systems in Advanced Chinese PWRs*, Shanghai, China, April 2008, paper C03.

[11] Y. H. Yang, "Research activities on nuclear passive safety at SJTU," in *Proceedings of International Workshop on Passive Safety Systems in Advanced Chinese PWRs*, Shanghai, China, April 2008, paper S02.

[12] W. B. Zhu, "Experimental research on passive residual heat removal system of Chinese advanced PWR," in *Proceedings of International Workshop on Passive Safety Systems in Advanced PWRs*, Shanghai, China, April 2008, paper E04.

[13] S. S. Tan, G. J. Leng, H. J. Neitzel, H. Schmidt, and X. Cheng, "Investigations on the passive containment cooling system of an advanced Chinese PWR," Wissenschaftliche Berichte, FZKA-6622, December 2001.

[14] W. S. Cui, J. X. Liu, and X. Cheng, "Performance analysis of passive safety containment cooling system," in *Annual Meeting of National Key Laboratory of Bubble Physics & Natural Circulation*, Chengdu, China, 2006.

[15] J. L. Rempe, D. L. Knudson, K. G. Condie, K. Y. Suh, F.-B. Cheung, and S.-B. Kim, "Corium retention for high power reactors by an in-vessel core catcher in combination with External Reactor Vessel Cooling," *Nuclear Engineering and Design*, vol. 230, no. 1–3, pp. 293–309, 2004.

[16] Z. V. Stosic, W. Brettschuh, and U. Stoll, "Boiling water reactor with innovative safety concept: the Generation III+ SWR-1000," *Nuclear Engineering and Design*, vol. 238, no. 8, pp. 1863–1901, 2008.

Hindawi Publishing Corporation
Science and Technology of Nuclear Installations
Volume 2009, Article ID 579430, 12 pages
doi:10.1155/2009/579430

Project Report

The SPES3 Experimental Facility Design for the IRIS Reactor Simulation

Mario Carelli,[1] Lawrence Conway,[1] Milorad Dzodzo,[1] Andrea Maioli,[1] Luca Oriani,[1] Gary Storrick,[1] Bojan Petrovic,[2] Andrea Achilli,[3] Gustavo Cattadori,[3] Cinzia Congiu,[3] Roberta Ferri,[3] Marco Ricotti,[4] Davide Papini,[4] Fosco Bianchi,[5] Paride Meloni,[5] Stefano Monti,[5] Fabio Berra,[6] Davor Grgic,[7] Graydon Yoder,[8] and Alessandro Alemberti[9]

[1] *Westinghouse, Science & Technology Center, 1344 Beulah Road, Pittsburgh, PA 15235, USA*
[2] *Nuclear & Radiological Engineering/Medical Physics Programs, George W. Woodruff School, Georgia Institute of Technology, Atlanta, GA 30332, USA*
[3] *SIET, S.p.A. Via Nino Bixio 27, 29100 Piacenza, Italy*
[4] *Department of Energy, CeSNEF-Nuclear Engineering Division, Politecnico di Milano, Via La Masa 34, 20156 Milano, Italy*
[5] *ENEA, Via Martiri di Monte Sole 4, 40129 Bologna, Italy*
[6] *Mangiarotti Nuclear, Viale Sarca 336, 20126 Milano, Italy*
[7] *FER, University of Zagreb, Unska 2, 10000 Zagreb, Croatia*
[8] *ORNL, P. O. Box 2008, Oak Ridge, TN 37831, USA*
[9] *Ansaldo Nucleare, Corso F.M. Perrone, 25, 16161 Genova, Italy*

Correspondence should be addressed to Roberta Ferri, ferri@siet.it

Received 31 October 2008; Accepted 25 May 2009

Recommended by Yanhua Yang

IRIS is an advanced integral pressurized water reactor, developed by an international consortium led by Westinghouse. The licensing process requires the execution of integral and separate effect tests on a properly scaled reactor simulator for reactor concept, safety system verification, and code assessment. Within the framework of an Italian R&D program on Nuclear Fission, managed by ENEA and supported by the Ministry of Economic Development, the SPES3 facility is under design and will be built and operated at SIET laboratories. SPES3 simulates the primary, secondary, and containment systems of IRIS with 1 : 100 volume scale, full elevation, and prototypical thermal-hydraulic conditions. The simulation of the facility with the RELAP5 code and the execution of the tests will provide a reliable tool for data extrapolation and safety analyses of the final IRIS design. This paper summarises the main design steps of the SPES3 integral test facility, underlying choices and phases that lead to the final design.

1. Introduction

The International Reactor Innovative and Secure (IRIS) is a modular, safe, economic, medium size Advanced Light Water Reactor that provides a viable bridge to Generation IV reactors and satisfies the Global Nuclear Energy Partnership requirements for grid-appropriate Nuclear Power Plants. Based on a safety-by-design philosophy, the IRIS integral configuration represents the advanced engineering solution of the latest LWR technology. This allows the reactor commercialisation without the construction of a demonstration prototype, once the FDA is obtained by NRC.

As a member of the IRIS consortium, ENEA coordinates the activities of design, construction and testing of a new Integral Test Facility, supported by the Italian Ministry of the Economic Development in the framework of a wider Italian R&D program on Nuclear Fission.

In the early 90s, the SIET company upgraded the SPES facility (simulating a three loop PWR for the Italian PUN) into SPES2, providing the experimental data that allowed the licensing of the Westinghouse AP-600 reactor. On the basis of the lessons learned from the past and relaying on the same auxiliary systems of SPES2, the SIET company is designing the SPES3 facility that will simulate accidental sequences

for providing the needed experimental results to verify the general behaviour of the system, allow a code assessment process and produce a reliable tool for the IRIS plant safety analyses.

A Phenomena Identification and Ranking Table, set up by an international team of experts, and a Hierarchical Two-Tiered Scaling Analyses, evolved into a Fractional Scaling Analysis, led to identifying the main facility scaling parameters resulting in 1:100 volume scale, 1:1 elevation scale, prototypical fluid at plant pressure and temperature full conditions. The detailed scaling of all plant components is the result of an iterative process aimed at verifying the SPES3 facility component design adequacy to appropriately represent what is expected in the plant.

The RELAP5 thermal hydraulic code is used to simulate the facility at different stages of the activity: design support, pretest for test and procedure design, post-tests for code assessment and data extrapolation to the real plant.

Thanks to the iteration between facility design and analyses, SPES3 will provide experimental data based on a list of accidental transients required by NRC for the licensing process. The code assessment on such data will guarantee the availability of reliable computational tools to perform the IRIS plant safety analyses for the Final Design Approval.

2. The IRIS Plant

The IRIS design was conceived to satisfy the DOE requirements for the new generation reactors, that is, improved proliferation resistance, enhanced safety, improved economics and reduced waste [1–4]. IRIS is a small-medium size (1000 MWth) pressurized water reactor with an integral configuration, suitable for modular deployment. A schematic of the IRIS integral layout is shown in Figure 1.

The reactor pressure vessel hosts all the main reactor coolant system components: core, pressurizer, spool-type reactor coolant pumps, steam generators and control rod drive mechanism. Eight once-through helical coil SGs are located around the riser and a pump is installed axially on top of each SG. The riser is defined by the extension of the core barrel. The "inverted hat" pressurizer occupies the RPV upper head.

The water flow path is from bottom to top through the core and riser, then the circulation reverses and water is pushed downward by the immersed pumps through the SG tubes. At the SG outlet, the flow path goes along the annular downcomer region outside the core to the lower plenum and then back into the core.

The integral arrangement of the plant allows avoiding pressurized components, like the SGs, outside the RPV and largely reduces the size and number of RPV penetrations. Large LOCAs are eliminated and the number of possible small LOCAs is reduced. The RCS integral layout leads to a RPV diameter of 6.2 m, larger than conventional PWR, with a total height of about 22 m. A compact spherical steel containment, 25 m in diameter, is part of the IRIS safety approach and is directly involved, through a coupled dynamic behaviour, in the passive mitigation strategy that

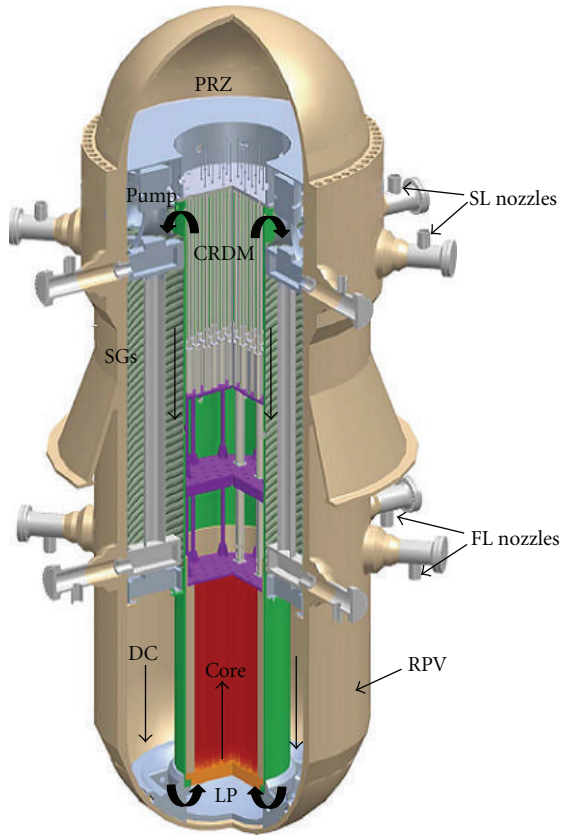

Figure 1: IRIS integral layout.

enhances the safety and reliability of IRIS. The IRIS containment and safety systems are shown in Figure 2.

The IRIS safety-by-design approach addresses small LOCA sequences by limiting and eventually stopping the loss of mass from the RPV rather than relaying on water injection by active or passive devices. This is achieved by

(i) a large coolant inventory in the RPV;

(ii) RPV depressurization achieved by means of Emergency Heat Removal Systems that remove the decay heat by condensing steam directly through the SGs;

(iii) a compact, high design pressure containment, thermodynamically coupled to the RPV during an accident, which limits the blowdown by rapidly equalizing RPV and containment pressure.

As shown in Figure 2, the containment vessel consists of different compartments, in particular the Dry-Well and the Reactor Cavity, the Pressure Suppression Systems and the Long-term Gravity Make-up Systems. An Automatic Depressurization System dumps steam in a Quench Tank in case of need during normal operation. Emergency Boration Tanks are connected to the Direct Vessel Injection lines which inject water into the vessel from the LGMS and eventually back from the Reactor Cavity. The EHRS heat exchangers are contained in the Water Refuelling Storage Tank and intervene

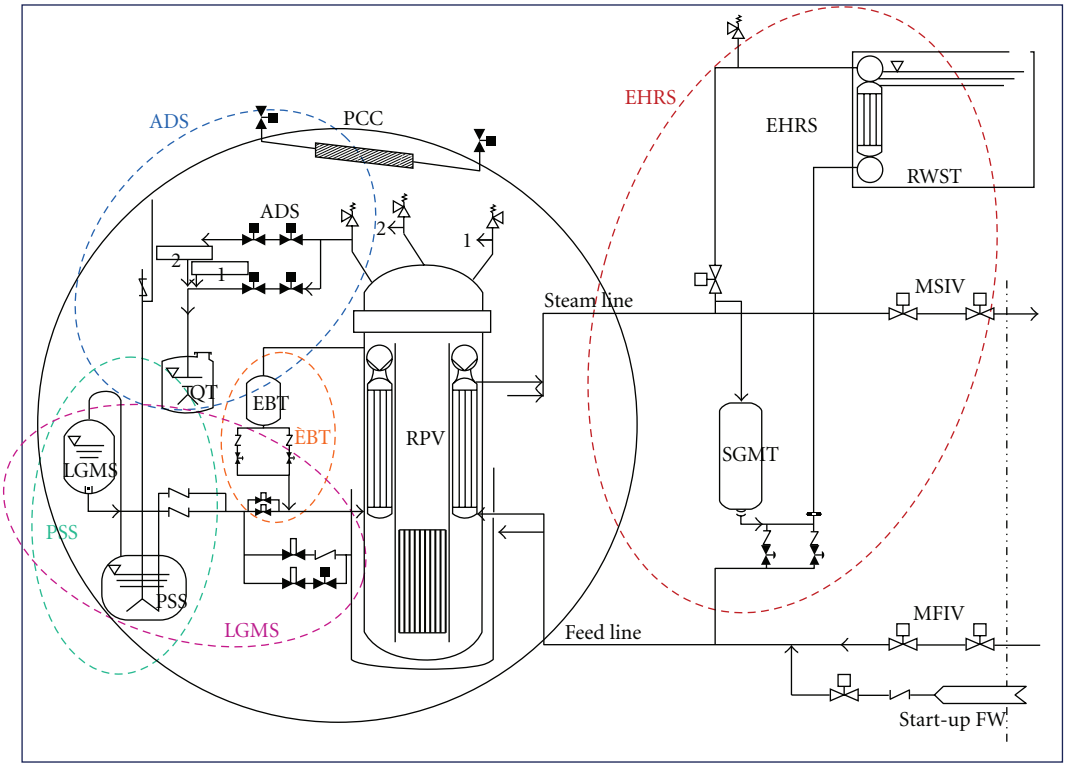

Figure 2: IRIS spherical containment and safety systems.

at isolated reactor condition. A Passive Containment Cooling System allows limiting the CV pressure in case of EHRS unavailability.

A typical sequence of LOCA events can be summarized in the following phases:

(i) blowdown: the RPV depressurises and looses mass to the containment;

(ii) reactor trip, pump trip, reactor isolation and EHRS intervention, ADS actuation, the EHRS depressurizes the primary system without loss of mass while, if the ADS intervenes, it carries out the same function with loss of mass;

(iii) the PSS limits the containment pressure, once the RPV-CV pressure equalization is reached, the blow-down phase ends;

(iv) the RPV-CV coupled system is depressurised by the EHRS that condenses steam and has the capability of removing more than the decay heat;

(v) once the pressure inside the RPV becomes lower than the containment pressure, a reverse flow of steam from the CV may occur through the break;

(vi) a long-term cooling phase follows the depressurization phase with the LGMS intervention and guarantees the core cooling.

3. IRIS Scaling Approach and SPES3 Simulation Choices

The scaling analysis and identification of similarity criteria is based on a Hierarchical, Two-Tired Scaling Analysis [5], which then evolved into a Fractional Scaling Analysis [6, 7]. The scaling analysis is part of an Evaluation Model Development and Assessment Process [8], which consists of six basic principles that in an iterative process provide the final decisions on the simulation choices:

(i) establish the requirements for the evaluation model capability, this specifies the purpose of the analysis; identifies the transient and the power plant class; identifies the systems, the component geometry, phases and processes of transients;

(ii) develop an assessment base, this performs scaling analyses and identifies the similarity criteria; identifies existing data or performs specific integral or separate effect tests; evaluates the distortion effects and experimental uncertainties;

(iii) develop an Evaluation Model, this establishes a plan to develop the EM, its structure and incorporates closure models;

(iv) assess the evaluation model adequacy, an iterative process between two different criteria is carried out: (a) Bottom-up (closure relations): assesses the

scalability of the models; determines the model applicability to simulate the physical processes; assesses the model fidelity and accuracy by preparing input and performing calculations; (b) Top-down (integrated EM): determines the capability of field equations and numerical solutions to represent processes and phenomena; assesses interaction among systems and components by performing calculations; assesses the scalability of integrated calculations and data for distortions;

(v) follow an Appropriate Quality Assurance Protocol, it applies quality assurance standards as in Appendix B of 10 CFR Part 50; it is based on a peer review by independent experts;

(vi) provide comprehensive, accurate, up-to-date documentation, it is needed for peer review, for the NRC review and to track of all changes.

On the basis of the six principles of the EMDAP, the Two-Tiered Scaling Analysis (H2TS) is subdivided in four stages:

Stage 1. a system decomposition that provides the system hierarchy and identifies the system characteristics: geometry, area and volume concentrations, initial conditions and time sequence of events, transfer processes;

Stage 2. a scale identification that provides the hierarchies for volume and area concentrations, residence times, process time scales;

Stage 3. a top-down system scaling analysis that provides the conservation equations, derives scaling groups, establishes hierarchies and identify important processes to be investigated iteratively with the bottom-up system scaling analysis;

Stage 4. a bottom-up process scaling analyses that performs detailed analyses for important local processes; derives and validates the scaling groups.

The Fractional Scaling Analysis is a quantitative methodology that accomplishes the EMDAP principles by scaling the time dependent evolution processes involving an aggregate of interacting components and processes. Moreover, the introduction of Fractional Rate of Change provides the proper time constants for scaling time-dependent processes and makes this approach more appropriate for scaling Integral Test Effects than the H2TS. FSA consists of two stages:

Stage 1. a system decomposition, with a hierarchical approach, down to components and to process levels (for IRIS: RCS to ESF to CV and then to related subsystems); identifies the dominant processes and ranks them according to their importance;

Stage 2. a fractional scaling that provides a synthesis of experimental data and generates quantitative criteria for assessing the effects of various design and operating parameters.

The FSA provides the tools to verify the accomplishment of the two Figures of Merit for IRIS specified in the PIRT [9], which are (a) the Reactor Vessel coolant inventory, which should be enough to avoid significant fuel cladding temperature excursions and (b) the Containment pressure within design value through successful heat removal to the environment, to limit the initial containment over-pressurization and guarantee its following depressurization.

The basis scaling parameters for SPES3 are:

(i) volume ratio 1 : 100;

(ii) same fluid properties (prototypical pressure and temperature);

(iii) same height;

(iv) area ratio 1 : 100, to maintain the same Resident time and velocity of fluid;

(v) same pressure drops.

the above listed choices lead to advantages and disadvantages:

(i) the full height provides prototypical distance between heat sources and heat sinks to properly simulate natural convection effects; both single phase and two phases natural convection loops can be simulated simultaneously; prototype and model fluid velocities and residence times in the loops are the same; horizontal inter-phase areas (i.e., transfer area concentrations) are properly scaled,

(ii) the prototypical fluid avoids distortions due to different fluid properties (i.e., the scaling analysis does not generate additional terms related to property distortions) and interpretation of the results is easier,

(iii) the area of the side walls decreases only 10 times (not 100 times as the volumes) and this results in 10 times larger transfer area concentrations for heat transfer (energy exchange) and wall friction (momentum exchange),

(iv) some components (e.g., heat exchangers and steam generators) might be represented with limited number of tubes (i.e., not ideal for reproducing side effects),

The FSA scaling analysis allows keeping into account and quantifying the distortions introduced by the scaling choices.

4. The SPES3 Facility

The SPES3 facility layout is shown in Figure 3 and its general view in Figure 4. SPES3 simulates the primary, secondary and containment systems of the IRIS reactor as follows:

(i) the primary system includes the Reactor Vessel and internals with power channel and fuel bundle box, lower riser and RCCA, upper riser and CRDM, pressurizer, upper downcomer in the steam generator zone, riser to downcomer connection check valves, lower downcomer, lower plenum, core bypass, and

a portion of the Direct Vessel Injection lines. A single outer pump simulates the eight IRIS internal pumps;

(ii) the three secondary systems, simulating four IRIS loops, include the steam lines and feed lines up to the Main Steam and Feed Isolation Valves, the eight IRIS Steam Generators are simulated by three helical coil SGs: two of them simulating two IRIS SG each and one simulating the remaining four.

(iii) the IRIS containment compartments are simulated in SPES3 by separate tanks properly connected, representing the Dry-Well, two Pressure Suppression Systems, two Long-term Gravity Make-up Systems, the Reactor Cavity and the ADS Quench Tank, shape and dimensions are fixed in order to reproduce the trend of IRIS compartment volumes versus height, the Passive Containment Cooling and a portion of the DVI lines are included in the containment as well.

(iv) the safety systems include the Emergency Boration Tanks, the Emergency Heat Removal Systems connected to the Refueling Water Storage Tank and the Automatic Depressurization System, three EHRS loops represent the four trains of IRIS.

The design pressure of the primary and secondary systems up to the main isolation valves is 17.25 MPa with its corresponding saturation temperature of 353.5°C. The primary and secondary side operating pressure is 15.5 MPa and 5.8 MPa, respectively. The containment design pressure is 2 MPa with its corresponding saturation temperature of 212.4°C. Its operating pressure is 0.1013 MPa.

According to the established scaling factors, SPES3 rod bundle power should be 10 MW. The SIET power capability for SPES3 is 6.5 MW, so the power to volume ratio is not preserved during the steady state, while it is rapidly matched at the beginning of the transient. The primary and secondary loop flowrates are therefore adjusted to maintain the steady state temperatures as in the IRIS plant. Table 1 reports a comparison of the main characteristics between IRIS and SPES3.

The facility configuration is suitable to investigate the natural circulation loops that allow removing the decay heat during the long-term accidental transients.

4.1. The Primary System. The SPES3 Reactor Pressure Vessel is shown in Figure 5.

The total height of the RPV is around 22 m with 0.65 m diameter. It consists of three main sections:

(i) the lower section that hosts the power channel, the lower plenum with closure plates and heater rod tightness system, the lower downcomer and DVI lower connections;

(ii) the intermediate section that hosts the riser, the steam generator annular zones, the feed lines and steam lines connections, the pump delivery and DVI upper connections;

Table 1: IRIS and SPES3 characteristic comparison.

System/Component	IRIS	SPES3
Primary side integral RPV	yes	yes apart the pump
Pumps	8	1
Core power (MW)	1000	6.5
EBT	2	2
Steam Generators	8	3
Secondary loops	4	3
SG tubes	~700	14, 14, 28
SG height (m)	8.2	8.2
SG tube average length	32	32
Containment system	yes	yes
EHRS	4	3
RWST	2	2
Dry Well	1	1
PSS	2	2
LGMS	2	2
QT	1	1
ADS trains	3	2

(iii) the upper section that hosts the "inverted hat" pressurizer and the ADS, the pump suction plenum, pump suction and EBT to RPV line connections.

The rod bundle consists of 235 heated and 1 dummy rods that reproduce the dimensions and pitch of the Westinghouse 17 × 17 rod assembly, also adopted in IRIS, Figure 6. The rods are indirectly heated and the axial power profile is constant. Two rods provides a greater power with 1.2 peak factor. They are maintained in their relative position by spacer grids located at different elevations. A double layer fuel bundle box envelops the rods and acts as downcomer barrel. A filler between the wall layers is chosen to scale correctly the thermal mass and the global heat transfer coefficient to compensate for the not correctly scaled side surface area, Figure 7.

The lower plenum contains a perforated cylinder that allows water from the downcomer to turn into the core, Figure 7. A tightness system, with graphite disks compressed between plates, allows the rods to exit the vessel bottom and join the electrical connections for power supply.

The SPES3 riser, over the core, simulates in one cylindrical volume the IRIS riser, annular space and SG central columns. Vertical tubes and perforated plates are inserted in the riser to simulate RCCAs, CRDMs and to adjust the pressure drops.

The helical coil Steam Generators consist of 14 tube rows wrapped around the barrel with prototypical diameter (17.48 mm), height (8.2 m) and length (32 m). The inner SGs have a single row while the outer one has two. Each SG is located in an annulus, obtained by vertical barrels concentric to the riser, and the tubes are maintained in their position by proper vertical plates. The tubes cross the vessel wall in correspondence of the Feed Line and Steam Line nozzles. In the nozzle area, the tubes bend to be welded on a plate between the nozzle flanges, Figure 8. This allows the feed

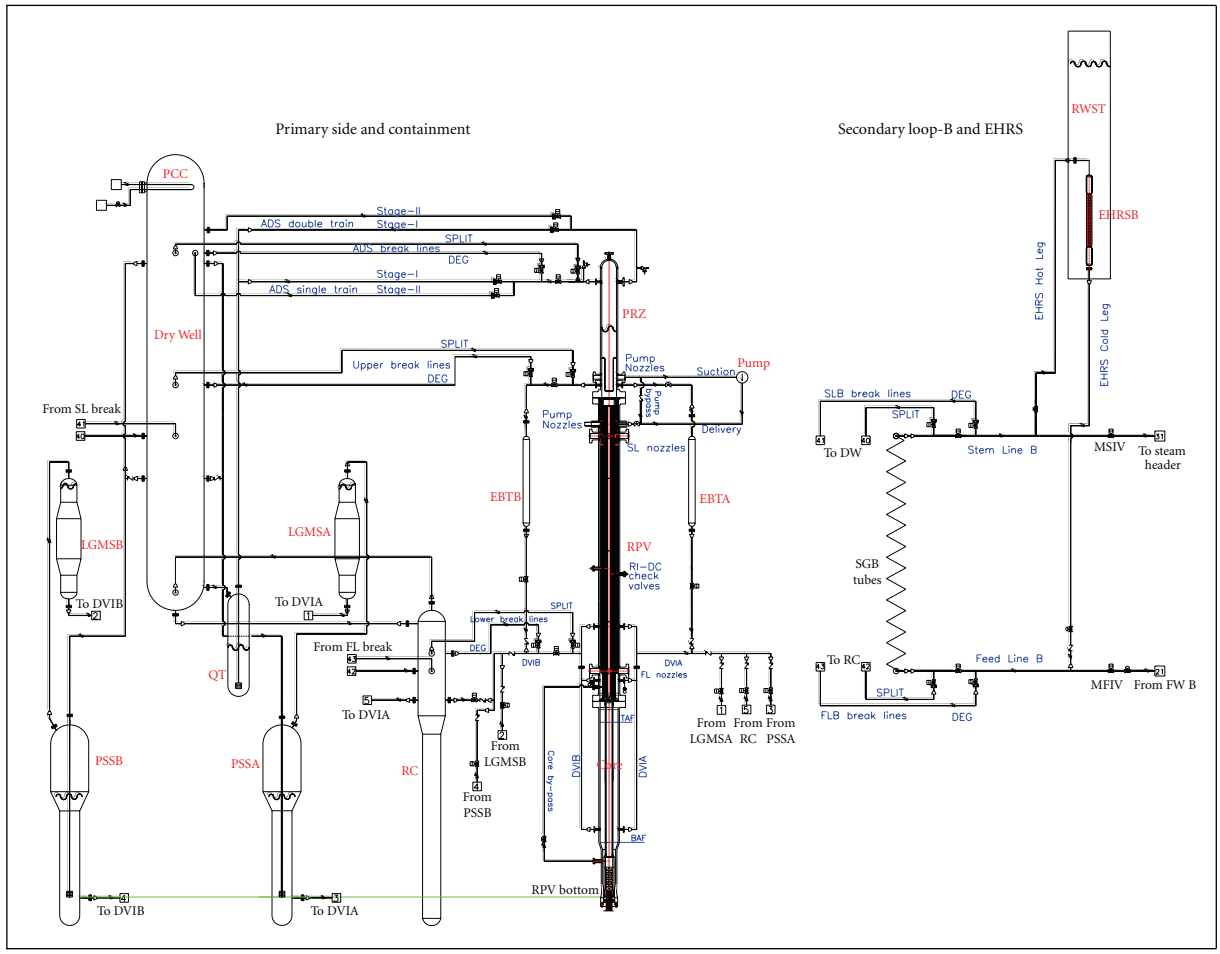

Figure 3: SPES3 layout.

water to redistribute in the tubes and steam to flow through the steam lines.

The "inverted hat" pressurizer reproduces the IRIS one; differently from IRIS, the SPES3 pressurizer will adopt electrical heaters vertically inserted from the RPV top, to set the pressure during the steady conditions. Proper holes at the PRZ bottom simulate the IRIS surge path. The pump suction plenum is the volume outside the PRZ hat.

The limited room inside the RPV does not allow fitting internal pumps, so a single outer pump distributes water to the three SG annuli through four separate nozzles, Figure 9. The mass flow balance is obtained by proper distribution plates at the SG top.

Nozzles on the RPV allow connecting the primary system to the DVI, the outer core by-pass, the pump suction and delivery, the ADS and the EBT balance lines.

Two Emergency Boration Tanks are connected to the RPV at the top, by the balance lines, and at the bottom through the DVI lines. They operate at the same RPV pressure.

4.2. The Secondary System and EHRS Loops. The SPES3 secondary system consists of three loops simulating four with a loop lumping two IRIS secondary trains. The feed lines and steam lines are simulated from the RPV nozzles up to the MFIV and MSIV. The piping size is chosen to maintain the same pressure drops as in the IRIS plant, even with different routing.

The Emergency Heat Removal Systems consist of three loops with vertical tube heat exchangers immersed in the RWST and hot and cold legs joined to the SLs and FLs, respectively. In particular, EHRS connected to the double secondary loop has a double heat exchanger. The heat exchangers are about 3 m high and contain 3, 3 and 5 tubes of 50.8 mm diameter.

4.3. The Containment System. The different IRIS containment compartments are simulated in SPES3 by tanks connected among them and to the RPV by piping. Such pipes do not exist in the IRIS plant and they are designed in terms of size and layout to limit their influence on the flow. The tank shape is chosen to reproduce the same volume trend versus height as in IRIS and, in specific cases, cylindrical tanks with variable sections are designed. The SPES3 containment tanks are: the Dry Well, the Reactor Cavity, two PSS, two LGMS, the Quench Tank.

Table 2: SPES3 Test matrix summary and main goals.

Test type	Break	Purpose	Notes
Lower break	SBLOCA: DEG and SPLIT break of DVI	Verify the dynamic coupling between primary system and containment; the maximum containment pressure, the RPV mass and core temperature	All safety systems available except for a single failure on an ADS train
Upper break	SBLOCA: DEG break of EBT to RPV line		
ADS break	SBLOCA: DEG break of ADS single train		Maximum PRZ steam space break
FL break	DEG break of FL	Verify the plant response to non-LOCA events	Partial EHRS actuation
SL break	DEG break of SL		
Safe Shutdown sequence	Loss of all power	Verify the safe-shutdown sequences	Investigate the primary coolant shrinkage, natural circulation, EHRS HX cool-down capability

Table 3: SPES3 calculated steady state conditions.

Quantity	Units	Value
PRZ pressure	MPa	15.55
Core power	MW	10
Primary side total mass flow	Kg/s	47.7
Inlet core temperature	K	566
Outlet core temperature	K	603
Core ΔT	K	37
SG-A outlet pressure	MPa	5.83
SG-A mass flow	Kg/s	1.25
SG-A inlet temperature	K	497
SG-A outlet temperature	K	595
SG-A ΔT	K	98
SG-A superheating (Tsat 546.8)	K	48.2
SG-B outlet pressure	MPa	5.83
SG-B mass flow	Kg/s	1.25
SG-B inlet temperature	K	497
SG-B outlet temperature	K	594
SG-B ΔT	K	97
SG-B superheating (Tsat 546.8)	K	47.2
SG-C outlet pressure	MPa	5.88
SG-C mass flow	Kg/s	2.5
SG-C inlet temperature	K	497
SG-C outlet temperature	K	593
SG-C ΔT	K	96
SG-C superheating (Tsat 547.4)	K	45.6
Containment pressure	MPa	0.1013
Containment temperature	K	323

The three IRIS ADS trains are simulated in SPES3 by two trains: a single and a double train. Each train consists of a safety valve, a line to the Quench Tank and a line to the Dry Well. The line to the QT ends with a sparger that enhances the steam condensation under the water level.

The PCC is a condenser installed at the DW top which consists of an horizontal tube bundle, with the only requirement of removing a specified power, without scaling the IRIS PCCS geometry (PCCS is an IRIS non-safety system and its use is foreseen only during beyond design basis accident sequences addressed in the Probabilistic Risk Assessment).

A thermal insulation is foreseen for all SPES3 tanks and piping to reduce the heat losses to the environment.

4.4. The Break Lines. Break line systems are designed to simulate both split and double ended guillotine breaks. Break locations are foreseen at different elevations, in particular

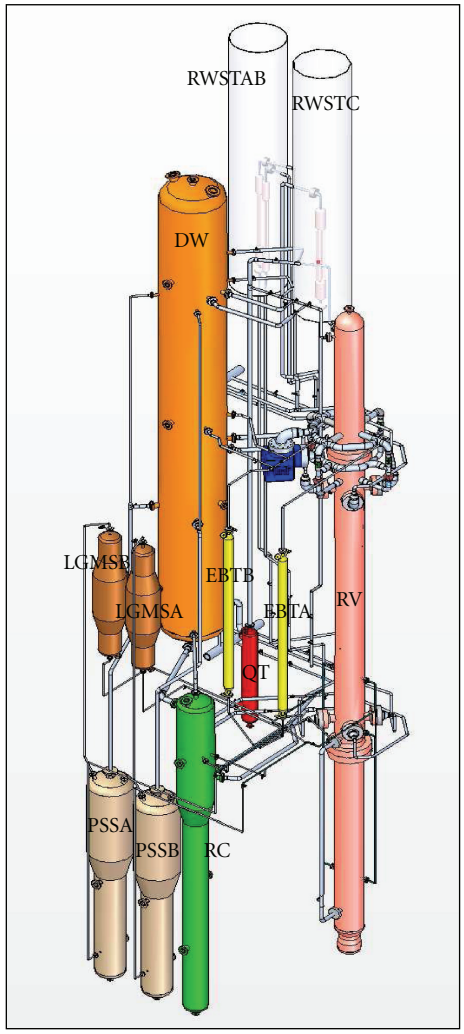

Figure 4: SPES3 general view.

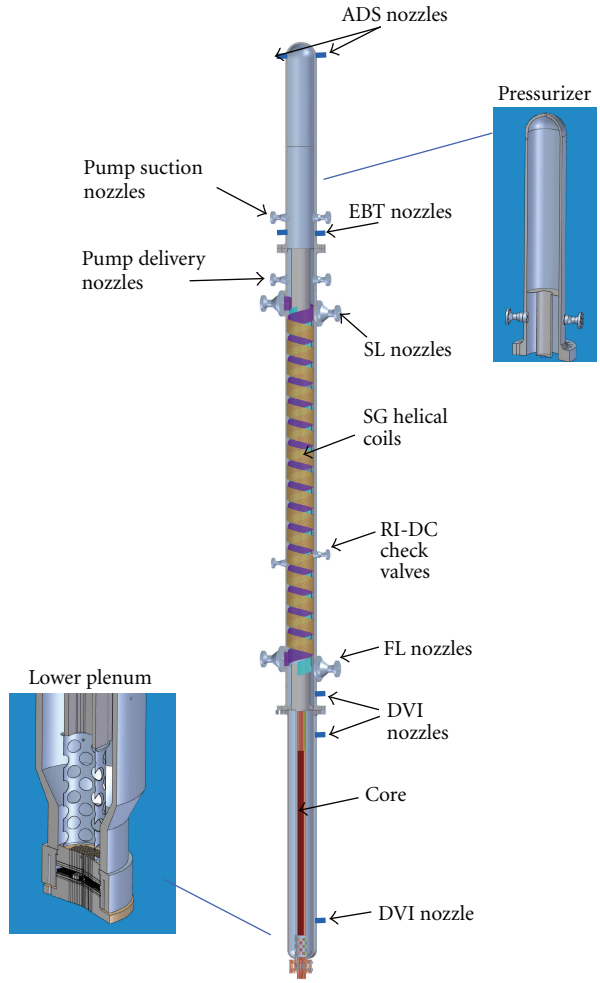

Figure 5: SPES3 reactor pressure vessel.

the lower break is on the horizontal part of the DVI and ends into the RC; the upper break is on the EBT to RV balance line top and ends into the DW; the ADS break is on the single train, upstream of the safety valve and ends into the DW; the FL break ends into the RC; the SL break ends into the DW (i.e., steam and feed line break in containment are simulated).

The exact break size is set by calibrated orifices that scale the IRIS plant pipe size.

4.5. The Auxiliary Systems. The auxiliary systems provide water to the experimental facility at the required temperature, pressure and mass flow. Direct current generators provide power to the fuel bundle and to the PRZ heaters. Some modifications to the already existing systems at SIET were needed to match the IRIS requirements, in particular to the condensation system (heat sink), to the machinery cooling loop, to the air circuit for valve operation and instrumentation, to the power channel electrical connection.

5. Instrumentation

A large set of instruments (about 600) is installed on SPES3 to provide data both for the test run and analysis. It consists of conventional instrumentation (i.e., relative and absolute pressure transmitters, temperature sensors) and special instrumentation for two-phase flow measurement. The quantities directly measured by conventional instrumentation are: fluid and wall temperatures, absolute and differential pressures, velocity, volumetric flow, voltage and current, while special instrumentation is used for void fraction and volumetric flow. Derived quantities are: level by differential pressure and density, mass flow by differential pressure and density, mass flow by volumetric flow and density, mass flow by volumetric flow and void fraction (wire mesh sensors and turbine), mass by level and density, mass flow by heat transfer (heated thermocouples), heat losses by wall thermocouples, power by voltage and current.

The rod bundle is instrumented with 120 wall thermocouples distributed at different levels, with a greater density at the upper levels. They provide the rod cladding temperature and provide the signals for core protection against superheating.

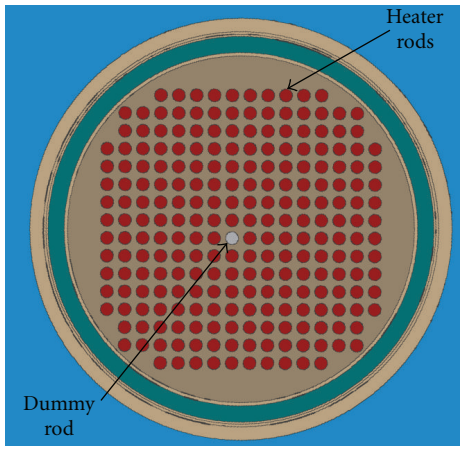

Figure 6: SPES3 heater rod bundle.

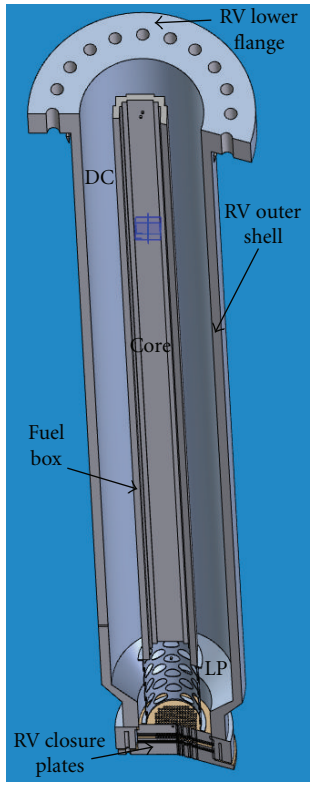

Figure 7: SPES3 fuel bundle box.

6. Test Matrix

The planned test matrix consists of 2 separate effects and 13 integral tests. The SETs are devoted to investigate the interaction and characterize the heat transfer of innovative components like the helical coil SGs and the EHRS heat exchangers for long-term decay heat removal. The ITs are devoted to investigate the general behaviour of the system, the primary and containment dynamic interaction during accidental transients, the effectiveness of the Engineered Safety Features, the IRIS capability to cope with postulated accidental transients.

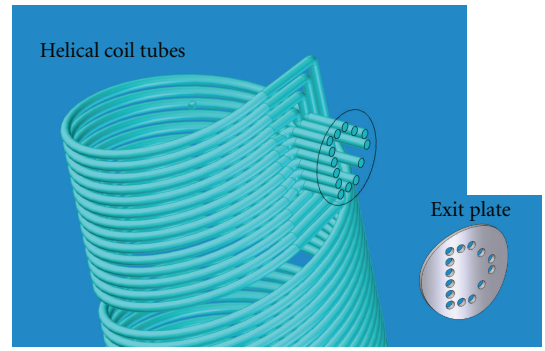

Figure 8: SPES3 SG tubes.

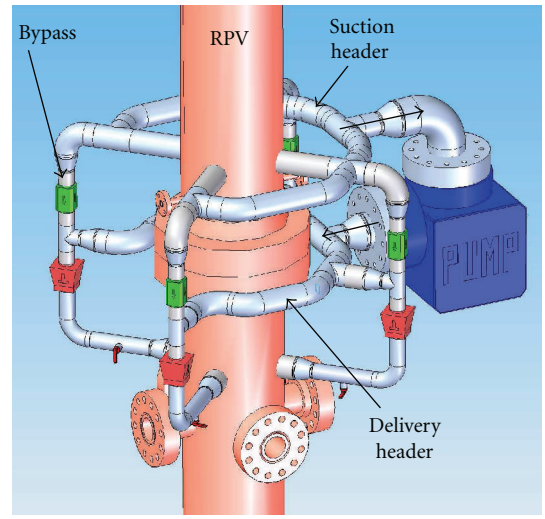

Figure 9: SPES3 coolant pump.

According to NRC requests for the licensing process, in terms of experimental data, both Design Basis Accidents (DBAs) and Beyond Design Basis Accidents (BDBAs) are foreseen together with long-term cooling transients. A synthesis of the text matrix is reported in Table 2.

All the worse LOCA cases foreseen on IRIS are simulated: 1 inch equivalent DVI split break; 2 inch equivalent DVI DEG break; 4 inch equivalent EBT to RPV balance line DEG break; 6 inch equivalent single train ADS DEG break. Secondary side line breaks such as the 12 inch equivalent FL DEG break and the 16 inch equivalent SL DEG break are also included in the test matrix.

The Design Basis cases verify the whole system response and mixture level in the core. The Beyond Design Basis cases verify the plant coolability even with the contemporary failure of some ESFs.

7. SPES3 Simulation with the RELAP5 Code

The IRIS plant simulation and analyses have been carried out at FER (University of Zagreb) by means of the RELAP5 and GOTHIC coupled codes to keep into account specific thermal hydraulic phenomena in the primary system

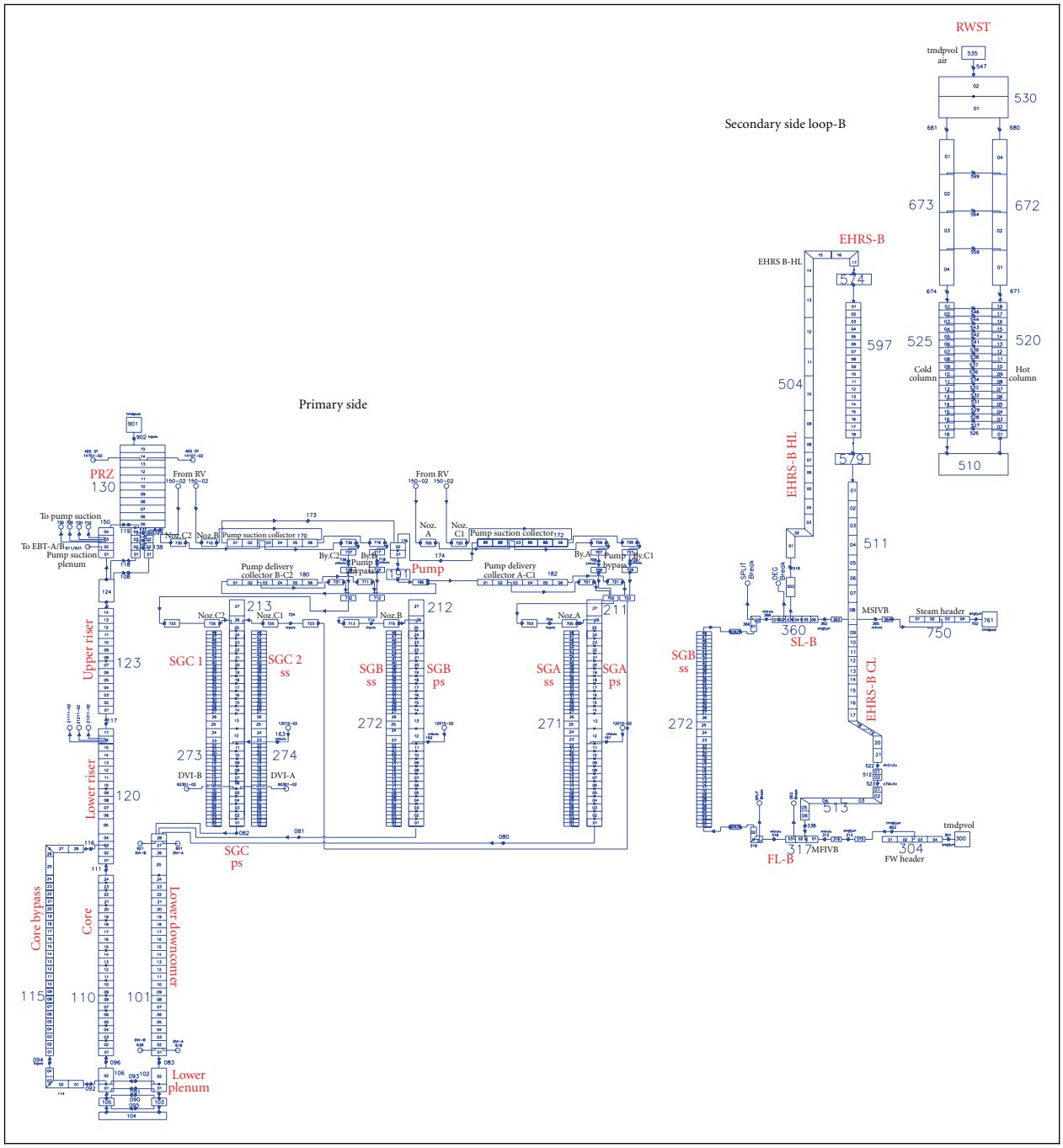

Figure 10: SPES3 nodalization for RELAP5 code: primary side and secondary loop B.

(with RELAP) and typical containment volume phenomena (with GOTHIC).

The reduced dimensions of the SPES3 components, while still allowing three dimensional circulations in the tests, allow also for simulating the whole facility with the RELAP5 code, which is applied during all the main phases of the facility design. A scheme of the SPES3 nodalization for the RELAP5 code is shown in Figure 10 for the primary and the secondary loops and in Figure 11 for the containment.

Three steps of code application are planned:

(1) supporting design analyses aimed at obtaining feedback information on the facility design, in particular the comparison between the SPES3 facility and the IRIS reactor simulations provides information on the appropriateness of the performed scaling choices;

(2) pretest analyses aimed at the test design and test procedure set-up;

(3) post-test analyses and code assessment on a set of qualified data.

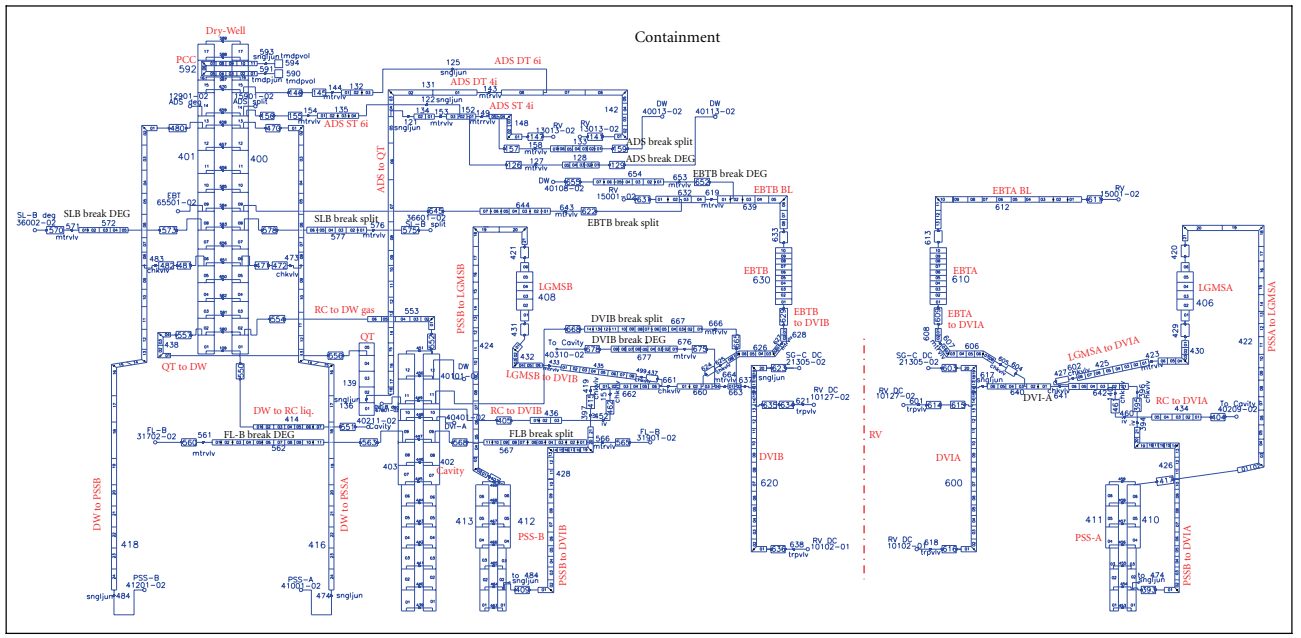

Figure 11: SPES3 nodalization for RELAP5 code: containment.

The IRIS plant safety analyses devoted to the FDA will be carried out with numerical codes validated on the SPES3 experimental data.

In order to compare the SPES3 results with the IRIS ones, the design support analyses have been carried out at 10 MW power. The calculated steady state results are summarized in Table 3.

8. Conclusions

In the frame of the IRIS reactor licensing process, the construction of experimental facilities is required to study separate effect phenomena on the innovative components and the integral system behaviour during postulated accidents.

This paper deals with the design of the SPES3 integral test facility to simulate the primary, secondary and containment systems of IRIS at full pressure and temperature conditions, with 1 : 1 elevation and 1 : 100 volume scaling factor, as required by NRC for this reactor.

The SPES3 facility is under design and will be built at the SIET laboratories, under the sponsorship of the Italian government and the coordination of ENEA.

The main design steps of the SPES3 integral test facility are shown, starting from the scaling approach and proceeding to the component and piping design, the RELAP5 code system simulation, the feedback on the design choices and finally the pretest and post-test analyses that will allow extrapolation of the experimental results to the prototype plant.

he SPES3 facility experimental data will provide a qualified data base for the accident analyses and code assessment.

Numerical codes, qualified via the SPES3 test results, will be used for the IRIS safety analyses to be submitted with the application for the NRC Final Design Approval.

Nomenclature

ADS:	Automatic Depressurization System
ALWR:	Advanced Light Water Reactor
BDBA:	Beyond Design Basis Accident
CV:	Containment Vessel
CFR:	Code of Federal Regulation
CRDM:	Control Rod Drive Mechanism
DBA:	Design Basis Accident
DC:	Downcomer
DEG:	Double Ended Guillotine
DOE:	Department of Energy
DVI:	Direct Vessel Injection
DW:	Dry-Well
EBT:	Emergency Boration Tank
ESF:	Engineered Safety Features
EHRS:	Emergency Heat Removal System
EMDAP:	Evaluation Model Development and Assessment Process
ENEA:	Ente per le Nuove tecnologie, l'Energia e l'Ambiente
EM:	Evaluation Model
FDA:	Final Design Approval
FL:	Feed Line
FSA:	Fractional Scaling Analysis
FW:	Feed Water
GNEP:	Global Nuclear Energy Partnership
GOTHIC:	Generation Of Thermal-Hydraulic Information for Containments
H2TS:	Hierarchical Two-Tiered Scaling Analysis
IRIS:	International Reactor Innovative and Secure
IT:	Integral Test
ITF:	Integral Test Facility
LGMS:	Long-term Gravity Make-up System
LOCA:	Loss Of Coolant Accident

LP: Lower Plenum
LWR: Light Water Reactor
MFIV: Main Feed Isolation Valve
MSIV: Main Steam Isolation Valve
NPP: Nuclear Power Plant
NRC: Nuclear Regulatory Commission
PCCS: Passive Containment Cooling System
PIRT: Phenomena Identification and Ranking Table
PRZ: Pressurizer
PSS: Pressure Suppression System
PUN: Progetto Unificato Nazionale (National Unified Project)
PWR: Pressurized Water Reactor
QT: Quench Tank
RC: Reactor Cavity
RCCA: Rod Cluster Control Assembly
RCS: Reactor Coolant System
RELAP: REactor Loss of coolant Analysis Program
RI: Riser
RPV: Reactor Pressure Vessel
RV: Reactor Vessel
RWST: Refueling Water Storage Tank
R&D: Research and Development
SET: Separate Effect Tests
SIET: Società Informazioni Esperienze Termoidrauliche (Company for Information on Thermal-hydraulic Experimentation)
SL: Steam Line
SG: Steam Generator
SPES: Simulatore Per Esperienze di Sicurezza (Simulator for Safety Tests)

References

[1] M. D. Carelli, "IRIS: a global approach to nuclear power renaissance," *Nuclear News*, September 2003.

[2] M. D. Carelli, L. E. Conway, L. Oriani, et al., "The design and safety features of the IRIS reactor," *Nuclear Engineering and Design*, vol. 230, no. 1–3, pp. 151–167, 2004.

[3] M. D. Carelli, B. Petrović, M. Dzodzo, et al., "SPES-3 experimental facility design for IRIS reactor integral testing," in *Proceedings of the European Nuclear Conference (ENC '07)*, Brussels, Belgium, September 2007.

[4] B. Petrović, M. D. Carelli, and N. Cavlina, "IRIS—international reactor innovative and secure: progress in development, licensing and deployment activities," in *Proceedings of the International Conference on Nuclear Options in Countries with Small and Medium Electricity Grids*, Dubrovnik, Croatia, May 2006.

[5] N. Zuber, "Appendix D—a hierarchical, two-tired scaling analysis," An Integrated Structure and Scaling Methodology for Severe Accident Technical Issue Resolution 20555, NUREG/CR-5809, U. S. Nuclear Regulatory Commission, Washington, DC, USA, November 1991.

[6] N. Zuber, W. Wulff, U. S. Rohatgi, and I. Catton, "Application of fractional scaling analysis (FSA) to loss of coolant accidents (LOCA), part 1: methodology development," in *Proceedings of the 11th International Topical Meeting on Nuclear Reactor Thermal-Hydraulics (NURETH-11 '05)*, Avignon, France, October 2005, paper 153.

[7] W. Wulff, N. Zuber, U. S. Rohatgi, and I. Catton, "Application of fractional scaling analysis (FSA) to loss of coolant accidents (LOCA), part 2: system level scaling for system depressurisation," in *Proceedings of the 11th Topical Meeting on Nuclear Reactor Thermal-Hydraulics (NURETH-11 '05)*, Avignon, France, October 2005, paper 111.

[8] Regulatory Guide 1.203, "Transient and accident analysis methods," USNRC, December 2005.

[9] T. K. Larson, F. J. Moody, G. E. Wilson, et al., "IRIS small break LOCA phenomena identification and ranking table (PIRT)," in *Proceedings of the International Congress on Advances in Nuclear Power Plants (ICAPP '05)*, Seoul, Korea, May 2005.

Hindawi Publishing Corporation
Science and Technology of Nuclear Installations
Volume 2009, Article ID 738480, 11 pages
doi:10.1155/2009/738480

Review Article

Experiments and Modelling Techniques for Heat and Mass Transfer in Light Water Reactors

W. Ambrosini, M. Bucci, N. Forgione, A. Manfredini, and F. Oriolo

Dipartimento di Ingegneria Meccanica, Nucleare e della Produzione, Università di Pisa, Via Diotisalvi 2, 56126 Pisa, Italy

Correspondence should be addressed to W. Ambrosini, walter.ambrosini@ing.unipi.it

Received 29 October 2008; Accepted 22 December 2008

Recommended by Xu Cheng

The paper summarizes the lesson learned from theoretical and experimental activities performed at the University of Pisa, Pisa, Italy, in past decades in order to develop a general methodology of analysis of heat and mass transfer phenomena of interest for nuclear reactor applications. An overview of previously published results is proposed, highlighting the rationale at the basis of the performed work and its relevant conclusions. Experimental data from different sources provided information for model development and assessment. They include condensation experiments performed at SIET (Piacenza, Italy) on the PANTHERS prototypical PCCS module, falling film evaporation tests for simulating AP600-like outer shell spraying conditions, performed at the University of Pisa, experimental data concerning condensation on finned tubes, collected by CISE (Piacenza, Italy) in the frame of the INCON EU Project, and experimental tests performed in the CONAN experimental facility installed at the University of Pisa. The experience gained in these activities is critically reviewed and discussed to highlight the relevant obtained conclusions and the perspectives for future work.

1. Introduction

The capability to correctly model heat and mass transfer phenomena has a key role in the analysis of postulated accidents in present nuclear reactors and designs conceived for future deployment. In particular, steam condensation and water evaporation in the presence of noncondensable gases have been the subject of extensive studies in the past decades, mainly aiming to close the problem from the modelling point of view.

This effort was performed in many countries, particularly, in connection with the design of third generation reactors based on passive mechanisms for removing decay heat from the reactor vessel and the containment. Downscaled experimental facilities were set up reproducing basic heat and mass transfer phenomena occurring during normal and off-normal operations in such plants in order to collect relevant data (see e.g., [1–4]). In Europe, the objective of a more in depth understanding of these phenomena was attained also by projects financed in different EU framework programs, as those included in the INNO and CONT clusters of FP-4 [5] and in the FP-5 SCACEX Project [6].

The University of Pisa had an active part in these activities, contributing both by model development and assessment and by original experiments on both evaporation and condensation. The research started on the modelling side, with the analysis of available theories and techniques for evaluating condensation and evaporation rates in reactor systems [7]. In addition to empirical engineering correlations, the analogy between heat and mass transfer, in the different forms appearing in literature, was adopted as the basic tool for predicting mass transfer rates. Then, experimental data from different sources provided the relevant information for model development and assessment. In particular, the following:

(i) condensation experiments performed at SIET (Piacenza, Italy) on the PANTHERS-PCC prototypical passive containment cooling system modules were addressed by a 1D model [8];

(ii) falling film evaporation tests for simulating outer shell spraying conditions similar to those envisaged in AP600 reactor, were performed at the University of Pisa by the EFFE experimental facility and were

simulated by both simplified models and a CFD code [9, 10];

(iii) condensation on finned tubes was then considered, adopting experimental data collected by tests performed at CISE (Italy) in the frame of the INCON EU Project [11];

(iv) experimental tests were carried out and are still running in the CONAN experimental facility installed at the University of Pisa [12] to study condensation in the presence of noncondensable gases, also in the frame of the EU Severe Accident Research Excellence Network (SARnet) of Excellence [13].

The experience gained in these different steps allowed refining modelling techniques ranging from simple engineering correlations to 1D and CFD models. In particular, the suitability of the analogy between heat and mass transfer was assessed in correlating both evaporation and condensation data [9, 10, 12, 14]. The further step of applying CFD models in predicting heat and mass transfer was aimed to develop up-to-date modelling tools for light water reactor containment analysis [13, 15, 16]; this represents one of the most challenging aspects to be coped with in the years to come, in order to take full profit of the experimental information collected in the last decades, making a reasonable use of the increased capabilities of computational means.

The paper summarizes the relevant conclusions obtained in the above mentioned steps, trying to point out the lesson learned in relation to the available methodologies for evaluating heat and mass transfer in conditions of interest for nuclear reactor applications.

2. Prediction of Condensation in a Prototypical PCCS Module

In support to the design of components of the General Electric SBWR reactor [17], SIET set up a facility named PANTHERS-PCC in order to evaluate the effect of noncondensable gas build-up in the tubes of the SBWR passive containment cooling system condenser [18, 19].

The PCC test loop consisted of a pool tank housing the full-scale prototype, made of two equal modules submerged in water (see Figure 1). The number of vertical tubes in each module was 248, having 5.08 cm (2 inches) outer diameter and being connected with upper and lower headers. The air-steam mixture was introduced in the condenser at prescribed values of air and steam flow rates, pressures, and temperatures. The steam condensed partly on the inner walls of the tubes and was collected in the lower header and routed to a drain tank; the latter represents the gravity driven coolant system pool of the full scale reactor. Coherently with the mechanisms envisaged to occur in the SBWR reactor, air accumulating in the gas space of the drain tank was discharged to a vent tank, maintained at a slightly lower pressure than the PCC inlet and outlet, thus, simulating the behavior of the pressure suppression pool in the SBWR. The experimental facility preserved the elevation of the full-scale plant, in order to correctly simulate the expected gravity driven phenomena.

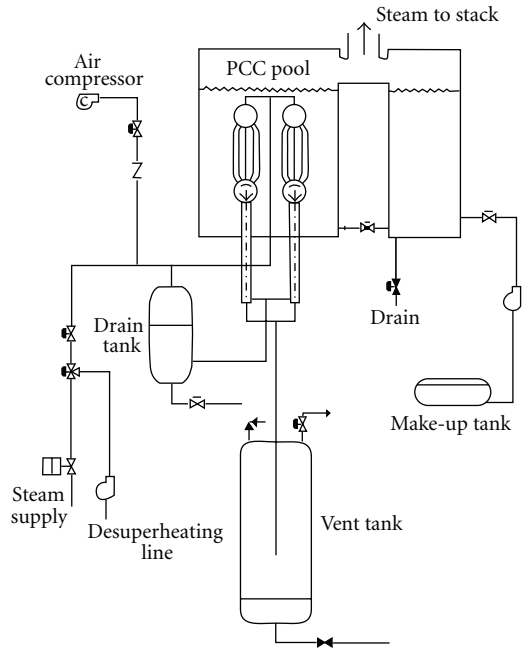

Figure 1: PANTHERS-PCC test facility.

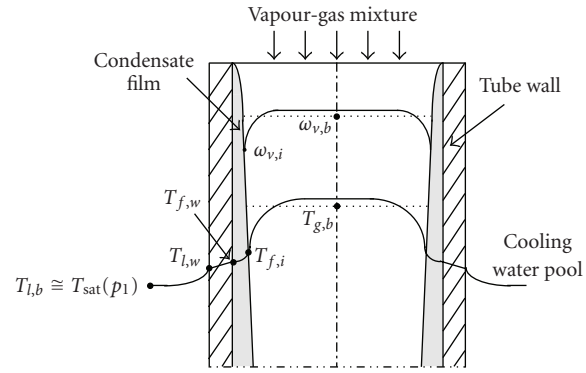

Figure 2: Physical model adopted for film condensation in tubes.

Different series of tests were performed in the facility aiming at simulating the main characteristics of the SBWR design basis accidents. The tests involved different degrees of superheating of the air-steam mixture and different air mass fractions; the effect of level in the water pool was also tested.

The 1D model adopted by the University of Pisa in this frame [8] was developed in order to simulate both filmwise condensation and falling film evaporation. A schematic representation of the geometrical and operating conditions assumed in the model in the case of film condensation in tubes is reported in Figure 2. The model makes use of a complete nonequilibrium two-fluid approach, solving separate steady-state mass, energy, and momentum balance equations for each phase, discretized by a finite difference scheme. Several tens of control volumes were adopted to axially discretize the PCC tubes.

The Rohsenow boiling heat transfer correlation [20] was adopted on the outer side of the heat exchanger tubes, as in many tests the outer fluid temperature was very close to saturation and boiling conditions could be envisaged. The modelling of the gas-liquid interfacial heat and mass transfer, having the greatest importance in order to evaluate the overall efficiency of the heat exchanger, relied on the analogy between heat and mass transfer, adopting different heat transfer correlations. In particular, in a base model, the classical Dittus and Boelter correlation [21] was adopted in the forms

$$\begin{aligned} \mathrm{Nu}_{g,i,\infty} &= 0.023\,\mathrm{Re}_{g,i}^{0.8}\,\mathrm{Pr}_{g}^{0.3}, \\ \mathrm{Sh}_{g,0,\infty} &= 0.023\,\mathrm{Re}_{g,i}^{0.8}\,\mathrm{Sc}_{g}^{0.3}. \end{aligned} \tag{1}$$

The asymptotic values of the heat transfer coefficients, applicable in long tubes, were then corrected taking into account entrance effects according to a correlation suggested by Bonilla [22]. Once the corrected Sherwood number at low mass transfer rate, $\mathrm{Sh}_{g,0}$, was calculated, the condensation heat transfer was evaluated by the following relationship:

$$\begin{aligned} q''_{\mathrm{cond}} &= h_{lv}\frac{\mathrm{Sh}_{g,0}\mathrm{D}_{vg}\rho_g}{D_h}\ln\left(1+B_m\right), \\ B_m &= \frac{\omega_{v,i}-\omega_{v,b}}{1-\omega_{v,i}}, \end{aligned} \tag{2}$$

taking into account the suction effect by the classical formulation derived from the solution of the Stefan's problem [23]. Similarly, the Ackerman correction for the heat transfer coefficient [24] was adopted.

As found in previous experiences of code applications by other researchers (see the discussion in [8]), two variants of the model were introduced, adopting a correlation by Banerjee and Hassan [25] and taking into account evidence from experiments pointed out by Almenas and Lee [26], concerning the dependence of heat transfer coefficients on system pressure. In particular, as in the Banerjee and Hassan [25] model, a minimum value of the Nusselt number was imposed adopting the formulations:

$$\begin{aligned} \mathrm{Nu}_{g,i,\mathrm{tu}} &= 0.023\,\mathrm{Re}_{g,i}^{0.8}\,\mathrm{Pr}_{g}^{0.3}, \\ \mathrm{Nu}_{g,i,\min} &= 5.5\left(\frac{p}{p_0}\right)^{1.2}, \\ \mathrm{Nu}_{g,i} &= \left[\left(\mathrm{Nu}_{g,i,\mathrm{tu}}\right)^3+\left(\mathrm{Nu}_{g,i,\min}\right)^3\right]^{1/3}, \end{aligned} \tag{3}$$

with $p_0 = 0.1$ MPa.

The obtained results showed an increasingly better behavior in predicting the trend of condenser efficiency by applying the basic model, the Banerjee and Hassan [25] model and the final proposed model, which implemented the suggestion by Almenas and Lee [26] expressed in (3). The overall performance of the model in predicting condensation efficiency, also as a function of pressure, is described in Figure 3, showing that the final proposed model was able to predict with good accuracy the observed experimental data.

3. Falling Film Evaporation

The EFFE experimental facility [27] was set up in order to provide separate effect data on falling film evaporation in conditions similar to those envisaged for the outer surface of the AP600 safety envelope after a postulated loss of coolant accident. The facility consisted in a 0.6 m wide, two-meter-long stainless steel plate, heated on the back side by 100 modular electric heaters. The heaters were arranged in three groups, supplied by the three phases of an electrical transformer, in order to separately control heat flux in the film inlet, middle, and outlet sections [9, 10].

The plate was mounted over a frame allowing to rotate it from the completely vertical to the completely horizontal position (Figure 4(a)), in order to allow for simulating the conditions occurring along the vertical part of the AP600 containment shell and in the upper dome. A water spray system, located at the top of the plate (labelled *Distr* in Figure 4(b)), allowed for distributing in a uniform fashion the falling film on the heated surface; a transparent screen (*Pp*), located approximately at a distance of 10 cm from the heated surface, contributed to enclose the evaporating region into a square channel. A countercurrent air flow was forced in the channel by a blower (*Bl*) located at the bottom of the plate itself, thus, reproducing conditions similar to those occurring in the external AP600 containment flow paths owing to natural draft. The overall evaporation rate was measured in different ways, in order to allow for cross-checking the measured values; the most accurate measurement was achieved by the rate of decrease of water level in the reservoir (*Mv*), obtained by continuously acquiring a differential pressure signal between the bottom of the vessel and the external atmosphere.

The experimental facility was operated in the frame of the EU DABASCO Project [5], devoted to acquire experimental data on containment phenomena. Both dry (i.e., pure forced convection) and wet (i.e., film evaporation) tests were performed, aiming to compare the average Nusselt number data obtained in the former with corresponding averaged Sherwood numbers obtained in the latter. Film flow rates from 20 to 100 g/s were adopted, together with velocities of the countercurrent air flow up to nearly 9 m/s and plate temperatures from 50 to 90°C.

The obtained heat and mass transfer experimental data showed a general coherence with the analogy between heat and mass transfer, as shown in Figure 5, reporting average values of the Nusselt and the Sherwood numbers for corresponding tests at 50 and 60°C of nominal plate temperature. As it can be noted, the heat transfer correlation obtained from dry tests approaches the classical correlation for heat transfer in closed ducts multiplied by a coefficient larger than unity, accounting for the limited length of the pipe and for the effect of the thrust generated by the blower located at channel inlet; on the other hand, wet test data, in terms of Sherwood number exhibit a similar behavior, supporting the applicability of the analogy between heat and mass transfer. This conclusion was confirmed by data at higher plate temperatures (from 70 to 90°C) [10].

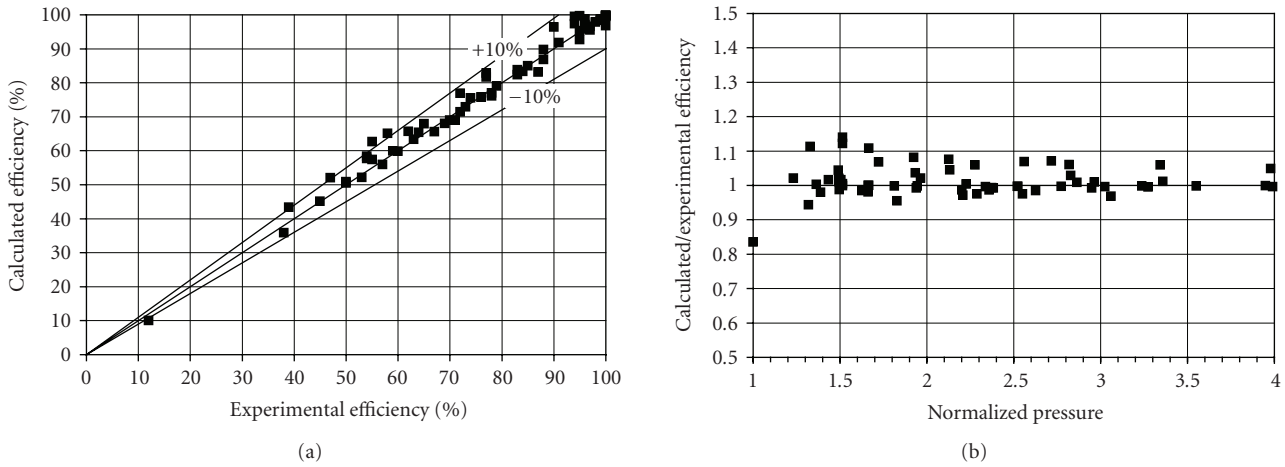

Figure 3: Performance of the adopted model in predicting condensation efficiency as observed in PANTHERS-PCC tests.

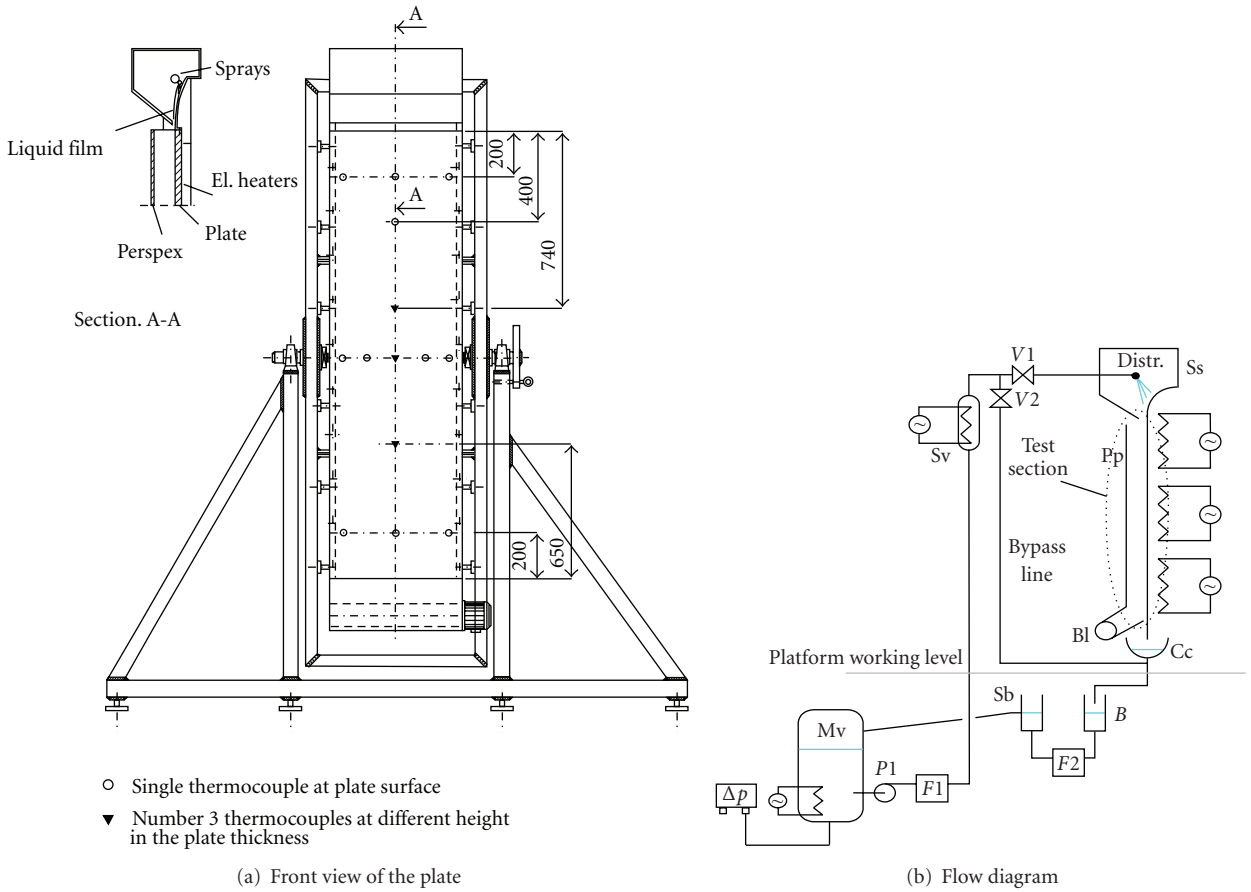

Figure 4: EFFE Experimental Facility.

The availability of experimental data on falling film evaporation offered a first opportunity to apply computational fluid dynamics in simulating heat and mass transfer in a flow duct [15]. The adopted model, quite similar to the ones to be used later on for filmwise condensation, exploited the opportunities offered by the FLUENT code [28] to simulate the near-wall region with models having different degrees of low-Reynolds number capabilities. In particular, the RNG k-ε model was adopted with the two-layer standard model available in the CFD code, making use of detailed discretizations close to the walls. In particular, a 2D 46×46, 90×90 or 180×180 grid was chosen with a refined distribution of meshes close to the lateral walls and at the channel inlet. The falling film was not

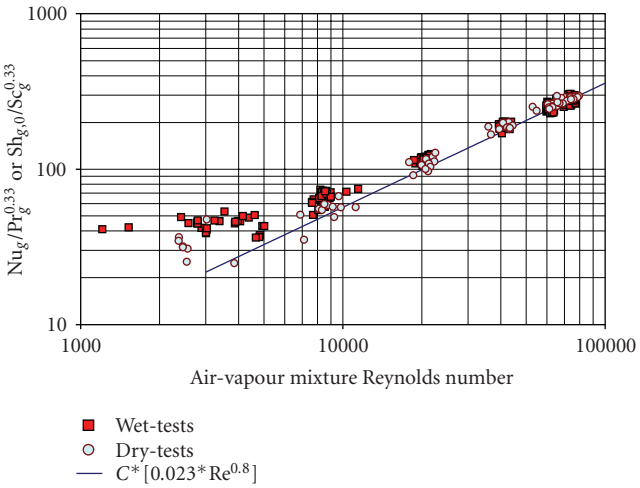

FIGURE 5: Comparison of dry and wet test data in the experimental test series at 50°C and 60°C of plate temperature in the EFFE experiments [6].

modelled, due to its minor role in determining heat and mass transfer; the evaporating wall was therefore assumed as a still interface at the measured average temperature. Water vapour concentration at the wall was assumed to be at the value corresponding to saturation at the wall temperature.

Since the evaporating wall could not be assumed permeable to vapour, as it should be for a transpiration problem in which vapour is continuously blown from the film into the gas-steam mixture, equivalent mass and energy sources were assumed to exist in the first mesh layer close to the wall, having a thickness Δ in the order of 10^{-4} m. This approach, subsequently used also for simulating film condensation, makes use of the available user defined functions to assume volumetric sources given by

$$S_m = \dot{m}_i''/\Delta = -\frac{\rho_{g,i} D_{vg}}{1-\omega_{v,i}} \frac{\partial \omega_v}{\partial y}\bigg|_i /\Delta \tag{4}$$

for mass, and

$$S_h = S_m h_v \tag{5}$$

for energy.

The results obtained for the dry and wet experimental tests, whose boundary conditions are reported in Table 1, showed a tendency to underestimate heat transfer and evaporation rates (see Table 2 for the case $V_{in} = 0$). This effect could be attributed to the location of the blower close to the channel inlet, possibly impressing a transversal component to the inlet velocity. As a matter of fact, the calculations performed with a 45°C degree inclination of the inlet flow rate (see Table 2 for the case $V_{in} = U_{in}$) showed powers and evaporation rates more coherent or even in excess with the measured values confirming the possibility that such an effect plays a role in the performed experiments.

4. Condensation on Finned Tubes

The proposal made in the early 90s by ENEL, Italy, the Italian electrical utility, of a double containment equipped with a completely passive heat removal system [29], stimulated a renewed interest for condensation on finned heat exchangers. In fact, the proposed design included a number of compact heat exchangers made of arrays of inclined finned tubes, connected through a natural circulation loop to an external heat exchanger.

As the efficiency of this system had to be clearly proven in front of safety requirements, an experimental campaign was then carried out by ENEL in cooperation with different Europe an partners. The activity involved an extensive testing of major components, including the internal heat exchanger, the intermediate loop, and the external pools. In particular, CISE performed an extensive campaign on both smooth and finned single tubes in natural convection conditions [30]; in addition, both CISE and PSI [31] performed functional tests on compact finned tube heat exchangers, making use of different modalities. Figure 7 shows sketches of the experimental apparatuses adopted by CISE in this purpose.

This new experimental information allowed the University of Pisa to set up models for finned tube condensation, testing different heat transfer correlation and applying the heat and mass transfer analogy. The main characteristics of the models were the following.

(i) Based on available correlations for heat transfer in free or forced convection on finned tubes and compact heat exchangers, the analogy between heat and mass transfer was applied in the form

$$\begin{aligned} &\mathrm{Nu} = f(\mathrm{Re}, \mathrm{Gr}, \mathrm{Pr}, \text{geometry}) \\ &\Longrightarrow \mathrm{Sh}_0 = f(\mathrm{Re}, \mathrm{Gr}, \mathrm{Sc}, \text{geometry}), \end{aligned} \tag{6}$$

where f represents the particular heat transfer correlation identified for the application and Sh_0 represents the Sherwood number at low mass transfer rate, to be corrected by the classical logarithmic relationship derived by the solution of the Stefan problem:

$$\mathrm{Sh} = \frac{h_m D}{\rho_g D_{vg}} = \mathrm{Sh}_0 \frac{\ln(1+B_m)}{B_m}, \tag{7}$$

the corresponding mass transfer rate was calculated as

$$\dot{m}_i'' = h_m B_m = h_m \frac{\omega_{v,i} - \omega_{v,b}}{1-\omega_{v,i}}. \tag{8}$$

(ii) Since in the case of condensation, the presence of a finned surface raises the problem of evaluating the overall surface efficiency and also the effect of "bridging" (or flooding) of the fins with liquid condensate, it was necessary to include models for both these effects; in particular, the Beatty and Katz model [32] was used to combine the heat transfer coefficients of the finned and unfinned surfaces

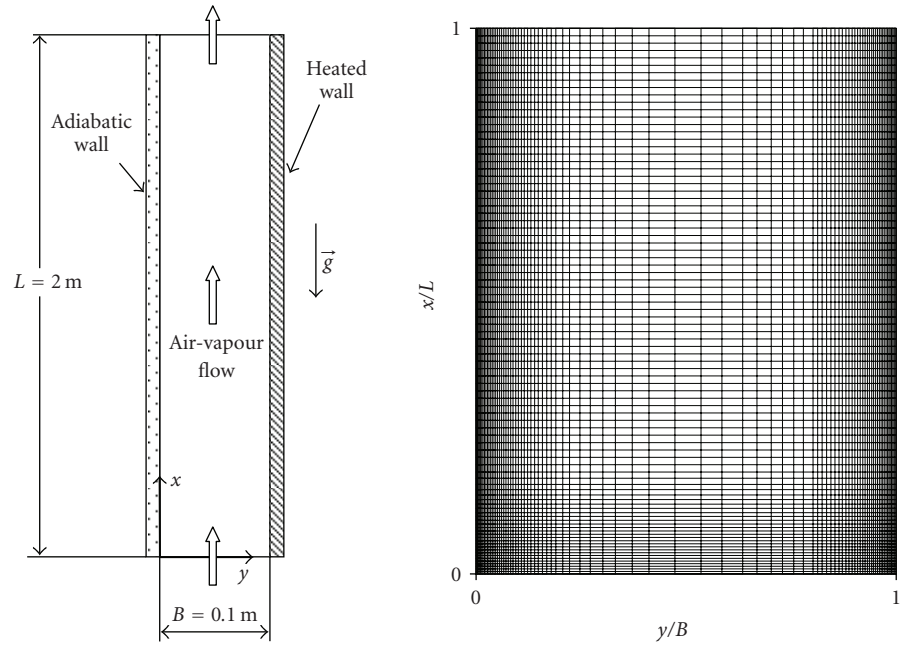

(a) Computational domain (b) Discretization

Figure 6: Computational domain and discretization of the channel of the EFFE experimental facility for the FLUENT code.

Table 1: Boundary conditions for the dry and wet EFFE tests addressed by FLUENT calculations [15].

	Test no.	Average plate temperature (°C)	Air flow Inlet temperature (°C)	Air flow Relative humidity (%)	Air flow Mean inlet velocity (m/s)
Dry	DTI	57.8	20.8	47.6	0.87
	DT2	56.9	21.2	47.5	4.25
	DT3	57.5	24.0	43.3	7.47
Wet	WTI	60.3	23.5	30.9	0.78
	WT2	60.8	23.6	34.6	4.07
	WT3	60.5	25.0	38.2	7.24

based on the film condensation Nusselt theory for flat plates; in addition, the Rudy and Webb model [33] was initially adopted for evaluating the possible effect of efficiency reduction due to bridging, but it was later recognized that this phenomenon played a minor role in the experiments and it was finally neglected; in the final form of the model, also the thermal resistance of the liquid film at the condensing surface was neglected, since it was found to introduce a very weak effect.

Figures 8 and 9 show the results obtained for both the case of single-finned tubes in natural convection and for compact-finned tube heat exchangers with natural draft (CISE) and forced convection (PSI). As it can be noted, also for this relatively more complicated case, the application of the analogy between heat and mass transfer showed to be successful enough as to provide a good comparison with the reference base of data.

5. Filmwise Condensation onto a Flat Plate

Recently, the University of Pisa undertook experiments on filmwise condensation in the CONAN experimental facility installed at its laboratories [12, 13, 16, 35]. As shown in Figure 10, the experimental facility includes three loops.

(i) The primary loop, containing a square cross-section (0.34 m × 0.34 m), two-meter-long test channel, facing a 4.5 cm thick aluminium plate (0.34 m × 2 m, in width and length) on which condensation takes place; the loop presently operates at atmospheric pressure and the steam content in the air-steam mixture circulated in the facility is controlled by the electrical power fed to the steam generator (capable of 60 kW).

(ii) The secondary loop provides the needed cooling on the back side of the cooling plate, by circulating relatively cold water in a narrow channel (5 mm of depth); the measurements of the secondary coolant

Table 2: Results obtained by the FLUENT calculations for the dry and wet EFFE tests [15].

	Test no.	Thermal power (kW)			Total evaporation rate (g/s)		
		Exp.	Calc. ($V_{in} = 0$ m/s)	Calc. ($V_{in} = U_{in}$)	Exp.	Calc. ($V_{in} = 0$ m/s)	Calc. ($V_{in} = U_{in}$)
Dry	DTI	0.35	0.24	0.32	—	—	—
	DT2	1.17	0.83	1.14	—	—	—
	DT3	1.59	1.19	1.72	—	—	—
Wet	WTI	2.82	2.38	3.08	1.19	0.92	1.20
	WT2	9.60	8.56	11.78	3.71	3.33	4.58
	WT3	15.34	12.86	18.46	5.72	5.00	7.18

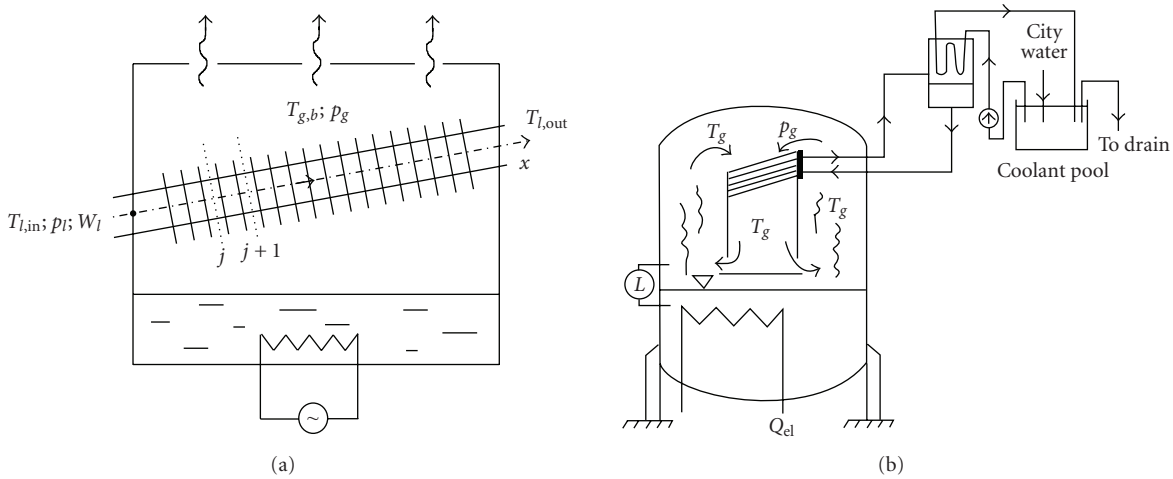

Figure 7: Sketches of the experimental apparatuses adopted by CISE for single tubes and full compact heat exchanger mock-ups [11].

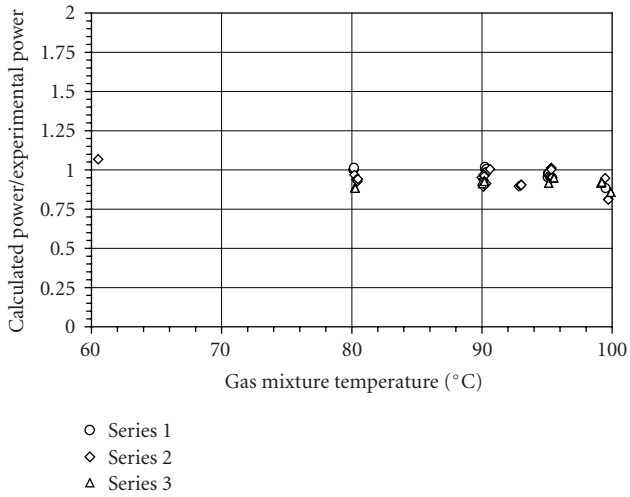

Figure 8: Results obtained for natural convection condensation on single-finned tubes by the Tsubouchi and Masuda model [34].

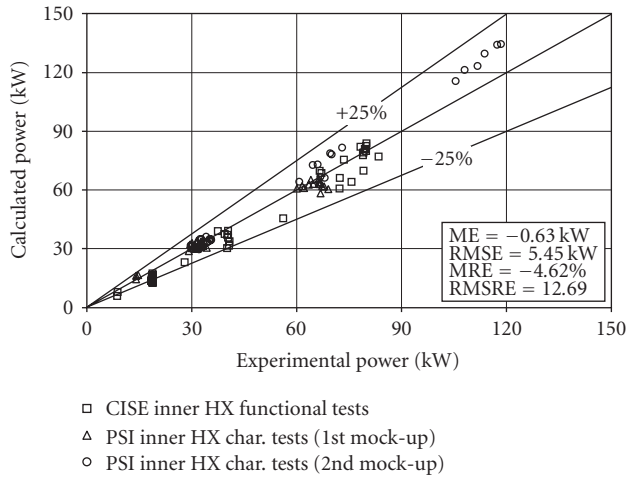

Figure 9: Results obtained for condensation on compact-finned tube heat exchangers making use of the Nir model [34].

conditions on the back side of the plate represent important information to be provided for modelling, relying on the measured inlet and outlet secondary coolant temperature and flow rate to evaluate the heat transfer coefficient and the average secondary fluid temperature.

(iii) The tertiary loop, interfaced with the secondary one through a mixing vessel, accomplishes with the function to remove heat from the test section, by extracting a prescribed flow of warm water from the vessel and replacing it with a same flow of colder water from a large reservoir.

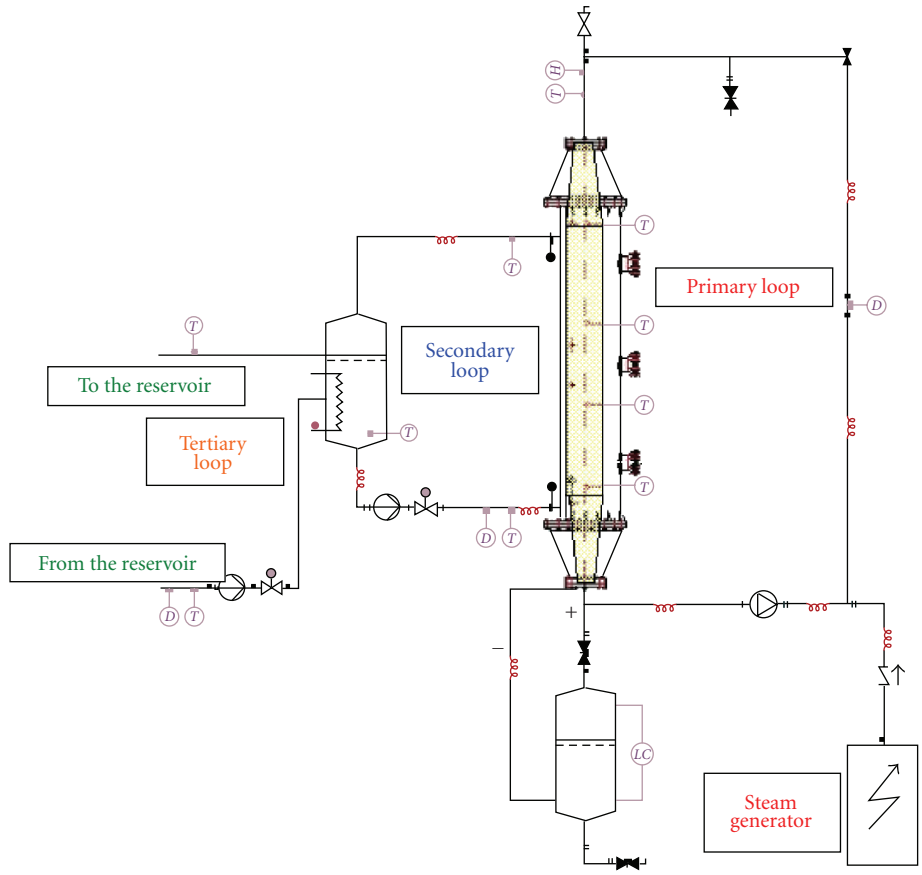

Figure 10: Flow diagram of the CONAN experimental facility.

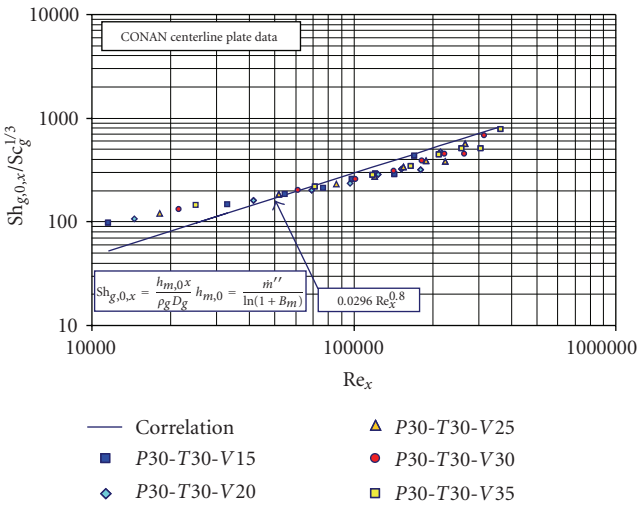

Figure 11: Comparison of a set of experimental data from the CONAN facility with an engineering correlation [16].

The relevant measurements available in the facility include the primary air-steam mixture flow rate (corresponding to channel velocities in the range from 1.5 to 3.5 m/s), dry-bulb and wet-bulb tempe ratures, the local tempe rature close to the surface and within the thickness of the cooled plate (from 30 to 70°C) and the overall condensate flow rate, as collected by a gutter.

In addition to comparing the results of the measurements in terms of local Sherwood numbers with available engineering correlations (see Figure 11), the experimental data were compared with the predictions obtained by the FLUENT code in which a 2D model very similar to the one adopted in the case of the evaporation tests described above (see Section 3) was used. In making use of the model, a conjugated heat transfer approach was successfully implemented, by discretizing the cooled plate and simulating heat conduction through it, in addition to condensation on the gas-side surface (Figure 12). Also in this case, the RNG k-ε model was used with a two-layer treatment near the wall. Appropriate sinks of mass and energy are introduced near the wall to simulate the steam suction. The overall good agreement obtained in the general comparison with data (Figure 13) encouraged to improve the measurement techniques and to analyze in greater detail the phenomena and the observed slight discrepancies with experimental data.

In particular, specific tests performed in the CONAN facility were proposed as Step 1 of a condensation benchmark organized by the University of Pisa in the frame of the EU SARnet of Excellence [13]. Several participants applied their CFD condensation models in predicting the observed behavior, obtaining in general a good agreement with experimental results.

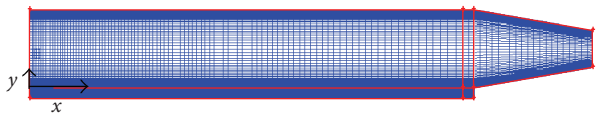

Figure 12: Discretization adopted in the analysis of CONAN experiments by the FLUENT code with conjugated heat transfer.

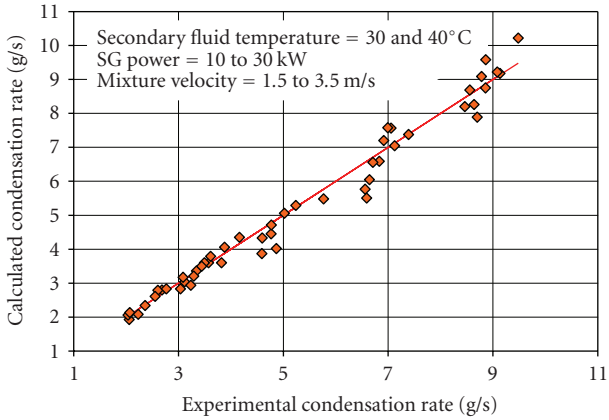

Figure 13: Comparison of a set of experimental data from the CONAN with FLUENT code predictions [35].

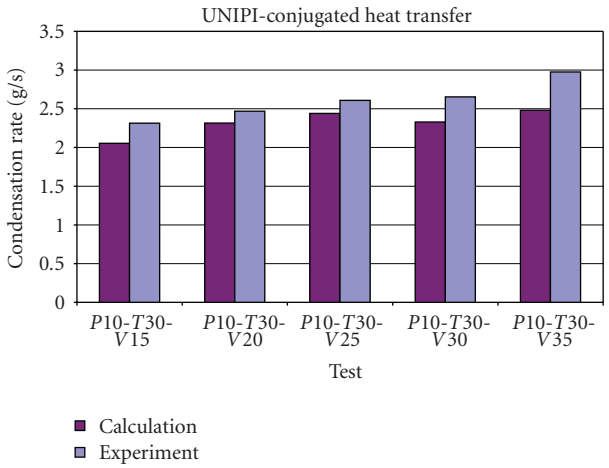

Figure 14: Results for the overall condensation rate obtained by the University of Pisa in the Condensation Benchmark Step-1.

Figures 14 and 15 illustrate the results obtained by the University of Pisa in the application of the FLUENT code to the 5 proposed tests. As it can be noted from Figure 14, the overall condensation rate is slightly underestimated, a feature that resulted common with other code results. This behavior can be explained considering Figure 15, that shows a corresponding underestimate of the local heat flux at the entrance of the test channel. Possible 3D effects as well as some degree of nonuniformity in the inlet mixture velocity can be considered as possible causes of this slight discrepancy.

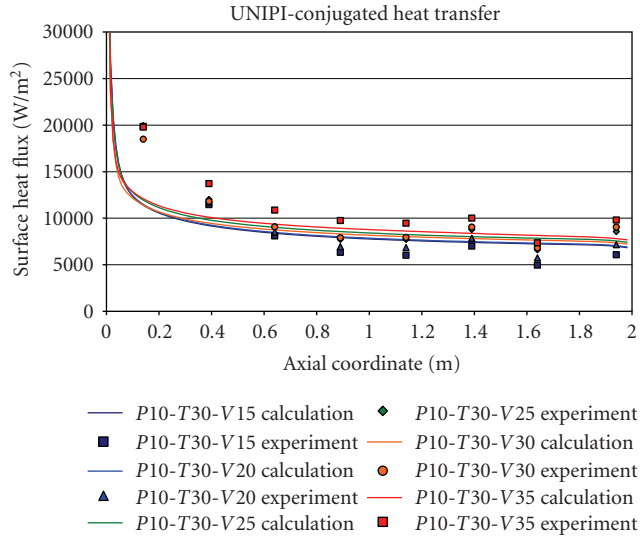

Figure 15: Results for the local heat flux obtained by the University of Pisa in the Condensation Benchmark Step-1.

6. Conclusions

The experience gained in simulating heat and mass transfer phenomena relevant for light water nuclear reactor applications provides a suitable basis to draw conclusions about the present capabilities of models in predicting evaporation and condensation in the presence of noncondensable gases.

As a first remark, it can be noted that, at both the level of engineering models and of CFD codes, evaporation and condensation can be dealt with by quite the same approaches, obtaining similar accuracy. On one side, the classical treatment of mass transfer on the basis of the definition of appropriate coefficients to be multiplied by a suitable driving force, making use of the analogy between heat and mass transfer, appears very effective. Once an applicable heat transfer correlation is selected for the addressed geometry, the analogy assures a reasonable degree of reliability of the corresponding mass transfer model. As a matter of fact, the step of selecting the heat transfer correlation is the one that differentiates the various applications discussed in this paper, ranging from rectangular channels with a falling film, to circular heat exchanger pipes and compact-finned tube heat exchangers. The diversity of the addressed geometries, in which the adopted approach proved to be effective, suggests a reasonable level of reliability.

In this respect, it must be also recognized that the role of the analogy between heat and mass transfer, though particularly evident in the case of the engineering correlation approach, is a key one also in CFD models. In fact, the adoption of constant values of the turbulent Prandtl and Schmidt numbers in defining the turbulent diffusivities on the basis of the eddy viscosity reveals the use of this assumption also in the case of mechanistic models having low Reynolds number capabilities. Therefore, even while using sophisticated two-equation turbulence models, we often still rely on the analogy between heat and mass transfer, something to be attentively considered when extrapolating

our modelling experience to different fluids or operating conditions, for which this approach may be not completely justified or successful.

The effectiveness of computational fluid-dynamic techniques in providing plenty of detailed local data, to be compared with experimental information, is quite evident, though their suitability for practical applications can be matter of discussion. In this respect, we can identify two separate orders of problems.

(i) On one side, even for simple geometries, refining the meshes close to the walls, in order to fully exploit low-Reynolds number capabilities, may be too costly, requiring a huge number of finite volumes or elements and a corresponding increase of computational effort.

(ii) On the other side, complex geometries, like the finned-tubes heat exchangers, may anyway require great detail to be described making the use of CFD models, resulting particularly expensive for production calculations.

It seems therefore that CFD must be considered as a very powerful tool for obtaining relatively accurate results, though it is still not always completely affordable for studying system behavior in cases like complex experimental apparatuses or full-scale reactor plants. In this respect, the job of engineering models and correlations seems not yet to be completed, not only for quick guesses of heat and mass transfer rates, but also for inclusion in system analyses, requiring to model simultaneously many interacting phenomena.

As noted in the conclusions about the SARnet Benchmark [13], at least for simple geometries efforts can be spent in providing CFD codes with models suitable to reasonably predict mass transfer phenomena without introducing an unaffordable number of nodes in the near-wall region. This could be achieved by the use of specialized wall functions allowing for a realistic description of boundary layers. Though a proposal in this aim is already available, dealing by wall functions with intrinsically complicated phenomena as mixed convection may be challenging enough; some sort of compromise modelling should be then achieved, while waiting for increased computing power allowing for adopting more fundamental and mechanistic approaches.

Nomenclature

Latin Letters

B: Width [m]
B_m: Driving force for mass transfer in terms of mass fractions
D_{vg}: Vapor diffusion coefficient in the gas mixture [m^2/s]
D_h: Hydraulic diameter [m]
g: Gravity [m^2/s]
Gr: Grashof number
h: Specific enthalpy [J/kg]
h_{lv}: Latent heat of evaporation [J/kg]
h_m: Mass transfer coefficient [$kg/(m^2s)$]
j: Node number
L: Length [m]
$\dot{m}_i''$: Interfacial mass flux [$kg((m^2s)$]
Nu: Nusselt number
p_0: Reference pressure [Pa]
Pr: Prandtl number
q'': Heat flux [W/m^2]
Re: Reynolds number
S_h: Energy volumetric source [W/m^3]
S_m: Mass volumetric source [$kg/(m^3s)$]
Sc: Schmidt number
T: Temperature [K]
U: X-component of fluid velocity [m/s]
V: Y-component of fluid velocity [m/s]
W: Mass flow rate [kg/s]
x: Longitudinal coordinate [m]
y: Transversal coordinate [m]

Greek Letters

Δ: Node thickness [m]
ρ_g: Gas mixture density [kg/m^3]
ω: Mass fraction

Subscripts

b: Bulk
cond: Condensation
f: Liquid
g: Gas mixture
i: Interface
in: Inlet
min: Minimum
tu: Turbulent
v: Vapor (steam)
w: Wall
0: At low mass transfer rate
∞: Asymptotic value

References

[1] M. D. Kennedy, F. E. Peters, M. D. Carelli, and A. T. Pieczynski, "Advanced PWR passive containment cooling system testing," in *Proceedings of the International Topical Meeting on Advanced Reactor Safety*, pp. 249–256, Pittsburgh, Pa, USA, April 1994.

[2] S. Tsunoyama, S. Yokobori, and K. Arai, "Development of passive containment cooling system," in *Proceedings of the International Topical Meeting on Advanced Reactor Safety*, Pittsburgh, Pa, USA, April 1994.

[3] M. Ishii, S. T. Revankar, R. Dowlati, et al., "Scientific Design of Purdue University Multi-Dimensional Integral Test Assembly (PUMA) for GE SBWR," Purdue University Report PU-NE-94/1, U.S. Nuclear Regulatory Commission Report NUREG/CR-6309, 1996.

[4] G. Yadigaroglu, "Scaling of the SBWR Related Test," Report NEDO-32258, November 1993.

[5] G. Van Goethem, A. Zurita, J. M. Bermejo, P. Lemaître, and H. Bischoff, "Main achievements of FP-4 research in reactor safety," in *Proceedings of FISA Meeting on EU Research in*

Reactor Safety (FISA '99), Luxembourg, Belgium, November-December 1999.

[6] K. Fischer, W. Ambrosini, N. Forgione, et al., "Scaling of containment experiments (SCACEX)," in *Proceedings of FISA Meeting on EU Research in Reactor Safety (FISA '03)*, Luxembourg, Belgium, November 2003.

[7] F. Oriolo, A. Manfredini, A. Villotti, F. De Rosa, and S. Paci, "Evaluation of Containment Heat and Mass Transfer Models with Consideration of the Phebus-FP Containment Vessel," EUR 16111 EN, JRC Ispra Site, 1994.

[8] W. Ambrosini, N. Forgione, F. Oriolo, P. Vigni, and S. Valisi, "Prediction of condensation in a prototypical passive containment condenser," in *Proceedings of the Post-SMiRT 14 International Seminar 18 on Passive Safety Features in Nuclear Installations*, Pisa, Italy, August 1997.

[9] N. Forgione, W. Ambrosini, F. Oriolo, and P. Wackers, "Falling film evaporation in a rectangular channel with different depth," in *Proceedings of the 10th International Conference on Nuclear Engineering (ICONE-10)*, vol. 4, pp. 699–704, Arlington, Va, USA, April 2002.

[10] W. Ambrosini, N. Forgione, F. Oriolo, and J. Wäsle, "Experimental investigation and modelling of film evaporation in the presence of countercurrent air flow," in *Proceedings of the 18th UIT National Heat Transfer Conference*, vol. 2, p. 617, Cernobbio, Italy, June 2000.

[11] L. Brusa, A. Bianchi, L. Mazzocchi, et al., "Modelling condensation on finned tube heat exchangers in the presence of noncondensable gases," in *Proceedings of the 2nd International Symposium on Two-Phase Flow Modelling and Experimentation*, Pisa, Italy, May 1999.

[12] W. Ambrosini, N. Forgione, F. Oriolo, C. Dannöhl, and H. J. Konle, "Experiments and CFD analyses on condensation heat transfer on a flat plate in a square cross section channel," in *Proceedings of the 11th International Topical Meeting on Nuclear Reactor Thermal-Hydraulics (NURETH-11)*, Avignon, France, October 2005.

[13] W. Ambrosini, M. Bucci, N. Forgione, et al., "Comparison and analysis of the condensation benchmark results," in *Proceedings of the 3rd European Review Meeting on Severe Accident Research (ERMSAR '08)*, Nesseber, Bulgaria, September 2008.

[14] W. Ambrosini, N. Forgione, A. Manfredini, and F. Oriolo, "On various forms of the heat and mass transfer analogy: discussion and application to condensation experiments," *Nuclear Engineering and Design*, vol. 236, no. 9, pp. 1013–1027, 2006.

[15] W. Ambrosini, N. Forgione, D. Mazzini, and F. Oriolo, "Computational study of evaporative film cooling in a vertical rectangular channel," *Heat Transfer Engineering*, vol. 23, no. 5, pp. 25–35, 2002.

[16] M. Bucci, M. Sharabi, W. Ambrosini, N. Forgione, F. Oriolo, and S. He, "Prediction of transpiration effects on heat and mass transfer by different turbulence models," *Nuclear Engineering and Design*, vol. 238, no. 4, pp. 958–974, 2008.

[17] A. S. Rao, C. D. Sawyer, and R. J. Candless, "Simplified boiling water reactor design," in *Proceedings of the 1st JSME/ASME Joint International Conference on Nuclear Engineering (ICONE-1)*, Tokyo, Japan, November 1991.

[18] P. Masoni, S. Botti, and G. W. Fitzsimmons, "Confirmatory tests of full-scale condensers for the SBWR," in *Proceedings of the 2nd JSME/ASME Joint International Conference on Nuclear Engineering (ICONE-2)*, pp. 735–744, San Francisco, Calif, USA, March 1993.

[19] P. Masoni, G. Bianchini, P. F. Billig, et al., "Tests on full scale prototypical passive containment condenser for SBWR's application," in *Proceedings of the 3rd JSME/ASME Joint International Conference on Nuclear Engineering (ICONE-3)*, Kyoto, Japan, April 1995.

[20] W. M. Rohsenow, "A method for correlating heat transfer data for surface boiling of liquids," *Transactions of the ASME*, vol. 74, pp. 969–976, 1952.

[21] P. W. Dittus and L. M. K. Boelter, "Heat transfer in automobile radiators of the tubular type," *University of California Publications in Engineering*, vol. 2, no. 13, pp. 443–461, 1930.

[22] C. F. Bonilla, *Heat Transfer*, Interscience, New York, NY, USA.

[23] J. Stefan, "Versuche über die Verdampfung," *Sitzungsberichte der Akademie der Wissenschaften*, vol. 68, pp. 385–423, 1873.

[24] G. Ackerman, "Wärmeübertragung und molekulare Stoffübertragung im gleichen Feld bei grosser Temperatur und Partialdruckdifferenzen," VDI ForschHft. 382, 1937.

[25] S. Banerjee and Y. A. Hassan, "Condensation heat transfer coefficient with noncondensable gases for heat transfer in thermal-hydraulic codes," in *Proceedings of the 3rd JSME/ASME Joint International Conference on Nuclear Engineering (ICONE-3)*, Kyoto, Japan, April 1995.

[26] K. Almenas and U. C. Lee, "A statistical evaluation of the heat transfer data obtained in the HDR containment tests," University of Maryland, 1984.

[27] A. Manfredini, F. Mariotti, F. Oriolo, and P. Vigni, "A facility for the evaluation of heat flux from a plate cooled by a water film with counter-current air flow," in *Proceedings of the 11th National Congress on Heat Transfer of the UIT*, Milano, Italy, June 1993.

[28] Fluent Inc., "FLUENT 6.1 User's Guide," February 2003.

[29] V. Cavicchia and P. Vanini, "Innovative containment cooling for concrete containment of nuclear power plants," in *Proceedings of the International Conference on Nuclear Containment*, Cambridge, UK, September 1996.

[30] L. Mazzocchi, P. A. G. Vacchiani, and P. Vanini, "Finned tubes condensing heat transfer with mixtures of steam and non condensible gases," in *Proceedings of the European Two-Phase Flow Group Meeting*, Grenoble, France, June 1996.

[31] F. de Cachard, S. Lomperski, and G.-R. Monauni, "The first LINX-2 tests," in *Proceedings 5th International Conference on Nuclear Engineering (ICONE-5)*, Nice, France, May 1997, paper 2448.

[32] K. O. Beatty Jr. and D. L. Katz, "Condensation of vapors on outside of finned tubes," *Cemical Engineering Progress*, vol. 44, no. 1, pp. 55–70, 1948.

[33] T. M. Rudy and R. L. Webb, "An analytical model to predict condensate retention on horizontal integral-fin tubes," *Journal of Heat Transfer*, vol. 107, pp. 361–368, 1985.

[34] A. Nir, "Heat transfer and friction factor correlations for crossflow over staggered finned tube banks," *Heat Transfer Engineering*, vol. 12, no. 1, pp. 43–58, 1991.

[35] W. Ambrosini, N. Forgione, S. Mogliani, and F. Oriolo, "Discussion of heat and mass transfer models on the basis of experiments and CFD calculations," in *Proceedings of the United Kingdom National Heat Transfer Conference (UKHTC '05)*, Manchester, UK, September 2005.

Hindawi Publishing Corporation
Science and Technology of Nuclear Installations
Volume 2009, Article ID 473795, 12 pages
doi:10.1155/2009/473795

Research Article

Thermal Hydraulic Analysis of a Passive Residual Heat Removal System for an Integral Pressurized Water Reactor

Junli Gou, Suizheng Qiu, Guanghui Su, and Douna Jia

Department of Nuclear Science and Technology, Xi'an Jiaotong University, Xi'an, Shaanxi 710049, China

Correspondence should be addressed to Suizheng Qiu, szqiu@mail.xjtu.edu.cn

Received 14 August 2008; Accepted 22 December 2008

Recommended by Xu Cheng

A theoretical investigation on the thermal hydraulic characteristics of a new type of passive residual heat removal system (PRHRS), which is connected to the reactor coolant system via the secondary side of the steam generator, for an integral pressurized water reactor is presented in this paper. Three-interknited natural circulation loops are adopted by this PRHRS to remove the residual heat of the reactor core after a reactor trip. Based on the one-dimensional model and a simulation code (SCPRHRS), the transient behaviors of the PRHRS as well as the effects of the height difference between the steam generator and the heat exchanger and the heat transfer area of the heat exchanger are studied in detail. Through the calculation analysis, it is found that the calculated parameter variation trends are reasonable. The higher height difference between the steam generator and the residual heat exchanger and the larger heat transfer area of the residual heat exchanger are favorable to the passive residual heat removal system.

1. Introduction

Integral pressurized water reactor (IPWR) is being considered as one of the next-generation advanced nuclear reactors designed to be inherently safe by naturally and physically passive mechanisms. The primary coolant system components of the IPWRs, composed of the core, the pressurizer, the main coolant pumps (MCPs), and the once-through steam generators (OTSGs), are housed in the reactor pressure vessel (RPV). The adoption of the special in-vessel layout eliminates the pipe connection between those components, and thus the occurrence of large break loss-of-coolant accidents (LBLOCAs) is essentially excluded by the new design. In addition, one of the very important design features of the IPWRs is the simplifications and improvements in the safety systems. Especially, such passive safety systems as passive residual heat removal system (PRHRS) are employed to accomplish the inherent safety functions and mitigate the consequences of the postulated accidents. PRHRS is expected to safely remove the core decay heat, only through natural circulation, in case of both station blackout accident and long-term cooling for repair or refueling.

A literature survey reveals that there have been many experimental and numerical investigations on the characteristics of different PRHRSs. The Westinghouse advanced passive PWRs, AP-600, AP-1000, and EP-1000 (IAEA-TECDOC-1391, 2004; Adomaitis et al. [1]; Reyes and Hochreiter [2]; Zhang et al. [3]) adopt passive core cooling system (PXS) to protect the plant against reactor coolant system (RCS) leaks and ruptures of various sizes and locations. The PXS includes a 100% capacity passive residual heat removal heat exchanger (PRHR HX), which satisfies the safety criteria for loss of feedwater, feedwater and steam line breaks. The PRHR HX, immersed in the in-containment refueling water storage tank (IRWST), is connected through the cold leg and hot leg to the core. The IRWST water volume is sufficient to absorb decay heat for more than 1 hour before the water begins to boil. Once boiling starts in the IRWST, the steam passes to the containment and condenses on the inner surface of the steel containment vessel, and then drains by gravity back into the IRWST. The PRHR HX and the passive containment cooling system (PCCS) provide indefinite decay heat removal capability with no operator action required. The theoretical and experimental

investigations on the PXS characteristics of AP600 indicate that the design of the PRHRS is feasible and rational.

The PRHRSs via the secondary side of the steam generators for WWER-1000/V-392 and WWER-640/V-407 plants (Hyvärinen [4]; IAEA-TECDOC-1391, [5]; Krepper [6]; Mousavian et al. [7]) are intended to remove decay heat from the reactor in a case of a station blackout with intact primary and secondary circuits, and to depressurize the RCS under a small break LOCA. The PRHRS of V-392 consists of four independent trains, each of which has pipelines for steam supply and removal of condensate, valves, and an air-cooled heat exchanger installed outside the containment. The steam generated in the steam generators due to the heat released in the reactor condenses in the air-cooled heat exchanger and rejects its heat to the ambient air. The motion of the cooling medium takes place in natural circulation. While in the V-407 design, the PRHRS removes the heat to the heat exchangers immersed to the emergency heat removal tanks, which are installed outside the containment. The water inventory in the tanks is sufficient for the long-term heat removal (at least 24 hours) and can be replenished if necessary. The experimental investigation and calculation analyses show that the PRHRS for WWER can safely remove the decay heat in case of the station blackout accident and enhance the inherent safety of the plant. The experimental investigations have confirmed the design function of the passive safety means proposed and also created the necessary experimental database for modeling by the system thermo-hydraulic codes. Further investigations are being planned for additional verification of the passive safety systems and for the optimization of their design.

The PRHRS (Su et al. [8, 9], Qiu et al. [10], Zejun et al. [11]) for Chinese advanced PWR (AC-600) is used to remove the decay heat in the event of a station blackout by natural circulation. It may also be effective in a main steam pipe rupture or loss of feedwater event. The system consists of two independent trains, each of them being connected to the reactor coolant loops via the secondary side of the respective steam generator. Each train has a feedwater tank, an air cooler located in a chimney outside the containment, and piping (and valves) for steam and condensate circulation. The air cooler with the help of chimney rejects the core decay heat transferred from the steam generators into the atmosphere. Based on the experimental investigations, semiempirical theoretical model related to height between heat resource and heat sink has been established which can be applied to the system arrangement design for the PRHRS of Chinese advanced PWR. Transient experiment also provides the basis for the startup mode of the PRHRS. Furthermore, a way to avoid potential water hammer in the feedwater tank has been identified. Computer code MISAP2.0 has been developed with self-reliance copyright, which is a useful tool for the PRHRS design.

The PRHRS for SMART (Chang et al. [12]; Chung et al. [13]; Chung et al. [14]; Chung et al. [15]), a small modular integral-type pressurized water reactor developed by KAERI, is also a steam generator secondary side decay heat removal system. Two of the four independent PRHRS trains are sufficient to remove the decay heat. Each train is composed of a compensating tank pressurized by nitrogen, a heat exchanger immersed in an in-containment refueling water tank, valves and piping for steam and condensate. The compensating tank makes up the water volume change in the passive residual heat removal system and holds the water inventory for the filling system pipelines during a cooldown transient. The check valves are installed on the pipelines between the compensating tank and the heat exchanger outlet to keep the water from leaving the compensating tank in the first instants of a cooldown, which would prevent a natural circulation from being developed. The refueling water tank is located high enough above the steam generator to remove the heat transferred from the primary side in the steam generator by a natural convection when the secondary system loses its heat removal capability. The water in the refueling water tank is heated, boiled, and eventually evaporated into the atmosphere. The water inventory in the refueling water tank can remove the heat for 36 hours at least without any operator actions to respond to the design basis events. The heat transfer characteristics and the natural circulation performance of the PRHRS for the SMART have been experimentally investigated in the VISTA facility, and the experimental results have been analyzed using a best-estimated system analysis code, MARS. The comparison of the experimental data and the theoretical prediction shows good agreement accept for some parameters, such as the fluid temperature in the PRHRS condensate line. It seems that it is due to an insufficient heat transfer modeling in the pool such as the refueling water tank in the MARS calculation. Besides, PRHRSs for other reactors have been developed in the last decade (Iwamura et al. [16]; Samoilov et al. [17]; Peng et al. [18]; Jinling and Yujun [19]; Kusunoki et al. [20]; Xinian et al. [21]; Carelli et al. [22]).

A detailed review of the related literatures indicates that the PRHRSs are quite different from one another in design for different PWRs. The merits and demerits of different PRHRSs are very difficult to be evaluated. Both the test facilities for the corresponding PRHRSs and the commercial analysis codes (like Relap, Retran, etc.) have their own limitations. It is evident that due to the complexity of the thermal hydraulic process involved in the PRHRSs with their small inherent natural driving forces (i.e., gravity, natural circulation, etc.), experimental and theoretical investigations have to be performed for each specific design. Validated computer codes must be developed to support the expected operational performance. Consequently, considering the design features and operation performances of a new type of PRHRS, systematic analyses on the thermal hydraulic characteristics of it should be performed in detail at the conceptual design stage from both experimental and analytical points of view.

In the present paper, a theoretical investigation on the thermal hydraulic characteristics of a new type of PRHRS, which is connected to the reactor system via the secondary side of the steam generator, for an integral pressurized water reactor is conducted. With three-interknited natural coolant circulation loops, the core decay heat should be safely removed to an ultimate heat sink, a water pool (WP) with a large enough size. In order to estimate the thermal hydraulic

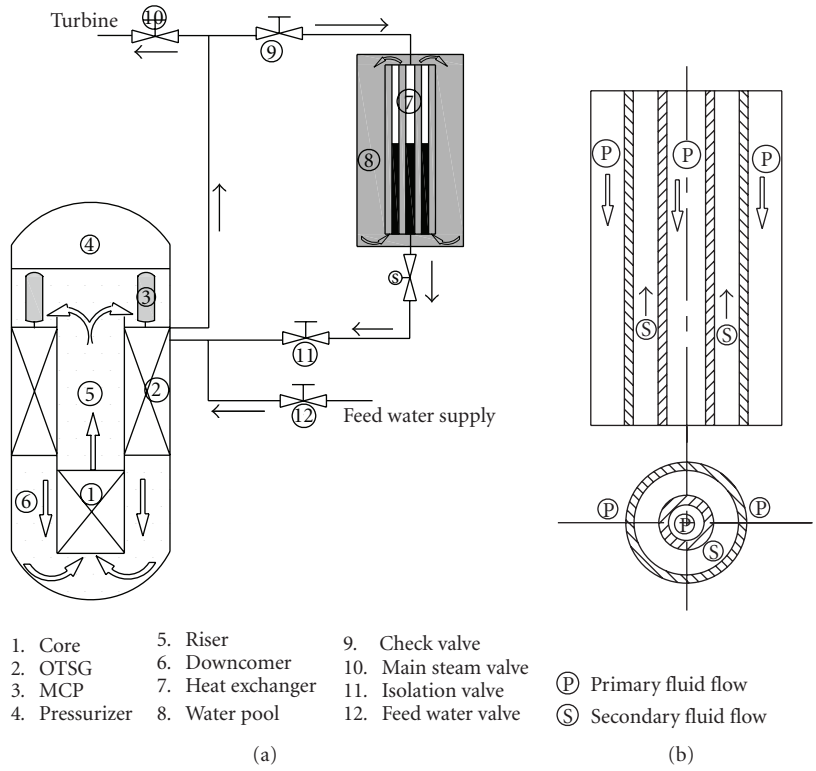

Figure 1: Schematic diagram of the PRHRS and OTSG heat transfer tubes.

characteristics and evaluate the heat removal capacity of the PRHRS, a one-dimensional two-phase flow model and a simulation code (SCPRHRS) are developed. The model is based on the fundamental conservation principles, namely, the mass, momentum, and energy conservation equations. System component models are included according to the special design features of it. All possible flow and heat transfer conditions are considered and the corresponding optional models are supplied in the simulation code. Using the code, the analyses results of the PRHRS transient behavior are presented in this paper.

2. System Description

The layout of the primary coolant system components and the PRHRS of this IPWR are shown in Figure 1(a). The primary coolant system components, including a core, a pressurizer, 2 main coolant pumps (MCPs), and 12 once-through steam generators (OTSGs), are contained in the reactor pressure vessel (RPV). The reactor core is located at the bottom of the RPV. The MCPs and the OTSGs are installed symmetrically in the annular space between the reactor barrel and the RPV. This configuration results in an integral and compact system. There is a long riser on the top of the core outlet to enhance the natural circulation capacity. At the same time, a natural circulation by-pass valve, installed between the inlet and the outlet of each MCP, is designed to reduce the natural circulation form loss.

Under forced circulation conditions, the natural circulation by-pass valve is kept closed and the primary coolant is driven by the MCPs to circulate along the primary circuit. The primary coolant enters the core from the lower plenum. After being heated, the coolant flows out of the core and upwards through the riser. Then, the coolant is pumped by the MCPs, located at the exit of the riser, and flows through the annular cavity on top of the primary entry of the OTSGs. Subsequently, it flows downwards through the primary side of the OTSGs, cooled by the secondary coolant and the downcomer until reaching the lower plenum. Finally, it flows back into the core and recirculates continually along the flow path. The heat transfer element of the OTSGs has a straight annular channel, composed of two concentric circular tubes with different diameters (see Figure 1(b)). In the steam generator, the secondary coolant flows upwards in the annular channel and is bilaterally heated by the primary coolant, which flows downwards in the shell-side of the annular channel outer tube and the inner tube of the annular channel, respectively.

There are two sets of independent residual heat removal system with identical characteristics. They are installed outside the reactor pressure vessel and connected to the secondary circuit loops (Figure 1(a)). The residual heat exchanger, which has a straight tubular bundle type, is immerged in a water pool with very large size. Under normal operating conditions, the heat exchanger is filled with water and isolated by a check valve and an isolation valve. The PRHRS removes the core decay heat by natural circulation under station blackout accident as well as in the case of long-term cooling for repair or refueling. After a reactor trip, the PRHRS will start to work automatically without any active

operation. The shutdown signal from the reactor control system makes the turbine tripped, the main steam valves and the feed water valves closed. The forced circulation in the primary loop turns into natural circulation. At the same time, the check and isolation valves open automatically and the water in the heat exchanger enters the secondary side of the OTSGs by gravity. After exiting the steam generator as superheated or saturated fluid, the secondary coolant enters the residual heat exchanger and flows downwards in the tube-inside, where it is cooled by the shell-side water in the water pool and condensed to subcooled water. Finally, the condensate flows back to the steam generator. Also, the natural circulation will establish in the water pool because of the continual heating from the secondary coolant. Consequently, the residual decay heat of the core is passively removed to the ultimate heat sink through three-interknited natural circulation loops, namely, (1) the primary circulation loop composed of the core, the primary side of the OTSGs, and the connecting plenums; (2) the secondary circulation loop including the secondary side of the OTSGs, the tube-inside of the heat exchangers, and the connecting pipes and plenums; (3) the third circulation loop in the water pool.

3. Theoretical Model

The basic field model is based on the fundamental conservation principles: the mass, momentum, and energy conservation equations. With the assumption of one-dimensional flow, these equations, including single-phase and two-phase conservative equations, can be easily found in the reference (Collier and Thome [23]). The characteristics of the theoretical model are introduced in the following in detail.

3.1. Core Power. The core power is calculated using the decay heat equation and point neutron kinetics equation with six groups of delayed neutron (Pingan et al. [24]). Each group has its own yield and decay constant. The reactivity feedback caused by the temperature change of the moderator and the fuel is specially considered. The axial power distribution is specified by a profile supplied. At the same time, the power distribution in the radial direction is assumed to be uniform.

3.2. System Components Model

3.2.1. Mass Flow Rate of the Primary Loop. By integrating the momentum conservative equation along the primary loop, the mass flow rate equation is given by

$$\begin{aligned}\frac{\partial W_P}{\partial \tau}\oint \frac{1}{A}dz = &-\oint \frac{\partial P}{\partial Z}dz - \oint \frac{1}{A}\frac{\partial}{\partial z}\left(\frac{W_P^2}{\rho A}\right)dz \\ &- \oint \rho g\, dz - W_P^2 \sum_{i=1}^{n}\left(\frac{c}{2\rho A^2}\right)_i \\ &- W_P^2 \oint f \frac{1}{2D_e \rho A^2}dz.\end{aligned} \tag{1}$$

In fact, the second terms on the right hand of (1) can be eliminated. By introducing natural circulation driving head B_P, (1) is simplified as follows:

$$\frac{\partial W_P}{\partial \tau} = \frac{(P_{\text{pump}} + B_P - \Delta P_{\text{loc}_P} - \Delta P_{f_P})}{\oint (dz/A)}, \tag{2}$$

where ΔP_{loc_P} and ΔP_{f_P} are the local pressure drop and the friction pressure drop along the primary loop, respectively; P_{pump} is the pressure head of the MCP. B_P, ΔP_{loc_P}, and ΔP_{f_P} are defined by

$$\begin{aligned}P_{\text{pump}} &= \rho g H_{\text{pump}}, \\ B_P &= -\oint \rho g\, dz, \\ \Delta P_{\text{loc}_P} &= W_P^2 \sum_{i=1}^{n}\left(\frac{c}{2\rho A^2}\right)_i, \\ \Delta P_{f_P} &= W_P^2 \oint f \frac{1}{2D_e \rho A^2}dz.\end{aligned} \tag{3}$$

The pressure head of the MCP during the transient process is a very important parameter to calculate the mass flow rate of the primary loop. However, the pressure head of the MCPs reduces rapidly to zero due to the small inertia rotation after a reactor trip. Moreover, as mentioned above, the MCPs stop and the by-pass valves are opened to enhance the natural circulation under natural circulation conditions. Because the local form loss coefficient of the by-pass valve is much less than that of the MCP, most of the primary coolant flows through the by-pass valve. The relationship between the local pressure drop of the MCP and the by-pass valve is expressed by

$$\Delta p_{\text{pump}} = \Delta p_v. \tag{4}$$

That is,

$$\frac{1}{2}c_{\text{pump}}\frac{W_{\text{pump}}^2}{A_{\text{pump}}^2 \rho} = \frac{1}{2}c_v \frac{W_v^2}{A_v^2 \rho}. \tag{5}$$

While

$$W_p = W_{\text{pump}} + W_v. \tag{6}$$

Substituting (5) and (6) into (4), the local pressure drop of the MCP is

$$\Delta p_{\text{pump}} = \frac{1}{2}c_{\text{pump}}\frac{W^2}{\left(1 + A_v\sqrt{c_{\text{pump}}/c_v}/A_{\text{pump}}\right)^2 A_{\text{pump}}^2 \rho}. \tag{7}$$

3.2.2. Mass Flow Rate of the Secondary Loop. Similarly, by integrating the momentum conservative equation along the secondary loop, the mass flow rate equation is given by

$$\frac{\partial W_s}{\partial \tau} = \frac{(B_s - \Delta P_{\text{loc}_s} - \Delta P_{f_s})}{\oint (dz/A)}, \tag{8}$$

where B_s, $\Delta P_{\mathrm{loc}_s}$, and ΔP_{f_s} are expressed by

$$B_s = -\oint \rho g\, dz,$$
$$\Delta P_{\mathrm{loc}_s} = W_s^2 \sum_{i=1}^{n} \left(\frac{c}{2\rho A^2}\right)_i, \tag{9}$$
$$\Delta P_{f_s} = W_s^2 \oint f \frac{1}{2D_e \rho A^2} dz.$$

3.2.3. Mass Flow Rate of the Third Loop. Because the size of the water pool is large enough, an assumption, that the change of the pool water temperature can be neglected, is rational. Similarly, by applying the momentum conservative equation, the mass flow rate of the third loop is written as

$$\frac{\partial W_t}{\partial \tau} = \frac{(B_t - \Delta P_{\mathrm{loc}_t} - \Delta P_{f_t})}{\sum_{i=1}^{k} (\Delta z/A)_i}, \tag{10}$$

where B_t, $\Delta P_{\mathrm{loc}_t}$, and ΔP_{f_t} are defined as follows:

$$B_t = \rho_p g L - \sum_{j=1}^{k} (\rho g \Delta z)_j,$$
$$\Delta P_{\mathrm{loc}_t} = W_t^2 \sum_{i=1}^{n} \left(\frac{c}{2\rho A^2}\right)_i, \tag{11}$$
$$\Delta P_{f_t} = W_t^2 \sum_{j=1}^{k} \left(\frac{f\Delta z}{2D_e \rho A^2}\right)_j.$$

It is noted that the equations for mass flow rate calculation of the three loops are simplified equations with an assumption of constant flow rate along the circuit. This simplification may cause inaccuracy especially in case of two-phase flow. However, this simplified model has been successfully adopted in our previous investigations (Su and Guo [8], Qiu et al. [10], Zejun et al. [11], Tian et al. [25, 26]). The comparisons of our results with those of RETRAN-02 and RELAP/MOD3 gave good agreements. So, using the simplified model in this calculation is still believed to be feasible for the conceptual design of the PRHRS.

3.2.4. Pressure of the Secondary Loop. Under normal operation condition with rated core power, the spatial variation of the pressure in the secondary loop cannot be neglected because of the large pressure drop from the inlet to the outlet of the OTSG secondary side (about 1.5 MPa). However, in case of natural circulation, the spatial pressure difference of the secondary loop becomes very small as a result of the loss of feed water pump head. Thus, an assumption, that the spatial variation of the pressure in the secondary loop is negligible, can be made. Consequently, by integrating the mass continuity equation along the secondary loop, the pressure equation of the secondary loop can be written as

$$\sum_{i=1}^{n} \left[\left(\frac{\partial \rho}{\partial h}\frac{\partial h}{\partial \tau} + \frac{\partial \rho}{\partial p}\frac{\partial p}{\partial \tau}\right) A \cdot \Delta Z\right]_i = -\oint \frac{\partial W}{\partial z} dz. \tag{12}$$

Table 1: Heat transfer correlations.

Flow regime	Correlation	Reference
Single-phase water		
Laminar	Collier	[27]
Transition	Interpolation	
Turbulent	Sieder-Tate	[28]
Subcooled boiling	Jens and Lottes	[23]
Saturated boiling	Chen	[23]
Transition/film boiling	Groeneveld	[29]
Superheated vapor	Sieder-Tate	[28]
Condensation	Shaha	[30]

Practically, the right-hand side of (12) equals zero. Thus, (12) is simplified as

$$\frac{\partial p}{\partial \tau} = -\frac{\sum_{i=1}^{n} (\rho^2 A \cdot \Delta Z (\partial v/\partial h)(\partial h/\partial \tau))_i}{\sum_{i=1}^{n} (\rho^2 A \cdot \Delta Z (\partial v/\partial p))_i}. \tag{13}$$

3.2.5. Tube Wall Heat Transfer. Because of the very small thickness of the tube wall, lumped parameter method is used to calculate the wall heat transfer. Ignoring the axial conduction heat transfer, the tube wall heat transfer equation is expressed by

$$mC_p \frac{\partial T_w}{\partial \tau} = H_1 A_1 (T_1 - T_w) - H_2 A_2 \cdot (T_w - T_2), \tag{14}$$

where T_w is the average temperature of the tube wall; H_1 and H_2 are heat transfer coefficients of the two surfaces of the wall, respectively; A_1 and A_2 are heat transfer area of the two surfaces of the wall, respectively; T_1 and T_2 are the fluid temperatures, respectively.

3.2.6. Pipe and Plenum. In the PRHRS, there are pipes and plenums to connect the major components. With an assumption of thermal isolation, the energy conservative equation of them can be expressed by

$$M\frac{dh}{d\tau} = W(h_{\mathrm{in}} - h). \tag{15}$$

3.2.7. Heat Transfer and Frictional Coefficient Correlations. The dominant heat transfer of the primary loop and the third loop is single-phase mode, and the modes of the secondary loop are single-phase and boiling heat transfer in the OTSG and condensation and single-phase heat transfer in the heat exchanger. According to the corresponding flow regimes, appropriate heat transfer and frictional coefficient correlations are selected. Two-phase frictional multiplier is used to calculate the two-phase flow pressure drop, that is,

$$f_{\mathrm{tp}} = f_{\mathrm{lo}} \cdot \Phi_{\mathrm{tp}}^2. \tag{16}$$

The involved heat transfer and frictional coefficient correlations are listed in Tables 1 and 2, respectively.

3.3. Nodalization of the PRHRS. In order to numerically simulate the thermal hydraulic characteristics of the PRHRS,

Table 2: Frictional coefficient correlations.

Flow regime	Correlation	Reference
Single phase		
Laminar flow	Darcy	[24]
Transition flow	0.048	
Turbulent flow	Blasius	
Two phase		
Homogeneous model		[31]
Drift flux model	Chisholm	[32]

Table 3: Main parameters of SG and PRHRS.

Parameter	Value
Initial core power	160 MW
Steam generator	
Primary operation pressure	15.5 MPa
Primary mass flow rate	980 kg /s
Primary inlet temperature	295°C
Primary outlet temperature	265°C
Secondary mass flow rate	60 kg /s
Secondary inlet temperature	60°C
Secondary outlet temperature	270°C
Secondary pressure	3.0 MPa
Diameter of inner tube	8 × 1mm
Diameter of outer tube	12 × 1mm
Length of the tube	2.0 m
Passive heat removal system	
Secondary initial temperature	30°C
Secondary initial pressure	3.0 MPa
Diameter of tube	25 × 2.5 mm
Length of the tube	2.0 m
Water temperature of WP	30°C
WP pressure	0.1 MPa

the whole system shown in Figure 1 is divided into many control volumes and junctions according to the different geometrical and heat transfer conditions. Figure 2 schematically shows the nodalization of the PRHRS. The primary circuit model used in the thermal hydraulic analysis consists of a core, a steam generator, a pump, a pressurizer, a downcomer, and plenums. The modeling of the PRHRS is composed of a steam generator, a heat exchanger, a water pool, pipes, plenums, and valves. In the core, the steam generator and the heat exchanger, fine control volume division is used to properly predict the heat transfer phenomena. The number of the control volume can be easily changed for different calculation requirements.

4. Numerical Method and Code Description

In order to theoretically analyze the thermal hydraulic characteristics of the PRHRS, the above equations need to be numerically solved. Through discretizing the spatial terms of the above differential equations, they have a form in common as follows:

$$\frac{d\vec{y}}{d\tau} = \vec{f}\,(t, \vec{y}, \vec{y}'), \qquad \vec{y}\,(\tau_0) = \vec{y}_0. \tag{17}$$

It is noted that numeric solution of these equations is an initial value problem of nonlinear first-order ordinary differential equations with variable coefficients. These differential equations used to describe the reactor system usually have large stiffness. It is shown that, using the traditional algorithm such as the Runge-Kutta algorithm to solve the stiff differential equations may result in failure in some cases. In the present paper, Gear algorithm (Yuan Zhaoding [33]; Su et al. [34]; Tian et al. [25]; Yun et al. [35]), which is a backward difference implicit algorithm and especially suitable for solving stiff differential equations, is adopted to solve the above equations.

Base on the theoretical model and solution method, a simulation code, SCPRHRS, is developed. The code is in Fortran 90 format and can be maintained in the PC/Windows environment. For convenient maintenance and readability of the code, modular programing techniques are adopted. The main function modules are data input module, initialization module, transient module, derivative module, numerical method module, auxiliary module, thermophysical property module, output module, and so forth. All involved heat transfer and friction coefficient correlations are supplied in the auxiliary module. Derivative module is used to calculate the right-hand side of the differential equations (like (17)). Modification of these modules or addition of new modules can be easily done for different calculation requirements. The calling relationship of these modules and the N-S flowchart of SCPRHRS are shown in Figures 3 and 4, respectively.

5. Initial Conditions

The major structural and initial parameters used for the theoretical analysis are shown in Table 3. There are two sets of PRHRS, each of which has the same characteristics and is connected with four OTSGs, respectively. In the calculation, because of the large heat capacity of the water pool, an assumption, that the inlet temperature of the third loop is constant, is made. Before the PRHRS starts up, the reactor is under a normal operating steady state, and the PRHRS and the third loop do not work.

6. Results and Discussion

6.1. Transient Thermal Hydraulic Characteristics of PRHRS. Figure 5 shows the core power, the heat transferred to secondary side of the steam generator, and the heat transferred to the WP after the reactor is shut down. It can be seen that the core power and the heat transferred to the secondary side of the steam generator decrease rapidly at the initial stage and at about 20 seconds they begin to decrease slowly.

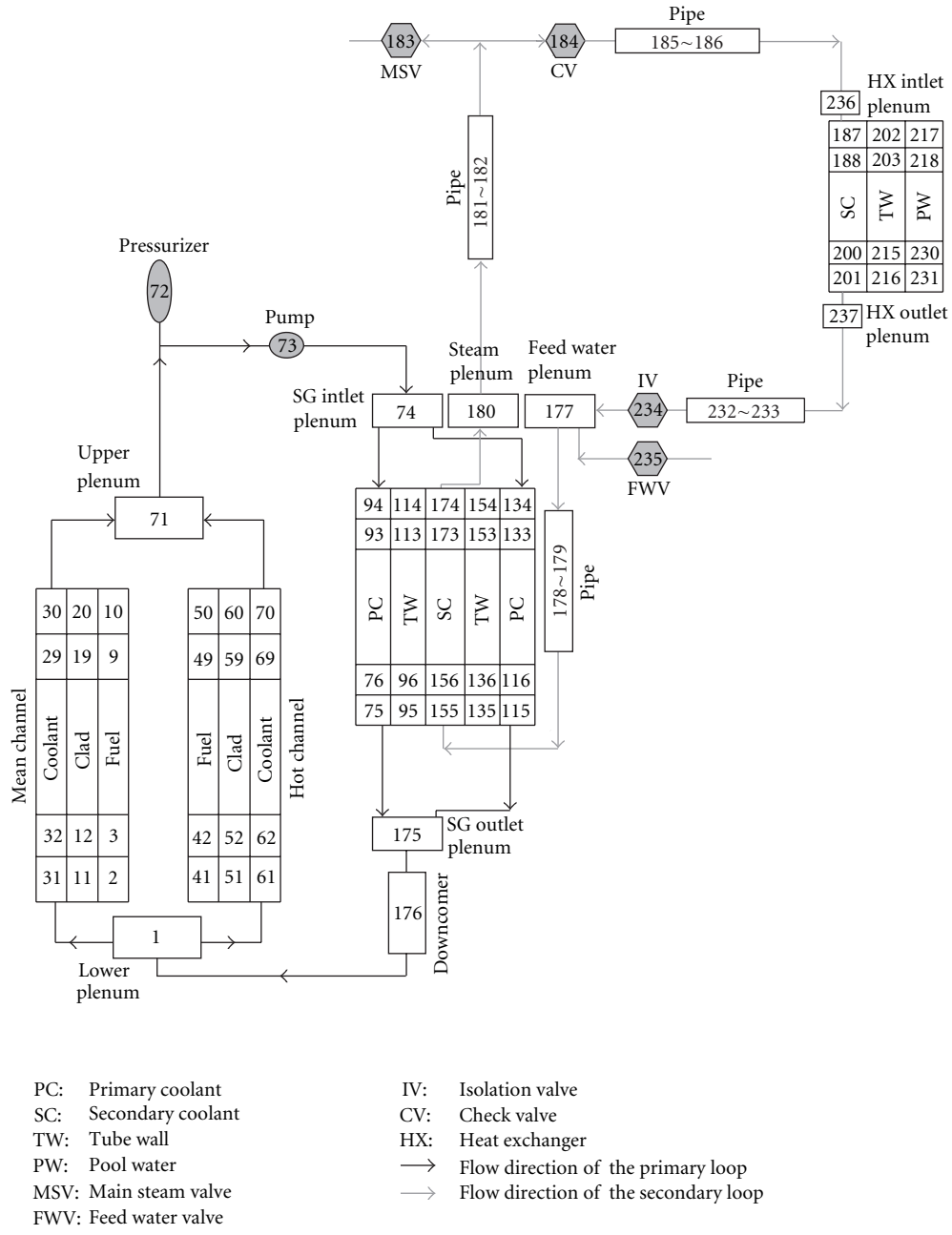

PC: Primary coolant
SC: Secondary coolant
TW: Tube wall
PW: Pool water
MSV: Main steam valve
FWV: Feed water valve
IV: Isolation valve
CV: Check valve
HX: Heat exchanger
⟶ Flow direction of the primary loop
⟶ Flow direction of the secondary loop

Figure 2: SCPRHRS nodalization for the PRHRS.

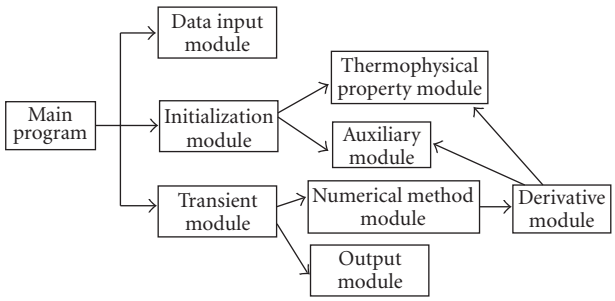

Figure 3: Calling relationships of the modules.

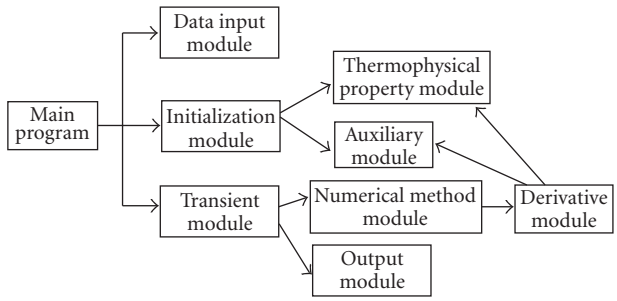

Figure 4: N-S flowchart of the code.

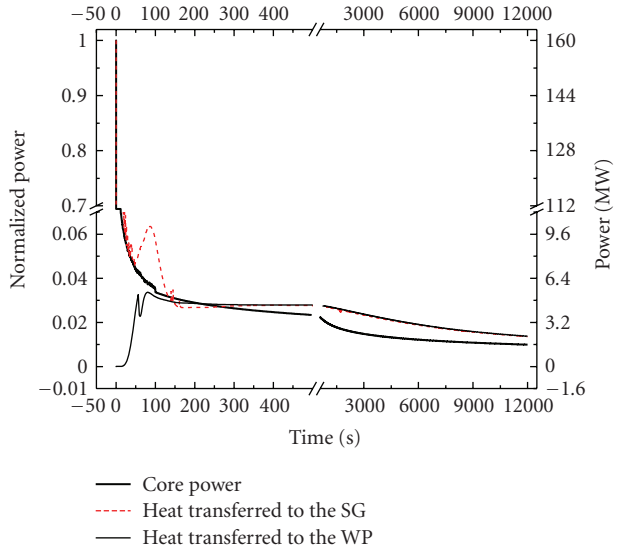

Figure 5: Decay power and heat transferred in the SG and PRHRS.

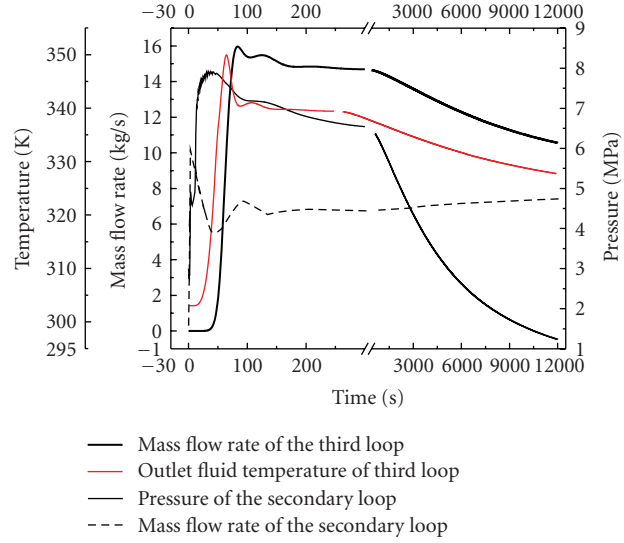

Figure 7: Mass flow rate and pressure of the secondary loop, mass flow rate and outlet temperature of the third loop.

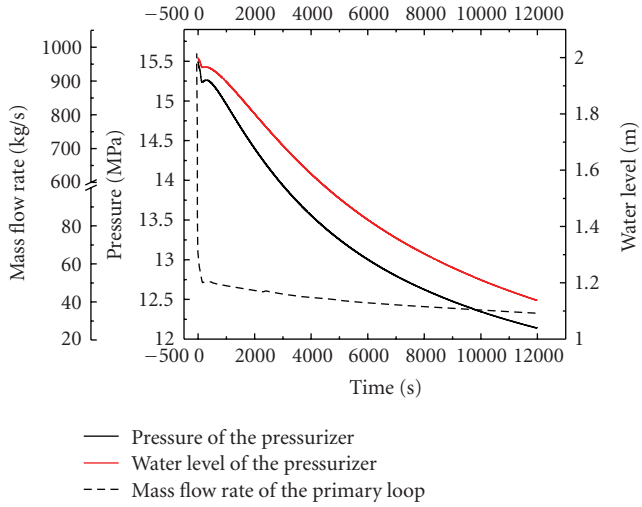

Figure 6: Mass flow rate of the primary loop, pressure, and water level of the pressurizer.

The heat transferred to the WP is under a very low level at the beginning of the transient process. With the establishment of the natural circulation in the PRHRS, the heat transferred to the WP increases gradually, and at about 150 seconds it becomes higher than that transferred to the secondary side of the steam generator. At about 300 seconds, the heat transferred to the secondary side of the steam generator is higher than the core power. It can be assumed that after this point the decay heat can be removed safely.

After the reactor is shut down, the control system makes the MCPs stopped, the forced circulation of the primary loop transits to natural circulation. The mass flow rate of the primary loop is shown in Figure 6. Because of the rapid decrease of the core power, the pressure and the water level of the pressurizer decrease immediately at the initial stage. On the other hand, with the increase of the secondary loop pressure (see Figure 7), the saturated temperature of the secondary loop increases correspondingly. The temperature difference of the two sides of the steam generator becomes smaller, which leads to the degradation of the heat transfer of the steam generator. Consequently, the pressure and the water level of the pressurizer have a slight increase. Subsequently, with the farther decrease of the core power and the establishment of the natural circulation of the three loops, they begin to decrease slowly.

At the initial transient stage, the sudden closure of the main steam valves as well as the higher heat transferred to the secondary side of the steam generator than that removed by the residual heat exchanger (see Figure 5) causes a rapid increase of the secondary loop pressure as shown in Figure 7. With the establishment of the natural circulation of the three loops, it begins to decrease slowly. It is noted that the peak value of the secondary loop pressure is very high without considering the overpressure protection. Thus, a pressure protection measure should be included to prevent the secondary loop pressure exceeding the acceptable value. The mass flow rate of the secondary loop is also shown in Figure 7. After the PRHRS starts up, the water in it immediately enters into the steam generators, which causes a rapid increase of the mass flow rates in the heat exchanger. The cold water in the shell-side of the heat exchanger is heated gradually after the high-temperature fluid from the steam generator enters the tube-inside of the heat exchanger. At about 40 seconds, the outlet fluid temperature of the third loop reaches its maximum value as shown in Figure 7. Correspondingly, the transient behavior of the third loop mass flow rate is similar to the outlet fluid temperature of the third loop (see Figure 7). Figure 7 also shows that the establishment of the natural circulation in the third loop needs a period of time (about 40 seconds). After reaching

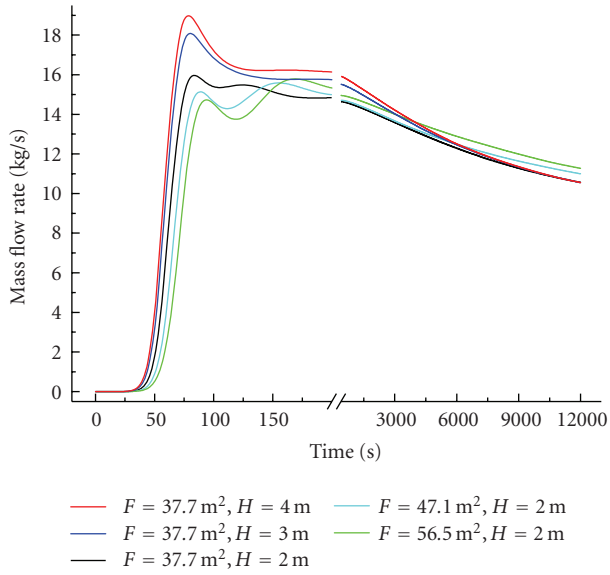

Figure 8: Mass flow rates of the third loop with different height differences and heat transfer areas.

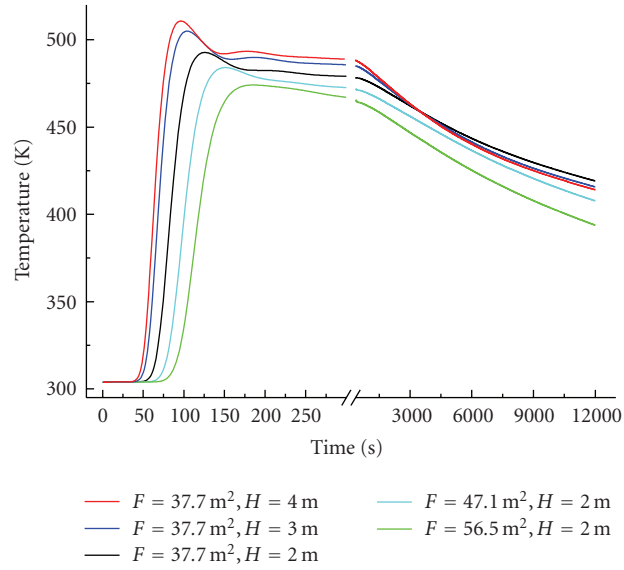

Figure 9: Outlet fluid temperature in the heat exchanger of the secondary loop with different height differences and heat transfer areas.

their peak values, they start to decrease slowly with the decrease of the heat transferred to the third loop.

6.2. Effect of Parameter on the Characteristics of PRHRS. Height difference, between the steam generator and the heat exchanger, and the heat transfer area of the heat exchanger are the two main parameters affecting the thermal hydraulic characteristics of the PRHRS. The effects of these two factors are investigated in this paper. The variation of the heat transfer area of the heat exchanger is carried out through changing the number of the heat transfer tube without changing their length.

The mass flow rates of the third loop with different height difference and heat transfer area are shown in Figure 8. F is the heat transfer area of the heat exchanger, while H is the height difference between the steam generator and the heat exchanger in Figure 8. It shows that the higher the height difference between the steam generator and the heat exchanger, the easier the establishment of the natural circulation in the water pool and the larger the peak value of the mass flow rate. The initial capacity of the cold water in the tube-inside of the heat exchanger increases with the increase of the heat transfer area of the heat exchanger, which leads that the time when the fluid with high temperature from the steam generator replaces the initial cold water is longer with larger heat transfer area (see Figure 9). Correspondingly, the smaller the heat transfer area of the heat exchanger, the earlier the outlet fluid temperature of the third loop reaching its maximum value as shown in Figure 10. Therefore, with the decrease of the heat transfer area, the establishment of the natural circulation in the water pool becomes earlier (see Figure 8).

The pressure of the secondary loop and the pressurizer are shown in Figures 11 and 12, respectively. The peak value

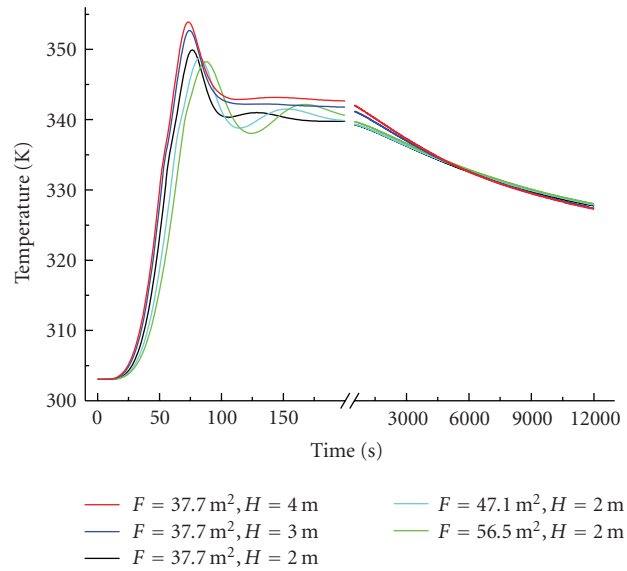

Figure 10: Outlet fluid temperature of the third loop with different height differences and heat transfer areas.

of the secondary loop pressure decreases with the increase of the height difference between the steam generator and the heat exchanger, and increases with the increase of the heat transfer area of the heat exchanger. Figure 11 also indicates that the effects of the height difference between the steam generator and the heat exchanger on the pressure of the secondary loop is larger than that of the heat transfer area of the heat exchanger. For the pressure of the pressurizer, the higher the height difference between the steam generator and the heat exchanger and the larger the transfer area of the

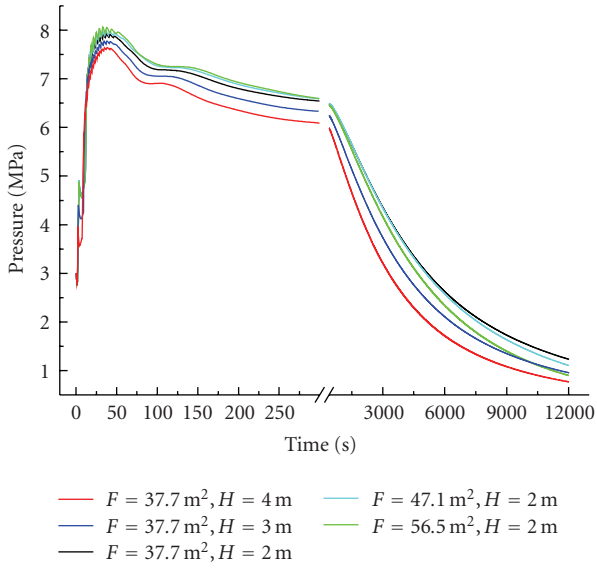

Figure 11: Pressure of the secondary loop with different height differences and heat transfer areas.

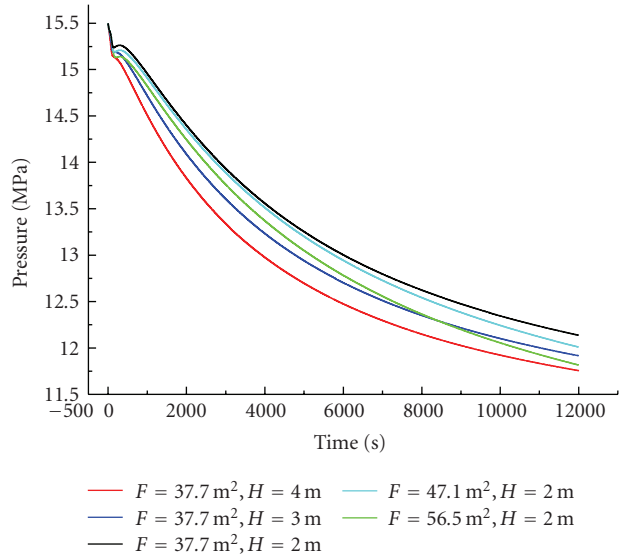

Figure 12: Pressure of pressurizer with different height differences and heat transfer areas.

heat exchanger, the quicker the decrease of it (see Figure 12). Consequently, the higher height difference between the steam generator and the residual heat exchanger and the larger heat transfer area of the residual heat exchanger are favorable to the passive residual heat removal system.

7. Conclusions

A theoretical one-dimensional model and a simulation code (SCPRHRS) are developed to investigate the thermal hydraulic characteristics of a new type of PRHRS, connected to the reactor coolant system via the secondary side of the steam generators, for an integral PWR. The model is based on the fundamental conservation principles: the mass, momentum, and energy conservation equations. System component models are included according to the special design features of it. All possible flow and heat transfer conditions are considered and the corresponding optional models are supplied in the code.

The transient behavior of the PRHRS and the effects of parameters such as the height difference between the steam generator and the heat exchanger and the heat transfer area of the heat exchanger are studied in detail. It is found that the calculated parameter variation trends are reasonable. The decay heat can be safely removed by the PRHRS. The higher height difference between the steam generator and the residual heat exchanger and the larger heat transfer area of the residual heat exchanger are favorable to the passive residual heat removal system. It is noted that the peak value of the secondary loop pressure is very high without considering the overpressure protection. Thus, a pressure protection should be included to prevent the secondary loop pressure exceeding the acceptable value. Also, experimental verification of the code as well as the model improvement is expected to be going on in the future since there is no experimental data can be adopted currently.

Nomenclature

A: Cross-section area of the flow channel, m^2
B: Natural circulation driving head, Pa
c: Local form loss coefficient
C_p: Specific heat, kJ/(kg·K)
D_e: Hydraulic equivalent diameter of the flow channel, m
f: Friction coefficient
g: Gravitational acceleration, m/s^2
h: Specific enthalpy, kJ/kg
H: Heat transfer coefficient, $kW/(m^2 \cdot K)$
L: Height of the residual heat exchanger, m
M: Fluid mass in the control volume, kg;
p: Pressure, Pa
T: Temperature, K
v: Specific volume, m^3/kg
W: Mass flow rate, kg/s
ΔP_f: Friction pressure drop, Pa
ΔP_{loc}: Local pressure drop, Pa.

Greek letters

ρ: Fluid density, kg/m^3
τ: Time, s
ω: Rotational speed, rps
Φ_{tp}^2: Two-phase frictional multiplier.

Subscripts

1: The side of fluid with higher temperature
2: The side of fluid with lower temperature
in: Control volume inlet
lo: Total flow assumed liquid
P: Primary loop
p: Water pool
pump: Main coolant water pump
s: Secondary loop
t: Third loop
tp: Two-phase flow
v: By-pass valve
w: Tube wall

References

[1] D. Adomaitis, G. Saiu, and M. Oyarzabal, "European passive plant program: a design for the 21st century," *Nuclear Engineering and Design*, vol. 179, no. 1, pp. 17–29, 1998.

[2] J. N. Reyes Jr. and L. Hochreiter, "Scaling analysis for the OSU AP600 test facility (APEX)," *Nuclear Engineering and Design*, vol. 186, no. 1-2, pp. 53–109, 1998.

[3] J. Zhang, S. M. Bajorek, R. M. Kemper, M. E. Nissley, N. Petkov, and L. E. Hochreiter, "Application of the WCOBRA/TRAC best-estimate methodology to the AP600 large-break LOCA analysis," *Nuclear Engineering and Design*, vol. 186, no. 1-2, pp. 279–301, 1998.

[4] J. Hyvärinen, "Heat transfer characteristics of horizontal steam generators under natural circulation conditions," *Nuclear Engineering and Design*, vol. 166, no. 2, pp. 191–223, 1996.

[5] International Atomic Energy Agency, *Status of Advanced Light Water Reactor Designs 2004*, IAEA Tecdoc Series no. 1391, IAEA, Vienna, Austria, 2004.

[6] E. Krepper, "Pre- and post-test calculations to natural circulation experiments at the integral test facility ISB-VVER using the thermalhydraulic code ATHLET," *Nuclear Engineering and Design*, vol. 190, no. 3, pp. 341–346, 1999.

[7] S. K. Mousavian, F. D'Auria, and M. A. Salehi, "Analysis of natural circulation phenomena in VVER-1000," *Nuclear Engineering and Design*, vol. 229, no. 1, pp. 25–46, 2004.

[8] G. H. Su, Y. J. Guo, et al., "On natural circulation behaviors of passive decay heat removal," *Journal of Xi'an Jiaotong University*, vol. 29, pp. 38–49, 1995.

[9] G. H. Su, Y. Guo, H. Xie, D. N. Jia, and T. Zhou, "Thermohydraulic characteristics of integrated nuclear power plant," *Journal of Xi'an Jiaotong University*, vol. 34, no. 1, pp. 33–36, 2000.

[10] S. Z. Qiu, T. Zhou, Y. J. Guo, et al., "Modeling and dynamic simulation for emergency residual heat removal system for AC-600," *A Chinese Journal of Nuclear Power Engineering*, vol. 20, pp. 142–147, 1999.

[11] X. Zejun, Z. Wenbin, Z. Hua, C. Bingde, Z. Guifang, and J. Dounan, "Experimental research progress on passive safety systems of Chinese advanced PWR," *Nuclear Engineering and Design*, vol. 225, no. 2-3, pp. 305–313, 2003.

[12] M. H. Chang, S. K. Sim, and D. J. Lee, "SMART behavior under over-pressurizing accident conditions," *Nuclear Engineering and Design*, vol. 199, no. 1-2, pp. 187–196, 2000.

[13] Y.-J. Chung, S. H. Kim, and H.-C. Kim, "Thermal hydraulic analysis of SMART for heat removal transients by a secondary system," *Nuclear Engineering and Design*, vol. 225, no. 2-3, pp. 257–270, 2003.

[14] Y.-J. Chung, S.-H. Yang, H.-C. Kim, and S.-Q. Zee, "Thermal hydraulic calculation in a passive residual heat removal system of the SMART-P plant for forced and natural convection conditions," *Nuclear Engineering and Design*, vol. 232, no. 3, pp. 277–288, 2004.

[15] Y.-J. Chung, H.-C. Kim, B.-D. Chung, M.-K. Chung, and S.-Q. Zee, "Two phase natural circulation and the heat transfer in the passive residual heat removal system of an integral type reactor," *Annals of Nuclear Energy*, vol. 33, no. 3, pp. 262–270, 2006.

[16] T. Iwamura, Y. Murao, F. Araya, and K. Okumura, "A concept and safety characteristics of JAERI passive safety reactor (JPSR)," *Progress in Nuclear Energy*, vol. 29, supplement 1, pp. 397–404, 1995.

[17] O. B. Samoilov, V. S. Kuul, V. A. Malamud, and G. I. Tarasov, "Integral nuclear power reactor with natural coolant circulation. Investigation of passive RHR system," *Nuclear Engineering and Design*, vol. 165, no. 1-2, pp. 259–264, 1996.

[18] M. Peng, C. Ma, S. Bi, et al., "Two passive safety systems in a 200 MW demonstration nuclear heating plant," *Nuclear Engineering and Design*, vol. 160, no. 1-2, pp. 213–220, 1996.

[19] Z. Jinling, G. Yujun, et al., "Influences of the passive emergence residual heat removed system upou the accident of loss of off-site power in nuclear power plant," *Atomic Energy Science and Technology*, vol. 31, no. 2, pp. 36–40, 1997.

[20] T. Kusunoki, N. Odano, T. Yoritsune, T. Ishida, T. Hoshi, and K. Sako, "Design of advanced integral-type marine reactor, MRX," *Nuclear Engineering and Design*, vol. 201, no. 2-3, pp. 155–175, 2000.

[21] Z. Xinian, G. Weijun, H. Bing, and S. Shifei, "Transient analyses of the passive residual heat removal system," *Nuclear Engineering and Design*, vol. 206, no. 1, pp. 105–111, 2001.

[22] M. D. Carelli, L. E. Conway, L. Oriani, et al., "The design and safety features of the IRIS reactor," *Nuclear Engineering and Design*, vol. 230, no. 1–3, pp. 151–167, 2004.

[23] J. G. Collier and J. R. Thome, *Convective Boiling and Condensation*, Oxford University Press, Oxford, UK, 3rd edition, 1994.

[24] Y. Pingan, Z. Ruian, Y. Zhenwan, and S. Xiuzhong, *Nuclear Reactor Thermal Hydraulics*, Shanghai Jiao Tong University Press, Shanghai, China, 2001.

[25] W. X. Tian, S. Z. Qiu, Y. Guo, G. H. Su, and D. N. Jia, "Development of a thermal-hydraulic analysis code for CARR," *Annals of Nuclear Energy*, vol. 32, no. 3, pp. 261–279, 2005.

[26] W. Tian, S. Qiu, G. H. Su, D. N. Jia, X. Liu, and J. Zhang, "Thermohydraulic and safety analysis on China advanced research reactor under station blackout accident," *Annals of Nuclear Energy*, vol. 34, no. 4, pp. 288–296, 2007.

[27] J. G. Collier, *Convective Boiling and Condensation*, Mcgraw-Hill, New York, NY, USA, 2nd edition, 1981.

[28] F. P. Incropera and D. P. DeWitt, *Introduction to Heat Transfer*, John Wiley & Sons, New York, NY, USA, 1985.

[29] D. C. Groeneveld, L. K. H. Leung, A. Z. Vasic, Y. J. Guo, and S. C. Cheng, "A look-up table for fully developed film-boiling heat transfer," *Nuclear Engineering and Design*, vol. 225, no. 1, pp. 83–97, 2003.

[30] M. M. Shah, "A general correlation for heat transfer during film condensation inside pipes," *International Journal of Heat and Mass Transfer*, vol. 22, no. 4, pp. 547–556, 1979.

[31] J. J. Xu and D. N. Jia, *Boiling Heat Transfer and Two-Phase Flow*, Atomic Energy Press, Beijing, China, 2001.

[32] D. Chisholm, "Pressure gradients due to friction during the flow of evaporating two-phase mixtures in smooth tubes and channels," *International Journal of Heat and Mass Transfer*, vol. 16, no. 2, pp. 347–358, 1973.

[33] Y. Zhaoding, *Algorithm for Initial Value Problem of Rigid Ordinary Differential Equations*, Science Press, Beijing, China, 1987.

[34] G. H. Su, D. N. Jia, K. Fukuda, and Y. Guo, "Theoretical study on density wave oscillation of two-phase natural circulation under low quality conditions," *Journal of Nuclear Science and Technology*, vol. 38, no. 8, pp. 607–613, 2001.

[35] G. Yun, G. H. Su, J. Q. Wang, et al., "Two-phase instability analysis in natural circulation loops of China advanced research reactor," *Annals of Nuclear Energy*, vol. 32, no. 4, pp. 379–397, 2005.

Hindawi Publishing Corporation
Science and Technology of Nuclear Installations
Volume 2009, Article ID 768947, 18 pages
doi:10.1155/2009/768947

Research Article

Application of REPAS Methodology to Assess the Reliability of Passive Safety Systems

Franco Pierro, Dino Araneo, Giorgio Galassi, and Francesco D'Auria

Nuclear Research Group San Piero a Grado (GRNSPG), Department of Mechanics, Nuclear and Production Engineering, University of Pisa, via Diotisalvi, 2 56100 Pisa, Italy

Correspondence should be addressed to Franco Pierro, franco.pierro@ing.unipi.it and Dino Araneo, d.araneo@ing.unipi.it

Received 9 December 2008; Accepted 3 August 2009

Recommended by Xu Cheng

The paper deals with the presentation of the Reliability Evaluation of Passive Safety System (REPAS) methodology developed by University of Pisa. The general objective of the REPAS is to characterize in an analytical way the performance of a passive system in order to increase the confidence toward its operation and to compare the performances of active and passive systems and the performances of different passive systems. The REPAS can be used in the design of the passive safety systems to assess their goodness and to optimize their costs. It may also provide numerical values that can be used in more complex safety assessment studies and it can be seen as a support to Probabilistic Safety Analysis studies. With regard to this, some examples in the application of the methodology are reported in the paper. A best-estimate thermal-hydraulic code, RELAP5, has been used to support the analyses and to model the selected systems. Probability distributions have been assigned to the uncertain input parameters through engineering judgment. Monte Carlo method has been used to propagate uncertainties and Wilks' formula has been taken into account to select sample size. Failure criterions are defined in terms of nonfulfillment of the defined design targets.

1. Introduction

Passive systems deserve a special attention within the nuclear technology owing to their potential to increase the safety level of the power plants and to reduce the cost for the energy production. The intensive use of passive systems in the new nuclear technology needs a robust assessment of their reliability. The passive safety systems for their nature, because their functioning depends only on natural physical laws and not on an external source of supplied energy, are more reliable than the active ones. Nevertheless the passive systems may fail their mission as consequence of components failure, deviation of physical phenomena, boundary and initial conditions.

The extensive use of passive safety systems, mainly in advanced reactors design, makes necessary to deeply study the approach to their reliability assessment. This implies not only the consideration of mechanical components, evaluated through classical risk assessment tools (e.g., Failure Mode and Effects Analysis (FMEA), FTA, Hazard Operational Analysis (HAZOP), etc.), but also the consideration of the associated TH phenomena in terms of the deviation from expected system behavior due to "alterations" in the environmental conditions.

In the present paper an overview of the REPAS methodology is reported with its application and its effectiveness is briefly shown. It is also shown how it can be used to support the design of the passive systems.

The reliability evaluation of passive system needs a suitable methodology aiming to determine the passive system reliability function, which is the failure probability of the physical principle upon which the system operation is relying [1].

A pioneering activity aimed to evaluate the reliability of passive systems was proposed in mid-1990s within the framework of bilateral contacts between CEA and ENEA. In 2000 this issue was studied by the University of Pisa (UNIPI) [2]. Later on, cooperation between ENEA, UNIPI, Polytechnic of Milan, and University of Rome leads to the proposal of a methodology called REPAS. The methodology

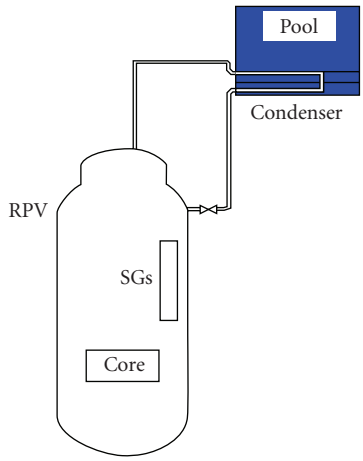

Figure 1: Passive pool heat removal system for a prototypical integrated system.

was applied to evaluate the reliability of an existing passive system design where two-phase Natural Circulation (NC) takes place.

The methodology was embedded in the Reliability Methods for Passive Safety (RMPS) methodology, developed within the framework of a project called RMPS functions, under the European 5th Framework program [3, 4].

Actually the methodology is in the setting up phase for an absolute evaluation of the reliability of passive safety system function.

It is important to give the following definition to understand the proposed issue

The Accuracy. Is the known bias (or difference) between a code prediction and the actual (measured) transient performance of a real facility.

The Uncertainty. Analysis *(of a code prediction)* implies a procedure to evaluate the precision (or the error) that characterizes the application of a best-estimate code.

The Reliability. Analysis *(of a system)* aims at characterizing the ability of a system "*to operate satisfactorily,*" following assigned specifications, over a period of time.

2. REPAS Methodology Overview

The REPAS methodology can be subdivided in the following main steps ([1, 5–9]):

(a) characterization of design/operational status of the system (identification of relevant parameters connected with the TH phenomenon: design and critical parameters),

(b) definition of nominal values, range of variation and assigned probability distributions to design and critical parameters,

(c) deterministic (based on engineering judgment) and statistic (e.g., through Monte Carlo procedure) selection of system status,

(d) definition of failure criteria for the system performance (starting from the knowledge of the system mission and the identification of the accident scenario and allowing the definition of design targets for passive system); the failure criteria are established as single targets (e.g., the system shall deliver a specific quantity of liquid within a fixed time) or as a function of time targets or integral values over a mission time (e.g., the system shall reject at least a mean value of thermal power all along the system actuation); in some cases, it can be better to define a global Failure Criterion (FC) of the complete system instead of a specific criterion concerning the passive system; for instance, the FC can be based on the maximal clad temperature during a specified period; in this case, it is necessary to model the complete system and not only the passive system,

(e) detailed code modeling; once the system mission, accident scenario, and FC are established, a system model has to be developed by means of a best-estimate TH code (e.g., RELAP5),

(f) direct Monte Carlo simulation applied to TH code; it involves the propagation of the uncertain selected parameters through the considered TH code obtaining a model response (i.e., output variable) which allows, by means of statistic methods, to estimate the probability of failure of the passive function,

(g) sensitivity analysis,

(h) quantitative reliability evaluation.

3. Description of Analyzed Systems

The REPAS methodology has been applied to three NC systems. The three systems are

(i) a prototypical integrated system: the related analysis can be considered as an exercise scope calculation;

(ii) the scaled Isolation Condenser (IC) of a Simplified Boiling Water Reactor (SBWR) [2];

(iii) the TTL-1 experimental apparatus [6].

In the first case the analyzed system is a typical "pool heat removal system." The heat source, the steam generator and the primary recirculation loop, are contained inside the Reactor Pressure Vessel [10].

The simplified layout of this prototypical reactor is shown in Figure 1, where there is also evidenced the external passive safety system. The performance of that system is the main objective of the analysis.

The second analyzed system is the IC, which is part of the SBWR design. A sketch of the system is given in Figure 2.

The third analyzed system, the TTL-1 experimental apparatus [6, 11], is a separate effect test facility that has been designed at the Atomic Energy Organization of Iran

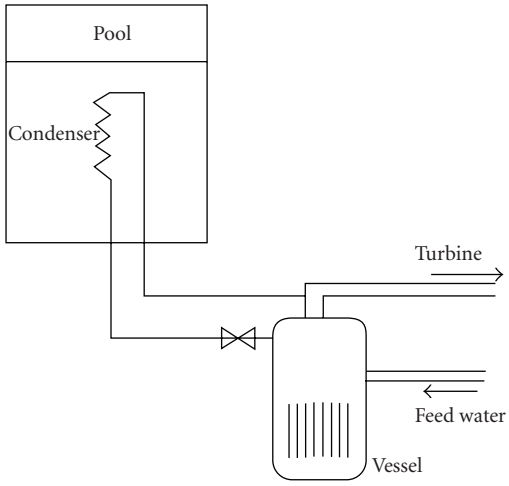

Figure 2: Standard IC of an SBWR.

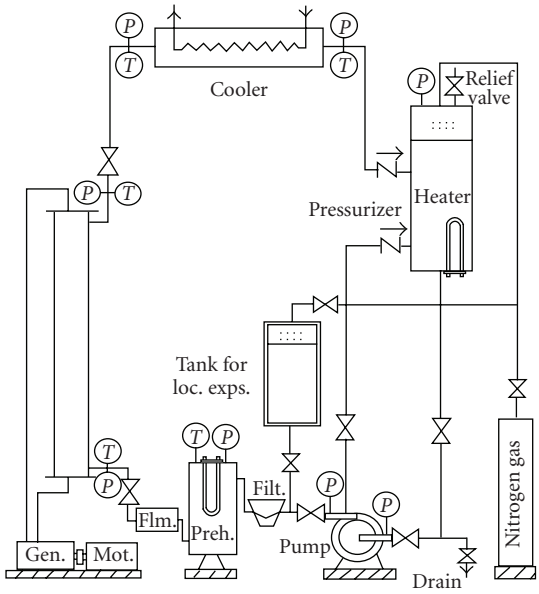

Figure 3: Sketch of TTL-1 loop.

Table 1: Design parameters case a.

Design parameter ID	Description
OP	Nominal Power
SD	SRAM delay
DF	Decay power factor
P1	Reactor nominal pressure
SP	SCRAM: pressure set point
P2	PHRS: pressure set point
L1	RPV: dome water level
M	PCS: mass flow rate
T1	PHRS: valves opening time
PT	PHRS: pool temperature
TT	PHRS: tube thickness

Table 2: Critical parameters case a.

Critical parameter ID	Description
C2	Heat Losses piping
W1	PHRS tube thickness
HL	RPV dome heat losses
F	PHRS friction
Psp	Safety valves: pressure set point

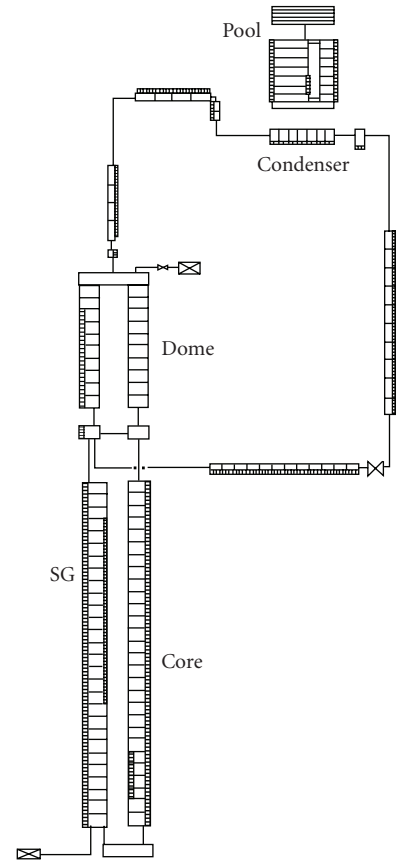

Figure 4: Simplified RELAP 5 nodalization for case a.

(AEOI), in the context of research programs in the NC field. The sketch of the loop is given in Figure 3. The maximum pressure and power at which the loop can operate are 1 MPa and 50 kW, respectively. More details about the system configuration are given in [6].

4. REPAS Application

In the following subsections are reported the application steps of the methodology above briefly described. In particular is deeply described the application and the results obtained of the REPAS methodology to a pool heat removal system of a prototypical integrated system (case a) while for the other two systems (cases b and c) are outlined only the main outcomes of the application (see Section 5).

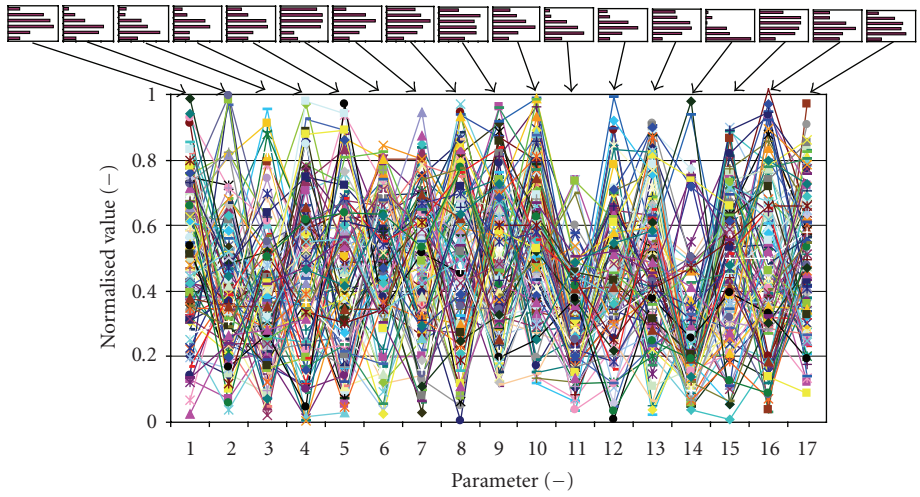

Figure 5: Cobweb plots of normalized parameters range.

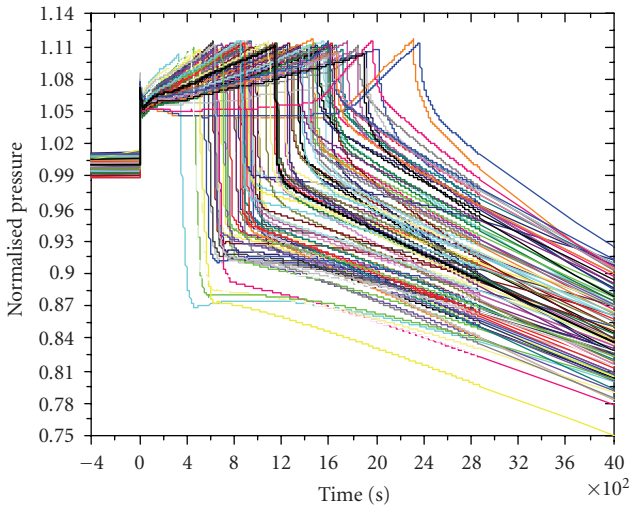

Figure 6: Pressure behavior—normalized scale—Short-term (stochastic selected and nominal case).

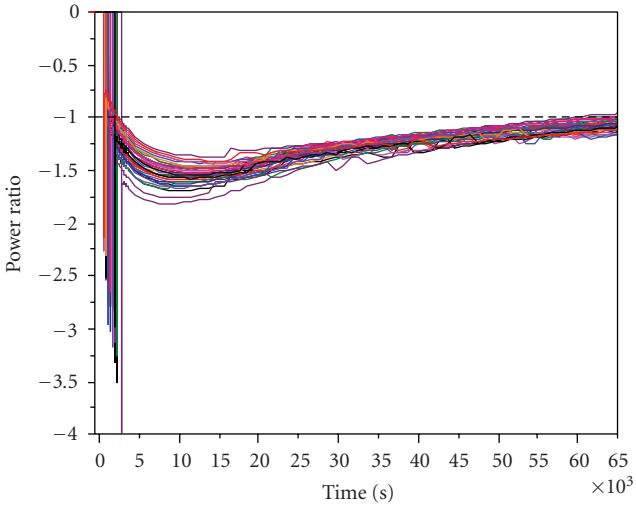

Figure 7: Power ratio evolution—long-term behavior (stochastic selected and nominal case).

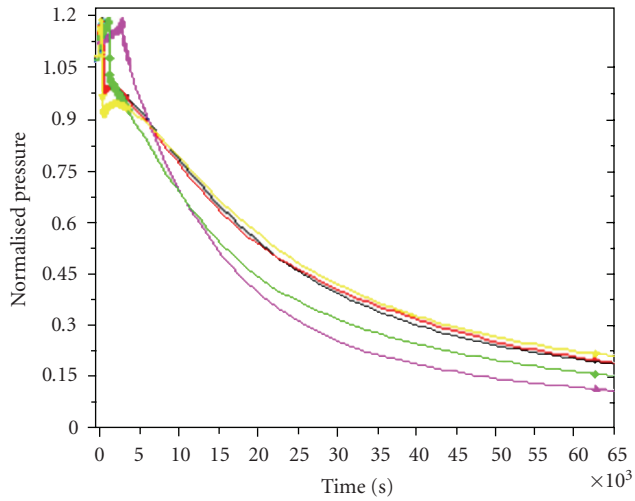

Figure 8: Pressure evolution—normalized scale—Long-term (a priori deterministic selected cases).

4.1. Characterization of Design/Operational Status for the System. The first step is the characterization of the system, in particular the identification of relevant parameters connected with the TH phenomenon. The relevant parameters are defined design and critical parameters.

Design Parameters. are mainly related to the nominal system configuration, for example, nominal power, pressure, level, and may include also geometrical parameters.

Critical Parameters. are physical quantities that may affect the mission of the passive system like presence of noncondensable gas in an NC system.

In Tables 1 and 2 are reported the design and critical parameters; for each of them are defined nominal values, range of variation, and an assigned probability distributions. The full characterization of a thermal-hydraulic system may need a very large number of such parameters.

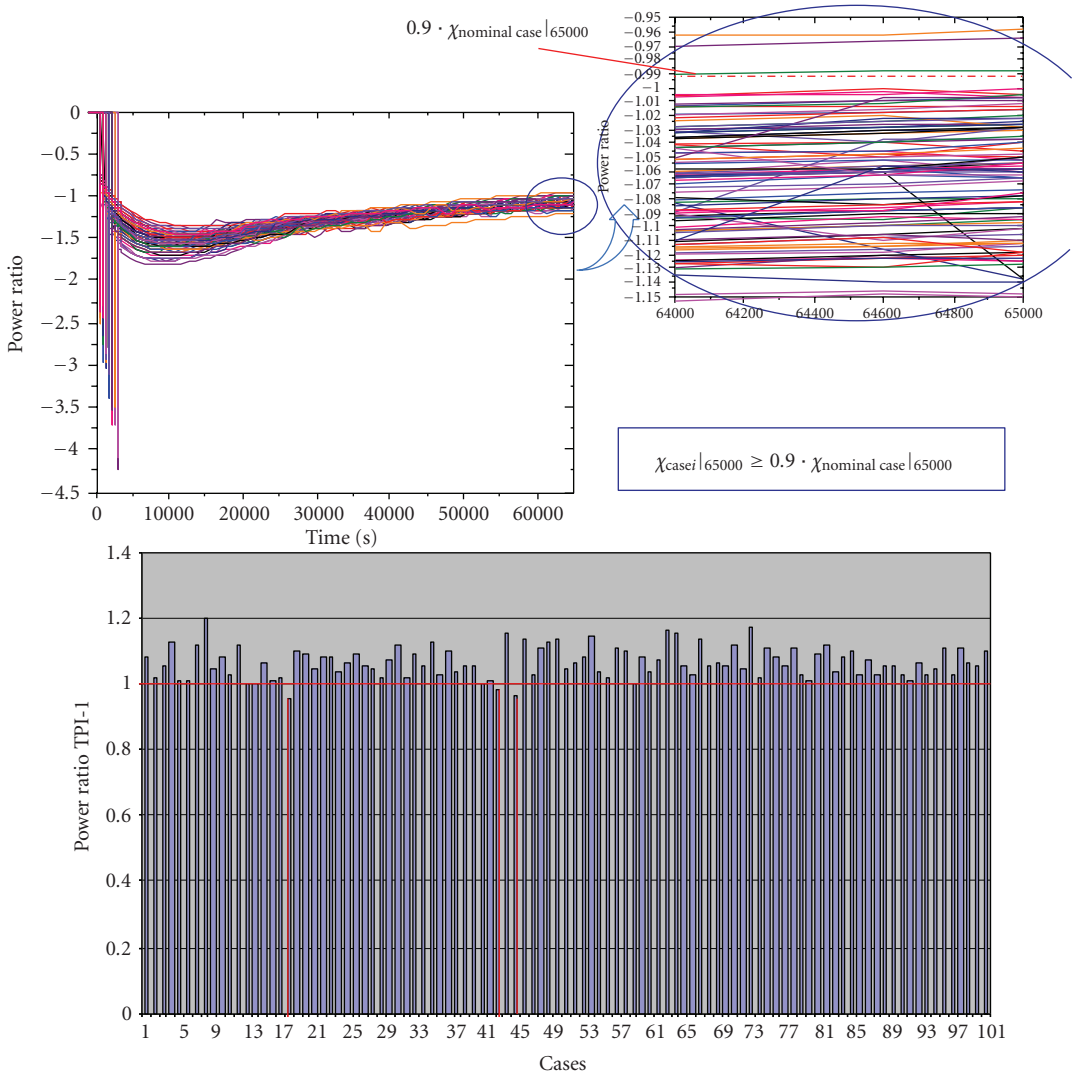

Figure 9: Transient performance indicator—1 result (long term).

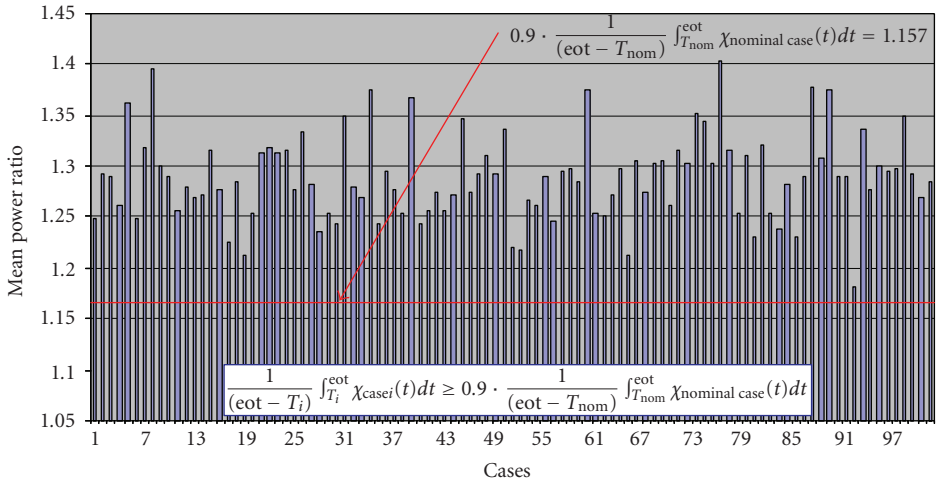

Figure 10: Transient performance indicator—2 results (long term).

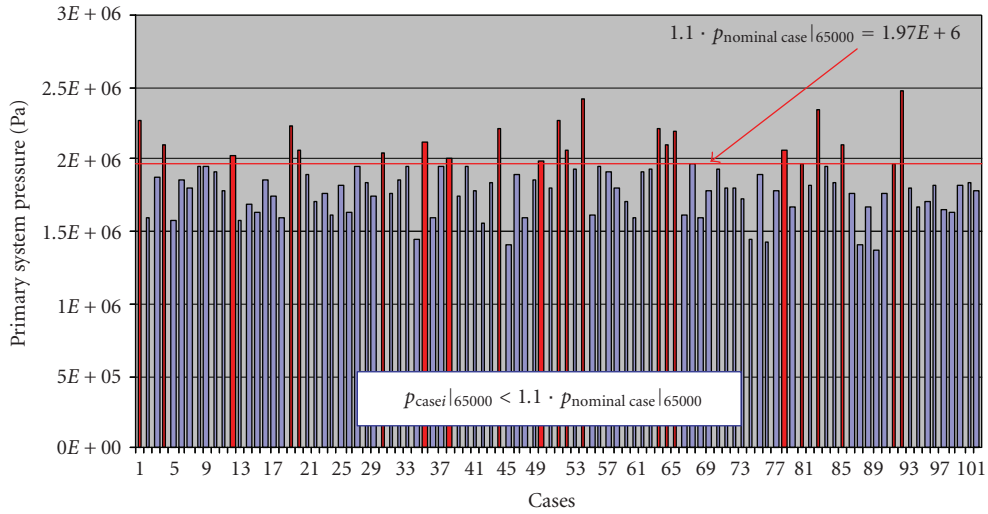

Figure 11: Transient performance indicator—3 results (long term).

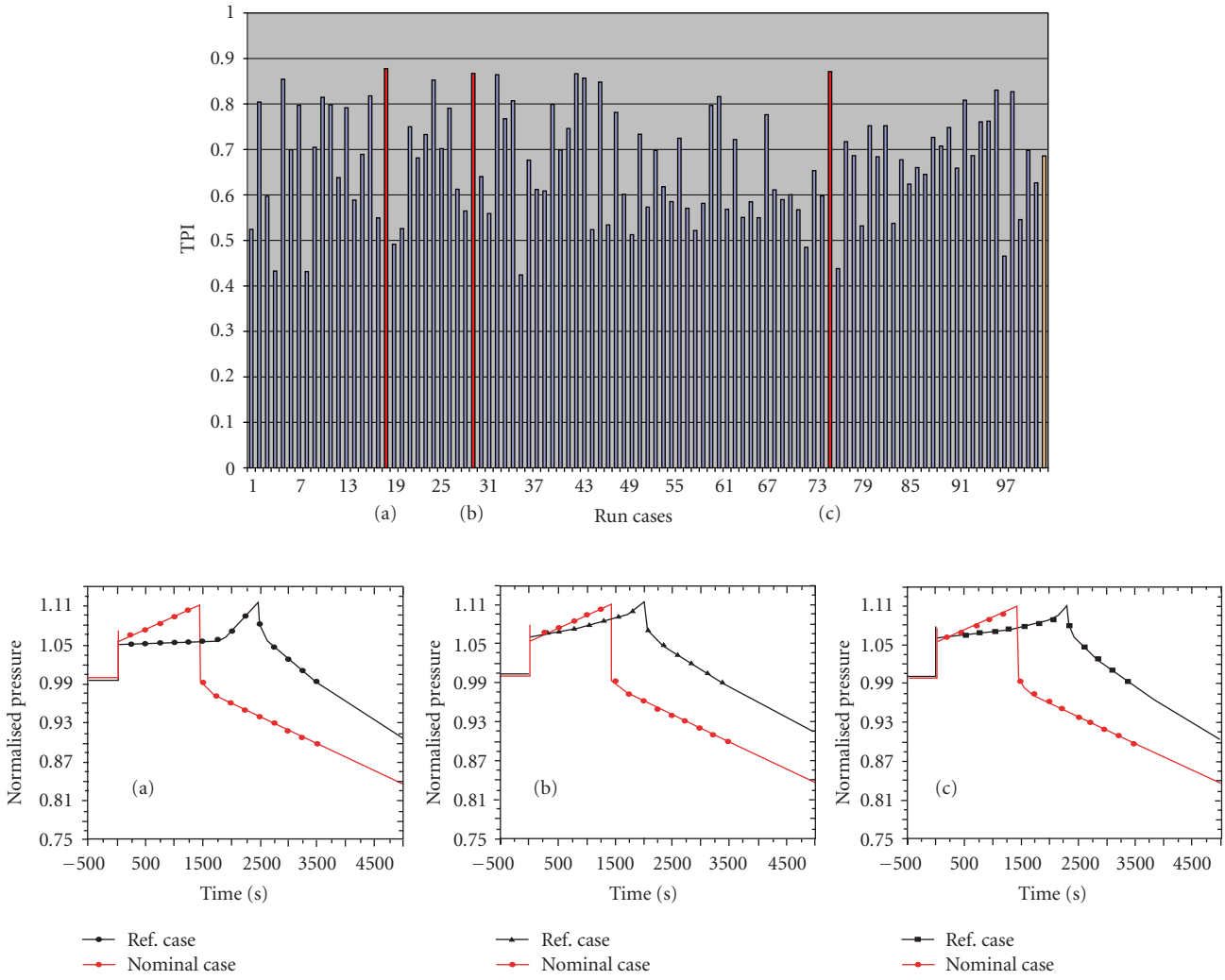

Figure 12: Sensitivity analysis to identify the worst system condition.

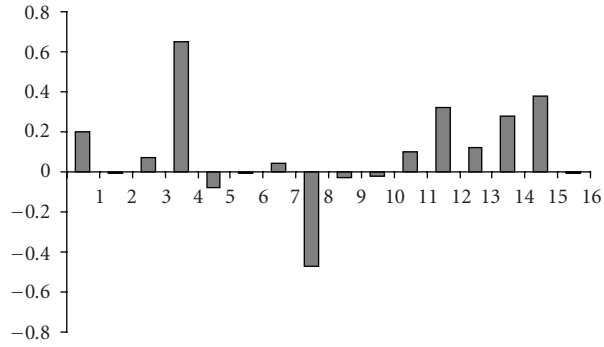

Figure 13: Standardized regression coefficients for the defined performance indicator.

Therefore, a bounded number of parameters should be selected deterministically (based on engineering judgment) and statistically (e.g., through a Monte Carlo procedure).

4.2. Definition of Failure Criteria. The knowledge of the system missions and failure modes allows evaluating the failure criteria. The accident scenario considered is a loss of the ultimate heat sink with the hypothesis of loss of all safety systems involved, no feed and bleed strategy is taken into account, and so forth Considering that transient, the system mission is to remove the decay heat reducing the pressure in the primary system.

The design FC defined for the transient sequence is the opening of the safety valves during any stage of the transient. To characterize the passive system behavior (or passive system performance) three Transient Performance Indicators (TPI) are defined. In particular they have to indicate how far the system is from the opening condition of the passive safety valve of the condenser system.

In terms of the system mission two design targets can be defined: long-term (e.g., hot shutdown condition) and short-term (e.g., primary overpressure) design target. The failure of the system is reached when passive safety valves are open.

The TPIs defined are

(i)

$$\chi_{(\mathrm{CASE}i)}\big|_{65000} \geq 0.9 \cdot \chi_{\mathrm{NOMINAL\ CASE}}\big|_{65000}, \tag{1}$$

(ii)

$$\frac{1}{(\mathrm{eot} - Ti)} \int_{Ti}^{\mathrm{eot}} \chi_{\mathrm{CASE}i}(t)dt \geq 0.9 \cdot \frac{1}{(\mathrm{eot} - T_{\mathrm{NOM}})} \int_{T_{\mathrm{NOM}}}^{\mathrm{eot}} \chi_{\mathrm{NOMINAL\ CASE}}(t)dt, \tag{2}$$

(iii)

$$p_{\mathrm{CASE}i}\big|_{65000} < 1.1 \cdot p_{\mathrm{NOMINAL\ CASE}}\big|_{65000}, \tag{3}$$

$$\chi(t) = \frac{P_{\mathrm{HX}}(t)}{P_{\mathrm{CORE}}(t)}. \tag{4}$$

where P_{HX} is the Power exchanged across the condensers tubes, P_{CORE} is the Core power, T_{PRHRS} is the activation time, p is the primary circuit pressure, eot is the end of transient (65000 seconds).

4.3. Detailed Code Modeling. RELAP5 mod 3.3 input deck has been developed to perform the TH analyses. The model involves the Primary System and the pool for the removal of decay heat (see Figure 4).

The primary circuit has been set up by modeling the most relevant components: Reactor Pressure Vessel (RPV), Steam Generator (SG), Down-Comer (DC), Core, Lower Plenum (LP) and Upper Plenum (UP).

The passive heat removal nodalization includes steam line and return line, condensers, and the pool.

In order to simulate properly the natural circulation inside the pool, a detailed model has been adopted with specific feature coming from engineering judgments and user experience (e.g., by pass line, slice nodalization).

4.4. Direct Monte Carlo Simulation Applied to TH Code. The purpose of direct Monte Carlo simulation is to assess the propagation of the uncertain parameters through the TH code in order to obtain a model response (set of code run). In particular it consists in sampling the identified parameters, running, for each obtained sample, the system model computer code and estimating the characteristics of the output variables. This method was used to evaluate the failure probability p_f (an estimation can be obtained dividing the number of simulation cycles in which the failure criteria take places by the total number of simulation cycles) associated with the failure criteria of the system defined above ([1, 3]).

In the following subsections the main steps of direct Monte Carlo simulation (i.e., sampling and best—estimate code run) are outlined, describing the used procedures and the results obtained. Also best estimate code run results are reported based on deterministic selection of input cases coming from engineering judgment and sensitivity analysis outcomes.

4.4.1. Sampling. Simple Random Sampling (SRS) method was adopted to obtain the parameters samples. The method generates randomly all values of parameter sample from their defined distribution.

Simple Random Sampling Procedure. The parameter samples, through SRS, are obtained considering the following three main steps.

(1) to draw the value of the truncated cumulative distribution function by sampling a uniform distribution $u = U(0, 1)$,

(2) to obtain the correspondent value ($y = F(x)$) of the non truncated cumulative distribution by means of the following correction:

$$y = F(x_{\min}) + u \cdot [F(x_{\max}) - F(x_{\min})], \tag{5}$$

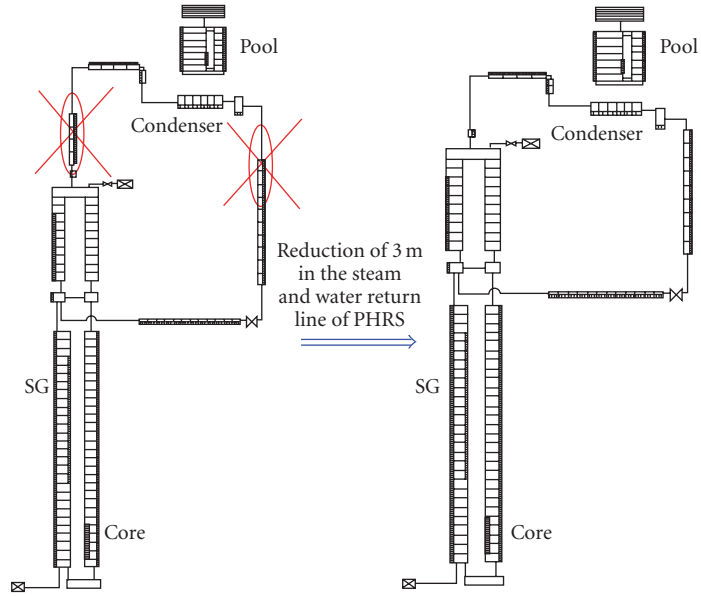

Figure 14: Lay-out modification: scope calculation.

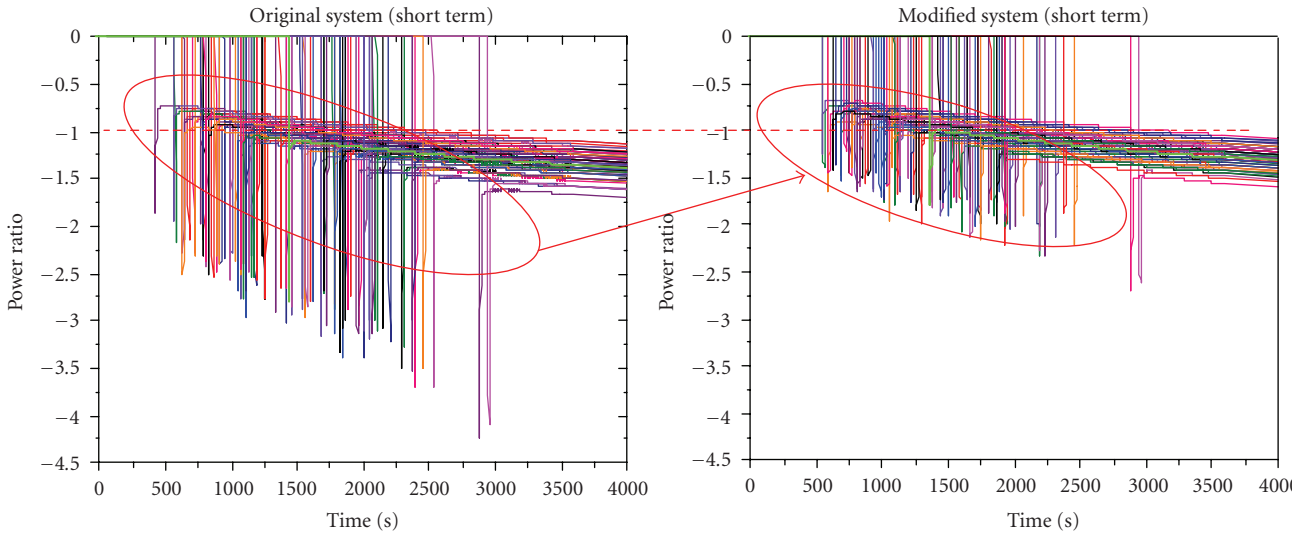

Figure 15: Power ratio comparison between the original and the modified system.

(3) to feed this probability into the inverse of the cumulative distribution function in order to obtain the parameter sample (x):

$$x = F^{-1}(y). \tag{6}$$

Consider the following definitions.

For normal distribution, we have the following.

(i) Cumulative function is

$$F(x) = \frac{1}{2}\left[\operatorname{erf}\left(\frac{(x-\mu)}{\sqrt{2}\sigma}\right)\right]. \tag{7}$$

(ii) Inverse of F is

$$F^{-1}(y) = \mu + \sqrt{2}\cdot\sigma\cdot\operatorname{erf}^{-1}(2y). \tag{8}$$

For lognormal distribution, we have the following.

(i) Cumulative function is

$$F(x) = \frac{1}{2}\left[\operatorname{erf}\left(\frac{\ln(x/e^{\mu})}{\sqrt{2}\sigma}\right)\right] \tag{9}$$

(ii) Inverse of F is

$$F^{-1}(y) = e^{\mu} + \exp\left(\sqrt{2}\cdot\sigma\cdot\operatorname{erf}^{-1}(2y-1)\right). \tag{10}$$

Parameters Sampling Results. The tool used to analyze the sampling results is the cobweb plot. The parameter samples are represented as points in vertical lines. Each set of inputs can be seen as a vector where its elements represent one

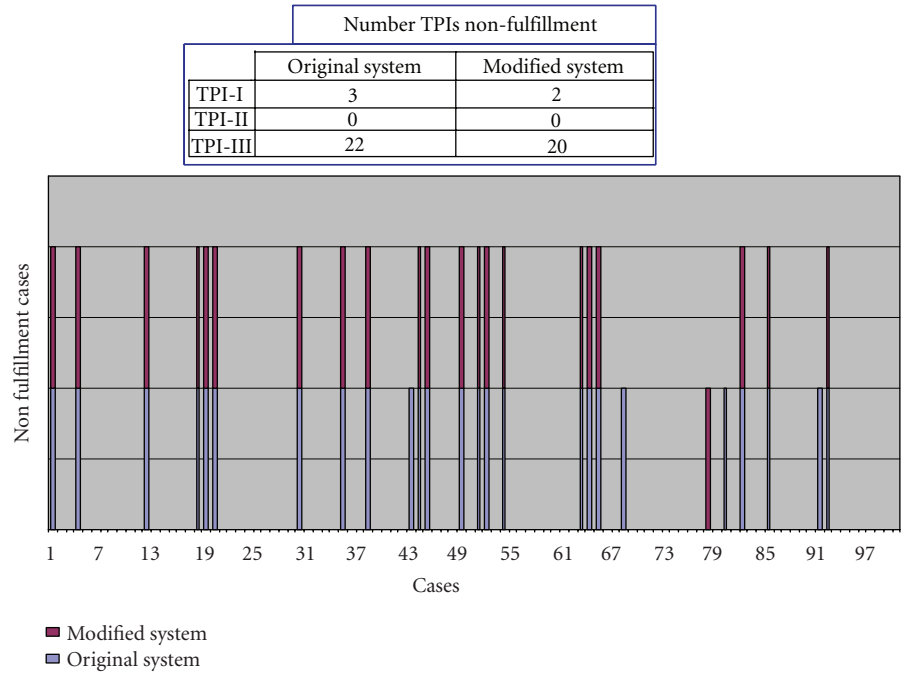

Figure 16: Transient performance indicators results comparison between original and modified system.

sample value for each parameter. In the plot shown in Figure 5 the overall input vectors are reported.

From the plot it can be seen that some parameters were not sampled in their full range (blank regions); this outcome led to the necessity of generating additional deterministic cases in order to add completeness to the study.

Stochastic and Deterministic Selection of Input Cases. The stochastic selection has been made sampling the defined design and critical parameters (Tables 1 and 2).

A hundred samples were obtained for each parameter implying the same number of code runs. The input set was built as follows

$$S_j = \left(P_{i-j} \right), \tag{11}$$

where S_j is the set of parameters used to perform the jth code run (with: $j = 1, 2, \ldots, 100$), and P_{i-j} is the jth sample value of parameter i.

The number of code runs (and then the number of samples for each parameter) was calculated by means of Wilks' formula [12].

Wilks' formula gives the proper number of independent observations of the random output (Y) (minimizing the number of calculations that characterize the system performance) in order to fulfill the following relationship:

$$P[P(U \le Y \le L) > \alpha] \ge \beta. \tag{12}$$

Based on the hypothesis that nothing is known about the output distribution function-$fY(y)$-except that it is continuous, we have the following.

(i) *α is the probability content limit*. It gives a lower limit to the proportion of the distribution included in the tolerance interval $[L, U]$. This proportion is called *probability content* (pc) and is given by the following expression:

$$\text{pc} = \int_L^U f_Y(y)\, dy. \tag{13}$$

(ii) *β is the confidence level*. It gives the probability that the tolerance interval $[L, U]$ has a *probability content* major than α.

The number of independent observations of the output variable (i.e., number of code runs) for the two-sided tolerance interval is calculated by the following equation:

$$1 - \alpha^N - N(1-\alpha)\alpha^{N-1} \ge \beta. \tag{14}$$

The tolerance interval $[L, U]$ is given by $L = y_1$, $U = y_N$; where $y_1 = \min[y_k]$ and $y_N = \max[y_k]$, with $1 \le k \le N$.

According to this, the number of codes runs obtained (N) results independent by the number of inputs parameters, their assigned distributions, and sampling method adopted.

The selected sample size, 100 samples, satisfies, the 95%/99% criteria (probability content = 95%, confidence level = 99%) for one-sided tolerance interval.

The deterministic selected cases have been made in order to add completeness to the analysis, additionally ten cases where added, based on engineering judgment, five "a priori"

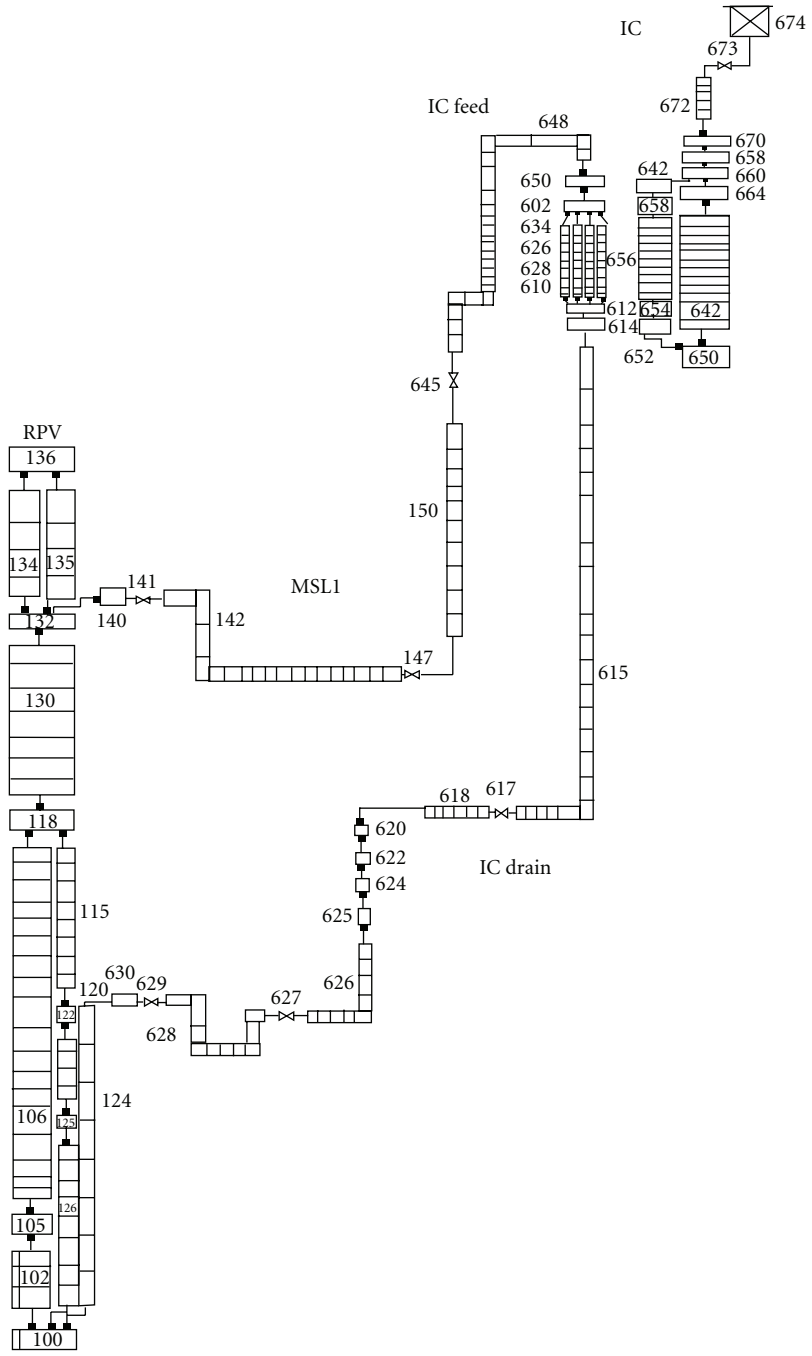

Figure 17: RELAP5 nodalization of IC of an SBWR case b.

to evaluate parameters combinations not achieved by the stochastic selection (blank region of cobweb plot) and five "a posteriori" considering as feedback the results obtained from sensitivity analysis.

Direct Monte Carlo Simulation: RELAP5 Calculations Results. The main outcomes, obtained by Direct Monte Carlo simulation, are linked to the design FC selected for the passive system. B-E code runs of the associated input vector are shown; in particular are reported the follows.

(i) the pressure trend:

  (a) short term (Figures 6 and 12);
  (b) a long term (Figure 9);

(ii) the power exchange ratio (power exchanged across the condensers tubes and core power) long term (Figure 7).

Below are reported the main outcomes of the three TPIs defined above (Figures 9, 10, and 11), in particular, the following.

Table 3: Design parameters case b.

Design parameter ID	Description	UNIT	Nominal value	Range	Discrete initial value
P1	RPV Pressure	MPa	7	0.2–9	0.2 1 3 7 10 ***0.05 0.1 0.15 0.5 0.2***
L1	RPV collapse level	M	8.7	5–12	5 7 8.7 10 12 ***0.05 0.1 0.5 0.2 0.15***
L3	POOL level	M	4.3	2–5	2 4.3 5 ***0.1 0.8 0.1***
Tp (0)	POOL initial temperature	K	303	280–368	280 303 368 ***0.1 0.8 0.1***
—	System geometry layout	—	—	Not assigned	— ***1.0***

Table 4: Critical parameters case b.

Critical parameter ID	Description	Unit	Nominal value	Range	Discrete initial value
X1	RPV Non-condensable fraction	—	0	0-1	0 0.01 0.1 0.2 0.5 0.8 1 ***0.719 0.12 0.07 0.05 0.03 0.01 0.001***
X2	Non-condensable fraction at the inlet of IC piping	—	0	0-1	0 0.01 0.1 0.2 0.5 0.8 1 ***0.71 0.12 0.07 0.05 0.03 0.01 0.01***
Θ	Inclination of the IC piping on the suction side	deg	0	0–10	0 1 5 10 ***0.5 0.4 0.08 0.02***
C2	Heat Losses piping –IC suction	kW	5	0–100	0 5 20 100 ***0.10 0.7999 0.10 0.0001***
L2 (0)	Initial condition liquid level –IC tubes, inner side	%	100	0–100	0 50 100 ***0.10 0.10 0.80***
UL	Undetected leakage	m^2	0	$0–10e^{-5}$	0 $1e^{-5}$ $5e^{-5}$ $10e^{-5}$ ***0.8899 0.1 0.001 0,0001***
POV	Partially opened valve in the IC discharge line	%	100	1–100	1 10 50 100 ***0.001 0.01 0.1 0.889***

(i) *TPI-I*. Only three probabilistically selected cases over 100 do not meet the first proposed TPI.

(ii) *TPI-II*. The second proposed TPI is verified by the all 100 probabilistically selected cases.

(iii) *TPI-III*. The third proposed TPI is verified by 78 over 100 probabilistically selected cases.

4.5. Additional Analysis. Sensitivity analysis can provide additional criteria in order to perform a further screening of the uncertain parameters. In this case, since the number of relevant parameters selected is reasonably low, the sensitivity analysis will be used just to determine those parameters that affect mostly the condenser system behavior.

As it can be observed (Figure 12) the worst system condition is linked to transients with slow pressurization phases since they allow a higher system energy accumulation.

The Standardized Regression Coefficients (SRCs) technique [13] allows the ranking of the parameters according to their relative contribution upon the system Performance Indicator (PI) and quantifying this contribution for each parameter.

The technique is based on the hypothesis of a linear relationship between response and input parameters.

For the use of the SRC technique it is supposed that the response Y (in this case the system PIs defined above) is a linear function of the random input variables Xi, that is, $Y = \beta_O + \sum_{i=1}^{p} \beta_i X_i$.

The SRCs are given by is

$$\mathrm{SRC}(Y, X_i) = \beta_i \sqrt{\frac{\mathrm{Var}(X_i)}{\mathrm{Var}(Y)}} \tag{15}$$

and indicate the importance of the individual input variables X_i with respect to the output Y.

The SRCs quantify the effect of varying each input variable from its mean value by a fixed fraction of its variance (maintaining all other variables at their expected values).

The SRC values are reported in Figure 13 in relation to each of the identified parameters listed in Tables 1 and 2.

4.6. Quantitative Reliability Evaluation. A preliminary qualitative reliability assessment is made by means of a so-called response surface calculation [12, 14]. It is based on

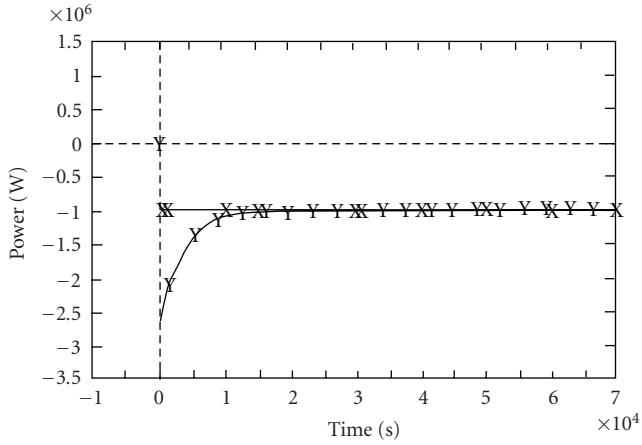

(a)

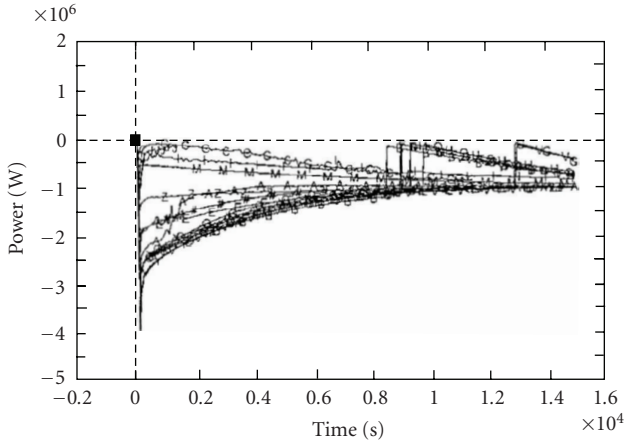

(b)

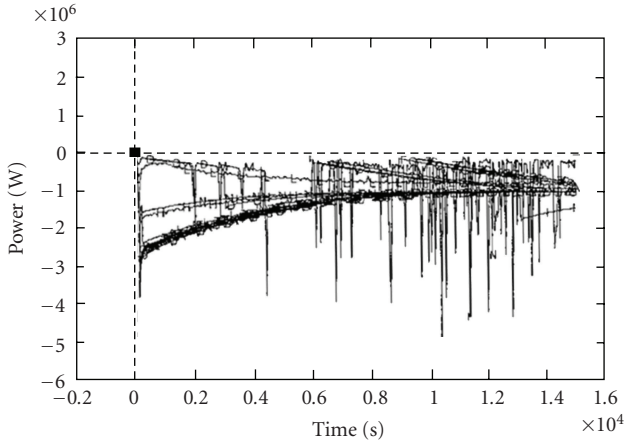

(c)

Figure 18: (a) Reference system performance: power exchanged through the IC. (b) Time trends related to the ensemble of 75 code runs (6 deterministic status and 69 probabilistic status—discrete probability distribution): power exchanged trough the IC. (c) Time thrends related to the ensemble of 75 code runs (6 deterministic status and 69 probabilistic status—continuous probability distribution): power exchanged through the IC.

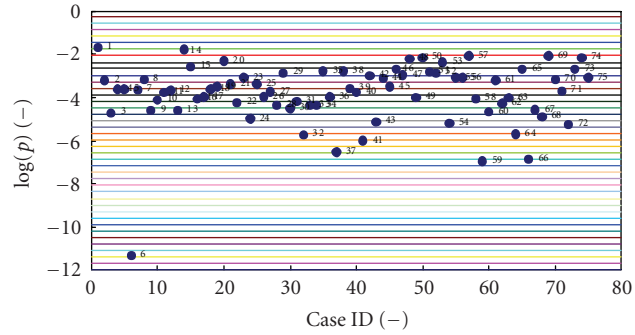

Figure 19: Characterization of system status on the basis of the probability. Six system status (1 to 6 in the figure) is deterministically derived and sixty-nine (7 to 75 in the figure) are statistically derived assuming a discrete probability distribution.

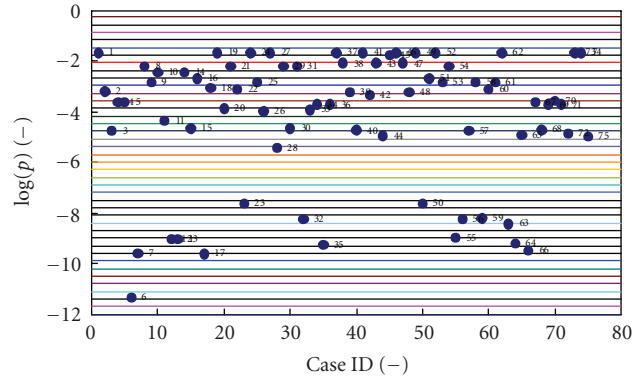

Figure 20: Characterization of system status on the basis of the probability. Six system status (1 to 6 in the figure) is deterministically derived and sixty-nine (7 to 75 in the figure) are statistically derived assuming a continuous probability distribution.

a simplified equivalent model that fits the initial data, which has good prediction capacities. After determining the response surface, a Monte Carlo Simulation was performed to assess the reliability of the passive safety system.

Several code runs were done without obtaining failure cases, showing that the use of Monte Carlo is limited to estimate rare events probabilities. This allows estimating a conservative boundary of the failure probability by means of equation used to evaluate the number of code runs necessary to set γ as a boundary of the failure probability (p):

$$1 - (1 - \gamma)^k \geq \beta, \tag{16}$$

where β represent the "confidence" that p will be lower than γ, and k can alternatively take the values N or $N + 1$.

Considering $k = N = 10^5$ and $\beta = 0.95$, the boundary achieved for the probability of failure is $\gamma = 3 \cdot 10^{-5}$.

The same can be achieved by the application of Wilks' formula [12, 15].

The result obtained shows the highly reliability of the investigated passive safety system.

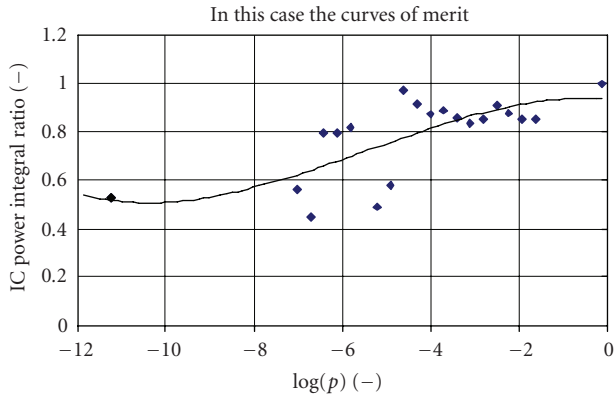

Figure 21: Curves of merit: probability for the performance indicator "IC power integral ratio" (discrete probability distribution).

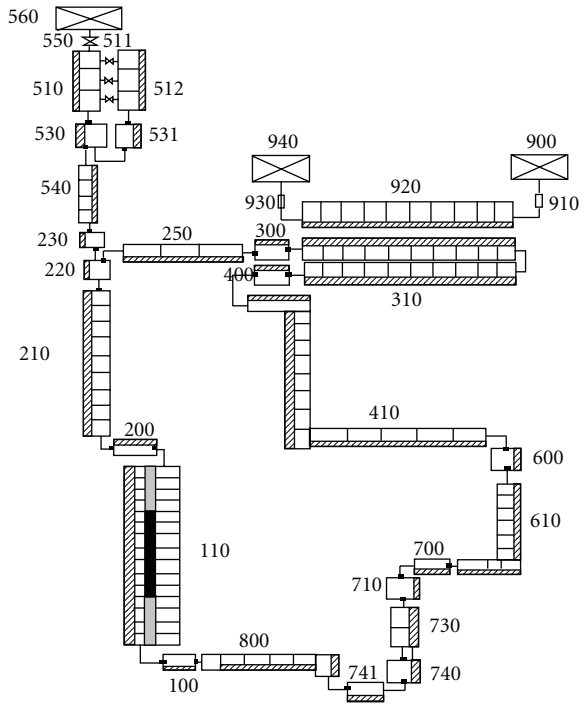

Figure 22: RELAP 5 nodalization TTL-1 apparatus case c.

4.7. Lay-Out Modification. A lay-out modification (see Figure 14) test study was also performed

(i) to analyze the methodology and the model developed,

(ii) to evaluate the long term transient,

(iii) to give support to the system design adding another judgment criterion

(iv) to add completeness to the sensitivity analysis.

In particular the length of the connection lines between the condenser pool and the reactor was reduced of about 3 meters.

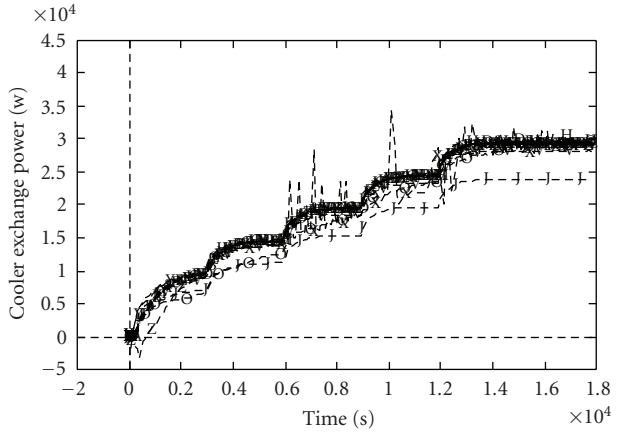

Figure 23: Time trends related to the ensemble of 137 code runs ([1–18] deterministic status): power exchanged in the cooler.

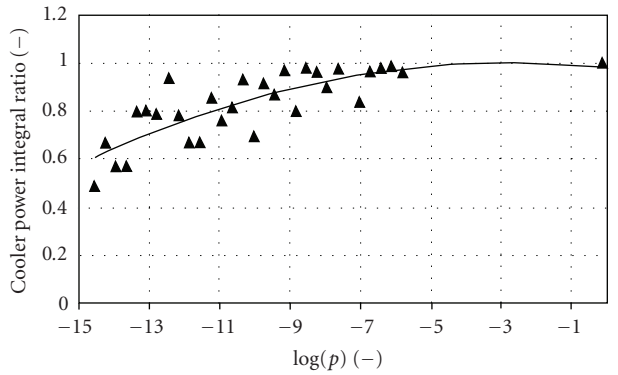

Figure 24: Probability distribution for the performance indicator: integral power ratio exchanged in the cooler.

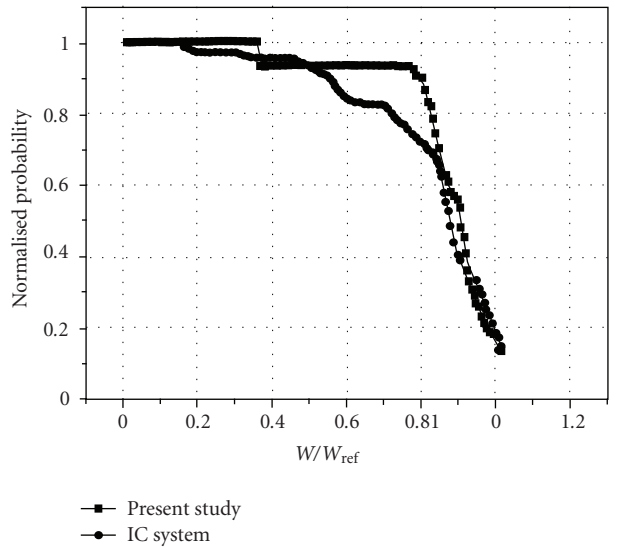

Figure 25: Comparison between thermal hydraulic reliability for two different systems: IC-SBWR (two-phase NC system) and TTL 1.

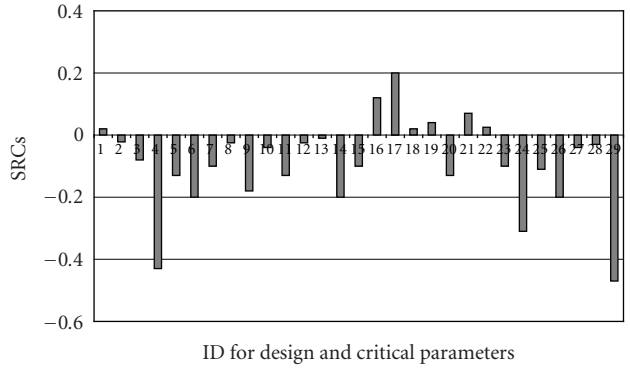

Figure 26: Standardized regression coefficients for the defined performance indicator: W/W_{ref}

One of the results of reducing the piping line of the safety system is the condensers tubes flooding after the system is demanded. This is due to the fact that the liquid column height is mainly affected by the overall friction across the safety system circuit.

The change proposed affects only the nonrelevant distributed frictions; thus, the return line equivalent liquid level is approximately sustained at original system values, which derives in the mentioned piping line flooding.

The liquid present into the piping affects the heat transfer reducing the power exchanged across the condensers. The relevance of this effect can be seen through the comparison between the power ratio values obtained for the original and modified systems (Figure 15).

From the simulations results (Figure 16) it has been shown that there are no differences in the long-term system behavior. The application of long-term defined TPI gives us a result similar to system performances, reflecting the condition stated before.

5. Main Outcomes of Cases (b) and (c)

In the following are reported the main results of the REPAS application to the following systems:

(i) a scaled IC of an SBWR (case b) [2],

(ii) TTL-1 experimental apparatus (case c) [6].

In particular in the following, according to Section 2 (methodology overview) and Section 4 (detailed description of case a), are presented only the main steps. Main purpose of this section is just to show how the REPAS grew up.

5.1. Case (b) Isolation Condenser (IC) of an SBWR. The system was modeled (Figure 17) and the design and critical parameter were selected (Tables 3 and 4).

For the analysis were chosen 6 system status selected deterministically and 69 system status selected probabilistically (for each of two probability distribution) discrete and continuous (Figures 18 through 20).

The FC considered was

$$\text{FC} = \frac{Z - Z_{\text{ref}}}{Z_{\text{ref}}} =< (-0,2), \tag{17}$$

where Z is

(i) the thermal power exchanged across the IC ($W2$);

(ii) mass flow rate at the IC inlet ($\Gamma 2$).

"ref" related to the code calculation for the reference or nominal system configuration.

Indicators of system performance are

(1) time during the calculation when the FC is verified, failure time $Ft(s)$,

(2)

$$\frac{\int_{T_{\text{nom}}}^{\text{eoc}} W2(t)dt}{\int_{T_{\text{ref}}}^{\text{eoc}} W2_{\text{ref}}(t)dt} = \frac{(1/\text{eoc} - T_{\text{nom}})\int_{T_{\text{nom}}}^{\text{eoc}} (P_{\text{HX}}(t)/P_{\text{CORE}}(t))dt}{(1/\text{eoc} - T_{\text{ref}})\int_{T_{\text{ref}}}^{\text{eoc}} (P_{\text{HX}}(t)/P_{\text{CORE}}(t))_{\text{ref}}dt}, \frac{\int_{T_{\text{nom}}}^{\text{eoc}} \Gamma 2(t)dt}{\int_{T_{\text{ref}}}^{\text{eoc}} \Gamma 2_{\text{ref}}(t)dt}, \tag{18}$$

(3) ratio between the failure time and the time of calculation. where P_{HX} is the Power exchanged across the condensers tubes, P_{CORE} is the Core power, T is the system activation time, and eot is the end of transient calculation.

In this case the curves of merit (Figure 21) were used to judge the system acceptability and to compare the selected system with different system. They show the PI values ($W2/W2_{\text{ref}}$) as a function of the probability interval range.

5.2. Case (c) TTL-1 Apparatus. The system was modeled (Figure 22) and the design and critical parameter were selected (Table 4).

The FC is expressed as

$$FC = \frac{W_{\text{ref}} - W}{W_{\text{ref}}} \leq 0.2, \tag{19}$$

where

$$W = \frac{\int_0^{\tau_{\text{obs}}} W(t)dt}{\tau_{\text{obs}}}, \tag{20}$$

where W is the integral of thermal power exchanged in the cooler, "ref" is the related to the code calculation for the reference or nominal system configuration, and τ_{obs} is the "observation time".

The system PIs to evaluate the Thermal Hydraulic Reliability (TH-R) are

(i) integral value over a mission time,

(ii) ratio W/W_{ref}.

The deterministic and statistic selection of system scenarios was done by means of Monte Carlo procedure. Four ways are pursued to arrive at four definitions for the TH-R of the TTL-1 loop, respectively, adopting the following.

Table 5: Design and critical parameters case c.

Parameter ID	Description		Unit	Nominal value	Range	Discrete initial value and associated probabilities
LP	Linear power of electrically heated rod		W/m	$30e^6$	$0–30e^6$	— ***1.0***
P1	Initial Pressure of the loop		bar	5	1–10	1 3 5 8 10 ***0.02 0.13 0.7 0.1 0.05***
T2	Temperature of the SS fluid at the cooler inlet		K	303	295–350	295 303 325 350 ***0.18 0.65 0.15 0.02***
HL1	Heat losses from the test section (TS). % of TS power		%	0.2	0–4.5	0.0 0.2 1.0 4.5 ***0.1 0.69 0.15 0.06***
HL2	Heat losses from the loop w/o (TS). % of TS power		%	3	0–20	0.0 3 10 20 ***0.1 0.69 0.15 0.06***
L1	Total length of the loop		m	21	12–34	12 21 28 34 ***0.05 0.69 0.14 0.12***
LV	Loop volume (change of the pre-heater tank)		m^3	0.09	0.07–0.2	0.07 0.09 0.12 0.2 ***0.05 0.65 0.18 0.12***
PV	Volume of PRZ		m^3	0.06	0.03–0.12	0.03 0.06 0.09 0.12 ***0.05 0.65 0.18 0.12***
PN	Noding of the PRZ		—	N	N1-N2	N1 N N2 ***0.1 0.8 0.1***
PP	Position of the PRZ	Upstream the cooler (U) Downstream the cooler (D)	—	U	U–D	U D ***0.85 0.15***
K1	Local pressure drop coefficient (K) at the inlet of the TS		—	0.2	0–1.2	0.0 0.2 0.4 1.2 ***0.05 0.53 0.3 0.12***
K2	K factor at the outlets of the TS		—	0.6	0-1	0.0 0.6 0.8 1.2 ***0.05 0.53 0.22 0.2***
TK	Sum of the K factors, w/o TS inlet and outlet		—	7.5	3–25	3 7.5 15 25 ***0.05 0.55 0.22 0.18***
EI	Electrical Insulation in the heater	AL_2O_3 (A) Boron nitride (B)	—	A	A-B	A B ***0.85 0.15***
CIT	Thickness of cooler tubes		mm	2	1–3	1 2 3 ***0.05 0.65 0.3***
CT	Cooler tubes		—	Cu	Cu–SS	Cu SS ***0.85 0.15***
E2	Equivalent diameter of secondary side of the cooler		mm	10	7–20	7 10 20 ***0.25 0.7 0.05***
E1	TS Equivalent diameter (coolant passage)		mm	8	5–12	5 7 8 12 ***0.05 0.3 0.55 0.1***
AR	Ratio of Heater heat transfer area to cooler heat transfer area		—	0.18	0.05–0.37	0.05 0.12 0.18 0.37 ***0.05 0.3 0.6 0.05***
PD	Axial power distribution	Uniform (U) Cosine (C) Semi cosine (S)	—	U	C–S	C U S ***0.1 0.65 0.25***
CO	Orientation of the cooler	Vertical (V) Horizontal (H) Inclined (I)	—	H	I–V	I H V ***0.08 0.65 0.27***
MF2	Secondary side mass flow rate		Kg/s	1.2	0.4–1.8	0.4 1.2 0.8 1.8 ***0.05 0.55 0.23 0.17***

Table 5: Continued.

Parameter ID	Description		Unit	Nominal value	Range	Discrete initial value
P2	Secondary side pressure		bar	1	1–10	1 5 10 ***0.6 0.3 0.2***
LS	Presence of U-pipe or loop seal in the cold part of the loop		—	No	Yes-No	Y N ***0.2 0.8***
D1	Riser diameter		mm	25	25–100	25 50 75 100 ***0.55 0.25 0.15 0.05***
D2	Down comer diameter		mm	25	25–75	25 50 75 ***0.55 0.25 0.2***
PC	PRZ Connection	Direct (D) Surge Line (S)	—	S	D–S	S D ***0.8 0.2***
G1	Non-condensable gas mass fraction at the inlet of cooler piping		—	0	0–1	0.0 0.05 0.2 0.5 0.8 ***0.58 0.3 0.1 0.01 0.01***
G2	Non-condensable gas mass fraction inside the TS		—	0	0–1	0.0 0.05 0.3 0.5 0.8 ***0.58 0.3 0.1 0.01 0.01***
UL	Undetected leakage		Kg/s	0	$0–1e^{-2}$	0.0 $0.1e^{-5}$ $0.1e^{-3}$ $0.1e^{-2}$ ***0.65 0.25 0.09 0.01***

(1) The "figure of merit" approach proposed by [2]: the result is given in Figure 24.

(2) The "cumulative probability" approach suggested by [16]: the result is given in Figure 25, where a comparison is made with the result from a previous REPAS application case b.

(3) The R1 single-valued reliability definition is

$$R_1 = 1 - \frac{\mathrm{NF}}{N} = 0.70, \tag{21}$$

where NF is number of failed runs and N is total number of runs.

The R2 single-valued reliability definition is

$$R_2 = \frac{\sum_1^N (W/W_{\mathrm{ref}})}{N} = 0.85. \tag{22}$$

The TH-R definition in Figure 24 (first TH-R definition) uses data elaboration given in Table 6.

The TH-R definition in Figure 25 (second TH-R definition) makes use of the classic Cumulative Distribution Function (CDF) concept. The TH-R is achieved by ordering the cooler power integral ratio (W/W_{ref}) with respect to the probability of occurrence of each configuration from the probabilistic and deterministic sets.

Sensitivity analyses identify the main contributors to the passive system performance. The SRC technique, see the above section, was used. The SRC values are reported in Figure 26 in relation to each of the defined critical and design parameters.

6. Conclusions

The assessment of the reliability of passive systems is a crucial issue to be solved for their extensive use in future NPPs.

Several physical parameters affect significantly the behavior of a passive system and their values at the time of operation are "a priori" uncertain: thus, there is the need to consider a multitude of scenarios of system response. This gives back the reliability assessment nonmanageable, the bottleneck being the need to simulate several system behaviors with time-consuming mechanistic computer codes.

To overcome these difficulties, it is necessary to identify those parameters which are most relevant to the system response and limit the probabilistic analysis to them. The REPAS procedure can be applied:

(i) to evaluate the acceptability of a passive system,

(ii) to compare two different passive systems having the same mission; moreover the methodology is still in assessment phase (by means of a suitable "experimental tests") for absolute reliability evaluation,

(iii) to evaluate the performances of an active and a passive system on a common basis,

(iv) to supplement deterministic criteria and analyses (e.g., TH) in the design process considering the reliability of accident prevention and mitigation functions,

(v) to optimize the design of a passive safety system,

(vi) to assess the economical impact in the design change.

REPAS method is described in Section 2 and its application in Sections 4 and 5. The first "embryonic" applications of the methodology are reported in [2, 5, 7] and so forth. It was the result of a joint cooperation between ENEA, UNIPI, and Polytechnic of Milan. Then this methodology was embedded in the RMPS EU project on the framework of the 5th EURATOM program [19], see also [3, 4, 16, 17] and so forth, In this report is shown an improvement

Table 6: Selected system performance indicator related to individual probability intervals.

Case ID	Probability	Accepted Run	Failed Run	W/W_{ref}
Reference	4.25E-06	□	—	1
1	1.21E-07	□	*	0.785
2	1.18E-06	□	—	1.004
3	1.31E-07	□	—	0.97
4	3.69E-07	□	—	0.953
5	3.69E-07	□	*	0.782
6	3.08E-07	□	—	1.02
7	7.39E-07	□	—	0.996
8	7.84E-07	□	—	1
9	3.27E-07	□	—	0.99
10	7.84E-07	□	—	0.995
11	5.31E-07	□	—	1
12	7.50E-07	□	—	1
13	9.62E-07	□	—	1
14	1.60E-06	□	—	1
15	1.39E-06	□	—	1
16	7.50E-07	□	—	1.007
17	1.96E-06	□	—	1
18	7.50E-07	□	—	1
19	3.03E-07	□	—	0.99
20	3.86E-07	□	—	0.995
21	7.72E-07	□	—	1
22	3.54E-07	□	—	1
23	3.54E-07	□	—	0.9
24	6.54E-07	□	—	1
25	1.77E-06	□	—	1
26	1.31E-06	□	—	1
27	1.42E-06	□	—	1
28	1.06E-06	□	—	0.98
29	3.86E-07	□	—	0.91
30	1.16E-06	□	—	0.95
31	1.06E-06	□	—	0.98
32	7.32E-08	□	—	1
33	7.32E-08	□	—	1
34	5.88E-07	□	*	0.77
35	1.87E-07	□	—	0.97
36	7.79E-08	□	*	0.4
37	1.08E-14	□	*	0.26
38	9.39E-11	□	—	0.9
39	4.48E-11	□	—	1.007
40	4.59E-12	□	—	0. 83
41	1.66E-10	□	—	0.93
42	6.65E-14	□	—	0.8
43	6.66E-10	□	—	0.94
44	1.16E-09	□	—	0.94
45	2.54E-14	□	—	1
46	4.64E-14	□	*	0.62
47	2.02E-12	□	*	0.67

of the methodology for the relative reliability evaluation including a more robust mathematical model based on Probabilistic basis.

REPAS method is described and three applications related to a pool heat removal system of a prototypical integrated system, a scaled IC of an SBWR and TTL 1 experimental apparatus, were presented.

The methodology is tested on examples of T-H passive systems.

Identification and quantification of the sources of uncertainties and determination of the important variables are done. The sources of Uncertainties are identified and they are mainly in the following:

(i) approximations in modeling of the process physics;

(ii) approximations in modeling of the system geometry;

(iii) the input variables.

The engineering judgment plays an important role in the REPAS and in the identification of source of uncertainty by means of selecting the range of uncertainty, the probability density function, and so forth.

The analysis of the results and the use of the system performance indicator (PI or TPI) allowed the achievement of the system performance evaluation. The relevant results are summarized in the above sections for all the three investigated cases. The sensitivity analysis has been completed by adopting the Standardized Regression Coefficients technique (SRCs).

Areas for further development and improvement of the procedure have been identified. They are summarized as follows.

(i) Absolute reliability evaluation is needed by means of a tailored experimental tests.

More rigorous and systematic basis is necessary to select the parameters that characterize the system status (e.g., a complete Expert Judgment procedure).

References

[1] L. Burgazzi, "Evaluation of uncertainties related to passive systems performance," *Nuclear Engineering and Design*, vol. 230, no. 1–3, pp. 93–106, 2004.

[2] F. D'Auria and G. Galassi, "Methodology for the evaluateon of reliability of passive systems," work performed in the frame of cooperation with DIMNP of Pisa University and ENEA (contract n. 9840 series 3A); DIMNP NT 420 (00) Rev. 01, October 2000.

[3] M. Marquès, J. F. Pignatel, P. Saignes, et al., "Methodology for the reliability evaluation of a passive system and its integration into a Probabilistic Safety Assessment," *Nuclear Engineering and Design*, vol. 235, no. 24, pp. 2612–2631, 2005.

[4] M. E. Ricotti, E. Zio, F. D'Auria, and G. Caruso, "Reliability methods for passive systems (RMPS) study strategy and results," in *Proceedings of the NEA CSNI/WGRISK Workshop on Passive Systems Reliability—A Challenge to Reliability, Engineering and Licensing of Advanced Nuclear Power Plants*, Cadarache, France, March 2002.

[5] F. Bianchi, L. Burgazzi, F. D'Auria, and M. Ricotti, "The REPAS approach to the evaluation of passive system reliability," in *Proceedings of the OECD International Workshop Passive System Reliability—A Challenge to Reliability Engineering and Licensing of Advanced Nuclear Power Plants*, Cadarache, France, March 2002.

[6] J. Jafari, F. D'Auria, H. Kazeminejad, and H. Davilu, "Reliability evaluation of a natural circulation system," *Nuclear Engineering and Design*, vol. 224, no. 1, pp. 79–104, 2003.

[7] F. Pierro, F. D'Auria, G. M. Galassi, and J. Jafari, "Application of REPAS method for reliability assessment of passive system," in *Proceedings of the IAEA Technical Meeting "Status of Validation and Testing of Passive Safety Systems for Small and Medium Sized Reactors (SMRs)"*, IAEA, Vienna, Austria, June 2006.

[8] G. Lorenzo, P. Zanocco, M. Giménez, et al., "Reliability assessment of the thermal hydraulic phenomena related to a CAREM-like passive RHR system," in *Proceedings of the European Safety and Reliability Conference (ESREL '08)*, 2008.

[9] M. Marquès, "Reliability of passive systems that utilize natural circulation," in *Proceedings of the IAEA Course on Natural Circulation in Water-Cooled Nuclear Power Plants, International Centre for Theoretical Physics (ICTP)*, Trieste, Italy, June-July 2004, paper id: T23 and T24.

[10] IAEA, "Status of innovative small and medium sized reactor designs 2005," IAEA Tecdoc-1485. 2006.

[11] J. Jafari, F. D'Auria, H. Kazeminejad, and H. Davilu, "Code-based design and stability analysis of a low pressure two-phase natural circulation test loop," *International Journal of Heat and Technology*, vol. 20, no. 2, pp. 87–95, 2002.

[12] S. S. Wilks, "Statistical prediction with special reference to the problem of tolerance limits," in *Proceedings of the Conference of the American Mathematical Society*, September 1942.

[13] A. Saltelli, K. Chan, and E. M. Scott, *Sensitivity Analysis*, John Wiley & Sons, New York, NY, USA, 2000.

[14] E. Volkova, B. Iooss, and F. Van Dorpe, "Global sensitivity analysis for a numerical model of radionuclide migration from the RRC "Kurchatov Institute" radwaste disposal site," *Stochastic Environmental Research and Risk Assessment*, vol. 22, no. 1, pp. 17–31, 2008.

[15] G. B. Wallis, "Evaluating the probability that the outputs of a computer code with random inputs will meet a set of evaluation criteria," *Reliability Engineering and System Safety*, vol. 91, no. 7, pp. 820–827, 2006.

[16] M. Marques, F. D'Auria, G. Cojazzi, et al., "Reliability methods for passive safety functions," in *Proceedings of the 10th ASME-JSME International Conference on Nuclear Engineering (ICONE '02)*, Arlington, Va, USA, April 2002, paper no. 22274.

[17] NEA/CSNI/R(2002)10, "Passive system reliability—a challenge to reliability engineering and licensing of advanced nuclear power plants," in *Proceedings of the International Workshop Hosted by the Commissariat à l'Energie Atomique (CEA '02)*, Cadarache, France, March 2002.

[18] L. Burgazzi, "State of the art in reliability of thermal-hydraulic passive systems," *Reliability Engineering and System Safety*, vol. 92, no. 5, pp. 671–675, 2007.

[19] EUROPEAN COMMISSION, 5th EURATOM framework programme 1998–2002 key action: nuclear fission, "RMPS PROJECT," CONTRACT No. FIKS-CT-2000-00073, PROJECT No. FIS5-1999-00250, April 2002.

Hindawi Publishing Corporation
Science and Technology of Nuclear Installations
Volume 2009, Article ID 213981, 10 pages
doi:10.1155/2009/213981

Research Article

CFD Application to Hydrogen Risk Analysis and PAR Qualification

Jinbiao Xiong, Yanhua Yang, and Xu Cheng

School of Nuclear Science and Engineering, Shanghai Jiao Tong University, No. 800 Dongchuan Road, Shanghai 200240, China

Correspondence should be addressed to Jinbiao Xiong, superbear@sjtu.edu.cn

Received 19 September 2008; Revised 30 November 2008; Accepted 15 January 2009

Recommended by Walter Ambrosini

A three dimensional computation fluid dynamics (CFD) code, GASFLOW, is applied to analyze the hydrogen risk for Qinshan-II nuclear power plant (NPP). In this paper, the effect of spray modes on hydrogen risk in the containment during a large break loss of coolant accident (LBLOCA) is analyzed by selecting three different spray strategies, that is, without spray, with direct spray and with both direct and recirculation spray. A strong effect of spray modes on hydrogen distribution is observed. However, the efficiency of the passive auto-catalytic recombiners (PAR) is not substantially affected by spray modes. The hydrogen risk is significantly increased by the direct spray, while the recirculation spray has minor effect on it. In order to simulate more precisely the processes involved in the PAR operation, a new PAR model is developed using CFD approach. The validation shows that the results obtained by the model agree well with the experimental results.

1. Introduction

During severe accidents, hydrogen can be generated in water-cooled reactors by metal-steam reaction. Hydrogen which is released into the containment may form combustible or even detonable gas mixture in the containment. As one of the mitigation measures against severe accidents in the Qinshan-II NPP, the containment spray system which starts when the containment pressure reaches the threshold value is utilized to prevent the containment overpressure. In the viewpoint of hydrogen risk, the spray operation is concerned due to two aspects. In one respect, the condensation introduced by the operation of the containment spray reduces the steam concentration, which leads to an increase of the hydrogen concentration and adds to the hydrogen combustion or detonation risk. In the other respect, the containment spray brings a gas temperature difference in the containment which promotes the gas mixing and leads to a more uniform distribution of the gas concentration. In this paper, a three-dimensional CFD code GASFLOW [1] is utilized to simulate the gas mixing and distribution in the LBLOCA and to evaluate the effect of the containment spray on the hydrogen risk. The case assuming no activation of the containment spray is selected as the base case. Two other cases assuming different containment spray operation strategies are involved in this paper. One of the spray cases considers only the direct spray (indicated as Case A, hereafter), while the other simulates the complete spray operation according to the design of the containment spray system, which includes the direct and recirculation spray (indicated as Case B, hereafter). The same source term is used in all the cases.

As one of the major hydrogen mitigation measures, the passive autocatalytic recombiner (PAR) has been widely used in nuclear power plants. In most studies presented in open literatures, including lumped parameter code analysis and CFD code analysis, the PAR is simply simulated by introducing energy and mass source terms obtained from empirical correlations. According to the state-of-art report on PAR proposed by the PARSOAR project [2], a theoretical PAR model is recommended for the CFD analysis codes, such as GASFLOW, TONUS. In this paper, a PAR model is developed based on the CFD approach, in order to provide more insight into the processes inside a PAR.

2. Hydrogen Risk Analysis for Qinshan-II NPP

2.1. Containment Geometry and Mitigation Systems. The containment of Qinshan-II NPP is a large dry containment which consists of a cylindrical part and a spherical dome, as indicated in Figure 1. The height of the containment is about 60 m, and the diameter is about 38 m [3]. The compartments are mainly located below the operation deck at the height of 20 m. The main components of two primary loops are symmetrically arranged in the containment. The deck at the height of 4.5 m supports the major heavy components including the steam generators (SGs), the reactor coolant pumps (RCPs) and the safety injection tanks (SITs). Similar to most of the pressurized water reactor (PWR), the pressurizer (PZR) is located in a room next to one of the SG towers. The bottom of the PZR room is at a height of about 11 m. The PZR relief tank room is located on the 0 meter floor and right under the PZR room. The refueling pool is from 6 to 20 m in height. It connects with the reactor cavity in the center of the containment and reaches the containment wall. There are other small rooms accommodating the valve, piping, and heat exchangers on the 0 meter floor and the underground floor. All the above-mentioned rooms are located inside a cylindrical missile shielding wall which protects the containment from ejected missiles. The space above the operation deck is much opener. Only the SG towers and the PZR room extend beyond the deck. moreover, in the dome a crane is installed. GASFLOW can generate structural mesh in both Cartesian and cylindrical coordinates. According to the characteristics of the containment geometry, the cylindrical coordinate is selected. The mesh size is adjusted according to the location of the structures in the containment so that the geometry can be described with a coarser mesh system without increasing the computation cost. In the mesh system 18, 60, and 51 cells are, respectively, arranged in radial, circumferential, and axial directions. The free volume of the containment is about 50 000 m^3. The average cell volume is about 1.4 m^3. The total wall surface area is about 24 000 m^2, most of which is considered as concrete. The components in the primary loop are treated as adiabatic because the adiabatic layer is utilized on them. In order to mitigate the hydrogen risk during severe accidents, 22 passive autocatalytic recombiners (PAR) of Siemens type are installed in the Qinshan-II NPP containment compartments. Table 1 lists the position and type of the PAR. Each PAR is simulated with a single mesh cell.

In Qinshan-II NPP, two separated containment spray systems are installed. According to the design of the spray systems, the containment can be depressurized with only one of them during the severe accidents. Each system includes two nozzle rings, as shown in Figure 2, on which about 250 nozzles are attached. The mass flow is uniformly distributed to every nozzle. Heat exchangers in the system control the temperature of spray water. The spray systems are designed to operate in two modes: direct spray mode and recirculation spray mode. The direct spray starts while the pressure in the containment reaches 2.36 bar. During the direct spray, the spray water comes from the refueling tank, and the temperature at the nozzle outlet is in the range from 20 to 40°C. In this paper, the temperature of spray water is given to be 27°C. In about 30 minutes, the water in the refueling tank will be used up. Then the spray switches to the recirculation mode. In the recirculation mode, the spray water is pumped from the water sump in the containment. Because the water

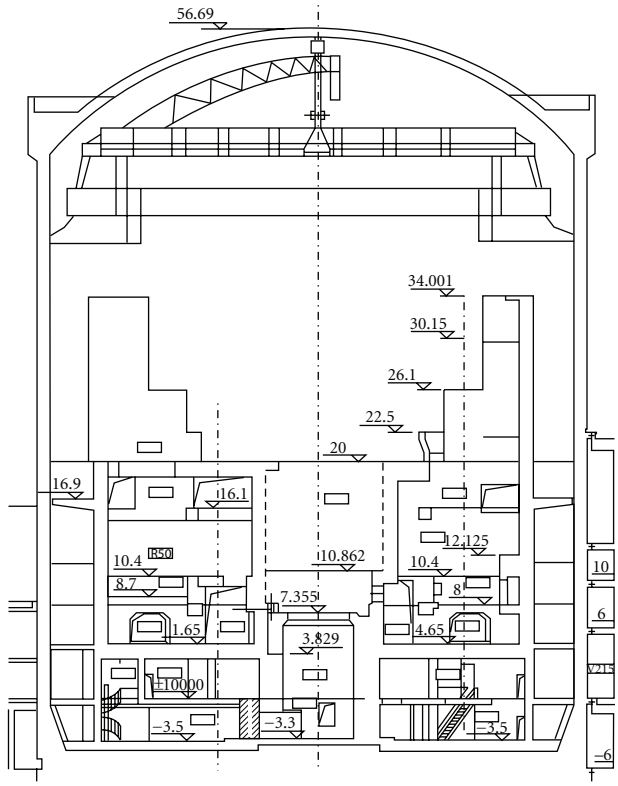

Figure 1: Vertical view of Qinshan-II containment geometry.

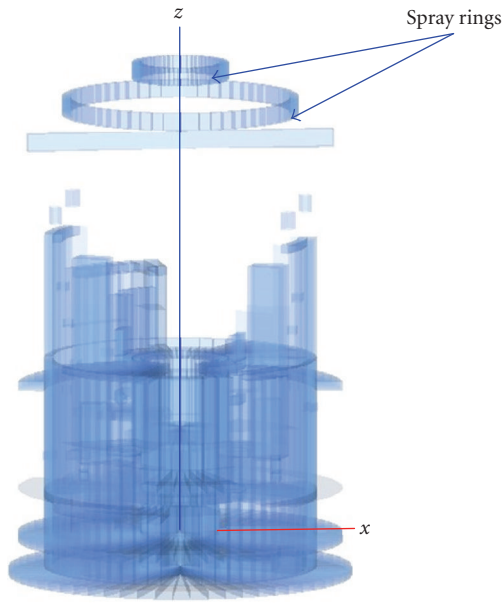

Figure 2: Containment geometry model.

Table 1: Arrangement of recombiners.

Location	Type	No.
PZR relief tank room	FR90/1–1500	3
Surge line room	FR90/1–960	1
PZR room	FR90/1–960	1
No. 1 SG compartment	FR90/1–1500	3
No. 2 SG compartment	FR90/1–1500	3
No.1 RCP room	FR90/1–960	1
No.1 RCP room	FR90/1–960	1
SIT room	FR90/1–960	1
Dome region	FR90/1–1500	4
Annular compartment	FR90/1–1500	4

in the sump originally comes from the primary loop or the spray water and is at a high temperature, the temperature of the recirculation spray water is higher and is designed to be from 40 to 120°C. In this paper, the water temperature of the recirculation spray is given as 77°C. According to the design of the system, the spray mass flow rates in the direct and the recirculation spray modes are 814 and 1050 ton per hour, respectively [3].

2.2. Physics Model. In GASFLOW two approaches are provided for two-phase flow simulation [4]. In the case that the spray model is not activated, the homogeneous equilibrium approach is applied automatically, which assumes the liquid and gas phases are in both thermodynamic and mechanical equilibrium. Because the containment spray brings strong transient and thermodynamic non-equilibrium, in order to more exactly simulate the interaction between the liquid and gas phases during the spray operation, GASFLOW offers another approach in which the thermodynamic non-equilibrium between liquid and gas phases is considered, but the difference of mechanical behavior between the liquid and gas phases is still neglected. The GASFLOW spray model has been validated with TOSQAN experiments and provided satisfactory predictions of the experiment data [5].

The spray simulation induces a much smaller time step size and increases the computation time by several times. Due to heavy time consumption in the spray simulation, turbulence model is not used in all the cases because the computational cost becomes unacceptable while using the turbulence model. According to the experience from Karlsruhe Research Center (FZK), GASFLOW predicts nearly the same flow field and vortex formation with and without turbulent models in a coarse grid [6], such as the grid used in containment geometry model. The heat conduction inside the structures is simulated in a one-dimensional approach. The PARs installed in the containment were simulated with the standard model provided by the GASFLOW code.

2.3. Accident Scenario. The hydrogen/water source term for this analysis was obtained by scaling from GKN surge line LBLOCA source term reported in [6], as indicated in Figure 3. The break is located in the lower part of the SG tower which is next to the pressurizer room. At the

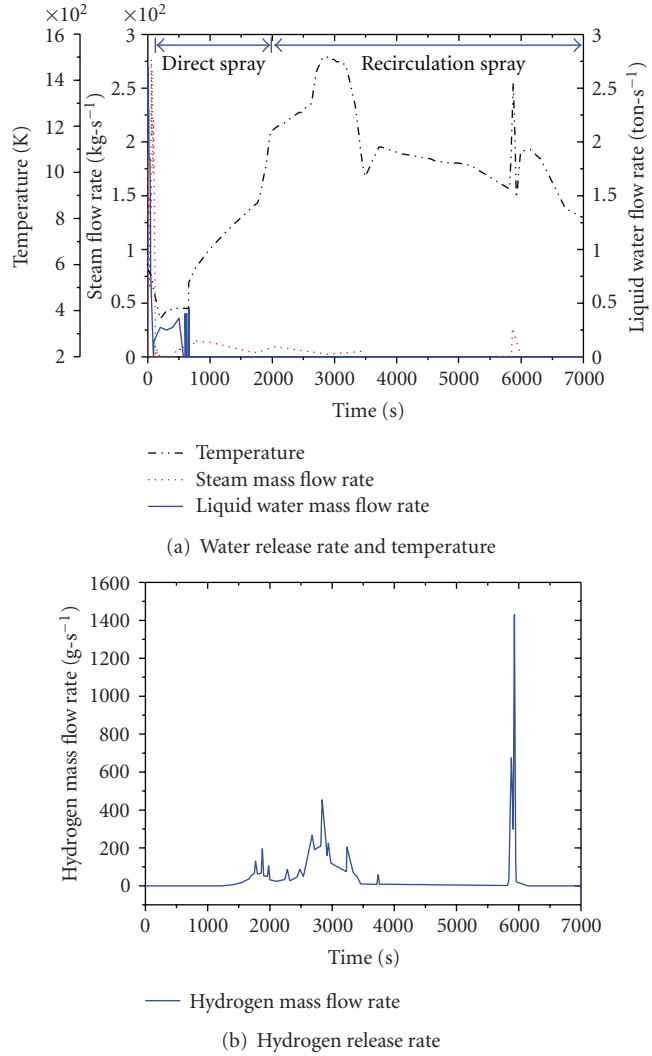

Figure 3: Source term and spray activation.

beginning, a large amount of saturated water is discharged to the containment. The water discharge flow rate decays promptly due to the limited coolant inventory in the primary loop. Water in the reactor core is heated by the decay heat which rises the water temperature to superheated condition after the saturated release period. At about 1400 seconds, hydrogen generation and release starts. About 270 kg hydrogen is released into the containment during the first 7000 s.seconds At 5930 seconds, hydrogen release peak rate is produced due to an enhancement of steam/zirconium reaction after the failure of the core support. Besides the source term, Figure 3(a) indicates also the two spray periods. The start time of direct spray is determined according to the pressure variation obtained in the base case. In about 60 seconds, the pressure in the containment reaches the threshold value and the direct spray starts.

2.4. Thermal Hydraulics. At the beginning of the LBLOCA accident, along with a heavy discharge of water to the containment, the pressure and gas temperature inside

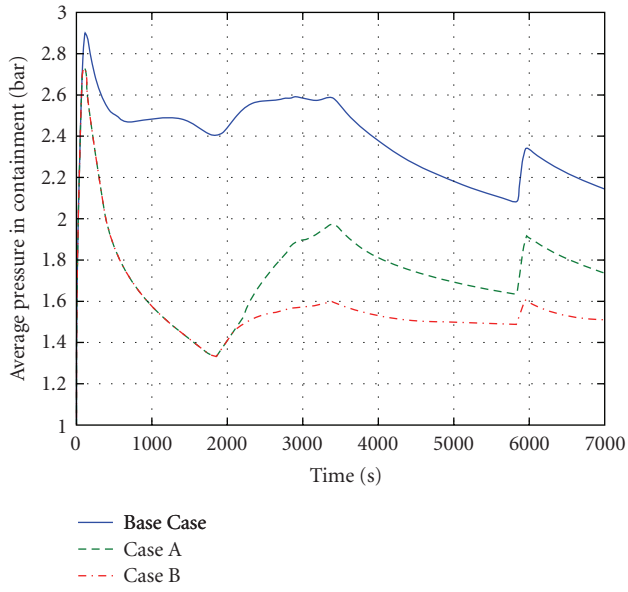

Figure 4: Pressure variation in three cases.

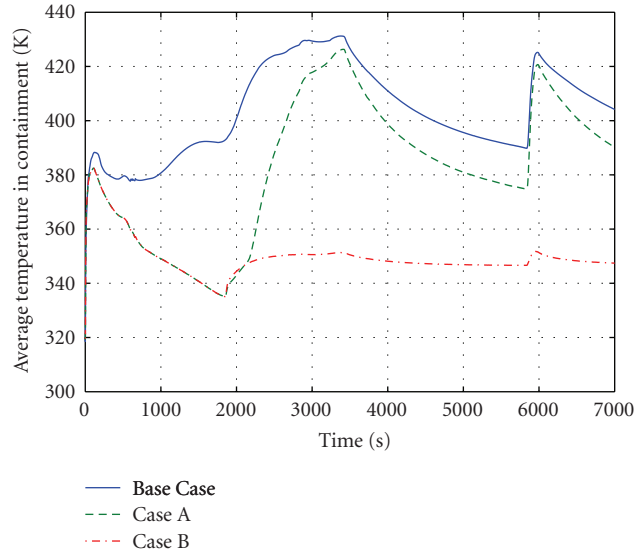

Figure 5: Average temperature variation.

the containment increase sharply. The hot steam mixes promptly and intensively with the atmosphere and soon spreads through the containment, which results in strong condensation on the structure surface. The condensation helps delaying the containment pressurization in the severe accident. Figures 4 and 5 compare the pressure and gas temperature variation in three cases. In all the cases, a sharp pressure and temperature increase occurs and the pressure reaches the maximum at the beginning of the blowdown. Although different approaches are utilized to deal with the two phases in the base case and spray cases, large discrepancies of the global behavior are not observed before the spray activation in the cases. For the base case, the pressure and gas temperature variation inside the containment is mainly affected by the water injection and the condensation on the structure. The computation result shows that, with the current source term, the pressure does not exceed the design value. In Case A and B, the pressure and the gas temperature inside the containment show lower peak values and decrease fast after the activation of the direct spray until its shutdown. Without the circulation spray, the pressure and gas temperature rebounds to high level in Case A because the hot steam continues being discharged after the shutdown of the direct spray. In Case B, the recirculation spray holds the pressure and the gas temperature slightly higher than the lowest value induced by the direct spray.

Figure 6 presents the bulk evaporation rate in the containment during all the cases. The direct containment spray introduces intensive bulk condensation (negative value in Figure 6). Conversely, the recirculation spray brings bulk evaporation. The evaporation of the spray water is beneficial with respect to hydrogen risk because it increases the steam concentration and builds up an inertial atmosphere which resists the hydrogen combustion. With respect to hydrogen risk, the outlet temperature of the recirculation spray should be optimized to enhance the evaporation of the spray water.

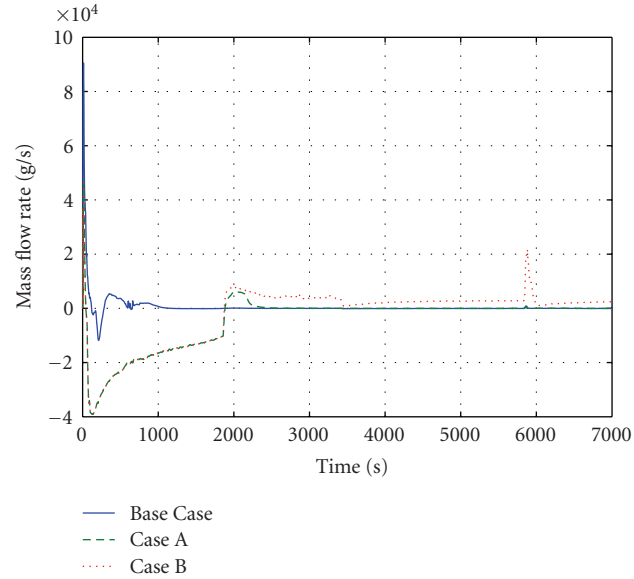

Figure 6: Bulk evaporation rate in all cases.

Figure 7 gives the total condensation rate on the structure surface. During the direct spray phase in the Cases A and B, the condensation on the structures is at a much lower rate than that in the base case due to the enhancement of the bulk condensation which reduces both the gas temperature and steam concentration. The condensation on the structures is one of the major ways in which heat is transferred from the atmosphere to the structures. Hence, a low condensation rate leads to a low heat transfer rate from the gas to the structures, as indicated in Figure 8. However, during the recirculation spray in Case B, the condensation on the structures is observed to be at a similar rate with that in the base case. In Case B, both the bulk evaporation and the

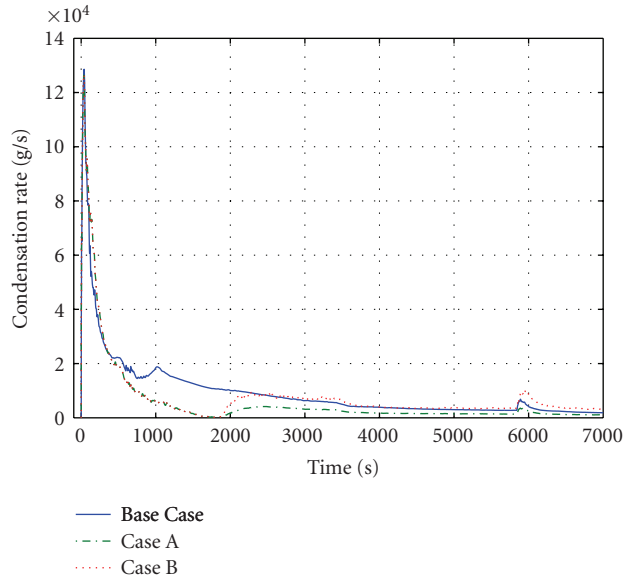

Figure 7: Total condensation rate on structure surfaces.

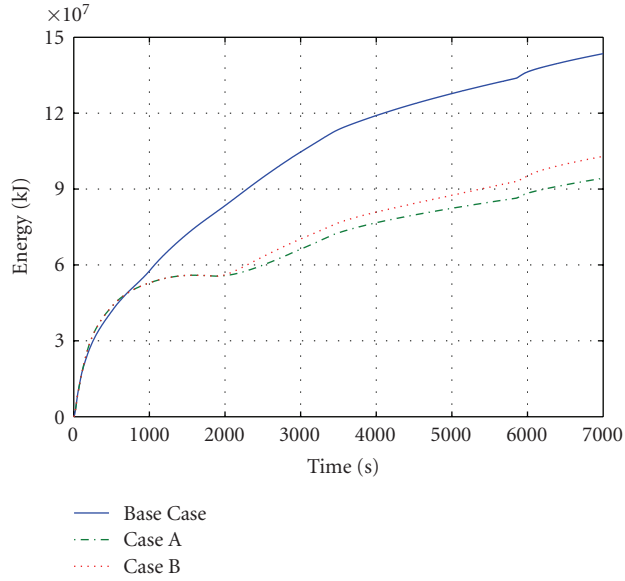

Figure 8: Energy absorption by structures.

surface condensation are enhanced by the recirculation spray. The evaporation of spray water takes away a lot of sensible heat from the atmosphere and contributes to stabilize the gas temperature inside the containment. Comparing both the bulk evaporation rate and the surface condensation rate in the Cases A and B shows that the recirculation spray generally increases the steam inventory inside the containment, which reduces the hydrogen combustion or detonation risk. Hence, it can be concluded that besides controlling the pressure and gas temperature inside the containment, the recirculation spray can build a comparatively inertial atmosphere for hydrogen.

2.5. Flow Field. Figure 9 presents the flow fields during the heavy hydrogen release period in all the cases. In the base case and Case A, similar flow fields are observed. Because the released gas is hydrogen-rich and of high temperature and low density, a buoyancy jet flow forms above the SG tower in which the break is located. The jet flow is reflected by the dome and flows downward into the other side of the containment. A large-scale vortex can be observed in the upper space. The condensation and the convection heat transfer on the structures remove the steam and heat from the atmosphere, the gas near the structures is heavier than the gas in the bulk. Hence, the downward flow can be observed near the structure surfaces. During the hydrogen release peak in the base case and Case A, the magnitude of velocity is generally less than 0.5 m/s. A chaotic flow field is induced by the recirculation spray, as indicated in Figure 9(c). The flow velocities in Case B are much higher than that in the other two cases. As mentioned in Section 2.2, GASFLOW spray model uses the mechanical equilibrium assumption while dealing with the two-phase flow. Actually, the heavy liquid phase is more inclined to drop down than the gas phase. The assumption inevitably leads to an artificial flow. In the actual situation, mechanical interaction between the liquid and gas phases could lead to a flow pattern different from the obtained results.

2.6. Hydrogen Recombination, Hydrogen and Steam Distribution. In the analyzed scenario, the hydrogen release can be generally divided into two periods. The first period lasts from 1400 s to 3500 s. In this period, the global hydrogen volume fraction in the containment reaches 3%, but the flammable clouds (at hydrogen concentration above 4%) rarely appear. Due to the hydrogen-oxygen recombination, the hydrogen concentration can be reduced to less than 3% before the second hydrogen release period starts. During the second period, the hydrogen release is discontinuous. However, intensive hydrogen release between 5900 and 6000 s could lead to extremely high local hydrogen concentration. Figure 10 presents snapshots of hydrogen and steam clouds right after the hydrogen release peak. A clear gas stratification can be observed in both the base case and Case A. Hydrogen—rich clouds are enveloped by steam-rich clouds during most of the time, which provides an inertial atmosphere for hydrogen and prevents early hydrogen combustion. The combustible hydrogen cloud in Case A is of the biggest size among the three cases. Compared with the base case, the steam concentration is low in the spray cases. Due to strong mixing induced by the recirculation spray, hydrogen stratification is not observed in Case B, as shown in Figure 10(c). Hence, the direct spray reduces the steam volume fraction and increases the hydrogen volume fraction, while the recirculation spray does not lead to an increase of hydrogen concentration but prevents the hydrogen concentration stratification.

In the Siemens PAR correlations [4], the recombination rate depends on the pressure and inlet hydrogen and oxygen concentration. Although the pressure is very different in the

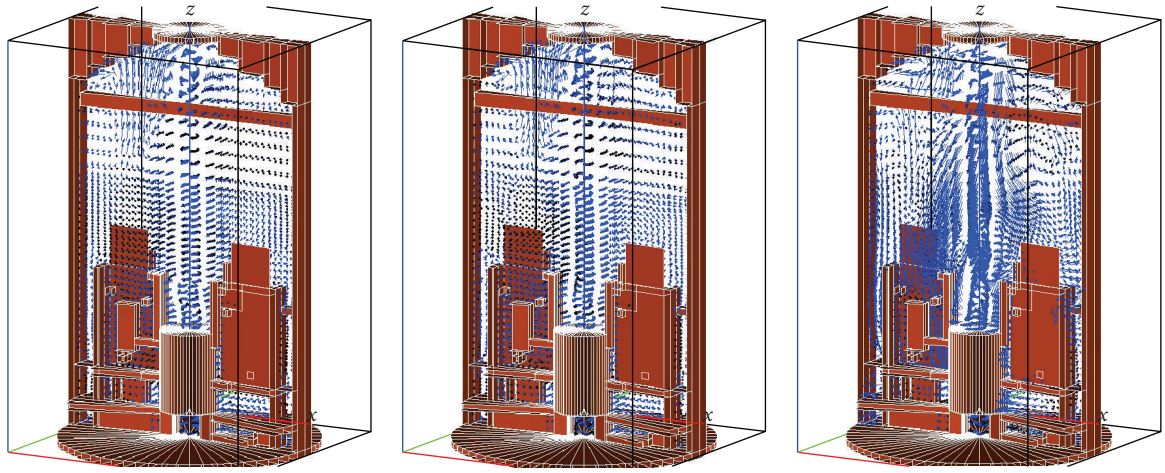

(a) base case $t = 5910$ s (b) Case A $t = 5910$ s (c) Case B $t = 5910$ s

Figure 9: Flow fields during the hydrogen release peak.

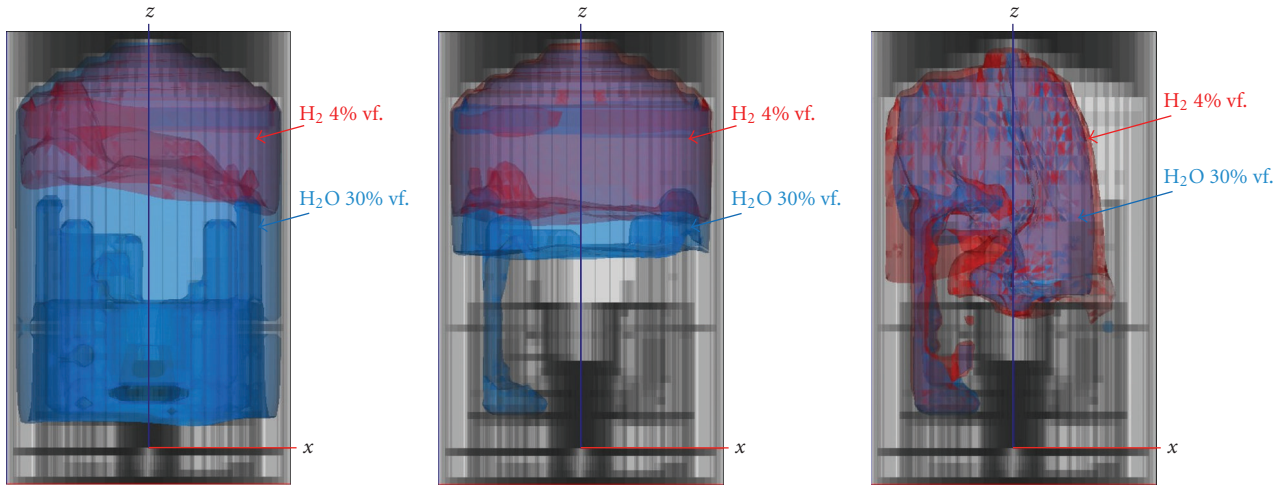

(a) base case at 5960 s (b) Case A at 5960 s (c) Case B at 5950 s

Figure 10: Hydrogen and steam clouds at the moment when hydrogen release reaches peak value.

analyzed cases, as mentioned in Section 2.4, the total recombination rate of 22 PARs does not show great difference in all the cases, as shown in Figure 11. Generally, the evolution of the recombination rate is in the same trend. Following the hydrogen release into the containment, the recombiners start up when the inlet hydrogen concentration reaches the startup threshold (2 vol. %). Along with the hydrogen accumulation in the containment, the recombination rate ascends. At the end of the first hydrogen release period, the recombination is at an almost stable rate. During the second period, when the hydrogen release is discontinuous and at a quite low rate, the recombination rate reduces smoothly and slowly. The oscillation of recombination rate is observed in this period in Case B because strong flow caused by the spray brings the strong variation of hydrogen concentration at the inlet of PARs. After 5900 s, the spray cases show a higher hydrogen removal capability than the base case due to higher global hydrogen concentration. In GASFLOW, the volume flow rate through the PAR is deduced from the recombination rate obtained from Siemens correlations. In this case, the recombination rate is affected only by the gas species concentration and pressure at the inlet of PAR. However, BMC Zx test results [7] suggest an increase of the volume flow rate through PARs and recombination rate due to the spray.

In order to indicate the characteristics of the hydrogen mixture and the hydrogen combustion risk in the containment, the volume of sigma cloud is involved in this paper. The sigma cloud is a volume of the hydrogen-air-steam mixture with a combustion expansion ratio higher than the critical value obtained from experimental data [8]. Flame acceleration could occur in a sigma cloud. Figure 12 presents

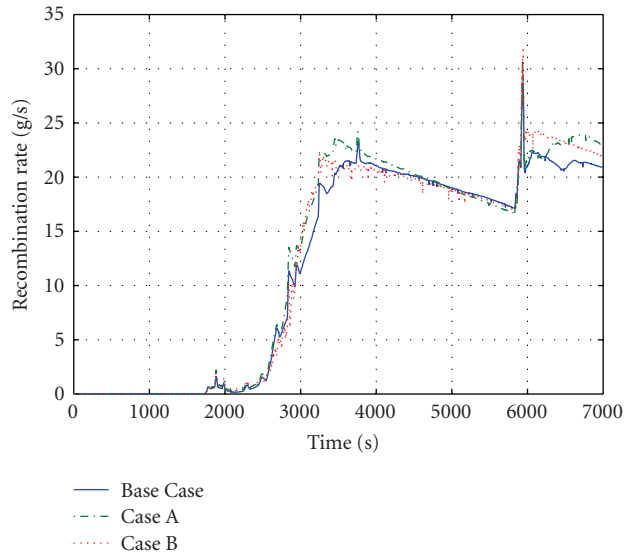

Figure 11: Total recombination rate of 22 PARs.

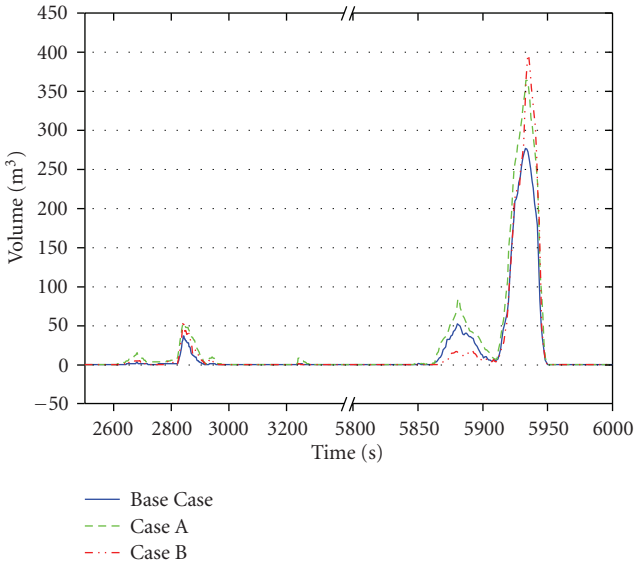

Figure 12: Total volume of sigma clouds.

the evolution of total sigma volume inside the containment in three cases. During the analyzed accident, a sigma volume peak can be observed in all the cases. And the maximum sigma volume in the spray cases is larger than that in the base case, while the maximum sigma volume in the Cases A and B is not quite different. However, if compared carefully, it can be found that the sigma volume in Case A shows to be larger than that induced by Case B at the second peak, and smaller at the third peak. It implies that the recirculation spray reduces the hydrogen risk during the slow hydrogen release period, but can slightly increase the local hydrogen concentration around the hydrogen source and lead to a larger sigma volume at the moment when the peak hydrogen release rate occurs.

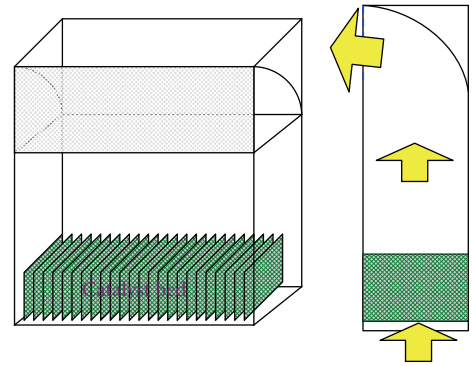

Figure 13: Schematic of a typical PAR [9].

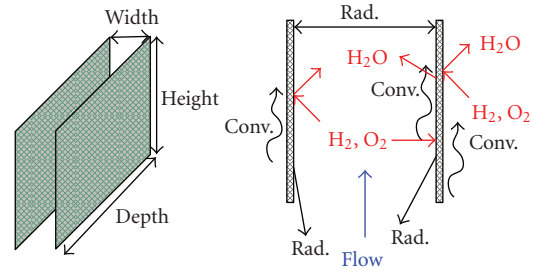

Figure 14: Physics phenomena in the catalyst flow channel [10].

3. Recombiner CFD Model

3.1. Passive Autocatalytic Recombiner. A passive autocatalytic recombiner consists of a vertical channel and a stack equipped with a catalyst bed in the lower part, as presented in Figure 13. In the case of severe accidents, the catalyst is in contact with the gas mixture of the containment. Hydrogen reacts with oxygen at the catalyst surface and generates steam, as indicated in Figure 14. The reaction heat released at the catalyst surface causes a buoyancy-induced flow which increases the inflow rate and thereby feeding the catalyst with a larger amount of hydrogen that ensures high efficiency of recombination. The buoyancy-driven circulation ensures a continuous gas supply to the PAR [2]. The catalyst sheets can be heated up to 900 K or even higher; so, considerable amount of heat is also transferred from the catalyst to the environment by heat radiation.

Left in Figure 14 shows a typical channel between two catalyst sheets. For small and medium recombiners of Siemens type, both height and depth are about 15 cm. The width of flow channel is less than 1 cm. In the PAR, the gas velocity, u, is in the magnitude of 1 m/s. The gas temperature could vary from 300 K to 700 K. Assuming the gas in the PAR is dry air, the Reynolds number of the flow between the catalyst sheets is $\mathrm{Re} = 2\,ud/v = 400 \sim 1250$. The flow is considered as a laminar flow in the channel.

3.2. Model Development. A two-dimensional PAR model is developed to simulate the flow in the channel, the heat transfer between the catalyst sheet and gas flow, the heat

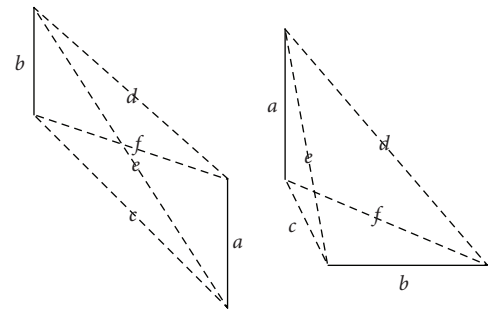

$$X_{a,b} = \frac{e + f - (c + d)}{2a}$$

Figure 15: View factor of parallel and perpendicular plates.

conduction in the catalyst sheet and the chemical reaction on the catalyst surface. The variation of flow velocity, temperature and gas concentration in the depth direction is then neglected. The continuity equation, Navier-Stokes equation, and energy equation are coupled and solved with the SIMPLE algorithm. The Boussinesq assumption is applied to consider the buoyancy caused by heatingup. Since the flow is laminar, no turbulence model is utilized in the present model. For the radiation heat transfer, the emissivity and absorption ratios of the catalyst sheet are assumed to be one. The view factor can be easily obtained for the parallel and perpendicular plates in a two-dimensional model, as indicated in Figure 15. An environment temperature is assigned at the inlet and outlet of the channel to calculate the radiation heat transfer between the catalyst and the environment. The effect of steam in the heat radiation is currently not considered in this model. In the catalyst plate two-dimensional heat conduction is simulated. It was observed that the temperature difference can be neglected in the normal direction of catalyst plate surface. It can be concluded that one-dimensional heat conduction will be enough.

Besides the basic equations, the concentration equations (1) are solved for all the gas species except for nitrogen

$$\rho u \frac{\partial c_i}{\partial x} + \rho v \frac{\partial c_i}{\partial y} = \rho D_i \left(\frac{\partial^2 c_i}{\partial x^2} + \frac{\partial^2 c_i}{\partial y^2} \right) + S_{\rho,i}. \quad (1)$$

A one-step reaction model developed by Ikeda et al. [11] is applied to simulate the chemical reaction on the catalyst surface

$$H_2 + \frac{1}{2} O_2 \longrightarrow H_2O \quad (2)$$

with

$$\dot{R} = 14 \phi_{H_2} \exp\left(- \frac{3580}{R \cdot T} \right). \quad (3)$$

In (3), the gas temperature in the cell next to the catalyst surface is applied in order to avoid an extremely high reaction rate. Based on the reaction rate obtained from (3), the source term for the energy and species equation can be easily calculated.

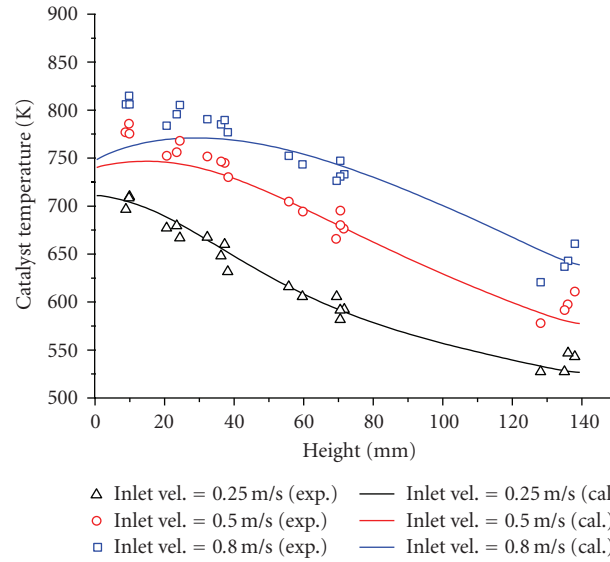

Figure 16: Catalyst temperature, model prediction versus experiment.

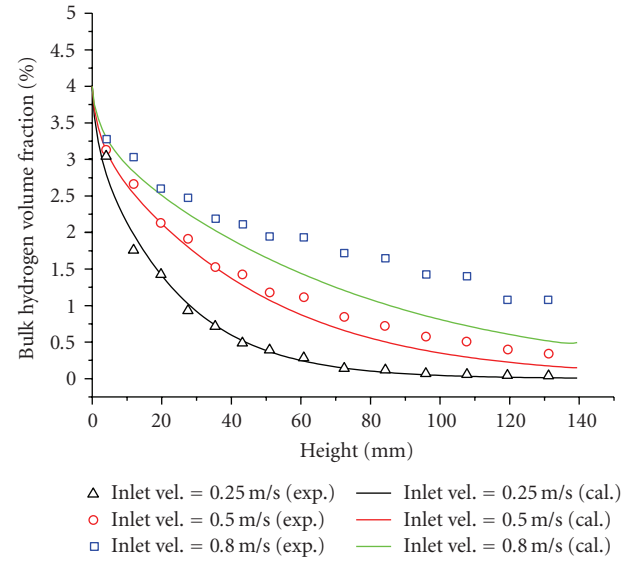

Figure 17: Average hydrogen concentration in the flow channel, model prediction versus experiment.

3.3. Model Validation. The REKO-3 experiment results [9] are utilized to validate the model. REKO-3 experiments are conducted by Forschungszentrum Juelich, Germany. The test section of the REKO-3 facility consists of four catalyst sheets forming three flow channels. The facility provides the measurement of catalyst temperature and gas concentration at different heights. Experiment results are obtained at different inlet velocities.

Figures 16 and 17 compare the numerical results with the experimental data under three inlet velocities. The hydrogen volume fraction at the inlet is 4% in all cases. Among all

the cases, the model gives the best prediction at lowest inlet velocity (0.25 m/s). A clear deviation of the catalyst temperature near the inlet is observed for other two cases. An increasing catalyst temperature leads to a significant heat loss from the catalyst to the environment, especially for the inlet neighborhood where both the temperature and the view factors to the environment are high. The deviation of the catalyst temperature can be minimized by optimizing the environment temperature and by setting the exact emissivity and absorption ratio of the catalyst material. In the cases where the inlet velocity is 0.5 m/s and 0.8 m/s, an overestimation of recombination by the model is observed. This could be caused by overestimating the chemical reaction rate on the catalyst or by overpredicting the mass transfer to the catalyst. Generally, the model gives satisfactory prediction of the experiment results.

4. Conclusion

The hydrogen analysis with the CFD code GASFLOW is conducted to investigate the effect of spray modes on hydrogen risk in the Qinshan-II NPP containment during a large break loss of coolant accident (LBLOCA). The direct spray sharply depresses the pressure and temperature in the containment and reduces the heat transfer from the atmosphere to the structures. However, the direct spray mode (case A) is still not capable of controling the pressure and gas temperature during the accident due to the strong release of hot steam after the shutdown of the direct spray. A considerable evaporation of the recirculation spray water is observed. Compared with Case A, the enhancement of the condensation on the structures is also observed during the recirculation spray (case B). Because the evaporation induced by the recirculation spray is generally stronger than the enhancement of surface condensation, the steam inventory inside the containment is increased due to the recirculation. During the hydrogen release peak, a chaotic mixing flow field is produced by the recirculation spray, while a regular natural convection flow forms in the other two cases. From the aspect of hydrogen safety, the direct spray increases the global hydrogen concentration and the maximum sigma volume, but does not prevent the stratification. The recirculation spray does not increase the global hydrogen concentration inside the containment and promotes mixing, but can increase the local hydrogen concentration near the hydrogen release source. The effects of the containment spray on the PAR performance are found to be minor.

A CFD recombiner model is developed in order to provide more detailed insights into the process along the catalyst sheets. The model is validated with the data from the REKO-3 experiment [9] and gives satisfactory prediction. Further work is needed to develop a full recombiner model by incorporating the chimney part. For implementation of the CFD PAR model in containment analysis, appropriate boundary conditions are needed at the inlet of the PAR.

Nomenclature

c_i: Mass fraction of ith gas species
D_i: Diffusion coefficient of ith gas species, m^2/s
d: Gap width between two catalyst plates, m
R: Universal gas constant, J/(mol-K)
$\dot{R}$: Reaction rate, mol/(m^3-s)
Re: Reynolds number
$S_{\rho,i}$: Mass source term of ith gas species per unit volume, kg/(m^3-s)
T: Temperature, K
u: Velocity in x direction, m/s
v: Velocity in y direction, m/s
ρ: Gas density, kg/m^3
ϕ_{H_2}: Hydrogen molecular concentration, mol/m^3
υ: Kinetic viscosity, m^2/s

Acknowledgments

The authors would like to thank National Basic Research Program of China (no.2007CB209800) for providing the financial support for this study. The authors would also like to thank the experts from FZK GASFLOW group for their kind help.

References

[1] J. R. Travis, J. W. Spore, P. Royl, et al., "GASFLOW: a computational fluid dynamics code for gases, aerosols, and combustion," Vol. 2, User's Manual, LA-13357-MS, FZKA-5994, October 1998.

[2] E. Bachellerie, F. Arnould, M. Auglaire, et al., "Generic approach for designing and implementing a passive autocatalytic recombiner PAR-system in nuclear power plant containments," *Nuclear Engineering and Design*, vol. 221, no. 1–3, pp. 151–165, 2003.

[3] T. Zhang, et al., "Operation manual of nuclear power plant," Nuclear Power Qinshan Joint Venture Company Ltd., 2005.

[4] J. R. Travis, J. W. Spore, P. Royl, et al., "GASFLOW: a computational fluid dynamics code for gases, aerosols, and combustion," Vol. 1, Theory Manual, LA-13357-MS, FZKA-5994, October 1998.

[5] J. Malet, L. Blumenfeld, S. Arndt, et al., "Sprays in containment: final results of the sarnet spray benchmark," in *Proceedings of the 3rd European Review Meeting on Severe Accident Research (ERMSAR '08)*, pp. 1–19, Nessebar, Bulgaria, September 2008.

[6] P. Royl, H. Rochholz, W. Breitung, J. R. Travis, and G. Necker, "Analysis of steam and hydrogen distributions with PAR mitigation in NPP containments," *Nuclear Engineering and Design*, vol. 202, no. 2-3, pp. 231–248, 2000.

[7] OECD/NEA, "SOAR on Containment Thermalhydraulics and Hydrogen Distribution," Tech. Rep. CSNI-R99-16, OECD Nuclear Energy Agency, Nuclear Safety, Paris, France, June 1999.

[8] S. B. Dorofeev, M. Kutznetsov, V. Alekseev, A. A. Efimenko, and W. Breitung, "Evaluation of limits for effective flame acceleration in hydrogen mixtures," Report IAE-6150/3, Kurchatov Institute, Moscow, Russia, 1999.

[9] E. A. Reinecke, J. Boehm, P. Drinovac, S. Struth, and I. M. Tragsdorf, "Numerical and experimental investigations on catalytic recombiners," in *Proceedings of the 13th International Conference on Nuclear Engineering (ICONE '05)*, Beijing, China, May 2005, ICONE 13-50267.

[10] M. Heitsch, "Fluid dynamic analysis of a catalytic recombiner to remove hydrogen," *Nuclear Engineering and Design*, vol. 201, no. 1, pp. 1–10, 2000.

[11] H. Ikeda, P. A. Libby, F. A. Williams, and J. Sato, "Catalytic combustion of hydrogen—air mixtures in stagnation flows," *Combustion and Flame*, vol. 93, no. 1-2, pp. 138–148, 1993.

Hindawi Publishing Corporation
Science and Technology of Nuclear Installations
Volume 2009, Article ID 759878, 13 pages
doi:10.1155/2009/759878

Project Report

GASFLOW Validation with Panda Tests from the OECD SETH Benchmark Covering Steam/Air and Steam/Helium/Air Mixtures

Peter Royl,[1] John R. Travis,[1] Wolfgang Breitung,[1] Jongtae Kim,[2] and Sang Baik Kim[2]

[1] *Forschungszentrum Karlsruhe, Institut für Kern- und Energietechnik, 76021 Karlsruhe, Germany*
[2] *Division of Thermal-Hydraulics and Safety Research, Korean Atomic Energy Research Institute, Yseong, Daejeon 305-353, South Korea*

Correspondence should be addressed to Peter Royl, royl@iket.fzk.de

Received 19 November 2008; Revised 2 March 2009; Accepted 22 April 2009

Recommended by Walter Ambrosini

The CFD code GASFLOW solves the time-dependent compressible Navier-Stokes Equations with multiple gas species. GASFLOW was developed for nonnuclear and nuclear applications. The major nuclear applications of GASFLOW are 3D analyses of steam/hydrogen distributions in complex PWR containment buildings to simulate scenarios of beyond design basis accidents. Validation of GASFLOW has been a continuously ongoing process together with the development of this code. This contribution reports the results from the open posttest GASFLOW calculations that have been performed for new experiments from the OECD SETH Benchmark. Discussed are the steam distribution tests 9 and 9bis, 21 and 21bis involving comparable sequences with and without steam condensation and the last SETH test 25 with steam/helium release and condensation. The latter one involves lighter gas mixture sources like they can result in real accidents. The helium is taken as simulant for hydrogen.

1. Introduction

The CFD code GASFLOW solves the time-dependent compressible Navier-Stokes Equations with multiple gas species [1]. It models two-phase effects of condensation and/or vaporization in the fluid mixture region with the assumption of the homogeneous equilibrium (HEM) model, two-phase heat transfer to and from walls and internal structures by convection and mass diffusion, and the chemical kinetics of hydrogen combustion with general ignitor models and catalytic recombination. The code is applied in the 3D analysis of steam/hydrogen distribution in various PWR containments to simulate scenarios of beyond design basis accidents. Validation of GASFLOW with thermal hydraulic experiments that simulate such scenarios or some of their aspects is an ongoing effort with involvement of all members of the GASFLOW users group, which comprises industrial and research partners. GASFLOW successfully participated in the blind and in the open posttest analysis of the international standard problem ISP47 [2]. The OECD Panda SETH experiments and their results, which are accessible to members of the funding countries, have further widened the database for predicting such containment-related severe accident scenarios. The tests were designed by the Swiss Paul Scherrer Instiute and performed in their Panda facility [3]. GASFLOW analyses of some of these tests have been jointly made by the Korean Atomic Energy Research Institute (KAERI) and by Forschungszentrum Karlsruhe. This contribution will report the results from the open posttest GASFLOW calculations that have been performed for the steam distribution tests 9 and 9bis, 21 and 21bis involving comparable sequences without and with steam condensation and for the latest Panda SETH test 25 with steam/helium release and condensation. The latter one involves lighter gas mixture sources like they can result in real accidents. The helium is taken as the simulant for hydrogen. Figure 1 shows one of the 3D cartesian GASFLOW facility models applied in the analysis of these tests.

2. Simulated Panda Seth Tests

The OECD SETH project has initiated a series of 25 tests in the two rooms DW1 and DW2 of the large-scale

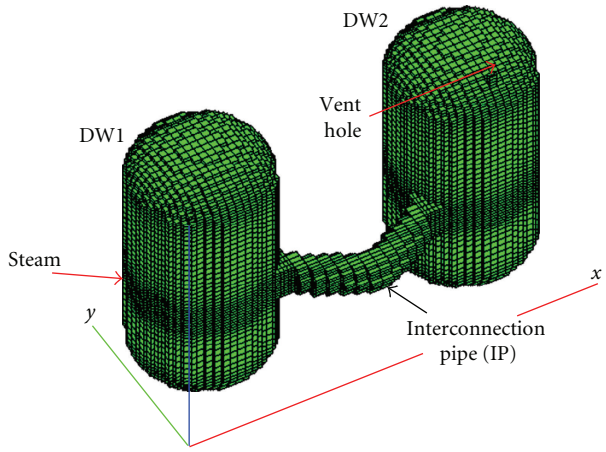

Figure 1: Fine 3D model of the Panda facility.

thermal hydraulic facility Panda to simulate mixing and stratification phenomena in a larger multicompartment gas volume approaching the dimension of actual containment compartments. Figure 2 gives an overview of the 6 experiments from this series that were simulated with GASFLOW. The two vessels DW1 and DW2 have the same volume of 90 m^3 each and are all initially filled with dry air. A feeding vessel DW1 is connected to the receiving vessel DW2 through a bended pipe with a large diameter. In all analyzed tests except test 25 a vent hole was active in the dome of DW2 that maintained a constant pressure of 1.3 bar. Tests 9 and 9bis investigated the spreading of a buoyant steam plume over these two compartments that resulted from a low-velocity horizontal injection into the lower region of DW1. Tests 21 and 21bis investigated the spreading from an axial steam injection high in the dome of DW1. Tests 9 and 21 were run with higher steam temperatures. The whole facility was preheated to a high-enough temperature to suppress steam condensation. Tests 9bis and 21bis were run in a less-preheated facility with a lower steam temperature that allowed for steam condensation. The 9 and 21 series tests all applied the same constant rate of steam injection of 14 g/s. They are well suited for testing condensation models currently implemented in CFD codes. The test facility is insulated but can absorb heat with its heat capacity. Test 25 is the final test from the SETH series. It simulated a sequence of steam/helium injections into the air-filled facility initially at room temperature [4]. The gas spreads into a dead end vessel DW2 because the vent valve in DW2 is closed. Gas venting in test 25 occurs through a vent pipe in DW1 below the source and interconnecting pipe. This vent pipe connects to the large wet well (WW) volume. The vent pressure in this test is recorded. It rises monotonically with time and can be applied as a pressure boundary condition in the analysis instead of the constant vent pressure in DW2. In test 25 only the pressure but not the volume flow rates at the entrance to the vent pipe could be measured. The problem times to analyze the 9 and 21 series tests were 7000 seconds. Test 25 involved two equally long phases of 7200 seconds with a steam/helium injection in phase 1 followed by a pure steam injection in phase 2. The total problem time to analyze for this test is 14400 seconds.

3. Gasflow Models of the Test Facility

The facility has been simulated in coarse (13 000), fine (115 000), and extremely fine (365 000) 3D Cartesian meshes (Figure 3). A fine mesh with 115,351 cells was developed with a smaller number of blocked cells (orientation I). The source had to be split up into equal x and y components with this mesh to achieve the proper injection angle of 45 degrees because the steam injection was not on the x-coordinate axis. The coarse model for orientation II simulated the injection along the x-axis. It had 24,180 cells with nearly equidistant xyz meshes of 33 cm and a higher fraction of blocked cells. The finest grid model for orientation II had 365,040 cells with fine axial grid sizes of 5 cm between the injection location and the horizontal sensor plane at 380 cm and fine xy meshes of 5 cm on the source side of DW1. Good agreement with the test data was found with all meshes. Comparisons showed that neglecting the bend of the connection pipe and modeling a straight pipe with a length of 5 m between the vessels has no strong impact on the results. To economize on the CPU time we then ran most tests with the straight pipe model which allows to simulate the tests with only 13,182 numerical cells of nearly equidistant meshes of 33.33 cm. For the studied tests, coarse and fine meshes gave quite good overall results as long as condensation did not come into play. With condensation we obtained nearly mesh independent overall results when the heat transfer with the applied wall functions was enhanced in the ratio of the coarse and fine wall mesh. Analysis of test TH13 from ISP47 showed a similar agreement when going from a fine to a coarse mesh with this type of wall function adjustment. The large fractions of structure surfaces in the facility, that have mostly stagnant flow conditions during the test justifies this enhancement. Like in all other CFD codes that apply wall functions to avoid resolving the boundary layer there is still a need for a wall function formulation that gives a mesh-independent heat transfer in the transition to stagnant flow conditions. The automatic wall function option in CFX could not be demonstrated as a solution so far in problems involving steam condensation. GASFLOW applies a specific set of wall functions together with an explicit setting for no slip conditions on all structures. But these wall functions are also largely valid for forced flow conditions only. All injections are simulated from a source reservoir with a single cell with a single injection node. The structure model simulates the heat capacity of a 2 cm steel vessel that is insulated with a 20 cm layer of rock wool on the outside with one-dimensional heat conduction and adiabatic boundary conditions using 44 heat conduction nodes. An area balance prior to the simulation adjusts the surface of the stair-stepped Cartesian model to the specified facility data. A first-order time integration and a second-order (van Leer) advection scheme is applied and the use is made of the standard k-e turbulence model in all simulations. Table 1 gives an overview of the analyzed tests, the key test parameters, and the applied meshes.

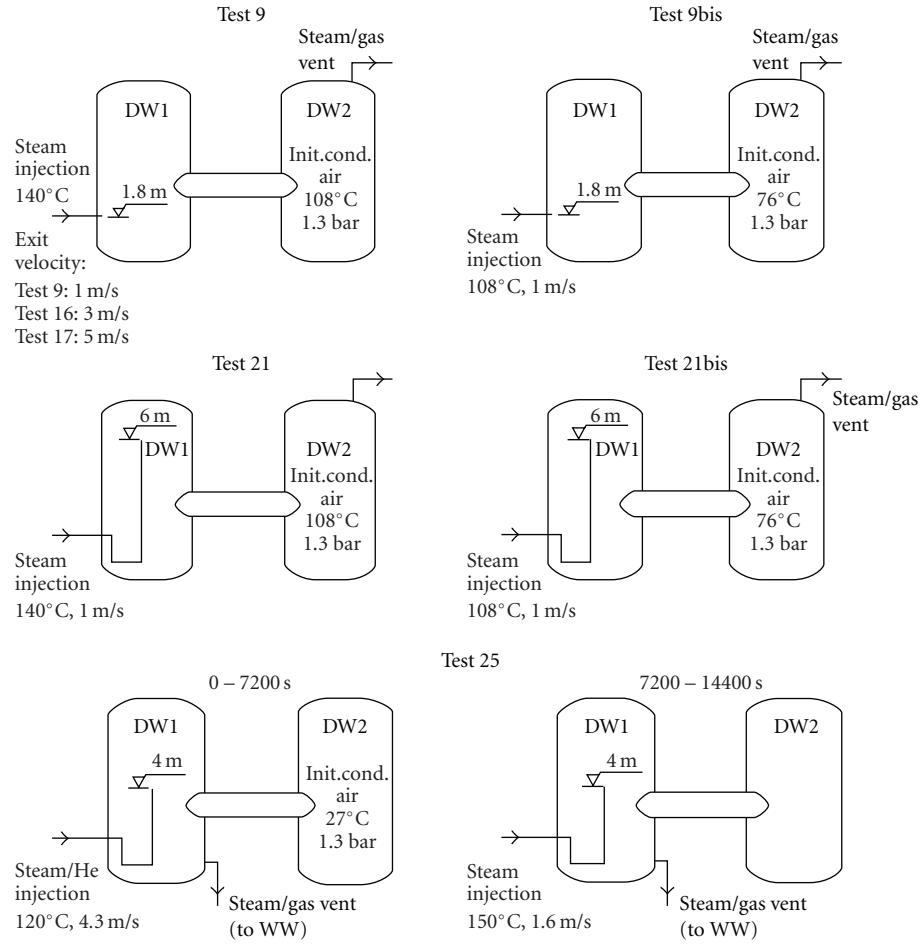

Figure 2: SETH tests analyzed with GASFLOW.

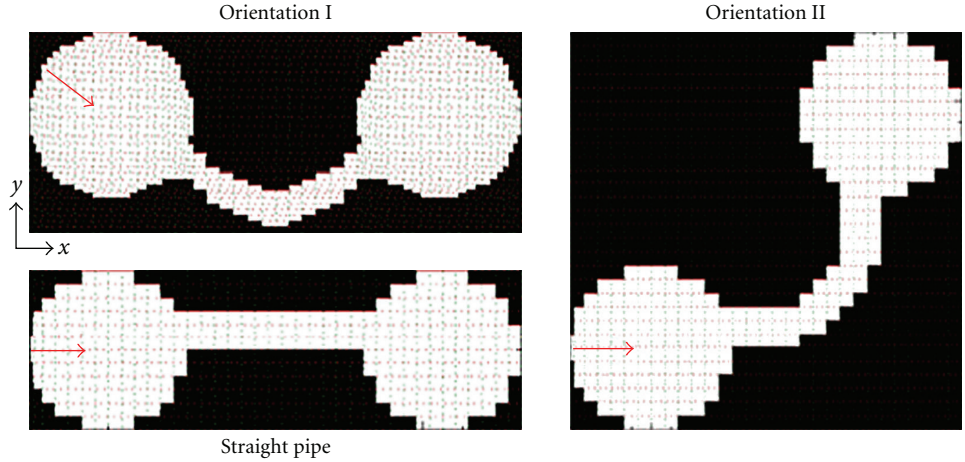

Mesh	Orientation	Cells
Coarse	I	15,392
	II	24,180
	Straight pipe	13,182
Fine	I	115,351
Finest	II	365,040

Figure 3: Applied horizontal meshes.

Table 1: SETH test parameters and GASFLOW facility models.

test	To vessel [C]	Model	steam source [g/s]	Helium source g/s	inj. velocity [m/s]	steam Temp. [C]	Steam condensation	Problem Time [S]
9	108	coarse	14	—	1	140	no	7000
		str. pipe						7000
		fine						4000
		finest						250
9bis	76	coarse	14	—	1	108	yes	7000
		str. pipe						7000
		fine						4000
		finest						250
21	108	str. pipe	14	—	1	140	no	7000
21bis	76	str. pipe	14	—	1	108	yes	7000
25	27	str. pipe	64	8	4.3	120	yes	14400

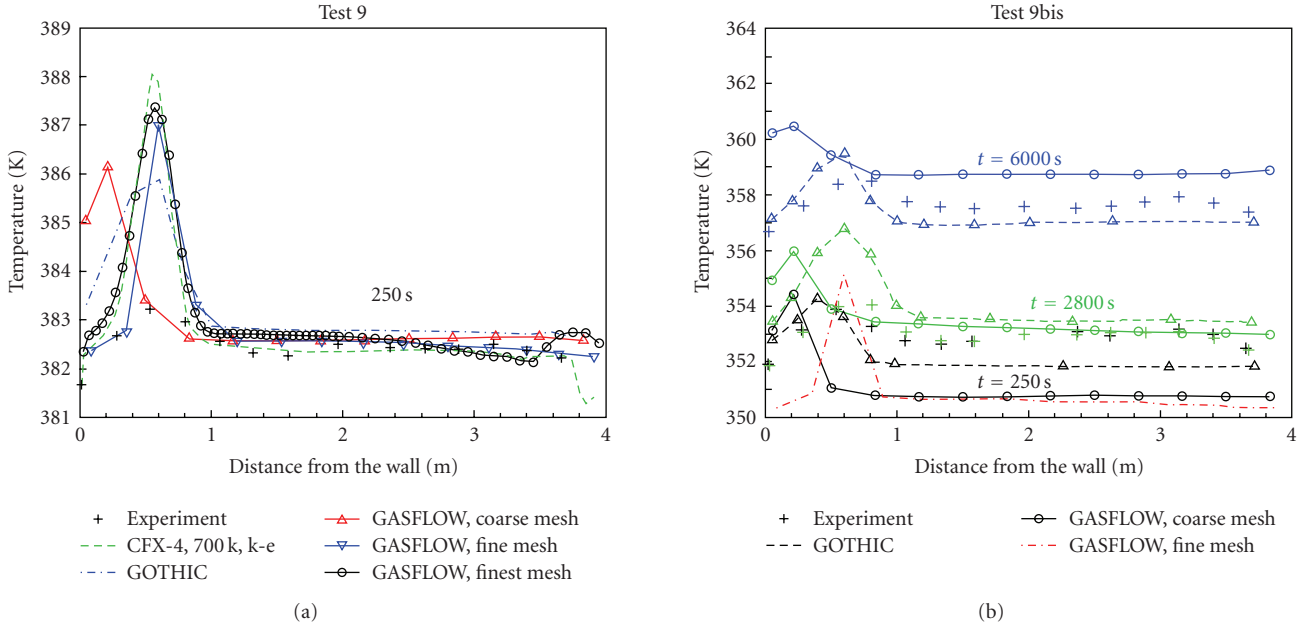

Figure 4: Horizontal temperature profiles 2 m above injection jet.

4. Results

4.1. Tests 9 and 9bis. The fine and finest mesh simulations of these tests all adapted the mesh to make the faces of the feeding cells for the horizontal buoyant plume to match the area of the injection orifice to inject the steam with its correct injection momentum. In test 9 with the finest mesh the horizontal temperature profile 2 m above the injection location (Figure 4) shows the same location and height of the peak at 250 seconds as the CFX-4 simulation with the finest mesh of 700,000 cells. Calculations with a coarse GOTHIC model with 26,000 cells give about the same peak location but lower peak temperatures [5–7]. The coarse mesh GASFLOW model injects with a too low injection momentum and gives the peak closer to the wall with similar peak temperatures as GOTHIC. More mixing of the momentum, mass, and energy occurs in the coarser mesh. So far all CFD analyses of test 9 predict higher than measured peak temperatures at the comparison point. The reasons for this are not yet understood. Condensation does not affect modeling of test 9 in any calculation. Some influence could come from radiation cooling of the hotter steam plume, which was not accounted for in any calculation. The measured temperature peaks from test 9bis at 250 seconds are better predicted. Over predictions are again seen around 2800 and 6000 seconds. The tail values outside the peak are in better agreement than the peaks.

In the early test phase the results with the fine and coarse mesh showed significant differences in the velocity profiles. But these did not alter the overall convective flow between the two test vessels, because local mesh effects generally smeared out during the deflection of the buoyant flow in the dome region. The axial profiles of the steam concentrations along

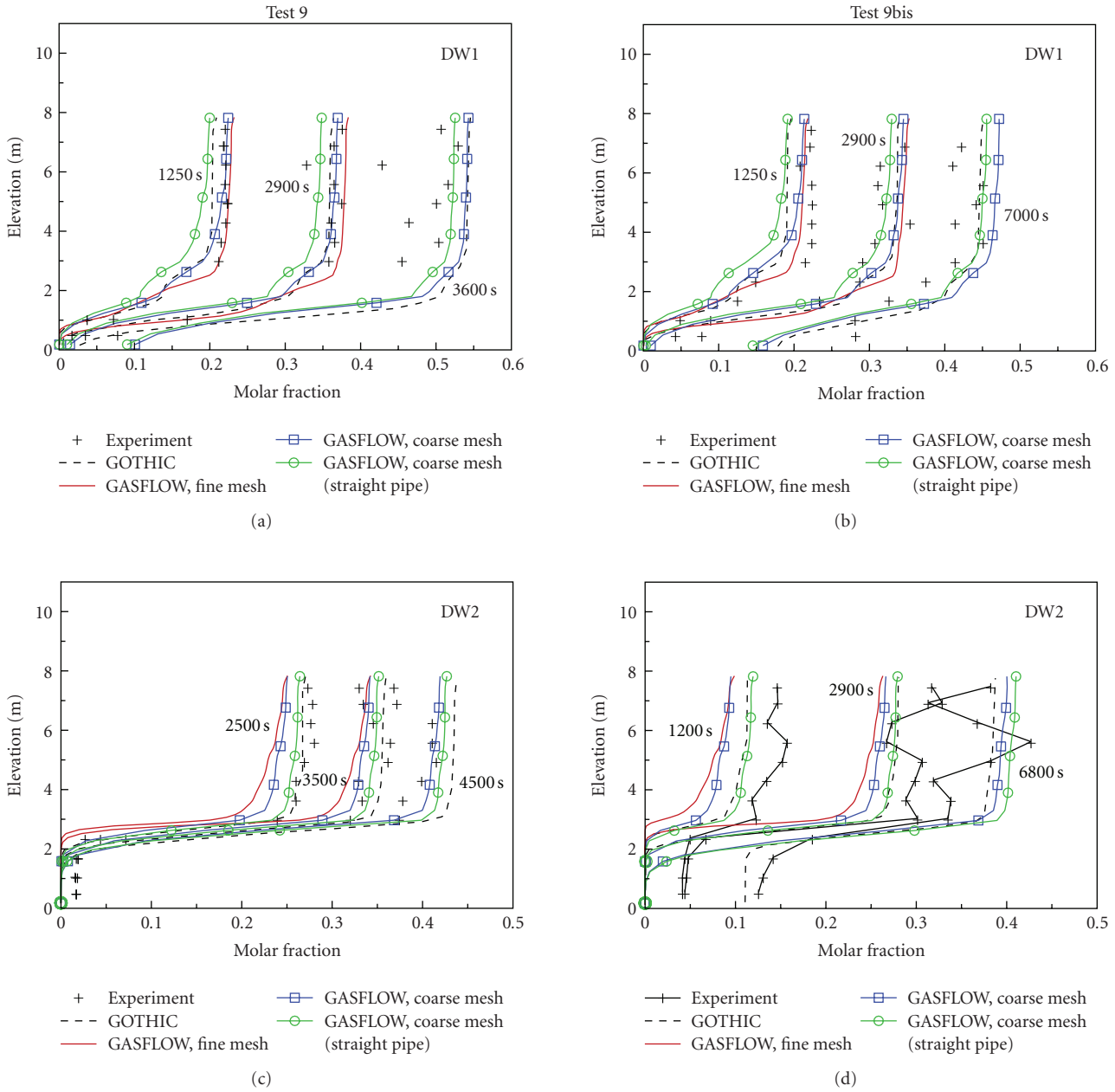

Figure 5: Axial steam concentration profiles in the centerline of DW1 and DW2.

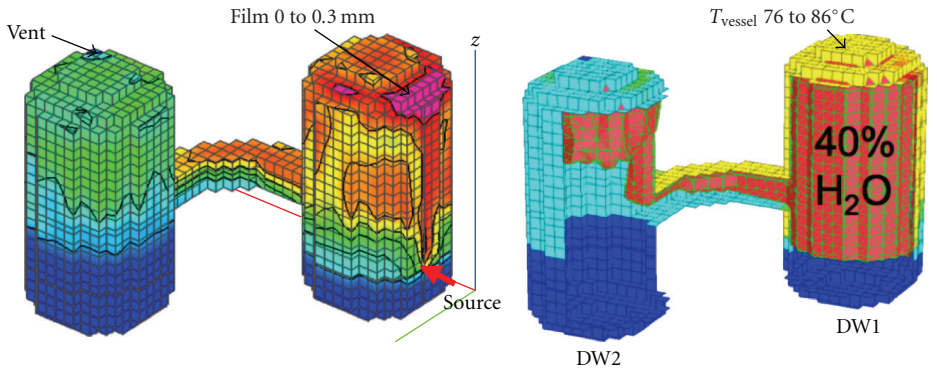

Figure 6: Test 9bis final condensate film, steam cloud, and vessel temperature (7000 seconds).

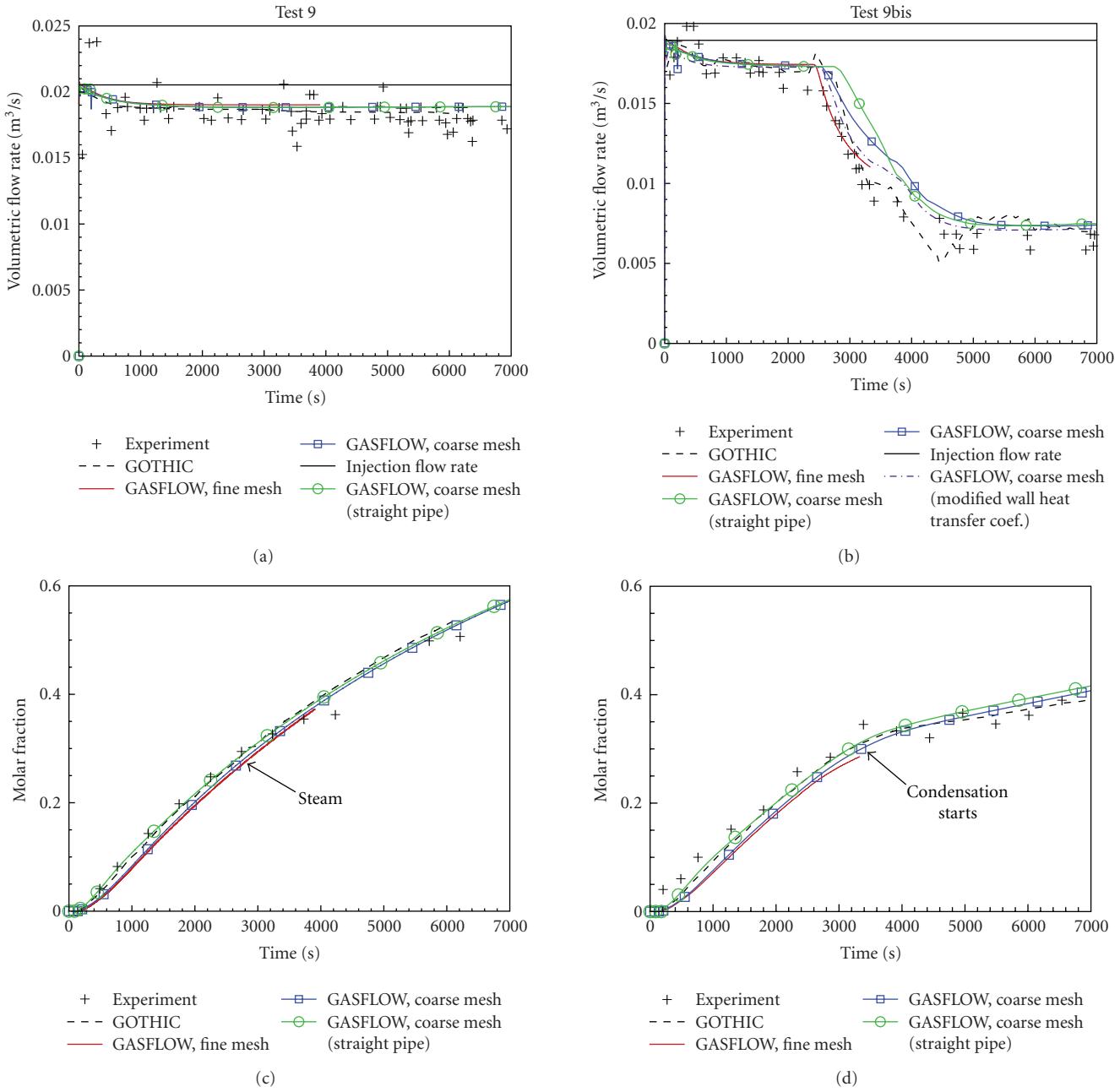

Figure 7: Volume rate and steam concentration at the vent (test 9 and 9bis).

the centerline of DW1 and DW2 (Figure 5) show acceptable agreements with the test data. The straight pipe model gives a little more spreading into DW2 with lower concentrations in DW1. The results for the coarse and fine mesh model with the bended connection pipe are closer. Test 9bis with steam condensation shows higher steam concentrations near the bottom of the facility. They are likely to originate from the vaporization of a draining film into the dry air region below the steam cloud [5]. GASFLOW only simulates a static film and shows no film in DW2 below the connection pipe in the final snap shot with the coarse 3D model (Figure 6) that also gives the 40% steam cloud together with the more elevated vessel temperature in the regions with higher steam concentrations.

The recorded volume flow rates at the vent in DW2 rapidly reduce over the inlet flow to some plateau values that reflect the cooling of the injected steam by mixing with air (Figure 7). A further decay to a second plateau occurs in test 9bis after onset of condensation around 3000 seconds. This plateau is controlled by the constant pressure of 1.3 bar at the vent and predicted well. Thermodynamically this pressure enforces a quasistationary condensation rate with saturated conditions. But the transition to the second plateau is too slow with the coarse model while the fine mesh

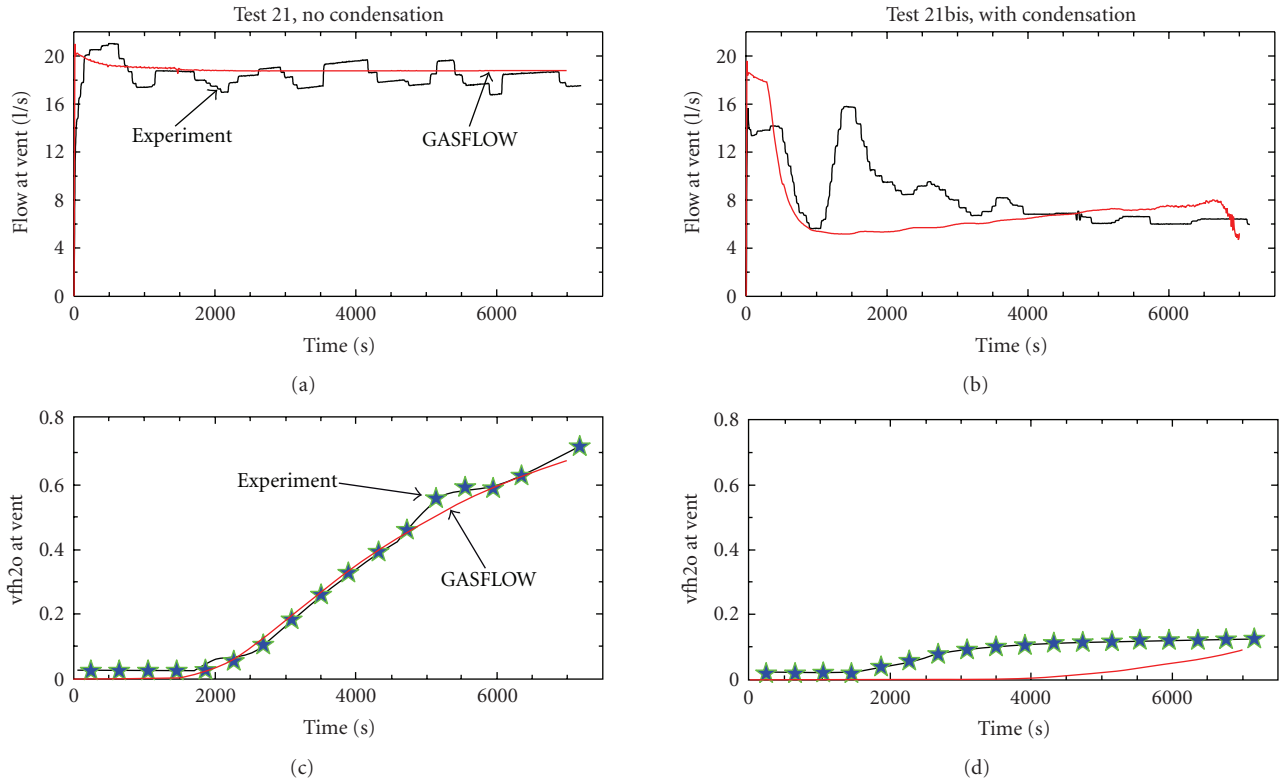

Figure 8: Volume rate and steam concentration at the vent (test 21 and 21bis).

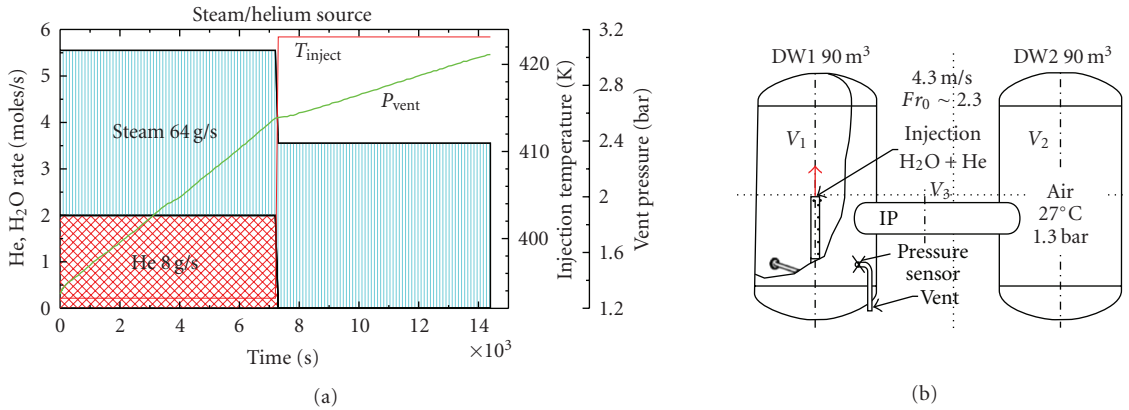

Figure 9: Source and boundary conditions for test 25.

results follow the test data more closely. The transition in the coarse mesh simulation in which the heat transfer was enhanced by the ratio of the coarse and fine wall mesh (factor 2) falls right on the result of the fine mesh. The measured steam concentration at the vent (lower graph in Figure 7) is well predicted in GASFLOW with the coarse and fine meshes. It shows similar initial increases and a pronounced slowing down of the growth in test 9bis after condensation onset. Calculated steam distributions in DW1, in the interconnection pipe, and in DW2 show a somewhat better agreement for the coarse models with the bended versus the straight pipe. But from the tendency both models capture the correct phenomenology.

4.2. Tests 21 and 21bis. The GASFLOW simulation of test 21 with the straight pipe model also gives excellent predictions for the volume rates and steam concentrations at the vent in DW2 (Figure 8) in particular for the time of steam arrival. With the direct impingement of steam in the dome condensation in test 21bis comes very early and the volume rates reduce more rapidly than in test 9bis. Only the regular wall functions were applied and no special model was available to simulate the heat and mass transfer from the impinging steam jet. Steam condensation heats up the dome, and the volume rate at the vent valve goes through a minimum when the dome structure is saturated and cannot condense so much steam anymore.

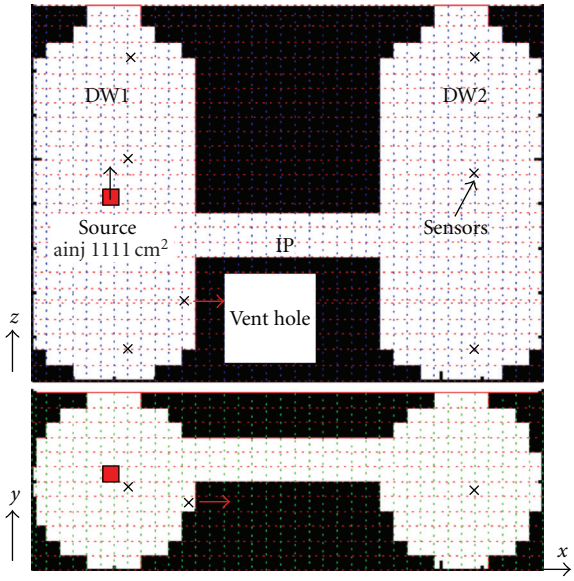

Figure 10: 3D Cartesian GASFLOW model of the Panda SETH facility for analysis of test 25 (straight pipe model).

After this, GASFLOW predicts it to rise only gradually as the steam cloud propagates into the vessel regions below the larger dome surface. Initially the test data show a similar behavior but then rise again shortly to an intermediate peak before they decay to similar rates as calculated in GASFLOW. Andreani [5], Paladino [4] attribute this peak to an additional volume source from the vaporization of the condensate film draining on the preheated structures into regions with dry air. This interpretation is consistent with the earlier steam arrival in the test relative to the much later arrival predicted in GASFLOW, which does not model a moving film. The final steam concentration from GASFLOW at 7000 seconds approaches the test data well. The quasistationary condensation then reflects the thermodynamic boundary condition set by the vent valve pressure. The late drop of the volume flow in test 21bis after 6500 seconds marks the onset of condensation in DW2 where the steam concentration eventually exceeds the limit for condensation.

4.3. Test 25. The steam/helium distribution test 25 investigates the distribution of light gas mixtures with condensing steam in air over two rooms with a dead end like it can occur in containment rooms in severe accidents [8]. Figure 9 gives the applied steam/helium source and the pressure boundary in this test with an axial injection near the mid height of DW1. The initial injection velocity is 4.3 m/s. Injection starts with a Froude number of 2.3, which is characteristic for a rising plume whose buoyancy dominates over the injection momentum already at short distance from the source. The vent is located in the lower region of DW1 far below the injection source and the interconnection pipe (IP). GASFLOW uses a pressure boundary condition at the location of this vent with the recorded monotonic increase of the pressure from Figure 9.

Figure 10 shows the Cartesian model with the straight interconnection pipe that was used in the calculation. A refinement at the top also simulates the man-hole region. The coarse model uses 12,300 cells ($39\,x$, $13\,y$, and $28\,z$ nodes) and simulates the total free gas volume of 180 m^3 with an average cell volume of 32 liters. The interconnection pipe is simulated three dimensionally with a cross section of 3×3 cells. The red arrow marks the location of the vent hole where the pressure boundary condition from Figure 9 was applied. The red box gives the location of the injection cell. The source gas is injected from a sealed-off reservoir cell in the 3D fluid mesh with a time-dependent steam/helium composition using a velocity boundary condition at the open feeding side on the top of the source cell. GASFLOW has an option to reduce the area of the feeding source cell to inject with the correct injection momentum. But the cell surface of 1111 cm^2 in the coarse mesh is much larger than the 314 cm^2 cross section of the 20 cm injection pipe. The use of this option introduced a too strong air entrainment into the fluid cell right above the source. This diluted the steam/helium mixture close to the source and the concentration of the helium layer built up from steam condensation in the dome did not reach the measured high level. For the buoyancy dominated plume rise in this experiment it turned out better to use the cell face from the coarse mesh without the area reduction and neglect the error from a too low injection momentum.

Figure 11 compares the calculated and measured helium concentrations in the dome, middle and low regions of DW1 and DW2 (locations see Figure 10). The two variations apply the mesh face of 1111 cm^2 (solid line) and the reduced area of 314 cm^2 (dashed). The initial helium volume fraction in the source gas is 36%. As the source plume rises to the dome, steam condenses on the cold vessel, which increases the helium volume fraction. More and more helium accumulates in the dome and builds up a stratified high-concentration helium layer that isolates itself and prevents the further addition of source gas and energy from below. The stratified layer is not affected when the steam/helium/air mixture below flows over into DW2 after 2000 seconds, which temporarily reduces the helium volume fraction in the middle region of DW1. Too much air entrainment due to the local reduction of the cell area prevented the buildup of this layer and gave more mixed concentrations in the middle and upper region of DW1. It also caused a faster increase of the helium concentration in DW2. The gas flowing over into DW2 has already a reduced steam content and nearly all steam that is brought into the cold DW2 condenses. This builds up another low-density self-insulating high-concentration helium layer also in DW2 that is even thicker than in DW1 with almost the same helium concentrations in the dome and middle region. The switch to a pure steam injection after 7200 seconds has nearly no impact on the stratified layers. They are predicted to remain stable throughout the analysis. The steam only dilutes the helium concentration in the middle region. GASFLOW predictions without the area reduction are in very good agreement with the test data. The temporarily higher concentration

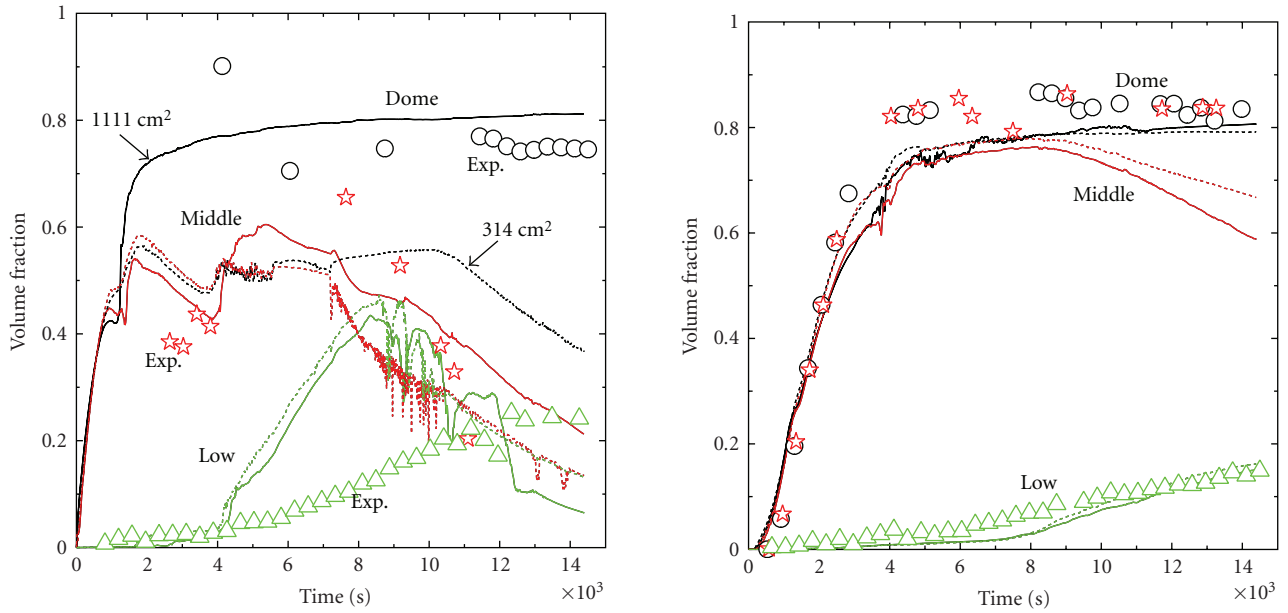

Figure 11: Helium concentrations (a) DW1 and (b) DW2 in test 25.

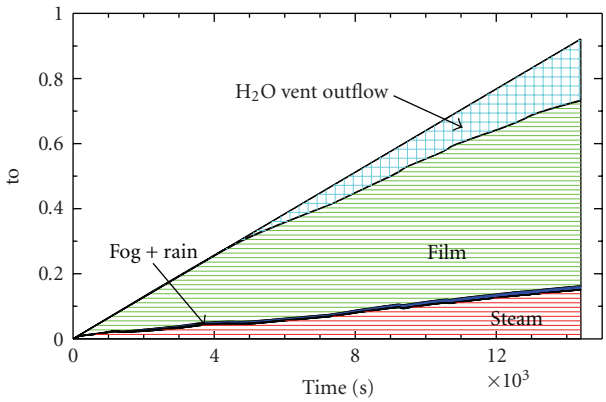

Figure 12: Mass balance of water and steam for test 25.

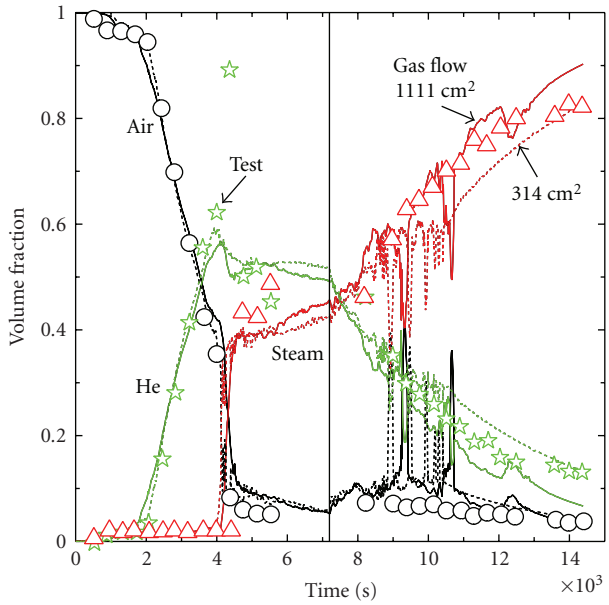

Figure 13: Gas concentrations test 25 at the vent.

predicted in the lower region of DW1 indicates a stronger than measured helium increase that starts after 4000 seconds.

The high helium volume fraction developing in the stratified cloud has a too low density to be eroded from the heavier mixture with the released steam below. The THAI test HM2 during which a hydrogen cloud was gradually eroded from a steam release below [9] only had 35 volume % hydrogen and smaller density differences between the steam and the light gas cloud. The parametric handling of fog rainout from bulk condensation sensitively impacted on the erosion kinetics in the THAI test. Only small amounts of fog are predicted for test 25, most steam condenses as film on the structure. Figure 12 gives the H_2O mass balance for test 25. The steam loss at the vent pipe starts after about 4000 seconds. Film draining was not simulated in test 25. Like in most containment simulations it should have a small effect when the film drains on cold structures, which have a benign potential for film vaporization only. The conditions in test 21bis in which a film drains on a hot surface into dry air is quite different.

The measured concentrations of helium and steam at the vent pipe show helium to arrive 2000 seconds before any steam reaches this location (Figure 13). This earlier arrival of helium far below the injection location is well predicted. It is related to the fact that drying steam/helium/air mixtures on condensing surfaces initially gives locally higher dry

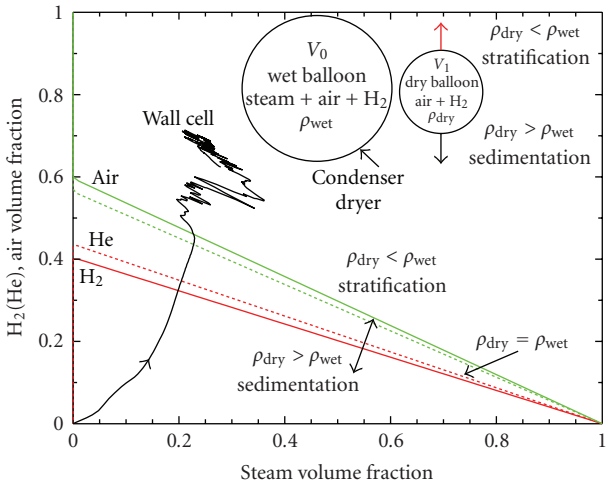

(a)

Equilibrium lines obtained from solving for ψ_{lg}

$$\frac{\rho_{wet}}{\rho_{dry}} = 1 = \frac{\left(\psi_{H_2O} * \mu_{H_2O} + \psi_{air} * \mu_{air} + \psi_{lg} * \mu_{lg}\right)}{\left(\left(\psi_{air}/\left(\psi_{lg} + \psi_{air}\right)\right) * \mu_{air} + \left(\psi_{lg}/\left(\psi_{lg} + \psi_{air}\right)\right) * \mu_{lg}\right)}$$

$\psi_{air} = 1 - \psi_{H_2O} - \psi_{lg}$
ψ = volume fractions
μ = molecular weights
lg = (H_2 or He), ρ = density

(b)

Figure 14: Thought experiment on density changes from drying steam/helium(hydrogen) mixtures.

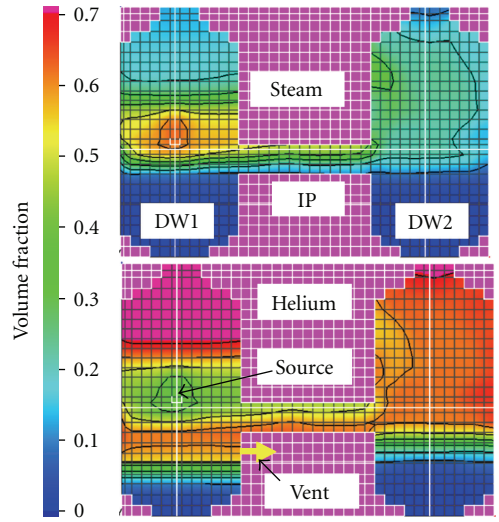

Figure 15: Steam and helium distribution in test 25 at 3700 seconds.

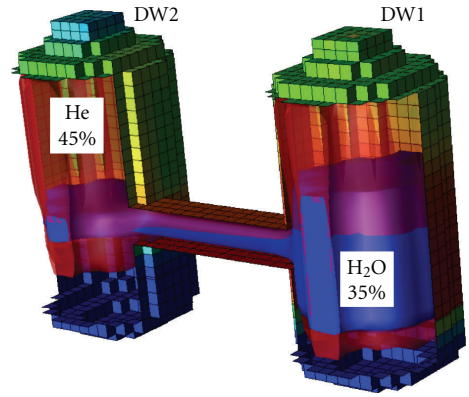

Figure 16: Steam and helium clouds in test 25 near end of helium injection (6600 seconds).

air/helium densities and causes a local down flow of the dried helium/air mixture next to the wall. As more and more helium is added the dried steam/helium/air mixtures become lighter. Then they rise and contribute to the stratified gas region. A negative buoyancy develops early in test 25. We call this the condensation sedimentation effect. It is of relevance for all containment applications, where increased hydrogen concentrations are eventually predicted in the lower region during most scenarios [8] because hydrogen release is limited to lower mixture concentrations than in test 25.

Figure 14 gives the regime map in which steam condensation out of a steam/helium/air mixture can result in a sedimentation (negative buoyancy) or stratification (positive buoyancy) depending on the mixture composition. The equilibrium line for which the dry and the wet mixture have the same density is derived from solving the quadratic correlation in Figure 14 for the light gas volume fraction ψ_{1g}. The correlation holds for drying under constant pressure and temperature condition. It does not depend on the pressure and temperature level. It says that a wet mixture with 20% steam, 32% hydrogen, and 48% air has the same density as the dried mixture, which then has 40% hydrogen and 60% air. The concentration development during test 25 in a near wall cell has been entered in Figure 14 with time advancing along the added arrow. It goes through an initial sedimentation phase followed by stratification after the helium/steam concentration crosses the 35/20% limit. The data from test 25 validate the predicted hydrogen sedimentation that has been questioned in earlier containment applications with GASFLOW.

During the steam release after 7200 seconds the helium concentration in Figure 13 reduces. The spikes that occur after 7200 seconds come from calculated backflows each time when the rising pressure at the vent exceeds the vessel pressure during a short time leading to a brief inflow of some air and a corresponding reduction in the steam and helium concentration. The steam released after 7200 seconds compresses the stratified helium clouds in DW1 and DW2. It cannot penetrate into the clouds with lighter gas, so their temperatures increase only slightly from the compression. Figure 15 gives more background to the calculated condensation sedimentation effect that causes the earlier arrival of helium at the vent pipe The snap shot shows a central cut of the steam and helium concentration some time before steam arrival at the vent. The helium concentration around the source is lower due

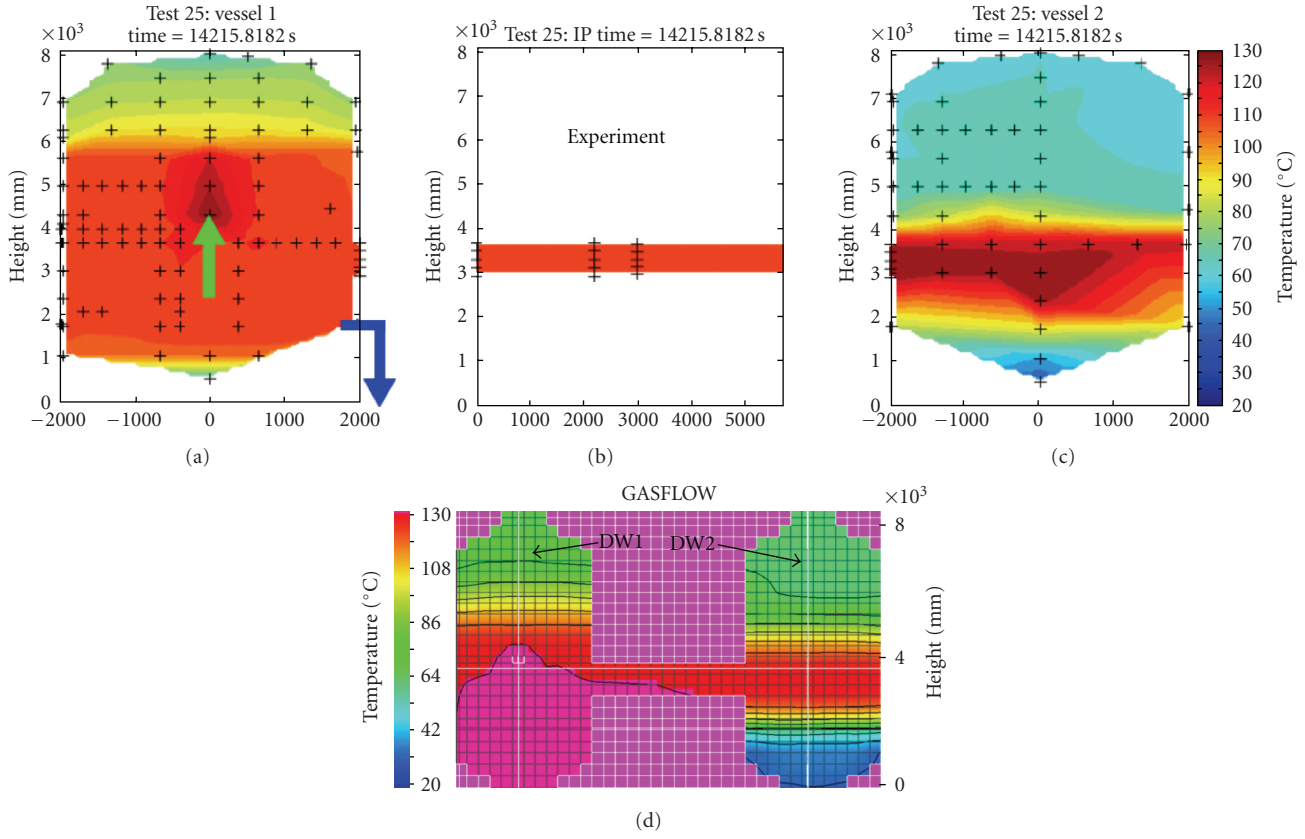

Figure 17: Final fluid temperatures test 25 at 14400 seconds.

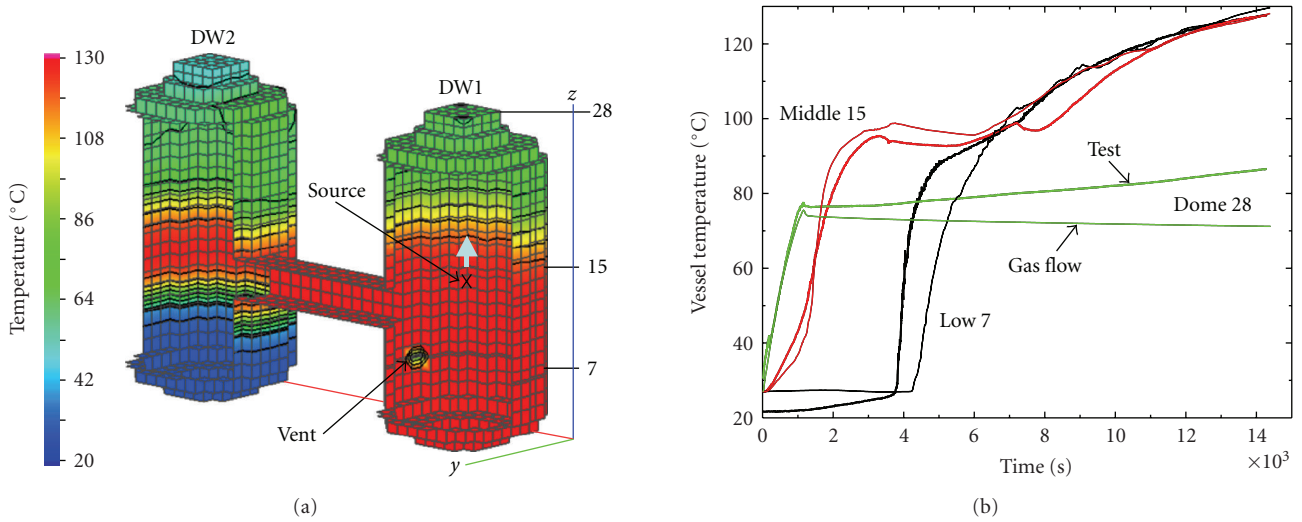

Figure 18: Final structure temperatures test 25 and test data for DW1.

to the steam, but it increases as the steam condenses away from the source and a heavier helium/air cloud with nearly no steam develops in DW1 below the interconnection pipe. The low sensor in Figure 11 records little helium at this time which is in agreement with the test data. The stronger than measured helium increase after 4000 seconds starts when the steam/helium overflow into DW2 has lead to a first equilibrium. Sharp interfaces to the pure air region at the bottom are calculated in GASFLOW and the temporarily higher than measured helium concentrations predicted in the low region of DW1 may be related to the difficulty to catch this lower helium front in phase 1. The 3D result animation in Figure 16 with the steam and helium clouds near the end of phase 1 displays this sharp interface in DW1. In the test, it must have occurred at a somewhat higher location.

Figure 17 compares the calculated and measured final fluid temperatures. The high temperatures indicate the steam regions under the colder region with stratified helium. They are well reflected also in the GASFLOW results. The color scaling differs from the test data, however. The hot steam region is calculated to expand deeper into DW1 than what is shown by the test data and the gas temperature in the dome is somewhat lower than measured. The temperatures in DW2 agree fairly well with the test data. Vessel temperatures in Figure 18 also show low values in the region next to the stratified helium cloud in the dome of DW1 and higher fairly uniform temperatures in the steam cloud underneath. Agreement with the measured data in DW1 is quite good except for the slight increase in the dome region, which is not reflected in the displayed node 28. This GASFLOW node already includes the full heat capacity in the man hole region and cannot follow the temperature increase induced by the gas compression. Figure 18 also shows the applied 3D Cartesian GASFLOW model of the test facility that was simulated adiabatic on the outside as a composite structure with 2 cm steel and 20 cm rock wool assuming 1D heat conduction with 44 nodes with 4 nodes in the steel wall and 40 nodes in the insulation. The vessel thickness was doubled in the two uppermost nodes due to the thicker structure in the man hole region. The temperature profile in the structure shows a flat behavior in the steel and a hyperbolic decay toward the outside of the insulation for which only a 10 degree temperature increase is calculated over the simulation period of 14,400 seconds. This demonstrates negligible heat losses in the analyzed test period and justifies the use of the adiabatic boundary condition.

5. Conclusions

The GASFLOW simulations for the selected Panda tests 9 and 9bis have shown that in the absence of condensation the results with the finest mesh agree well with other calculations for test 9 at the compared reference time of 250 seconds, yet all give higher than measured temperatures. Coarser meshes locally mix mass, momentum and energy too fast, yet globally they give nearly the same results as the fine mesh. This holds both for tests 9 and 9bis. Convergence of local data could not be reached with the different meshes. But the successful interpretation of tests 9 and 9bis demonstrates that broad atmospheric changes can be captured with coarse meshes quite well. Transient locally heterogeneous conditions will not impact much and do not have to be zoomed with extra-fine meshes. GASFLOW calculations with coarse meshes for test facilities of widely different sizes (up to full containments like HDR in test E11.2) [2] confirm that one can reliably predict thermal-hydraulic processes in full reactor containments with such models. The failure to properly determine the volume rates at the vent in test 21bis indicates that a moving film model may be a desirable feature for implementation. Both tests 9bis and 21bis are well suited for testing and further improving the steam condensation/vaporization modeling in CFD codes.

Our analysis predicts the high-concentration stable helium layers in test 25 quite well in both DW1 and DW2 that result from the steam condensation out of the source gas mixture on the cold vessel walls. This includes a good simulation of helium accumulation in a dead end compartment, like it is found in many reactor containments. The earlier arrival of helium relative to steam at the vent pipe in test 25 far below the injection source was well predicted. It is related to the fact that steam/helium/air mixtures can temporarily get heavier on condensing walls and give a secondary convection that brings down helium (hydrogen) into the lower region of the containment. As more and more helium is added these dried helium/steam/air layers become lighter and contribute to the stratified gas region. The measured temporary condensation sedimentation effect (motion under negative buoyancy) in test 25 is of relevance also for containment applications. They exhibit such effect in many scenarios because hydrogen/steam injections barely reach high enough hydrogen volume fractions for a condensation stratification. On larger time scales higher hydrogen concentrations are thus often accumulated in the lower rather than in the upper containment regions. Test 25 validates this predicted sedimentation effect from containment analyses with GASFLOW that has sometimes been questioned.

Test 25 also shows up conditions under which one can reach hydrogen clouds with high volume fractions in certain regions of the containment. The composition of the steam/helium source with 36% helium and 64% steam is quite representative for certain SBLOCA source terms. The high and potentially sensitive helium volume fraction of 85% can develop from steam condensation when the steam/helium source fills the dome by expelling air through the vent line. Without venting the source gas mixes with air and the heavy air component effectively drives the atmospheric mixing during steam condensation. Subregions with air displacement can be found in the component rooms of Konvoi-type containments [8] under certain opening conditions of the rupture disks, also in the steam generator boxes of VVER type containments [10] where the communication paths with the dome are not sufficient to circulate the expelled air back through other openings. Such recirculation paths and the amount of air replacement must be considered with more detail in the effected containment regions, with the help of detailed CFD analysis.

The condensation phenomena controlling this test are relevant for all accident scenarios in reactor containments. Their good interpretation backs up the predictive quality of GASFLOW for full containment simulations. The coarse model applied in the simulation of the facility was sufficient for capturing the dominant phenomena. Using the GASFLOW option to strongly reduce the area of the feeding source cell to match the injection momentum turned out to give too much local entrainment at the source so that this parameter should not be applied to inject with the correct momentum in a coarse mesh. The wall functions to describe heat, mass and momentum transfer in a coarse mesh still require further work to arrive at a heat transfer that is mesh independent when approaching stagnant conditions.

Acknowledgments

Dr. Michele Andreani from the Paul Scherrer Institute, Switzerland, contributed to this work and gave many details on all experiments and on their current status of interpretation with other CFD codes. He also shared the results from his GOTHIC analysis of test 25 for comparison and solving of open questions from our analysis. This work was partially funded with a research grant from the brain pool program of the Korean government. The authors are also grateful for the financial support of the participating countries to the joint cooperative SETH project run under the auspices of the Nuclear Energy Agency, Organization for Economic Cooperation and Development.

References

[1] P. Royl, U. J. Lee, Travis, et al., 2007, http://www.gasflow.net/.

[2] P. Royl, P. U. J. Lee, J. R. Travis, and W. Breitung, "Benchmarking of the 3D CFD code GASFLOW II with containment thermal hydraulic tests from HDR and ThAI," in *Proceedings of the CFD4NRS Meeting*, Munich, Germany, 2006.

[3] O. Auban, R. Zboray, and D. Paladino, "Investigation of large-scale gas mixing and stratification phenomena related to LWR containment studies in the PANDA facility," *Nuclear Engineering and Design*, vol. 237, no. 4, pp. 409–419, 2007.

[4] D. Paladino, R. Zboray, P. Benz, and M. Andreani, "Three-gas-mixture plume inducing mixing and stratification in a multi-compartment containment," in *Proceedings of the 12th International Topical Meeting on Nuclear Reactor Thermal Hydraulics (NURETH 12)*, Pittsburgh, Pa, USA, 2007, abstract no. 195.

[5] M. Andreani, "Comparison between simulations and experiments," in *Proceedings of the 9th Meeting of the Program Review Group OECD SETH Project*, Villingen, Germany, May 2005.

[6] M. Andreani, K. Haller, M. Heitsch, et al., "A benchmark exercise on the use of CFD codes for containment issues using best practice guidelines: a computational challenge," *Nuclear Engineering and Design*, vol. 238, no. 3, pp. 502–513, 2008.

[7] M. Andreani, D. Paladino, and T. George, "Simulations of basic gas mixing tests with condensation in the Panda facility using the Gothic code," in *Proceedings of the 16th International Conference on Nuclear Engineering (ICONE '08)*, Orlando, Fla, USA, 2008.

[8] P. Royl, H. Rochholz, W. Breitung, J. R. Travis, and G. Necker, "Analysis of steam and hydrogen distributions with PAR mitigation in NPP containments," *Nuclear Engineering and Design*, vol. 202, no. 2-3, pp. 231–248, 2000.

[9] P. Royl, J. R. Travis, W. Breitung, J. Kim, T. Kanzleiter, and S. Schwarz, "GASFLOW analysis of steam/hydrogen mixing with nitrogen in the OECD-NEA THAI HM-2 Benchmark," in *Proceedings of the NURETH 13*, Kanazawa, Japan, September-October 2009, paper N13P1412.

[10] U. J. Lee, P. Royl, et al., "Three dimensional analyis of steam-hydrogen distribution from a hypothetical small break severe accident in a VVER1000 type reactor containment using GASFLOW II," in *Proceedings of the NURETH-10 Conference*, Seoul, Korea, 2003.

Hindawi Publishing Corporation
Science and Technology of Nuclear Installations
Volume 2009, Article ID 862934, 7 pages
doi:10.1155/2009/862934

Research Article

Non-Boussinesq Integral Model for Horizontal Turbulent Buoyant Round Jets

J. Xiao,[1] J.R. Travis,[2] and W. Breitung[1]

[1] *Institute for Nuclear and Energy Technologies, Forschungszentrum Karlsruhe, P.O. Box 3640, 76021 Karlsruhe, Germany*
[2] *Dubois, Pitzer, Travis GmbH, Offenbach, Germany*

Correspondence should be addressed to J. Xiao, jianjun.xiao@iket.fzk.de

Received 19 November 2008; Accepted 25 May 2009

Recommended by Xu Cheng

Horizontal buoyant jet is a fundamental flow regime for hydrogen safety analysis in power industry. The purpose of this study is to develop a fast non-Boussinesq engineering model the horizontal buoyant round jets. Verification of this integral model is established with available experimental data and comparisons over a large range of density variations with the CFD codes GASFLOW. The model has proved to be an efficient engineering tool for predicting horizontal strongly buoyant round jets.

1. Introduction

Turbulent buoyant jet is a fundamental flow regime in hydrogen safety analysis since it affects hydrogen distribution and mitigation measures when accidents occur [1]. Recent works on the numerical simulation of helium and steam jet release experiments in the German THAI facility have shown that the Helium distribution (simulating hydrogen) may depend sensitively on the jet modeling [2]. A systematic investigation was therefore started on numerical modeling of horizontal turbulent buoyant jets [3].

Few experimental data and calculations on horizontal turbulent buoyant jet with large density variation can be found in the open literatures. Most of the experiments were carried out for the small density variation when the Boussinesq approximation is valid. Pantokratoras [4] modified the integral Fan-Brooks model [5] to calculate the horizontal penetration of inclined thermal buoyant water jets, and the modified model predictions are in a good agreement with the trajectory measurements. Jirka [6, 7] formulated integral model, namely, CorJet for turbulent buoyant jets (round and planar) in unbounded stratified flows, that is, the pure jet, the pure plume, the pure wake. Guerra [8] simulated horizontal buoyant jets (64% helium into air with various inlet velocity) using CFD code FLOVENT, but unfortunately his work is only from calculation results and he did not provide any experiment data for this case. Swain [9, 10] studied horizontal round hydrogen jets and determined the maximum horizontal distance at which a horizontal hydrogen leak can be ignited. Houf and Schefer [11] developed a model to study the small leaks of hydrogen in the Froude number range where both buoyant and inertial forces are important.

In this study non-Boussinesq integral model for horizontal buoyant round jet was derived with the modified entrainment hypothesis. The system of conservation equations of the integral model was solved by a forth order Runge-Kutta method to obtain numerical solutions in the transition region from jet-like to plume-like.

The problem description and modeling efforts are presented in Sections 2 and 3. Sections 4 and 5 documents the validation and modeling uncertainties of the integral model. The concluding remarks are given in Section 6.

2. Problem Description

The horizontal buoyant jet formed from a round orifice is discharged into the unbounded stagnant uniform ambient, as shown in Figure 1. The density of the ambient is ρ_a. The axis of the jet is taken as a parametrical coordinate s, and the coordinate n is taken to be normal to the axis s. θ is the angle of s-axis with the horizontal direction. The initial density, velocity, and diameter in the orifice are ρ_0, U_0, r_0. The density and velocity along the s-axis are ρ_s , u_s.

3. Formulation of Horizontal Buoyant Jets

3.1. Basic Governing Equations. In this study, the pressure across the flow is assumed to be uniform and equal to the ambient pressure outside of the boundary. The basic governing equations (neglecting the dissipation and turbulent transport in comparison with the mean flow) consist of mass, momentum, energy, and concentration conservation equations,

$$\begin{aligned}
\nabla \cdot \left(\rho \, \vec{u}\right) &= 0, \\
\frac{\partial(\rho u u_i)}{\partial x} &= 0, \\
\frac{\partial\left(\rho u u_j\right)}{\partial y} &= \Delta\rho g, \\
\nabla \cdot \left(\rho \, \vec{u} \, h\right) &= 0, \\
\nabla \cdot \left(\rho \, \vec{u} \, \phi_m\right) &= 0,
\end{aligned} \tag{1}$$

where h is the specific enthalpy and Φ_m is the mass concentration.

The divergence theorem is applied, and the basic governing equations become

$$\begin{aligned}
\frac{d}{ds}\int_0^{2\pi}\int_0^{\infty}(\rho u) r \, dr \, d\varphi &= 2\pi\beta_{j-p} b \rho_a u_s = E_m, \\
\frac{d}{ds}\int_0^{2\pi}\int_0^{\infty}(\rho u u \cos\theta) r \, dr \, d\varphi &= 0, \\
\frac{d}{ds}\int_0^{2\pi}\int_0^{\infty}(\rho u u \sin\theta) r \, dr \, d\varphi &= \int_0^{2\pi}\int_0^{\infty}(\rho_a - \rho) g r \, dr \, d\varphi, \\
\frac{d}{ds}\int_0^{2\pi}\int_0^{\infty}[\rho u (C_P T - C_{Pa} T_a)] r \, dr \, d\varphi &= 0, \\
\frac{d}{ds}\int_0^{2\pi}\int_0^{\infty}(\rho u \phi_m) r \, dr \, d\varphi &= 0, \\
\frac{dx}{ds} &= \cos\theta, \\
\frac{dy}{ds} &= \sin\theta,
\end{aligned} \tag{2}$$

where E_m is the local mass entrainment rate and α_{j-p} is the local mass entrainment coefficient.

A system of first-order ordinary differential equations was obtained after the integration, where the seven unknowns are the density, velocity, temperature along the trajectory, ρ_s, u_s, T_s, the characteristic jet width b, the local angle of the jet with respect to the horizontal axis θ, and the local coordinates of the jet trajectory x, y. With initial conditions, the system of ordinary differential equations was solved by aforth order Runga-Kutta method to obtain the horizontal buoyant jet trajectory, the velocity, the density, the temperature and the tracer concentration.

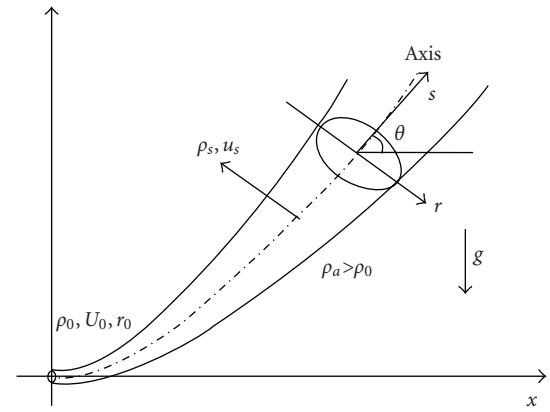

Figure 1: Definition diagram for horizontal buoyant jet discharges from round orifice into the unstratified ambient.

3.2. Basic Assumptions. The general assumptions made in this investigation are as follows.

(1) The flow is fully turbulent which means there is no Reynold number dependence.

(2) The profiles of velocity, density, and temperature are similar at all cross-sections normal to the jet trajectory.

(3) Longitudinal turbulent transport is small compared with latitudinal convective transport.

3.3. Profiles of Velocity, Density, and Temperature. Velocity profile is assumed to be Gaussian distribution:

$$u = u_s e^{-r^2/b^2}, \tag{3}$$

where b is a characteristic jet width.

Density deficiency profile with respect to the ambient density in a uniform ambient is assumed to be Gaussian:

$$\frac{\rho_a - \rho}{\rho_a} = \left(\frac{\rho_a - \rho_s}{\rho_a}\right) e^{-r^2/(\lambda b)^2}, \tag{4}$$

where λb is the characteristic length of the profiles; λ^2 is the turbulent Schmidt number, which is assumed to be constant and is usually found to be somewhat larger than 1 for small density ratio cases. In this study λ is 1.2. It should be noted that λ^2 is not necessarily constant as the buoyant jet evolves from jet-like to plume-like.

Due to the large density or temperature variation between the jet and the ambient considered in the non-Boussinesq model, the density in the trajectory ρ_s is the function of temperature T_s and mass faction Φ_{ms}. Therefore, the energy equation should be solved. It is well known that the cross-sectional profiles of normalized mean axial velocity and concentration are Gaussian-like in the zone of established flow (ZEF). In this study, the profile of temperature is also assumed to be Gaussian distribution:

$$\frac{T_a - T}{T_a} = \left(\frac{T_a - T_s}{T_a}\right) e^{-r^2/(\lambda b)^2}, \tag{5}$$

3.4. Entrainment Hypothesis. To close the equations system, the mass entrainment rate should be specified. The entrainment relation for the horizontal round jet is given by:

$$E_m = 2\pi b\rho_a u_e = 2\pi\alpha_{j-p} b\rho_a u_s, \tag{6}$$

where E_m is the local mass entrainment rate, u_e is the local entrainment velocity, u_s is the characteristic velocity along s-axis, ρ_s is the local density along s-axis, ρ_a is the density of ambient, and α_{j-p} is the local mass entrainment coefficient .

For low-momentum buoyant jets, experimental data indicates that the local rate of entrainment increases as the jets leaves the momentum-dominated region and enters a region where the effects of buoyancy become more pronounced. In Jirka's paper [6], the local rate of entrainment is specified as

$$E_m = 2\pi b U_s\left(\alpha_j + \alpha_p \frac{Fr_p^2}{Fr_s^2}\sin\theta\right). \tag{7}$$

List summarized much of the work on the entrainment hypothesis and proposed values of $\alpha_j = 0.052 \pm 0.003$ for the pure jets and $\alpha_p = 0.0833 \pm 0.0042$ for the pure plumes [12]. To model the entrainment in the region of transition from jet-like to plume-like, an empirical function for the vertical plane jet proposed,

$$\alpha_{j-p} = \alpha_j + \left(\alpha_p - \alpha_j\right)\left(\frac{Ri_{j-p}}{Ri_p}\right)^2, \tag{8}$$

Ri_{j-p} is the local Richardson number in the trajectory which is defined as

$$Ri_{j-p} = \frac{m\beta^{1/2}}{mo^{5/4}}, \tag{9}$$

where m is the mass flux, mo is the momentum flux, β is the local buoyancy flux. The Richardson number in the pure plume region Ri_p is a constant.

In the non-Boussinesq model, the effect of large density variation should be considered in the entrainment coefficient. In this study the local entrainment coefficient for the horizontal buoyant jet is assumed as:

$$\alpha_{j-p} = \left[\alpha_j + \left(\alpha_p - \alpha_j\right)\left(\frac{Ri_{j-p}}{Ri_p}\right)^2 \sin\theta\right] * \left(\frac{\rho_s}{\rho_a}\right)^{1/2} \tag{10}$$

for the round jet, the exponent is 1/2, $\alpha_j = 0.055$ for the pure jets and $\alpha_p = 0.085$ for the pure plume. We should note that the value of α_j here is obtained from the flow with low velocity. For the flow with high velocity, α_j may be varied. It will be discussed in the section of modeling uncertainties.

4. Validations

4.1. Pure Jet. For the pure jet ($\theta = 0°, \rho_a = \rho_0$), there is no buoyancy acting on the flow and the jet is only dominated by the momentum. The conservation equations of the pure jet can be expressed as:

$$\frac{d}{ds}(\pi\rho_a u_s b_s^2) = 2\pi\alpha_{\text{jet}}\rho_a u_s b_s,$$
$$\frac{d}{ds}\left(\frac{\pi}{2}\rho_a u_s^2 b_s^2\right) = 0, \tag{11}$$
$$\frac{d}{ds}\left(\frac{\pi\lambda^2}{1+\lambda^2} c_s u_s b_s^2\right) = 0.$$

The ratio of u_s and the initial velocity U_0 is,

$$\frac{u_s}{U_0} = \frac{\sqrt{2}}{4\alpha_j}\left(\frac{s}{D_0}\right)^{-1}. \tag{12}$$

The centerline dilution is,

$$\frac{1+\lambda^2}{\lambda^2} S_c = \left(\sqrt{8\pi}\alpha_j\right)\frac{s}{D_0}. \tag{13}$$

The centerline velocity decay and concentration dilution are shown in Figures 2 and 3. When α_{jet} and λ are 0.055 and 1.2, the results of the non-Boussiensq integral model developed in this study have good agreement with the experimental data and the analytical solutions in (12) and (13).

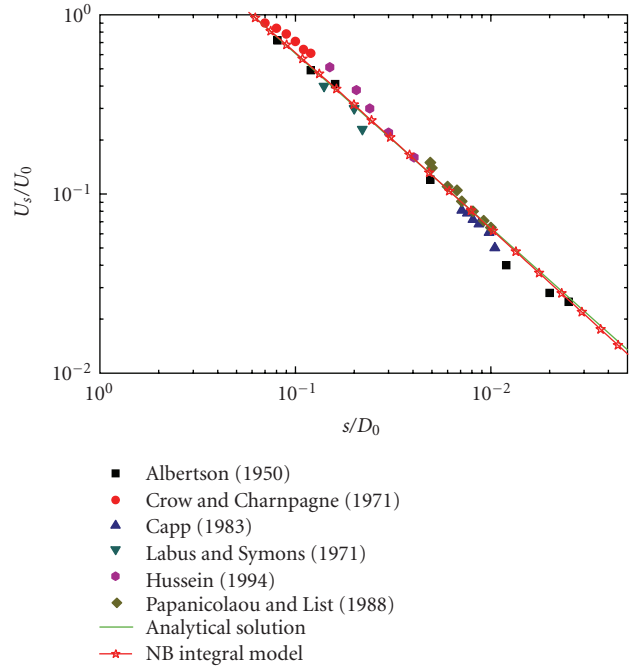

FIGURE 2: Centerline velocity decay for pure jets.

4.2. Bouyant Jet with Small Density Variation. The horizontal buoyant jets with small density variations (<5–10%) are predicted with the non-Boussinesq integral model. The nitrogen (300 K, 1 bar) is injected horizontally into the ambient (300 K, 1 bar) with various initial Froude numbers. Figure 4 shows the normalized vertical trajectory Y/L_M as a function of X/L_M for a variety of experimental conditions

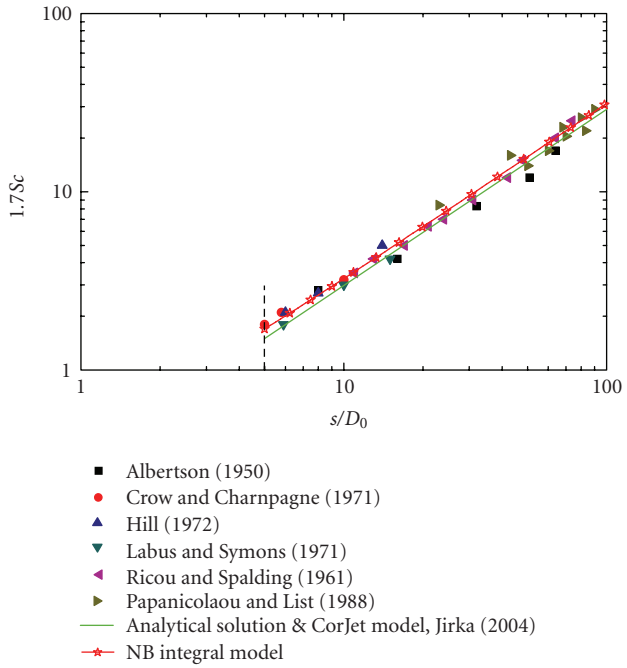

Figure 3: Concentration decay along the centerline for pure jets.

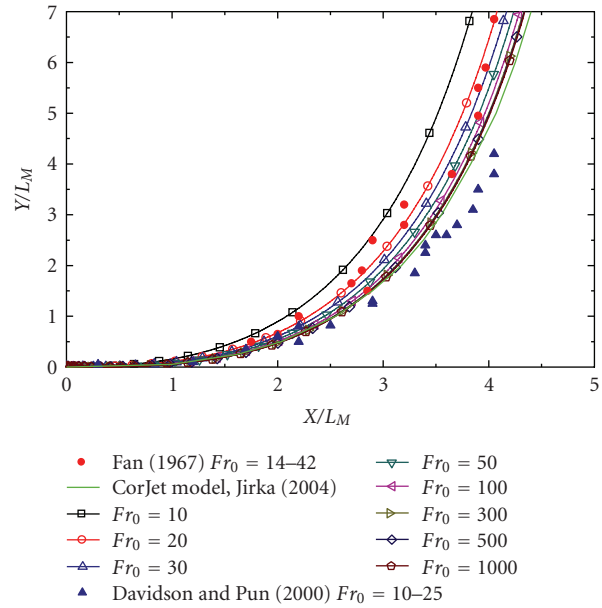

Figure 4: Normalized trajectories of horizontal buoyant jet.

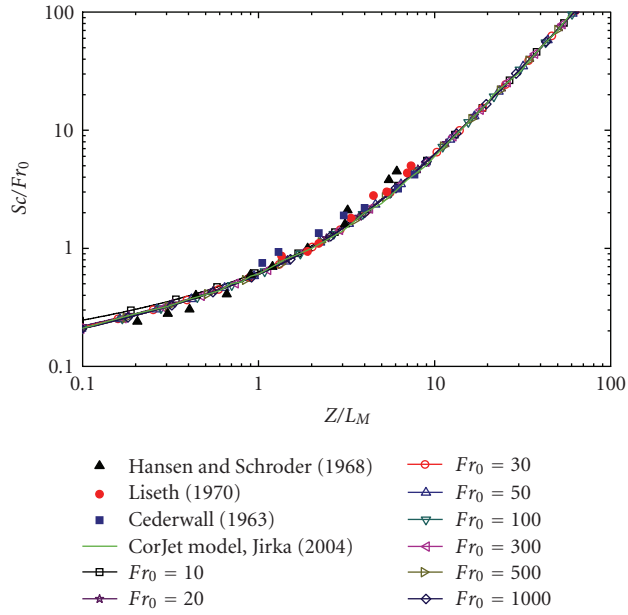

Figure 5: Normalized centerline dilutions of horizontal buoyant jet.

and the comparisons of the non-Boussinesq integral model and the Boussinesq-based CorJet model.

The length scale L_M for the transition of horizontal buoyant round jet to plume is defined as

$$L_M = \frac{mo_0^{3/4}}{j_0^{1/2}}, \tag{14}$$

where

$$mo_0 = U_0^2 A_0,\ j_0 = U_0\left(\frac{(\rho_a - \rho_0)g}{\rho_0}\right)A_0. \tag{15}$$

The normalized centerline dilution$\mathrm{Sc}/\mathrm{Fr}_0$ as a function of Y/L_M is depicted in Figure 5. The Froude number is:

$$Fr_0 = \frac{U_0}{\sqrt{((\rho_a - \rho_0)g/\rho_0)R_0}}. \tag{16}$$

The predictions of non-Boussinsq model agree well with the experimental data. When the initial Froude number Fr_0 is high enough the non-Boussinesq model's results will collapse to the CorJet model. It indicates that in high Froude number flow the influence of small density variation can be neglected. However in the flows with low Froude numbers it seems that the effects of the buoyancy should be considered. The normalized trajectory will not collapse when the Froude number is small which means the Boussinesq approximation is invalid when the buoyancy effect is comparative with the momentum effect.

The non-Boussinesq integral model provides a satisfactory transition behavior for the horizontal buoyant jets with small density variations from the jet-like to plume-like region. Figures 6, 7, and 8 depict the predictions of non-Boussineq integral model: the decays of velocities, Froude numbers, and the entrainment coefficients along the centerline of the horizontal buoyant jets.

4.3. Buoyant Jet with Large Density Variation. The horizontal buoyant jets with large density variations, for instance hydrogen or helium injecting into air, have not received sufficient research before, and almost no experimental data could be found in the open literature. CFD code GASFLOW [13, 14] was used to validate the non-Boussinesq integral model. Helium at 300 K, 1 bar is injected into the air (300 K, 1 bar) with various efflux velocities. The diameter of the orifice is 0.0845 m.

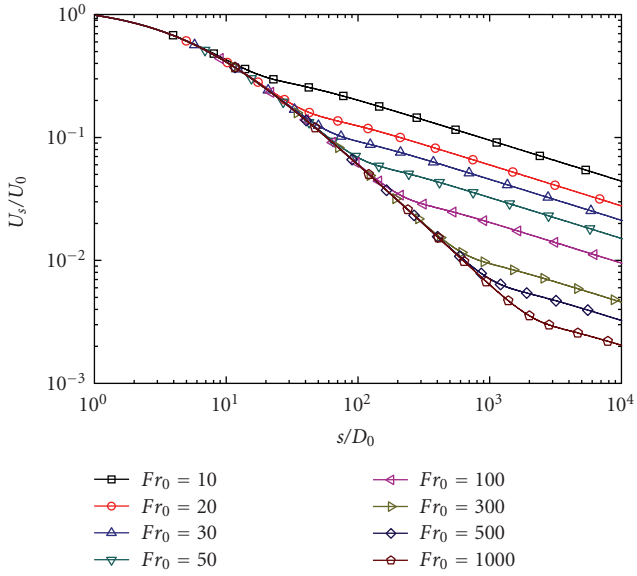

Figure 6: Velocity decay of horizontal buoyant jet.

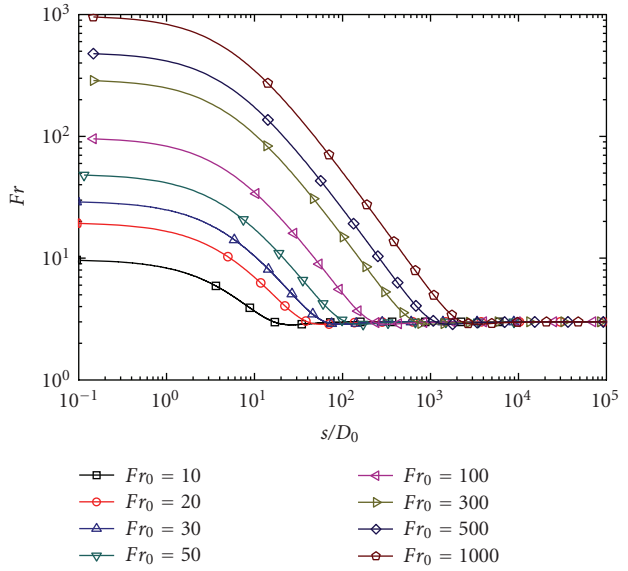

Figure 7: Froude number decay of horizontal buoyant jet.

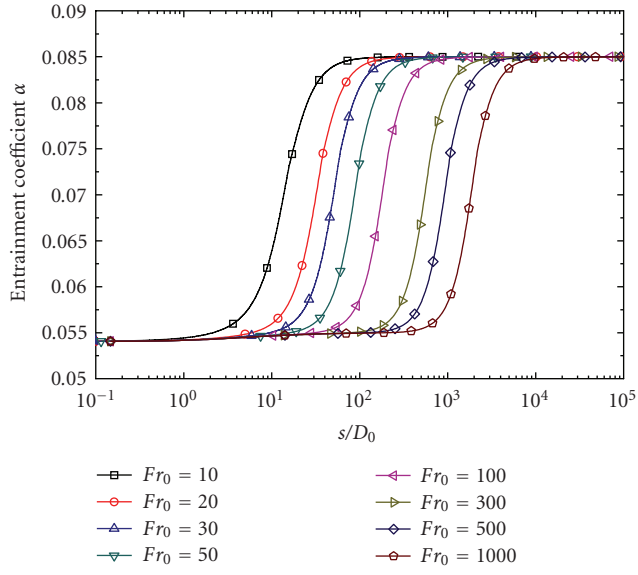

Figure 8: Entrainment coefficients of horizontal buoyant jet.

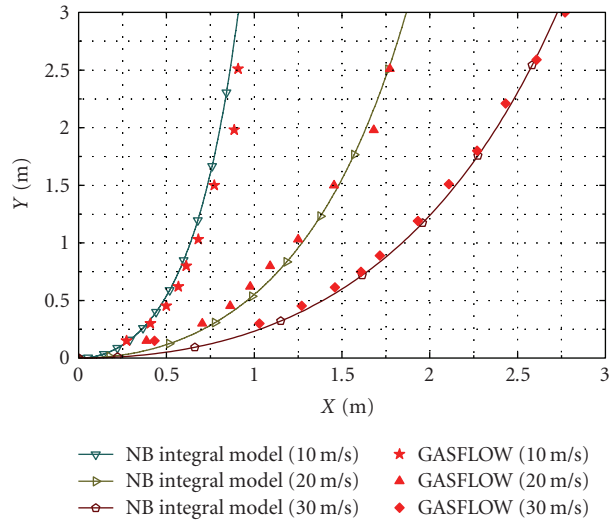

Figure 9: Trajectories of horizontal buoyant jet with large density variations.

Figure 9 shows the trajectories of the horizontal buoyant jets. The non-Boussinesq integral model also provides good transition behavior for the horizontal buoyant jets with large density variations. The decays of the velocity and concentration along the trajectory are shown in Figures 10 and 11. Although small discrepancies exist between the results of the integral model and CFD code GASFLOW, the non-Boussinesq integral model is capable of predicting the horizontal buoyant jets with large density variations. Experimental data are expected for the further validation of the model.

5. Modeling Uncertainties

Before the Gaussian profiles are reached, the initial unsheared profiles undergo changes in form of peripherally growing axis symmetric mixing layers. This initial region is called the zone of flow establishment which lacks of self-similarity. The transition in this region is complex and rapid, and the distance is up to 5–10 diameter of the orifice. A distance of 5–10 diameters from the orifice is shifted in the study.

The mass entrainment coefficients in this study were obtained under the experimental conditions when the velocity and density variation are not so high. How the high velocity and large density variation affect the entrainment coefficient is not clear. In the recent simulation of the underexpanded hydrogen jet [15], it indicates that the entrainment coefficient for the pure jet, α_j, increases from 0.055 to 0.065–0.07 when the velocity is sonic or supersonic.

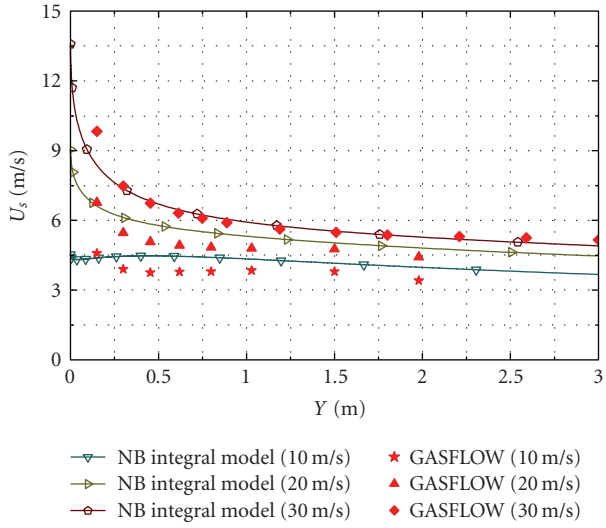

FIGURE 10: Velocity decay of horizontal buoyant jet with large density variations.

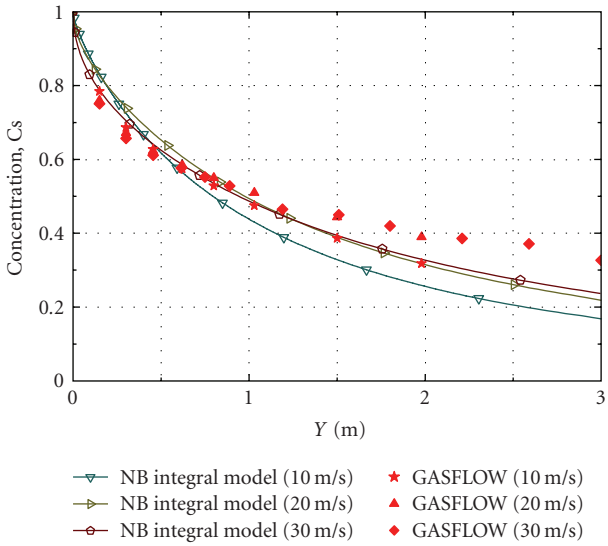

FIGURE 11: Concentration decay of horizontal buoyant jet with large density variations.

The mechanisms of these uncertainties needs further study in the future work.

6. Concluding Remarks

This non-Boussinesq integral model developed in the study is a fast engineering model to solve the horizontal buoyant round jets problems. The model was validated by the pure jet, horizontal buoyant jets with small/large density variations, and good agreements with the experimental data, and CFD predictions were obtained.

For strongly buoyant jet the Boussinesq approximation is violated which will over-predict the mass entrainment and under-estimate the buoyancy effect [16]. It reveals that the Boussinesq approximation is valid when the density variation is less than 10%.

The entrainment assumption is a key requirement for the integral model. The entrainment assumption taking into account the Richard number and the angle θ was used in the integral model, and satisfactory predictions for the modeling of horizontal buoyant jets were provided. The effects of large density variation and high velocity on the entrainment coefficient need further study in the future.

References

[1] W. Breitung, "State of the art report on containment thermal hydraulics and hydrogen distribution," OECD/NEA, 1999.

[2] P. Royl, U. J. Lee, J. R. Travis, and W. Breitung, "Benchmark of the 3D CFD code GADFLOW II with containment thermal hydraulic tests from HDR and THAI," in *CFD4NRS Conference*, Munich, Germany, September 2006.

[3] J. Xiao, J. Travis, and W. Breitung, "Numerical simulation of free horizontal turbulent buoyant planar jets and plumes," in *Proceedings of the Annual Meeting on Nuclear Technology*, Karlsruhe, Germany, May 2007.

[4] A. Pantokratoras, "Horizontal penetration of inclined thermal buoyant water jets," *International Communications in Heat and Mass Transfer*, vol. 25, no. 4, pp. 561–569, 1998.

[5] L. N. Fan and N. H. Brooks, *Numerical Solution of Turbulent Buoyant Jets Problems*, California Institute of Technology, Pasadena, Calif, USA, 1969.

[6] G. H. Jirka, "Integral model for turbulent buoyant jets in unbounded stratified flows—part I: single round jet," *Environmental Fluid Mechanics*, vol. 4, no. 1, pp. 1–56, 2004.

[7] G. H. Jirka, "Integral model for turbulent buoyant jets in unbounded stratified flows—part 2: plane jet dynamics resulting from multiport diffuser jets," *Environmental Fluid Mechanics*, vol. 6, no. 1, pp. 43–100, 2006.

[8] D. Guerra, *Modelisation du transfert d'un aerocontaminant dans un local ventile en champ proche d'une source d'emission accidentelle*, Ph.D. thesis, Polytechnique of Toulouse, Toulouse, France, 2004.

[9] M. Swain, "Codes and standards analysis, 2004 annual program review meeting of the hydrogen," Fuel cell & infrastructure program of the US DOE, 2004.

[10] M. Swain, "Hydrogen properties testing and verification," in *Proceedings of the Fuel Cell Summit Meeting*, Coral Gables, Fla, USA, June 2004.

[11] W. Houf and R. Schefer, "Small-scale unintended releases of hydrogen," in *Proceedings of the Annual Hydrogen Conference and Hydrogen Expo*, San Antonio, Tex, USA, March 2007.

[12] W. Rodi, *Turbulent Buoyant Jets and Plumes*, vol. 6 of *HMT The Science & Applications of Heat and Mass Transfer*, Pergamon Press, Oxford, UK, 1982.

[13] J. R. Travis, J. W. Spore, P. Royl, et al., *GASFLOW: A Computational Fluid Dynamics Code for Gases, Aerosols and Combustion. Volume 1: Theory and Computational Model*, FzK and LANL, 2001.

[14] J. R. Travis, J. W. Spore, P. Royl, et al., *GASFLOW: A Computational Fluid Dynamics Code for Gases, Aerosols and Combustion. Volume 2: User's Manual*, FzK and LANL, 2001.

[15] A. Veser, G. Stern, M. Schwall, et al., "Structure and flame propagation regimes in turbulent hydrogen jets," in *Proceedings of 7th International Symposium on Hazards, Prevention, and Mitigation of Industrial Explosions*, vol. 1, pp. 198–207, Saint-Petersburg, Russia, July 2008.

[16] J. Xiao, J. Travis, and W. Breitung, "Non-boussinesq integral model for horizontal turbulent strongly buoyant plane jets," in *Proceedings of the 16th International Conference on Nuclear Engineering*, Orlando, Fla, USA, May 2008.